EFFECT OF SOME ISOVALENT AND ALIOVALENT SUBSTITUTIONS ON STRUCTURE AND FERROELECTRIC PROPERTIES OF $BaBi_4Ti_4O_{15}$

A Thesis Submitted in Partial Fulfillment of the
Requirements for the Degree of

DOCTOR OF PHILOSOPHY

by

ARUNDHATI CHAKRABARTI
(Roll No: 50708001)

Supervisor:

Dr. Japes Bera

DEPARTMENT OF CERAMIC ENGINEERING
NATIONAL INSTITUTE OF TECHNOLOGY, ROURKELA,
ORISSA, INDIA
JANUARY, 2011

DEDICATED TO MY
BELOVED
PARENTS
&
HUSBAND

NATIONAL INSTITUTE OF TECHNOLOGY
ROURKELA, INDIA

CERTIFICATE

This is to certify that the thesis entitled "**Effect of some Isovalent and Aliovalent Substitutions on Structure and Ferroelectric Properties of $BaBi_4Ti_4O_{15}$**" being submitted by Arundhati Chakrabarti for the degree of Doctor of Philosophy in Engineering from N.I.T. Rourkela, is a record of bonafied research work carried out by her under my supervision at Department of Ceramic Engineering. In my opinion, this is a fit piece of work for submission for the degree of Doctor of Philosophy. To the best of our knowledge, the work has not been submitted to any other University or Institute for the award of any degree or diploma.

(Dr. J. Bera)
Head and Associate Professor,
Department of Ceramic Engineering,
N. I. T. Rourkela, Rourkela- 769008.
E-mail id: jbera@nitrkl.ac.in, jbera@rediffmail.com, japesb@gmail.com
Phone No: +91-661-2462204 (O), +91-661-2463204 (R), +91-9437246159 (M)

CONTENTS

Page No

1. Introduction

2. Literature Review

3. Experimental Work

4. Results and Discussion

4.1. Synthesis of $BaBi_4Ti_4O_{15}$ through modified chemical route

4.2. La^{3+}substitution for Bi^{3+} in $BaBi_4Ti_4O_{15}$

4.3. Zr^{4+}substitution for Ti^{4+} in $BaBi_4Ti_4O_{15}$

4.4. Na^+ and La^{3+}substitution for Ba^{2+} in $BaBi_4Ti_4O_{15}$

4.5. Nb^{5+} and Al^{3+}substitution for Ti^{4+} in $BaBi_4Ti_4O_{15}$

4.6. Na^+ for Ba^{2+} and $Nb^{5+}$for Ti^{4+}substitution in $BaBi_4Ti_4O_{15}$

4.7. $Mg^{2+}/Ca^{2+}/Sr^{2+}/Ba^{2+}$ for Bi^{3+} and $Nb^{5+}$for Ti^{4+}substitution in $BaBi_4Ti_4O_{15}$

5. Conclusions and Future Work

ACKNOWLEDGEMENTS

The last few years that I spent at National Institute of Technology, Rourkela has been the source of the most valued experience of my life. I take this opportunity to express my gratitude to all who have directly and indirectly helped me through this journey in my humble acknowledgment.

I owe my deepest gratitude to my supervisor Prof. Japes Bera, Department of Ceramic Engineering, N. I. T. Rourkela, for his expert advice and unparallel guidance from the initial stage of this research. His wide knowledge and logical way of thinking have been of great value for me. Above all he provided me with constant encouragement and support. He has been as excellent mentor throughout the work and it would have not been possible for me to bring out this thesis without his help.

I extend my heart-felt thanks to Prof. Santanu Bhattacharyya, Department of Ceramic Engineering, for his keen interest in the progress of my work. I wish to record my thanks and gratitude to him for his valuable suggestions and encouragements.

I am also grateful to Prof. S. K. Pratihar, Department of Ceramic Engineering, for his constructive suggestions and fruitful discussions at various stages of my research work.

I would like to extend my sincere thanks to Prof. B. B. Nayak, Prof. D. Sarkar, Prof. R. Mazumdar, Prof. S. K. Pal, Prof. R. Sarkar and Prof. A. Choudhury of Ceramic Engineering Department for their useful suggestions and help whenever I had asked for it.

I sincerely thank Prof. P. Kumar, Department of Physics, for his wholehearted cooperation to carry out hysteresis loop measurement.

It was a nice association with all the staff of Ceramic Department. I wish to extend my thanks to them for their constant help.

I am also thankful to Bose Institute, Kolkata and CGCRI, Kolkata for permitting me to carry out the electrical measurements.

During this work I have collaborated with many friends for whom I have great regard, and I wish to extend my warmest thanks to Pradeep bhaiya, Kiran bhaiya, Rana bhaiya,Yuga bhaiya, Sarat, Subrat, Hemlata didi, Bhabani, Ganesh, Abhisek, Geetanjali who have helped me with my work and also in thesis preparation. I like to thank my research colleagues in Physics Department, Prakash and Naresh for their help and cooperation. I would like to take this opportunity to recall few of my best friends Evelyn, Kakoli, Nirupama, Liza, Anuj, Ved, Shekhar. Their friendship is a boon that my heart will always cherish. I would also like to thanks all my teachers and professors, form academic and nonacademic levels, who have inspired me. I am truly indebted to each and everyone who have supported me and brought me so far.

I am happy to acknowledge University of Grants Commission, New Delhi and N. I. T., Rourkela for sponsoring me.

Above all, I owe a deepest sense of indebtedness to my beloved parents Mr. Dilip Kumar Chakrabarti & Mrs. Kaberi Chakrabarti for their unconditional love, affection and immeasurable support that they have given me at every stage of my life. This thesis could not have been accomplished without Subir Sen, my husband who is always with me no matter how dubious my decisions were. He always gives me encouragement and love in every situation. I thank each and every one of my family members for their love, unstinted moral support and wishes they have provided me throughout my life, which has been a constant source of strength and encouragement in everything I do.

Finally, I thank God for his blessings which have guided me through the thick and thin of my life.

Arundhati Chakrabarti

ABSTARCT

Bismuth layer-structured ferroelectrics are commercially attractive for applications such as non-volatile random access memory and high temperature piezoelectric devices due to their excellent fatigue endurance, fast switching speed, good polarization retention and high Curie temperature. $BaBi_4Ti_4O_{15}$ is a four layered member of this family and is relaxor ferroelectrics. The aim of the present study is to investigate the effect of different substitution on the properties of $BaBi_4TiO_{15}$ ceramics.

The effect of some isovalent substitutions such as La^{3+}, Zr^{4+} and aliovalent substitutions such as Na^+, Al^{3+}, and Nb^{5+} on the structural, ferroelectric and piezoelectric properties of $BaBi_4Ti_4O_{15}$ were studied. The pure and substituted $BaBi_4Ti_4O_{15}$ powders were synthesized by a modified chemical route. The precursor powders were prepared by precipitating bismuth and barium oxalate in the TiO_2 powder suspension. Exothermic decomposition of oxalates facilitated the formation of $BaBi_4Ti_4O_{15}$phase at 600°C onwards. Pure phase was formed after calcinations of precursor powder at 1000°C. The material was sintered at ~1100°C. Pure $BaBi_4Ti_4O_{15}$ showed relaxor behaviour with a critical exponent $\gamma \sim 1.88$. Its d_{33} coefficient was ~11 pC/N.

La^{3+} was substituted for Bi^{3+}in the range $x \leq 1.0$ in $BaBi_{4-x}La_xTi_4O_{15}$.La^{3+} ions was found to occupy the Bi_2O_2 layer for compositions with $x \geq 0.5$. A significant increase in the diffuseness and relaxor behaviour were observed with increasing La^{3+}. The increase in the relaxor behaviour can probably be attributed to the compositional fluctuation induced by La^{3+},partly in perovskite and partly in Bi_2O_2 layers. The substitution also resulted in a significant reduction in the *dc* conductivity for x=0.3 composition.

In $BaBi_4Ti_{(4-x)}Zr_xO_{15}$ ceramics, the solid solubility limit for Zr^{4+} was up to x ~0.2. However, the lattice parameters increased beyond the solid solubility limit. Dielectric studies revealed the relaxor nature of the ceramics decreased with the substitution and vanished at x =

0.5 composition. The dielectric loss decreased for x = 0.2 composition. The permittivity-temperature peak broadened significantly with increase in Zr^{4+} concentration.

Na^+ and La^{3+} cations were substituted for Ba^{2+} in $BaBi_4Ti_4O_{15}$.The lattice parameters decreased with increase in substituent's concentration accompanied with a structural change from orthorhombic to tetragonal. The grain sizes of the ceramics increased with increase in substations. The substitutions suppressed the relaxor behaviour and decreased the loss.

$BaBi_4Ti_{4-x}(Nb_{x/2}Al_{x/2})O_{15}$ ceramics showed the solid solubility limit of $(Nb_{x/2}Al_{x/2})$ up to x ~0.2. The permittivity increased significantly accompanied by a decrease in dielectric loss of the ceramics. In addition to these, the polarization and the piezoelectric coefficients also enhanced.

In $Ba_{(1-x)}Na_xBi_4Ti_{(4-x)}Nb_xO_{15}$ceramics the solid solubility was in the composition range $0.1 \leq x \leq 0.5$, while the composition with $x = 0.6$, showed the presence of secondary phases like Bi_2O_3 and $Na_2Ti_3O_7$. The lattice parameters decreased with an increase in orthorhombicity with the substitution. The ceramics with $x = 0.2$ showed highest resistivity.

In $BaBi_{3.8}M_{0.2}Ti_{3.8}Nb_{0.2}O_{15}$ (M = Mg, Ca, Sr, Ba) ceramics, the crystal structure was orthorhombic in case of Mg-based compound and was tetragonal for Ca, Sr and Ba-based compounds. The detailed Rietveld analysis revealed that Mg^{2+} ions seemed to occupy the Bi_2O_2 layer compared to the other cations occupying A-site of perovskite block. Maximum relatively permittivity and d_{33} piezoelectric coefficient increased in Mg-based compound, while the relaxor behaviour and remnant polarization enhanced the Ba-based compound.

Keywords:

$BaBi_4Ti_4O_{15}$; Relaxor Ferroelectrics; Modified chemical route; Isovalent substitutions; Aliovalent substitutions; Structural analysis; Ferroelectric properties; Piezoelectric properties; Impedance spectroscopy.

LIST OF FIGURES

Chapter 1

Chapter 2

Chapter 3

Chapter 4

LIST OF TABLES

Chapter 3

Chapter 4

NOMENCLATURE

MAUD	Materials Analysis Using Diffraction
N	Avogadro's number
PVA	Polyvinyl alcohol
IPA	Isopropyl alcohol
λ	X-ray wavelength
θ	Bragg's angle
d'	Lattice spacing
n	Order of diffraction
JCPDS	Joint committee on powder diffraction standards
XRD	X-ray diffraction
V	Volume
W_d	Dry weight of the sample
W_s	Soaked weight of the sample
W_a	Suspended weight of the sample
I	Intensity
°C	Degree celsius
(hkl)	Miller index
a, b, c	Lattice parameter
t	Tolerance factor
P_{App}	Apparent porosity
D_{bulk}	Bulk density
ρ	X-ray density
N	Avogadro's number
M_W	Molecular weight

R_b	Bragg factor
R_{wp}	Weighted residual error
R_{exp}	Expected error
G	Goodness of fit
C	Capacitance
R	Resistance
R_g	Grain resistance
R_{gb}	Grain boundary resistance
C_g	Grain capacitance
C_{gb}	grain boundary capacitance
P	Polarization
ε_o	Permittivity of free space
ε'	Dielectric constant
ε_m'	Maximum dielectric constant
ε_{rm}	Room temperature dielectric constant
k_B	Boltzmann Constant
A	Area
d	Thickness
d_{33}	Piezoelectric coefficient
DSC	Differential Scanning Caloriemetry
TG	Thermo-Gravimetric Analysis
f	Frequency
I	Current
V	Voltage
s	Second
SEM	Scanning Electron Microscope
T	Absolute temperature in K
tanδ	Dielectric loss

$\tan\delta_{rm}$	Room temperature dielectric loss
$\tan\delta_m$	Dielectric loss at peak
T_c	Curie temperature
T_m	Maximum permittivity temperature
P_r	Remnant magnetization
E_c	Coercive field strength
E	Electric field
BLSFs	Bismuth layer-structured ferroelectrics
BBT	$BaBi_4Ti_4O_{15}$
FRAM	Ferroelectric Random Access Memory
Z'	Real part of impedance
Z''	Imaginary part of impedance
τ	Relaxation time
ω	Angular frequency

Chapter I

Introduction

1.1 Introduction

Bismuth layer-structured ferroelectrics (BLSFs) were first synthesized by Aurivillius in 1949 [1]. BLSFs are commercially applicable as ferroelectric non-volatile random access memory (FRAM) storage devices, high temperature piezoelectric device applications, sensor applications, and as photo-catalyst [2-5]. These BLSFs possess some exclusively attractive electrical properties such as excellent fatigue endurance, fast switching speed, good polarization retention, relatively high Curie temperature, low aging rate and low operating voltage [6-9].

FRAMs are non-volatile memory devices which employ ferroelectric capacitors. They can retain information even when the power supply is interrupted, making them an important component in the computers. FRAM circuit includes a capacitor where information is stored in binary form. The commercial application of FRAM requires high fatigue resistance, large remnant polarization and low coercive field [2]. Though lead based perovskites have high polarization they have low fatigue resistance. In this respect, BLSFs have an advantage over the lead-based ones, as they possess fatigue resistance up to $\sim 10^{12}$ switching cycles [2].

High Curie temperature and low temperature coefficient of dielectric make BLSFs very much attractive as high temperature piezoelectric applications especially under high frequency and high temperature conditions [6-8, 10, 11]. The commercially available lead based piezoelectric materials possess high piezoelectric coefficients [12]. However, under the Environmental pollution act, lead based materials are banned due to their hazardous nature. Other lead free perovskite piezoelectric materials like $BaTiO_3$ possess low Curie temperature which hinders their high temperature applications. BLSFs based piezoelectric materials have Curie temperature more than 400^oC. This places BLSFs as a strong competitor in the development of lead free high temperature piezoelectric materials.

The structure of BLSF comprises of intergrowth of fluorite-like $(Bi_2O_2)^{2+}$ units and pseudo-perovskite slabs $(A_{n-1}B_nO_{3n+1})^{2-}$ as shown in Fig. 1.1. *A* is a relatively large size mono-, di- or tri-valent cation in 12-coordination site and the site is occupied by cations such as Na^+, K^+, Ba^{2+}, Ca^{2+}, Sr^{2+}, Pb^{2+}, Bi^{3+}, *etc*. For example, Sr^{2+} and Bi^{3+} are the *A*-type cations in the BLSFs shown in Fig.1.1 (a) and (b), respectively. *B* is a small size, highly charged tera-, penta- or hexa-valent cation in the octahedral coordination site of pseudo-perovskite unit and the site is generally occupied by Ti^{4+}, Ta^{5+}, Nb^{5+}, V^{5+}, W^{6+}, *etc*. For example, Ta^{5+} and Ti^{4+} are the *B*-type cations, respectively in the BLSFs as shown in Fig.1.1 (a) and (b), respectively. $(A_{n-1}B_nO_{3n+1})^{2-}$ perovskite slabs are sandwiched between Bi_2O_2 layers giving a characteristic layer structure. *n* indicates the number of perovskite units stacked along the *c*-axis between $(Bi_2O_2)^{2+}$ layers and $1 \leq n \leq 8$ [1, 13, 14]. Some typical examples of BLSFs are: Bi_2WO_6 ($n = 1$), $SrBi_2Ta_2O_9$ ($n = 2$), $Bi_4Ti_3O_{12}$ ($n = 3$), $MBi_4Ti_4O_{15}$ (M = Ca, Sr, Pb, Ba) ($n = 4$) and $Ba_2Bi_4Ti_5O_{18}$ ($n = 5$), etc. Fig.1.1 shows a typical two layer ($SrBi_2Ta_2O_9$, $n = 2$) [15] and three layer ($Bi_4Ti_3O_{12}$, $n = 3$) [16] BLSFs.

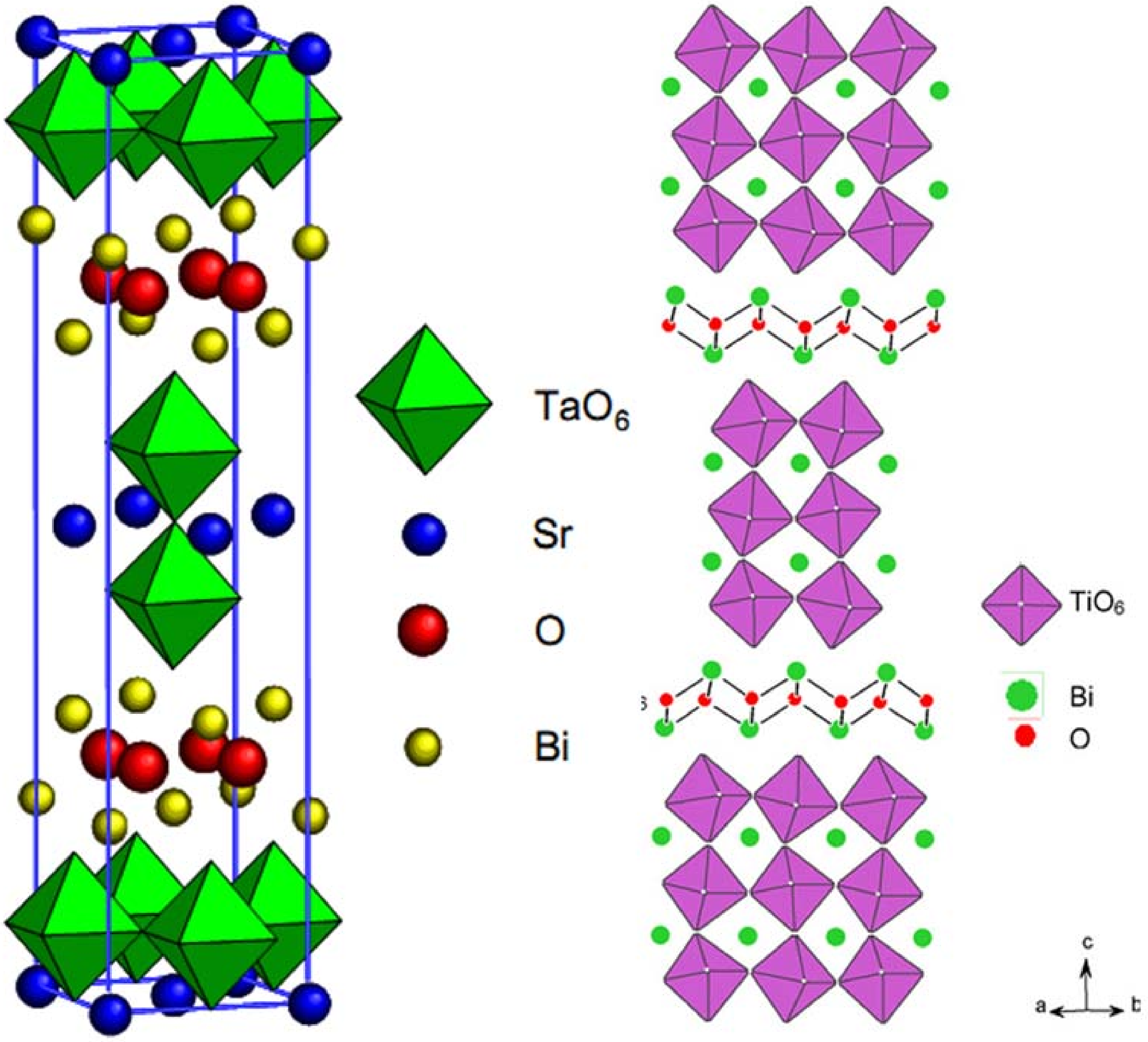

(a) **(b)**

Fig.1.1. Typical structure of **(a)** $SrBi_2Ta_2O_9$ ($n = 2$) [15] and **(b)** $Bi_4Ti_3O_{12}$ ($n = 3$) [16] BLSFs.

Most of the BLSFs possess non-centro-symmetric orthorhombic structure at room temperature. Ferroelectricity of BLSF compounds arises due to the three main distortions in the orthorhombic structure, when the high temperature paraelectric tetragonal phase transforms during cooling through Curie temperature. The distortions are: tilting of the oxygen octahedra (a) around the *a*-axis, (b) around the *c*-axis, and (c) a shift of *A* and/or *B*-cations along the polar *a*-axis [17, 18]. Ferroelectricity mainly arises in the perovskite blocks of BLSF [19]. Bi_2O_2 layers perform the function of an insulating layer and controls the electrical response such as electrical conductivity, band gap, *etc*. of the compound [20, 21]. The insulating behaviour of Bi_2O_2 layer arises due to the ability of self-regulated positioning of the layer in the lattice to compensate the space charge arising due to oxygen vacancies.

One of the most appealing advantages of BLSF compounds is their compositional flexible nature which allows modifying their properties according to the chemical composition. The members show various properties depending on the type of the cations occupying the *A* and *B*-site of BLSF. In the BLSF family, most of the member's exhibit normal ferroelectric behaviour while only a few such as $BaBi_2Nb_2O_9$, $BaBi_2Ta_2O_9$, $BaBi_4Ti_4O_{15}$ *etc*, compounds display relaxor behaviour [9, 14, 22, 23]. A small change in the composition of relaxor $BaBi_4Ti_4O_{15}$, that is, $CaBi_4Ti_4O_{15}$ and $SrBi_4Ti_4O_{15}$ show normal ferroelectric behaviour. Similarly, by varying the composition, ferroelectric and piezoelectric properties of various BLSFs are modified [24, 25]. Also the donor substitution improves the resistivity of the BLSF which generally have oxygen vacancies due to bismuth volatilization during high temperature processing. Acceptor and donor co-substitution at *A* and/or *B*-site of BLSFs have been found very effective to change the relaxor behaviour by forming localized charged polar pairs.

The BLSF compound $BaBi_4Ti_4O_{15}$, the topic of this thesis is a four layer relaxor ferroelectric and proposed for capacitor applications with broad temperature stability also proposed for piezoelectric application after appropriate compositional change. Relaxor ferroelectrics are attractive for a wide range of applications owing to their excellent high dielectric and piezoelectric responses over a wide range of temperatures [26, 27]. The structural formula of $BaBi_4Ti_4O_{15}$ is $(Bi_2O_2)^{2+}((BaBi_2)Ti_4O_{13})^{2-}$, where the Ba^{2+} and Bi^{3+} ions occupy the *A*-site and Ti^{4+} ions reside at the *B*-site of the pseudo-perovskite block, respectively. Room temperature structure of $BaBi_4Ti_4O_{15}$ is orthorhombic with space group $A2_1am$. The ferroelectric orthorhombic structure transforms to tetragonal structure with space group $I4/mmm$ above T_m (~400^{o}C) [22, 28]. Two structures are shown in Fig.1.2. It shows that four number of perovskite blocks are sandwiched between the Bi_2O_2 layers. Fig. 1.2(a) shows tilting of TiO_6 octahedra. As stated above ferroelectricity in $BaBi_4Ti_4O_{15}$ arises due to the tilting of the octahedra and shifting of *A*-type Bi^{3+} cation along *a*-axis. The remnant polarization increases with the increase in this off-center displacement of TiO_6 octahedral chain in four layered BLSF. *A* and/or *B*-site substitutions usually changes this off-centering. Fig. 1.2(b) shows that there is no tilting of TiO_6 octahedra in tetragonal structure that is why it is paraelectric. The recent investigation confirmed that there is partial occupancy of Ba^{2+} in Bi_2O_2 layer which is shown in the figure as Ba(3). The relaxor behaviour of $BaBi_4Ti_4O_{15}$ is explained due to this partial occupancy of Ba^{2+} in Bi_2O_2 layer. This is known as cationic disorder in $BaBi_4Ti_4O_{15}$, which creates a local charge center in its macro-domain. These polar clusters are responsible for its relaxor behaviour [22, 29].

As stated above, the BLSFs have been extensively studied for use in piezoelectric devices those which are suitable for high frequencies and high temperature. The piezoelectric activities in BLSFs are found to be very low in the range ~20 pC/N compared to lead based piezoelectrics (~200 pC/N). Different approaches have been used to improve the piezoelectric activities of BLSFs. The approaches like grain orientation techniques such as hot forging, template grain growth and spark plasma sintering have been proposed [8, 10, 30-34]. It has been reported that the piezoelectric coefficients d_{33} can be significantly improved by grain orientation technique. However, the grain orientation techniques stated above are not commercially viable. So it is desirable to prepare a high d_{33} BLSF ceramics by conventional sintering method which is more commercially viable. Some approaches like *A*-site rare-earth substitutions, *B*-site substitutions and *A*-site vacancy modification methodologies have been proposed for the conventional sintering [35-37]. However, the piezoactivities of these modified BLSF compounds are still low, requiring further intensive research on this substitution approaches. $BaBi_4Ti_4O_{15}$ shows a piezoelectric d_{33} coefficient of ~12 pC/N, whereas similar four layer $PbBi_4Ti_4O_{15}$ shows ~23 pC/N. But the material is lead based. Different substitutions and microstructural engineering through conventional sintering can play a major role to improve the piezoelectric activities of the compound.

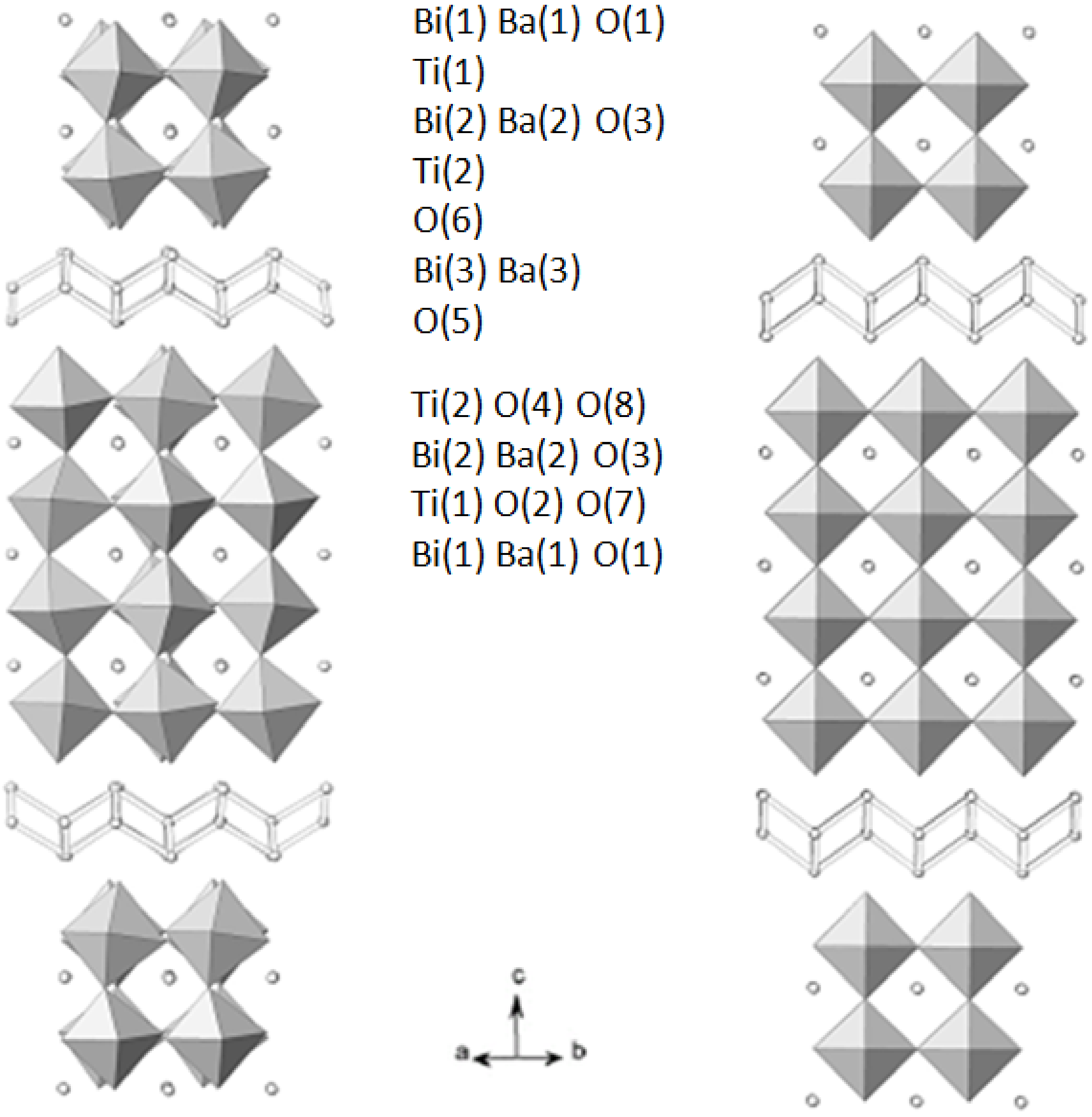

(a) **(b)**

Fig.1.2. Structure of $BaBi_4Ti_4O_{15}$ in (a) orthorhombic *A*2$_1$*am* and (b) tetragonal *I*4/*mmm* structures. Bi-atoms are represented by small shaded spheres and the oxygen atoms are at the edges of the TiO_6 octahedra [28].

The objectives of the present study are substitution in *A* and/or *B*-site of $BaBi_4TiO_{15}$ with an intention to improve the ferroelectric properties like remnant polarization, coercive field, to improve resistivity through donor/acceptor substitution mechanism and to improve the piezoelectric properties through substitution technique.

1.2 Organization of the Thesis

The thesis has been divided into five chapters:

Chapter–I presents a brief introduction on BLSF, $BaBi_4Ti_4O_{15}$ and organization of thesis.

Chapter–II deals with detailed literature review of BLSFs. Attempts have been made to systematically classify the available information under different sections. This chapter incorporates background information to assist in understanding the aims and objectives of this investigation, and also reviews recent reports by other investigators with which these results can be compared.

Chapter–III enunciates with the detail experimental process related to this research work.

Chapter–IV describes the results and discussion, which has been divided into 7 sections, where, **Section 1** describes the ferroelectric and piezoelectric properties of pure $BaBi_4Ti_4O_{15}$ ceramics synthesized through the modified chemical route, **Section 2** explains about the effect of La^{3+} substitution for Bi^{3+} on various properties of $BaBi_4Ti_4O_{15}$ ceramics, **Section 3** describes about the effect of Zr^{4+} substitution for Ti^{4+} on the various properties of $BaBi_4Ti_4O_{15}$, **Section 4** narrates the effect of Na^+ and La^{3+} substitution for Ba^{2+} on the various properties of $BaBi_4Ti_4O_{15}$, **Section 5** deals with the effect of substitution of Nb^{5+} and Al^{3+} for Ti^{4+} on the various properties of $BaBi_4Ti_4O_{15}$, **Section 6** describes the effect of Nb^{5+} substitution for Ti^{4+} and Na^+ for Ba^{2+} on various properties of $BaBi_4Ti_4O_{15}$, and finally **Section 7** explains the effect of Nb^{5+} substitution for Ti^{4+} and $Mg^{2+}/Ca^{2+}/Sr^{2+}/Ba^{2+}$ for Bi^{3+} on various properties of $BaBi_4Ti_4O_{15}$ ceramics.

Chapter–V contains the concluding remarks and the scope of future work.

A complete list of references has been provided at the end of the thesis. Finally, a concise list of publications in-peer reviewed international journals related to present research work has been presented at the end.

Chapter II

Literature Review

2.1 Introduction

In this chapter, an attempt has been made to present an overview on the various synthesis methodologies of Bi-layer structured ferroelectrics, and the effect of various isovalent and aliovalent cation substitutions on structure, dielectric, ferroelectric, piezoelectric properties of different BLSF compounds including $BaBi_4Ti_4O_{15}$.

2.2 Synthesis of BLSF Compounds

BLSFs have been prepared through various methods like conventional solid state method, co-precipitation, sol-gel, auto-combustion, polymeric precursor method (Pechini, *i.e.* complex citrate), molten salt synthesis, metal-organic decomposition etc. Synthesis of the compounds through solid state method [17, 29, 38-42] involves mixing of oxides and carbonates of the required metals in stoichiometric amounts. Repeated grinding and high temperature calcinations with long soaking periods are necessary to form a pure phase. A high sintering temperature of ~1150^{o}C is required to obtain a dense sample because particle sizes are larger compared to chemical route. Volatilization of bismuth due to higher sintering temperature is another drawback. Chemical synthesis routes can suppress this bismuth volatilization. Chemical routes provide homogenized fine powders and a lower formation temperature due to molecular scale mixing of precursors.

Various wet-chemistry routes can synthesize ultra-fine and nano-sized powders. Co-precipitation is one of the successful techniques for preparation of ultrafine powders with a narrow particle size distribution [43-47]. As an example, tantalum fluoride, bismuth nitrate and strontium chloride were used for the synthesis of $SrBi_2Ta_2O_9$. Bismuth nitrate was dissolved in dilute nitric acid, strontium chloride in distilled water and tantalum fluoride in hydrogen fluoride. Ammonia was added for complete precipitation from the mixed solution [44].

Polymeric precursor method based on Pechini process has also been adopted for the synthesis [48-53]. For example, titanium chloride, bismuth nitrate, barium chloride were used as raw materials for the synthesis of $BaBi_4Ti_4O_{15}$. Citric acid solution of metals was heated to form a gel. The main advantage of this method was its precise stoichiometric control. A pure phase $BaBi_4Ti_4O_{15}$ formed after heating at 900^{o}C for 72h with a grain size of ~1μm [48].

Sol-gel is another methodology for synthesis, which has been followed by some researchers [54-58]. For example, barium acetate, bismuth nitrate and tetrabutyl titanate were used as starting materials for $BaBi_4Ti_4O_{15}$ synthesis. Bismuth nitrate was dissolved in glacial acetic acid. Acetylacetone was used to stabilize tetrabutyl titanate and was added to Bi-Ba acetum mixed solution. Ethanolamine was added to the solution as complexation reagent. This procedure produces nanopowders in 150 to 180 nm range, but required water free atmosphere for its synthesis and possesses the problem of solution aging which may alter the microstructure [54].

Mechanochemical activation is another method for synthesis of BLSF. In particular, barium oxide, titanium dioxide and bismuth oxide are milled in planetary ball mill using zirconia balls for the synthesis of $BaBi_4Ti_4O_{15}$. [59].

Literature review shows that the $BaBi_4Ti_4O_{15}$ has been prepared by solid oxide route [38, 17, 29], sol-gel method [54], Pechini method [48], mechanochemical activation [59], *etc*. It shows that the advantage of solid oxide method is the use of simple oxide raw materials and easy processing steps while, higher calcination and sintering temperature add to its disadvantages. On the other hand, chemical route produces homogeneous powders with finer particle size. However, the costly raw materials are its disadvantages. Therefore, a combined method having advantages of solid oxide and chemical route will be more effective for industrial applications.

2.3 Substitutions in BLSF

Extensive researches have been focused on the improvement of different properties of BLSF by substitutions at *A* and/or *B*-site. The substituting cations may be classified as isovalent or aliovalent (acceptors and donors) cations. The review of various isovalent or aliovalent substitutions at *A* and/or *B*-site of $(Bi_2O_2)^{2+}(A_{n-1}B_nO_{3n+1})^{2-}$ BLSFs are summarized below.

2.3.1 Isovalent Substitutions for *A*-site

There are many reports on the lanthanide (La^{3+}, Nd^{3+}, Sm^{3+} and Dy^{3+}) substituted BLSFs [56, 60-68]. The lanthanide substitution showed improved fatigue behaviour and increased ferroelectricity in many BLSFs, especially in the three-layer member $Bi_4Ti_3O_{12}$. In general, with the decrease in ionic radii, Curie temperature and polarization increased as well as coercive field increased due to the increase in the structural distortion. Incorporation of La^{3+} changed the orthorhombic crystal structure of $Bi_{4-x}La_xTi_3O_{12}$ to tetragonal at $x \geq 1.0$ [24]. *Chen et al.* had reported that there was an optimum substitution amount for the maximum improvement of remnant polarization ($2P_r$) in different BLSF as shown in Fig. 2.1. In addition to the above improvements, substitution of La^{3+} for Bi^{3+} induced ferroelectric relaxor behaviour in many members such as $SrBi_2Nb_2O_9$, $Bi_4Ti_3O_{12}$, $SrBi_4Ti_4O_{15}$ and $Sr_2Bi_4Ti_5O_{18}$ [62, 69]. However, *Fang et.al.* reported that the relaxor behaviour was suppressed by La^{3+} substitution for Bi^{3+} in $BaBi_4Ti_4O_{15}$ [70]. Concentration of Bi-ion vacancies and oxygen vacancies in BLSF was reported to decrease by La^{3+} substitution [71]. La^{3+} was also found to improve the resistivity in ferroelectrics [72]. Contrary to these results, the Curie temperature increased for La^{3+} doping in $Bi_9Fe_5Ti_3O_{27}$ BLSF [73]. All these indicate that the lanthanide substitution for *A*-site has multi-faced effect in BLSFs.

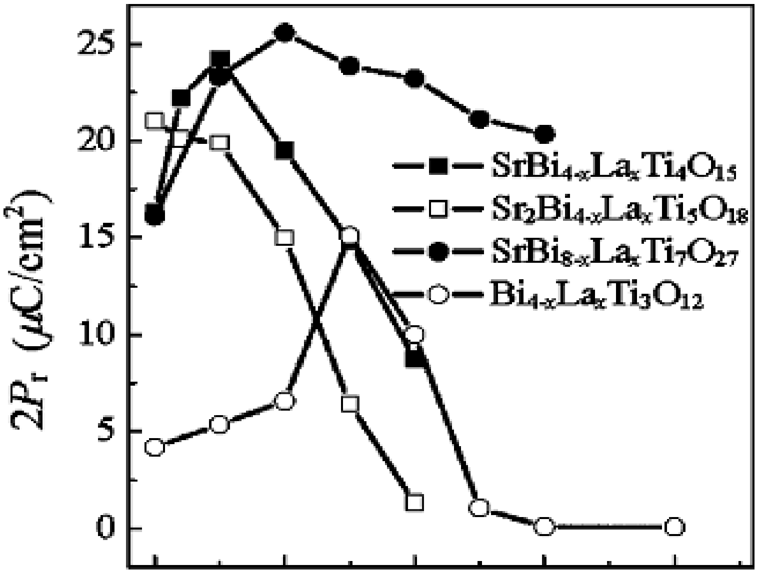

Fig.2.1. Dependence of La^{3+} concentration on $2P_r$ of various BLSF compounds [62].

Influence of other rare-earth cations substitution such as Eu^{3+}, Ho^{3+}, Pr^{3+} and Y^{3+} for Bi^{3+} in $Bi_4Ti_3O_{12}$ has also been investigated [74-78]. The remnant polarization slightly decreased with Eu^{3+} substitution while the ceramic showed best electrical properties with $2P_r$ of 44.2 $\mu C/cm^2$, $2E_c$ of 323.7 kV/cm, ε' of 489, dielectric loss of 0.018 (1 MHz) as well as strongest fatigue resistance for Ho^{3+} at $x = 0.4$ in $Bi_{4-x}Ho_xTi_3O_{12}$. Pr^{3+} doping in $Bi_4Ti_3O_{12}$ decreased the grain size and exhibited large remnant polarization, low coercive field. $Bi_{3.2}Y_{0.8}Ti_3O_{12}$ thin films were highly oriented in (117) direction, which was responsible for its high remnant polarization of 58 $\mu C/cm^2$ and coercive field of 116 kV/cm, with fatigue free characteristics up to $> 10^8$ switching cycles.

Reports are also available for isovalent substitutions for divalent *A*-site of BLSFs. Substitution of Ba^{2+} for Sr^{2+} in $SrBi_2Ta_2O_9$ and $SrBi_2Nb_2O_9$, and for Pb^{2+} in $PbBi_2Nb_2O_9$ induced a shift in the Curie temperature to lower values along with an introduction of relaxor behaviour [79-81]. In the latter case, P_r also increased. Similar behaviour was reported for $PbBi_2Nb_2O_9$ where Sr^{2+} replaced Pb^{2+} [82]. Inversely, the introduction of Sr^{2+} in $BaBi_2Nb_2O_9$ decreases the degree of diffuseness leading to a sharp phase transition [23]. The dielectric constant increased accompanied by peak broadening, as Cu^{2+} replaced Sr^{2+} in $SrBi_2Nb_2O_9$. The sintering temperature of the ceramics also reduced by 80^oC [83]. The substitution of Ca^{2+} for Sr^{2+} in $SrBi_3Ti_2NbO_{12}$, produced a mixture of orthorhombic and tetragonal phases and the Curie temperature increased. P_r also increased by substitution [84]. In the four-layer BLSFs, researchers had also investigated similar substitution such as $Sr_{1-x}Ba_xBi_4Ti_4O_{15}$ [85], $Ca_{1-x}Sr_xBi_4Ti_4O_{15}$ [86], and $Ca_xSr_{1-x}Bi_4Ti_4O_{15}$ [87]. d_{33} coefficient improved with a better temperature stability and the Curie temperature increased by the substitution of Ca^{2+} for Sr^{2+} in $Sr_2Bi_4Ti_5O_{18}$ [88].

In summary, the fatigue behaviour and ferroelectric properties improved by the substitution of various lanthanide cations in BLSF. The introduction of Ba^{2+} in BLSF structure induced a relaxor like behaviour, while Sr^{2+} and Ca^{2+} increased the Curie temperature and lead to a sharp phase transition. Additionally, Ca^{2+} improved the d_{33} coefficient. The substitution of La^{3+} decreased the concentration of bismuth and oxygen vacancies and improved the fatigue behaviour of BLSF. The review also showed that there was a contradiction about the change of relaxor behaviour in $BaBi_4Ti_4O_{15}$ when La^{3+} substituted Bi^{3+}, whereas the relaxor behaviour was induced in many BLSF compounds by the same substitution. Thus, a detailed study concerning the substitution of La^{3+} in $BaBi_4Ti_4O_{15}$ is necessary.

2.3.2 Isovalent Substitutions for *B*-site

Niobium, tantalum and vanadium based two-layered BLSF are widely studied. *D. Kajewski et al.* [89] studied the solid solution $SrBi_2(Nb_{1-x}Ta_x)_2O_9$. Incorporation of Ta^{5+} resulted in diffuse phase transition of the material. In a similar compositional change, *Sun et al.* [90] observed that substitution of Ta^{5+} for Nb^{5+} decreased the Curie temperature, maximum permittivity, remnant polarization and coercive field whereas temperature coefficient of resonance frequency increased with increase in Ta^{5+} concentration. Nb^{5+} and Ta^{5+} co-doped $Bi_4Ti_{3-2x}Nb_xTa_xO_{12}$ showed diffuse phase transformation behaviour due to *B*-site vacancies. Also this co-doping induced the distortion of the oxygen octahedra in $Bi_4Ti_{2.98}Nb_{0.01}Ta_{0.01}O_{12}$ [91] and the piezoelectric coefficient enhanced to 26 pC/N. Interestingly, it was noted that when Nb^{5+} was replaced by V^{5+} in $BaBi_2Nb_2O_9$, the sintering temperature of the ceramics were lowered by ~200°C. The dielectric constant of the ceramics increased significantly, while the loss remained constant. However, the relaxor behaviour of the ceramics decreased with increase in V^{5+} content [92]. In $SrBi_2(V_xNb_{1-x})_2O_9$ ceramics, dielectric constant increased with increase in V^{5+} content with a limit of ~15 at.% [93]. In the composition $Bi_2V_{1-x}Nb_xO_{5.5}$, the grain size increased with increase in Nb^{5+} concentration, while the dielectric constant increased accompanied by a decrease in the conductivity of the material [94].

For *B*-site titanium-based BLSF, only a few reports are available about isovalent substitution for Ti^{4+}. The replacement of Ti^{4+} by Zr^{4+} in the perovskite block of $Bi_4Ti_{3-x}Zr_xO_{12}$ resulted in increased lattice parameters along with a systematic decrease in phase transition temperature. The solid solubility limit of Zr^{4+} in the system was ~ 40 mole% [95]. The study on $Bi_4Ti_{3-x}Zr_xO_{12}$ ceramics by *Du et al.* showed that the composition with $x = 0.2$ depicted largest remnant polarization [96]. *Park et al.* analyzed the effect of substitution of Zr^{4+} for Ti^{4+} in four-layer $PbBi_4Ti_{4-x}Zr_xO_{15}$ and reported that the structure was orthorhombic up to $x = 0.2$. This substitution increased T_c from 554 to 563°C and decreased the relative permittivity. An increase in ferroelectric properties was observed at $x = 0.5$, with $2P_r$ and $2E_c$ values of 2.4 μC/cm^2 and 18.4 kV/cm respectively at room temperature, and 9.9 μC/cm^2 and 28.1 kV/cm respectively at 120°C at an electric field of 40 kV/cm [97]. The review showed that Zr^{4+} substitution for Ti^{4+} in BLSFs played a significant role in the improvement of different properties of the ferroelectrics. However, there was no report on the effect of Zr^{4+} substitution in $BaBi_4Ti_4O_{15}$ ceramics.

2.3.3 Aliovalent Substitutions for *A*-site

In comparison to the isovalent *A*-site substitutions, the aliovalent substitutions for *A*-sites have been studied more extensively. *Shrivastava et al.* studied the effect of La^{3+} substitution for Sr^{2+} in two layer $Sr_{0.8}La_{0.2}Bi_2Nb_2O_9$. The substituted samples showed a reduced dielectric loss and Curie temperature [98]. In another instance, K^+ and Na^+ were substituted for Sr^{2+} in $Sr_{0.8}(K,Na)_{0.2}Bi_2Nb_2O_9$ where the structure remained orthorhombic, and the peak dielectric constant increased by the substitution [99]. The substitution of Eu^{3+} for Sr^{2+} in $Sr_{1-x}Eu_xBi_2Ta_2O_9$ acts as a donor which increased the remnant polarization and d_{33} coefficient, being maximum at $x = 0.2$ [100]. *Prasanta et al.* studied the composition $Ca_{1-x}Bi_{2+y}Nb_2O_9$ ($0 \leq x \leq 0.4$ and $0 \leq y \leq 0.266$), whose dielectric constant was maximum at $x = 0.1$. However, the dielectric dispersion increased gradually with increasing bismuth content [101]. The piezoelectricity of $CaBi_2Nb_2O_9$ were significantly enhanced by (NaCe) substitution for Ca where the d_{33} coefficient was 16 pC/N for NaCe = 0.1 [102]. *Zhang et al.* studied *A*-site substituted $Ca_{1-x}M_xBi_2Nb_2O_9$ (M = Na, NaCe, NaLa, La) ceramics. The modified ceramics $Ca_{0.9}Na_{0.1}Bi_2Nb_2O_9$, $Ca_{0.9}(NaLa)_{0.1}Bi_2Nb_2O_9$, $Ca_{0.95}La_{0.05}Bi_2Nb_2O_9$ and $Ca_{0.9}La_{0.1}Bi_2Nb_2O_9$ were all single phase BLSFs and T_c was above 900°C for all. The donor dopants increased the *dc* electrical resistivity while the acceptor dopants decreased it. The donor doped $Ca_{0.95}La_{0.05}Bi_2Nb_2O_9$ had a higher piezoelectric constant of 12.8 pC/N compared with that of pure $CaBi_2Nb_2O_9$ of 5.8 pC/N and its electrical resistivity was higher than 10^6 Ωcm at 600°C [103]. Transition temperature increased from 392 to 485°C for Ba^{2+} and La^{3+} co-substituted $Ba_{0.1}Sr_{0.81}La_{0.06}Bi_2Nb_2O_9$ [104].

Aliovalent Ca^{2+}, Sr^{2+}, Ba^{2+} substitution for Bi^{3+} in three layer BLSF ceramics $Bi_2ANb_2TiO_{12}$ (A = SrCa, $Sr_{1.5}Ca_{1.5}$, Sr_2, $Sr_{1.5}Ba_{1.5}$, SrBa) showed the static disorder in form of mixed cation occupancies between Bi^{3+} and Sr^{2+}, Ca^{2+} or Ba^{2+} for the *A*-site. The degree of site mixing between the bismuth layer and *A*-site in the perovskite layer increased with increase in average *A*-site cation radius [105]. In the four layer composition $Ba_{1-(3/2)x}La_xBi_4Ti_4O_{15}$, for $x \leq 0.1$, the dielectric constant increased while T_m remained constant. In the range $0.1 < x \leq 0.4$, T_m shifted towards lower temperature accompanied by a decrease in the dielectric constant. Using Vogel-Fulcher relation, a decrease in the activation energy was observed for frequency dispersion with increase in x. With increase in La^{3+} content, the activation energy required for creating and move defects increased [106].

Newnham studied the cation disordering by the introduction of Na^+ for *A*-site of four-layered $Na_{0.5}Bi_{4.5}Ti_4O_{15}$. Na^+ was found to occupy the *A*-site of perovskite layer and does not substitute for Bi^{3+} in the bismuth oxide layer [107]. *Wang et al.* investigated the electrical properties of modified $Na_{0.5}Bi_{4.5}Ti_4O_{15}$. The Curie temperature and piezoelectric coefficient of $Na_{0.5}La_{0.5}Bi_4Ti_4O_{15}$ were 573°C and 29 pC/N, [108] while that of 0.3 wt% cobalt modified $Na_{0.5}Bi_{4.5}Ti_4O_{15}$ was 663°C and 30 pC/N, respectively [25]. Sr^{2+} substituted for divalent pseudo-cation (Na^+, Bi^{3+}) in the composition $Na_{0.5}Bi_{0.5}Bi_4Ti_4O_{15}$ decreased the Curie temperature along with a decrease in the dielectric permittivity [109]. In the four-layer member $K_{0.5}Bi_{4.5}Ti_4O_{15}$, its single crystals exhibited remnant polarization of 31 μC/cm^2 and the piezoelectric strain constant was 31 pmV [110].

Wang et al. investigated various properties of $K_{0.5}Bi_{4.5}Ti_4O_{15}$. Curie temperature and piezoelectric coefficients were 555°C and 21 pC/N, respectively [111]. CeO_2 modified $K_{0.5}Bi_{4.5}Ti_4O_{15}$ exhibited enhanced piezoelectric properties (d_{33} = 28 pC/N which was maximum at 0.50 wt% cerium) and the dielectric loss decreased [112]. The remnant polarization and coercive field of La^{3+} substituted potassium bismuth titanate $K_{0.5}La_{0.5}Bi_4Ti_4O_{15}$ was 8.6 μC/cm^2 and 60 kV/cm, respectively. T_c and d_{33} coefficients of the same were 413°C and 18 pC/N, respectively [113]. Introduction of Na and Ce in $CaBi_4Ti_4O_{15}$ had a remarkable effect on their piezoelectric properties. Na deficient composition $Ca_{0.8}(Ce_{0.1}Na_{0.05}\square_{0.05})Bi_4Ti_4O_{15}$ showed a very high piezoelectric coefficient, high temperature resistivity and also had high Curie temperature compared to $Ca_{0.8}(CeNa)_{0.1}Bi_4Ti_4O_{15}$ [114]. Substitution of La^{3+} for Sr^{2+} in $SrBi_4Ti_4O_{15}$, increased $2P_r$ up to 23.1 μC/cm2 and E_c decreased to 79.6 kV/cm. T_c decreased with increase in La^{3+} content, along with a decrease in the dielectric constant and increase in peak broadening [115].

In summary, introduction of La^{3+} for divalent *A*-site of BLSF increased Curie temperature accompanied by a decrease in loss and relaxor behaviour. Substitution of Na^+ and/or K^+ for divalent *A*-site enhanced the peak dielectric constant and increased Curie temperature. In addition, Na^+ and Ce^{3+} increased the piezoelectric coefficient of $CaBi_2Nb_2O_9$. Thus, the investigation of the effect of these cations on the various properties of $BaBi_4Ti_4O_{15}$ may be of interest.

2.3.4 Aliovalent Substitutions for *B*-site

This section presents an overview on the effects of aliovalent substitution for the *B*-site of the BLSF compounds. The donor dopants for the *B*-site improved the resistivity, i.e., decreased the conductivity of the system. Substitution of higher valence W^{6+} for $(TaNb)_{0.5}$ in two layer $SrBi_2(Ta_{0.5}Nb_{0.5})_2O_9$ thin film increased the dielectric permittivity but P_r and E_c were not improved [49]. W^{6+} substituted $SrBi_2(W_xTa_{1-x})_2O_9$ and $SrBi_2Nb_2O_9$ resulted in an increased T_c, significant reduction in dielectric loss, increased the remnant polarization and also resulted in decreased *ac* and *dc* conductivity [116, 117]. *Zhou et al.* prepared high temperature piezoelectric ceramics based on W^{6+} doped Bi_3TiNbO_9. W^{6+} decreased the conductivity by two orders of magnitude and the highest piezoelectric constant was found to be 12 pC/N [118]. Vanadium substituted strontium bismuth tantalate, $Sr_{0.8}Bi_{2.2}Ta_{2-x}V_xO_9$, and strontium bismuth niobate, $SrBi_2Nb_{2-x}V_xO_9$ ceramics exhibited room temperature P_r to be 4.9 and 5.4 μC/cm^2, respectively. Coupling factors of the substituted ceramics were higher compared to undoped ceramics, making them applicable as resonator materials [119]. Solid solubility limit of partially doped $SrBi_2Nb_{2-x}M_xO_9$ (M = Cr, Mo) was determined to be 20 mole%. Dielectric constant of the doped ceramics was also increased [120]. The effect of Mo^{6+} substitution on the various properties of substituted $SrBi_2Ta_2O_9$, suggested that the composition with Mo^{6+} in the range 0.025 to 0.05 was optimum to achieve maximum P_r and minimum E_c [121].

Analysis of the solid solubility limit in the three layered BLSF; for $Bi_2Sr_2Nb_2Ti_{(1-x)}M_xO_{(12-\delta)}$ (M = Fe, Cr, Mn, Ga) was found to be $x = 0.2$ [42, 122, 123]. *Snedden et.al* have also looked into the ionic conductivity and the limit of solid solubility with reference to Ga^{3+} in the Ti^{4+} site and reported the solubility limit ~0.2 mol% [42]. W^{6+} doped $Bi_4Ti_3O_{12}$ thin film showed $2P_r$ of 20 μC/cm^2 with $2E_c$ of 90 kV/cm under an applied field of 170 kV/cm. The film showed fatigue behaviour up to 4.5×10^{10} switching cycles [124, 125]. Partial substitution of Nb^{5+} for Ti^{4+} in $Bi_4Ti_3O_{12}$ reduced the conductivity and enabled poling. The piezoelectric coefficient of Nb^{5+} doped $Bi_4Ti_3O_{12}$ was 20 pC/N [7]. Nb^{5+} doping in $Bi_4Ti_3O_{12}$ thin films resulted in a marked improvement in $2P_r$, which was due to decrease in the oxygen vacancy concentration. However, degradation in the $2P_r$ was observed after 3×10^9 switching cycles. Increase in Nb^{5+} content lead to more resistive ceramics and the hysteresis loops were significantly narrowed [126, 127]. Nb^{5+} can decrease the processing temperature of the ceramics besides promoting an increase in grain growth, which is desirable to obtain good ferroelectric properties [128, 129].

Co-substitution of Nb^{5+} and Fe^{3+} for Ti^{4+} in $Bi_4Ti_3O_{12}$ ($Bi_4Ti_2Nb_{0.5}Fe_{0.5}O_{12}$) decreased T_c from 675 to 630°C [130]. Single crystals of $Bi_4Ti_{2.97}Mn_{0.03}O_{12-\delta}$ were investigated for leakage current and polarization properties where the substitution of Mn for Ti effectively suppressed the leakage current and enhanced the remnant polarization to 38 μC/cm2 and coercive field to 25 kV/cm [131]. V^{5+} doped four-layered BLSF, $SrBi_4Ti_4O_{15}$ thin films showed enhanced ferroelectricity compared to pure compound where $2P_r$ increased to 40 μC/cm^2 at a V^{5+} concentration of 0.09. Which was five times larger compared to that of pure material thin film [132]. V^{5+} doping in $CaBi_4Ti_4O_{15}$ was also found to play the same role. It enhanced the remnant polarization and decreased the coercive field, temperature coefficient of dielectric constant and dielectric loss at high temperature [133]. *Zhang et al.* studied the electrical properties of manganese modified $CaBi_4Ti_4O_{15}$. d_{33} coefficient and electrical resistivity of the modified ceramics increased to 14 pC/N and 1×10^7 Ωcm at 500°C, respectively [134]. Addition of 0-16.7% Bi_2SiO_5 in $BaBi_4Ti_4O_{15}$, increased the T_c gradually to 478°C and 9.1% Bi_2SiO_5 doped $BaBi_4Ti_4O_{15}$ was found to be a potential piezoelectric element [135]. Co-substitution of Nb^{5+} and Fe^{3+} for Ti^{4+} in $BaBi_4Ti_3Nb_{0.5}Fe_{0.5}O_{15}$ also retained relaxor behaviour [136]. The solubility limit for Fe^{3+} was < 12 mol% and for Nb^{5+} it was < 8 mol% in $BaBi_4Ti_4O_{15}$. Conductivity was suppressed by Nb^{5+} while it increased by Fe^{3+} substitution in $BaBi_4Ti_4O_{15}$ [137, 138]. Donor doping in five-layered member of BLSF was also helpful in improving its properties. The ceramics with composition $(Li_{0.5}Ce_{0.5})_x(Na_{0.5}Bi_{0.5})_{1-x}Na_{0.5}Bi_{4.5}Ti_5O_{18}$ showed promising piezoelectric constant. The highest piezoelectric constant was 26.5 pC/N at room temperature for $x = 0.11$[139].

The review shows that substitution of various pentavalent and hexavalent aliovalent cation for *B*-site improves the properties of different BLSFs. However, there are only a few reports regarding solid solubility limit for trivalent aliovalent cations for *B*-site. Substitution of higher valence W^{6+} in BLSF, reduced its dielectric loss, improved the remnant polarization and decreased the *ac* and *dc* conductivity of the ceramics. Investigation of the solubility limit for Fe, Cr, Mn, Ga aliovalent cations in BLSF was found to be ~0.2. Substitution of Nb^{5+} for Ti^{4+} effectively reduced the conductivity enabling poling and depicted a marked improvement in remnant polarization. V^{5+} was also found to play the same role as that of Nb^{5+} but it decreased relaxor behaviour.

2.3.5 Aliovalent Substitutions for *A* and *B*-site

In this section, co-substitutional effects of aliovalent cations for *A* and *B*-site are discussed as studied by various authors. *Duran-Martin et al*. synthesized solid solutions of $Bi_{2-x}Te_xSrNb_{2-x}B_xO_9$ (B = Zr, Hf; $0 \leq x \leq 0.5$). Changes in the unit cell parameters at room temperature showed that the doping for *A* or *B* sites dominated the size of (001) plane in the structure, while the *c* value was largely dependent on the cations occupying the bismuth position in the layer. Dielectric permittivity versus temperature plot revealed the presence of two-phase transitions and all the ceramics exhibited d_{33} coefficients in the range 5 to 9 pC/N [140]. Dielectric properties increased for $x = 0.2$ composition of Bi^{3+} and V^{5+} substituted $Sr_{1-x}Bi_{2+(2/3)x}V_xNb_{1-x}O_9$ ceramics [141], whereas in case of tantalate, T_c and dielectric constant also increased in Bi^{3+} and V^{5+} substituted $Sr_{1-x}Bi_{2+(2/3)x}V_xTa_{1-x}O_9$ (x = 0.1 and 0.2) composition [142]. In case of Pr^{3+} and V^{5+} co-doped $Bi_{3.25}Pr_{0.75}Ti_{2.97}V_{0.03}O_{12}$, no fatigue was observed up to 10^8 switching cycles [143].

Hervoches et al. analyzed the solid solutions $Bi_{2-x}Sr_{2+x}Ti_{1-x}Nb_{2+x}O_{12}$, and established the solubility limit to be $x < 0.6$. Sr^{2+} was partially substituted in the bismuth oxide layer and the maximum amount of substitution being about 30 mol % at $x = 0.6$ [144]. *Jennet et al*. analyzed the solid solutions of $Bi_{4-x}Ba_xTi_{3-x}Nb_xO_{12}$ and established the solubility limit to be $x = 1.4$. For low values of x ($0 \leq x \leq 0.4$), the compounds behaved as normal ferroelectrics and T_c decreased with increasing x. For $x \geq 0.6$, the compounds exhibited relaxor ferroelectric behaviour [145]. The properties of Nd^{3+} and V^{5+} co-substituted $Bi_4Ti_3O_{12}$, *i.e.* $(Bi_{4-y}Nd_y)_{1-(x/12)}(Ti_{3-x}V_x)O_{12}$ ceramics showed these to be superior materials for ceramic resonators. The resistivity values of these ceramics lie in the range 10^{13} to 10^{14} Ωcm. Other studies also showed the ceramics to exhibit $2P_r$ of 26 – 31 μC/cm^2 and $2E_c$ of 41 – 57.5 kV/cm [146, 147]. The ferroelectric and piezoelectric properties of $Sr_xBi_{4-x}Ti_{3-x}Ta_xO_{12}$ exhibited enhanced properties, with remnant polarization of 12.3 μC/cm^2 and electromechanical quality factor of 0.37 for $x = 0.3$ [148]. $Bi_{3.25}La_{0.75}Ti_{2.9}Ge_{0.1}O_{12}$ thin films crystallized in a single phase and showed P_r of 12 μC/cm2 and E_c of 66 kV/cm at an applied voltage of 5V. The surface morphology of the films was also greatly improved [149]. $Bi_{3.25}La_{0.75}Ti_{3-x}Nb_xO_{12}$ ($0 \leq x \leq 0.1$) thin films exhibited an increased remnant polarization by 26% and decreased coercive field by 4% for $x = 0.04$ along with a 27% increased fatigue endurance [150]. *A*-site donor and *B*-site acceptor co-substituted $K_{0.45}Bi_{0.05}Bi_4Ti_{3.8}M_{0.2}O_{15}$ (M = Mn, Fe, Ni) thin films displayed improved ferroelectricity. Mn^{3+} and Fe^{3+} substituted thin films showed remnant polarization of 39 and 34 μC/cm^2, respectively [151]. Substitution of 5 at% Ta^{5+}, Nb^{5+} or V^{5+}

for Ti^{4+} and substitution of 5 at% Ba^{2+} for Bi^{3+} in $BaBi_4Ti_4O_{15}$ resulted in a shift in the T_c to higher temperature for V^{5+} substitution and lowering temperature for Ta^{5+} and Nb^{5+} substitution [152, 153].

In summary, the simultaneous aliovalent co-substitutions for *A* and *B*-sites also revealed some interesting results. Substitution of Te^{6+} and Zr^{4+} revealed presence of two-phase transitions in the system. In two layer niobate and tantalate, Bi^{3+} and V^{5+} substitutions enhanced the dielectric constant. Substitution of Ba^{2+} and Nb^{5+} induced relaxor ferroelectric behaviour in the three-layer member of BLSF. Ferroelectric and piezoelectric properties of Sr^{2+} and Ta^{5+} substituted ceramics were improved. Nd^{3+} and V^{5+} co-substituted $Bi_4Ti_3O_{12}$ showed high resistivity values for the ceramics. In addition, the simultaneous substitution of La^{3+} and Nb^{5+} resulted in an increased remnant polarization, decreased coercive field and increased fatigue endurance. In the four-layer member, *A*-site donor and *B*-site acceptor pair were found to improve the ferroelectricity of the ceramics. Therefore, the insight investigation of these various substitutions on $BaBi_4Ti_4O_{15}$ may create a new prospect for it.

2.4 Summary and Scope of Work

There are reports on the synthesis of $BaBi_4Ti_4O_{15}$ through conventional solid oxide method, which has the major advantage of using cheaper raw materials based on oxide and carbonates. There are also many reports of its synthesis through different chemical routes, which have the major advantage of homogeneous molecular level mixing of different raw materials. However, chemical process uses costly metal alkoxides raw materials. For example, titanium isopropoxide, titanium tetrabutoxide, are used for the synthesis of $BaBi_4Ti_4O_{15}$. On the other hand, titanium dioxide TiO_2 used by the solid oxide method is cheap compared to its alkoxide. Therefore, a partial chemical method utilizing TiO_2 as a raw material along with other soluble metal salts may be an alternative method for the synthesis of $BaBi_4Ti_4O_{15}$.

The review shows that lanthanide cations, especially La^{3+} substitution for Bi^{3+} enhances the relaxor behaviour, improves the fatigue behaviour of the material as well as their ferroelectric properties. The effect of La^{3+} substitution on the different properties of $BaBi_4Ti_4O_{15}$ has not been studied in details. Some contradictory reports are available about the decrease in relaxor behaviour of the same by the substitutions. Thus, a detailed study on the La^{3+} substitution for Bi^{3+} in the $BaBi_4Ti_4O_{15}$ has a wide scope.

There are very few reports on the isovalent cation substitutions for *B*-site Ti^{4+} of BLSF. Amongst all, Zr^{4+} substitution showed an encouraging result, for example, the remnant polarization increased in $Bi_4Ti_3O_{12}$ and $PbBi_4Ti_4O_{15}$ by substitutions. However, there is no report on the effect of Zr^{4+} substitution for Ti^{4+} in $BaBi_4Ti_4O_{15}$ ceramics.

It has been found that alkali cations like Na^+ or K^+ substitution for divalent *A*-site cation of BLSF improves dielectric constant and piezoelectric coefficient. These aliovalent substitutions require charge compensation in the structure. It has also been found that Ce^{3+} and La^{3+} cations in combination with Na^+ or K^+ are effective charge compensating pair for *A*-site. Although, $Na_{0.5}La_{0.5}Bi_4Ti_4O_{15}$ has been reported in literature, detailed reports regarding the gradual substitution of the aliovalent charge compensating pair in $BaBi_4Ti_4O_{15}$ is not available.

Nb^{5+} cation substitution for Ti^{4+} at *B*-site of different BLSF has been reported to improve the relaxor behaviour and ferroelectric properties. As stated above, these substitutions also require charge compensation in the structure. The charge may be compensated at *B*-site or *A*-site of the structure. There are a few reports on trivalent charge compensating cation substitution at *B*-site and divalent cation for Bi^{3+} at *A*-site of $BaBi_4Ti_4O_{15}$. Monovalent cation charge compensation for divalent *A*-site may be another approach for the problem. Therefore, a systematic study for the charge compensation at *B*-site and divalent or trivalent *A*-site cation may be studied to observe the broad spectrum of the change in different properties by different charge compensation mechanism.

2.5 Objectives of the Work

The purpose of this work is to synthesize $BaBi_4Ti_4O_{15}$ through modified chemical method and to investigate the effect of some isovalent and aliovalent substitutions for the *A* and/or *B*-site of $BaBi_4Ti_4O_{15}$ on the structure and ferroelectric properties with following details:

a) Preparation of substituted $BaBi_4Ti_4O_{15}$ ceramics through modified chemical route and its characterization.

b) Effect of La^{3+} substitution on the ferroelectric behaviour of $BaBi_{4-x}La_xTi_4O_{15}$ $(0.1 \leq x \leq 1.0)$.

c) Zr^{4+} substitution as per $BaBi_4Ti_{4-x}Zr_xO_{15}$ $(0.1 \leq x \leq 0.5)$: Solid solubility limit, structural and electrical properties.

d) Aliovalent Na^+ and La^{3+} ions substitution for Ba^{2+} as per $(Ba_{1-x}Na_{x/2}La_{x/2})$ $Bi_4Ti_4O_{15}$ (x = 0.25, 0.5, 0.75, and 1.0): Structural, dielectric and piezoelectric characterization.

e) Effect of aliovalent Nb^{5+} and Al^{3+} substitution for Ti^{4+} in $BaBi_4(Ti_{4-x}Nb_{x/2}Al_{x/2})O_{15}$ (x = 0.1, 0.2, 0.3) ceramics on structural, dielectric and ferroelectric properties.

f) Aliovalent Nb^{5+} substitution for Ti^{4+} and compensation by Na^+ for Ba^{2+} in $(Ba_{1-x}Na_x)Bi_4(Ti_{4-x}Nb_x)O_{15}$ (x = 0.1, 0.2, 0.3, 0.4, 0.5, 0.6).

g) Aliovalent Nb^{5+} substitution for Ti^{4+} and compensating by A^{2+} cation for Bi^{3+} in $Ba(Bi_{3.8}M_{0.2})(Ti_{3.8}Nb_{0.2})O_{15}$, ($M^{2+} = Mg^{2+}, Ca^{2+}, Sr^{2+}, Ba^{2+}$).

Chapter III

Experimental Work

3.1 Introduction

$BaBi_4Ti_4O_{15}$ (BBT) and isovalent/aliovalent substituted BBT, synthesized in the present investigation, are listed in Table 3.1. The compositions can be categorized under five groups, namely; (a) isovalent substitutions for *A*-site, (b) isovalent substitutions for *B*-site, (c) aliovalent substitutions for *A*-site, (d) aliovalent substitutions for *B*-site, and (e) aliovalent substitutions for *A*- and *B*-site.

All these ceramics were synthesized through modified chemical route. The modified chemical route is based on co-precipitation of some components from solution in the suspension of other solid oxide component. The conventional solid state route uses simple processing steps and relatively less costly raw materials. However, the temperature requirement for the formation of pure phase powder and its densification is quite high. On the other hand, preparation of powder through the chemical method results in a more homogeneous mixing of raw materials, low temperature phase formation and low temperature sintering compared to solid-state method. Usually, chemical routes use the Ti-alkoxides or Ti-chlorides as the Ti-metal source. Since Ti-alkoxides/chlorides are relatively costlier and highly unstable/volatile than TiO_2, the use of TiO_2 powder can reduce the powder synthesis cost, compared to chemical synthesis process. So in this modified chemical route, Ba- and Bi-components were precipitated from their solution in the suspension of TiO_2 solid oxide. Detailed procedure is described below.

Table 3.1 List of compositions synthesized.

1.	Pure compound	$BaBi_4Ti_4O_{15}$
2.	Isovalent substitution for *A*-site	$BaBi_{4-x}La_xTi_4O_{15}$ (x = 0.1, 0.2, 0.3, 0.5, 1.0)
3.	Isovalent substitution for *B*-site	$BaBi_4Ti_{4-x}Zr_xO_{15}$ (x = 0.1, 0.2, 0.3, 0.5)
4.	Aliovalent substitution for *A*-site	$Ba_{1-x}(Na_{x/2}La_{x/2})Bi_4Ti_4O_{15}$ (x = 0.25, 0.5, 0.75, 1.0)
5.	Aliovalent substitution for *B*-site	$BaBi_4Ti_{4-x}(Nb_{x/2}Al_{x/2})O_{15}$ (x = 0.1, 0.2, 0.3)
6.	Aliovalent substitution for *A*-and *B*-site	$Ba_{1-x}Na_xBi_4Ti_{4-x}Nb_xO_{15}$ (x = 0.1, 0.2, 0.3, 0.4, 0.5, 0.6)
		$BaBi_{3.8}M_{0.2}Ti_{3.8}Nb_{0.2}O_{15}$ (M = Mg^{2+}, Ca^{2+}, Sr^{2+}, Ba^{2+})

3.2 Powder Synthesis

3.2.1 Synthesis of $BaBi_4Ti_4O_{15}$

BBT powder was synthesized using reagent grade barium nitrate $Ba(NO_3)_2$ (Merck India Ltd., Assay >99%), bismuth nitrate $Bi(NO_3)_3.5H_2O$ (Merck India Ltd., Assay >99%), titanium dioxide TiO_2 (Merck India Ltd., Assay >99%, particle size: d_{10} = 0.27 μm, d_{50} = 0.35 μm, d_{90} = 0.48 μm), oxalic acid $(COOH)_2.2H_2O$ (Merck India Ltd., Assay >99%) and concentrated nitric acid HNO_3 (Merck India Ltd., GR Grade) as raw materials. Fig. 3.1 shows a flow chart for the synthesis of the powders by modified chemical route. The total mole of oxalic acid required for the precipitation of cations was estimated from the mole requirements of barium and bismuth cations in the solution.

To prepare a 10 gm batch of BBT powder, 1.8294 gm of barium nitrate was dissolved in 200 ml of deionized water and separately 13.5819 gm of bismuth nitrate was dissolved in minimum quantity of concentrated nitric acid. A low concentration of barium nitrate solution (~0.035M) was used in order to avoid cations precipitation during the addition of bismuth nitrate solution in aqueous solution of barium nitrate. 2.2372 gm of TiO_2 was dispersed in 0.4M oxalic acid solution in a separate vessel. This suspension was ultrasonicated for 15 minutes to break the soft agglomerates of TiO_2. Now, the barium-, bismuth- nitrate mixed solution was added drop-wise into the TiO_2-oxalic acid suspension under vigorous stirring. The pH of this solution was less than 2. Barium-oxalate and bismuth-oxalate hydrates were precipitated inside the suspension by heterogeneous nucleation. Finally, the pH of the suspension was adjusted to 7 by adding ammonium hydroxide solution. The precipitated mixture of TiO_2 and barium- and bismuth-oxalates was separated by filtration and washed thoroughly using deionized water, followed by drying at 60^oC for 24h.

The powder was calcined at various temperatures at an interval of 100^oC, in the temperature range $400\text{-}1000^oC$ in air atmosphere to study the phase formation behaviour. A pure phase of BBT was found in the specimen after calcination at 800^oC for 4h followed by heat treatment at 1000^oC for 4h.

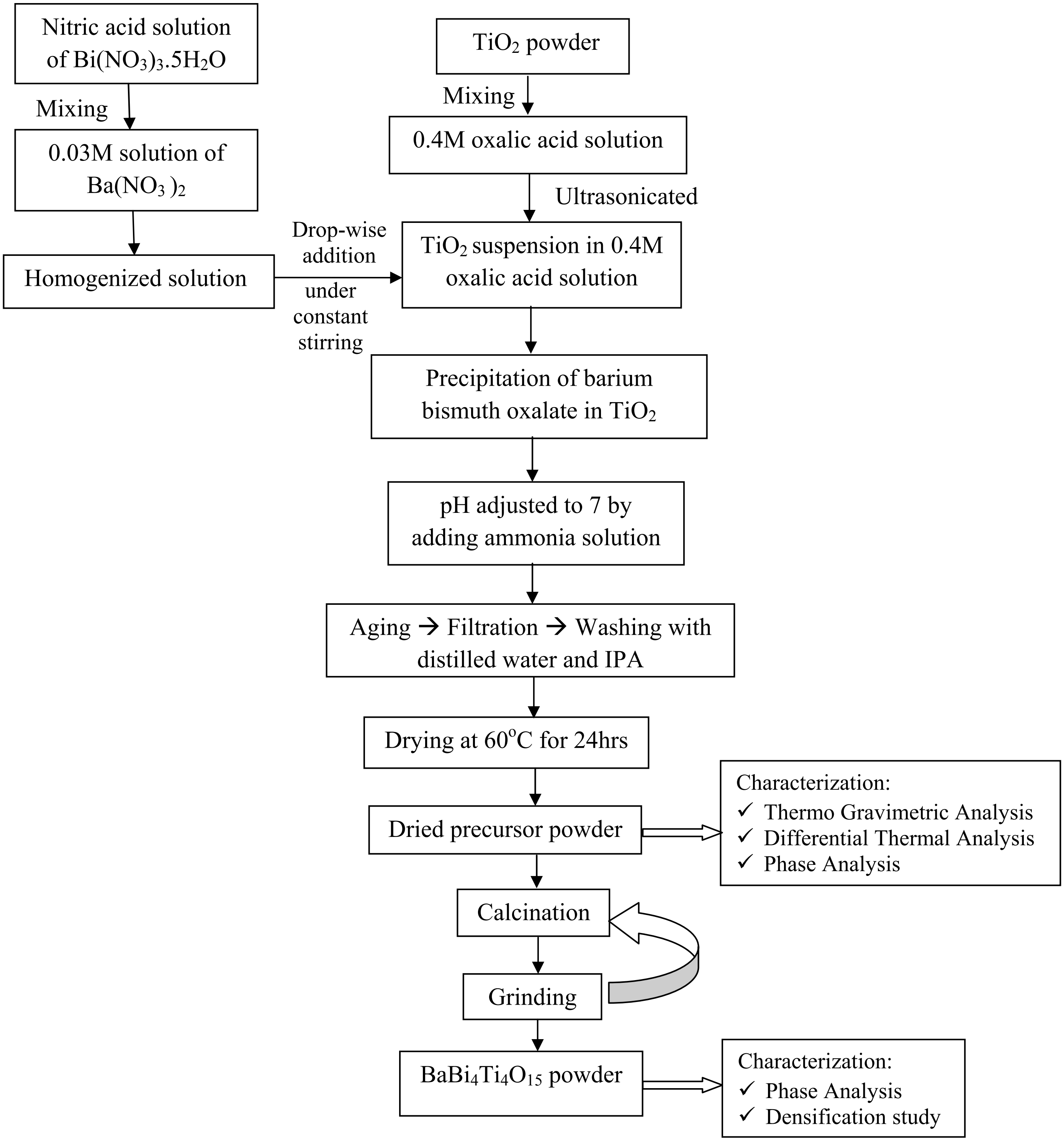

Fig.3.1. Generalized flow chart for synthesis of $BaBi_4Ti_4O_{15}$.

3.2.2 Synthesis of $BaBi_{4-x}La_xTi_4O_{15}$ (x = 0.1, 0.2, 0.3, 0.5, 1.0)

In addition to the above raw materials, lanthanum oxide La_2O_3 (Merck, India Ltd., Assay >99%) was used for synthesis. After dissolving bismuth nitrate in minimal quantity of nitric acid, required amount of lanthanum oxide was added to this solution. The solution was stirred vigorously until dissolution of lanthanum oxide to form a clear transparent solution. After that, similar procedure was followed as stated above (Section 3.2.1) for precipitation, washing and drying. Samples with $0.1 \leq x \leq 0.5$ were finally calcined at 900°C for 4h with an intermediate heating and grinding step at 800°C for 4h and the ceramic with $x = 1.0$ was finally calcined at 950°C for 4h with same intermediate step to form the pure phase.

3.2.3 Synthesis of $BaBi_4Ti_{4-x}Zr_xO_{15}$ (x = 0.1, 0.2, 0.3, 0.5)

Zirconium oxychloride $ZrOCl_2.8H_2O$ (Loba, India, GR grade) was used in combination with the other raw materials stated in Section 3.2.1. A 0.05M aqueous solution of zirconium oxychloride was prepared. This solution was simultaneously added drop-wise into the TiO_2-oxalic acid suspension along with the barium and bismuth nitrate mixed precursor solutions. This precipitates barium, bismuth and zirconium oxalates in TiO_2 suspension. The synthesized powders were finally calcined at 950 and 1000°C for 4h with intermediate heating and grinding steps at 800 and 900°C for 4h.

3.2.4 Synthesis of $Ba_{1-x}(Na_{x/2}La_{x/2})Bi_4Ti_4O_{15}$ (x = 0.25, 0.5, 0.75, 1.0)

Barium carbonate $BaCO_3$ (Merck, India Ltd., Assay >99%), bismuth oxide Bi_2O_3 (Merck, India Ltd., Assay >99%), TiO_2 (Merck, India Ltd., Assay >99%), sodium carbonate Na_2CO_3 (Qualigens, India Ltd., Assay >99%) and La_2O_3 (Merck, India Ltd., Assay >99%) raw materials were used. The above stated composition was synthesized via the conventional solid-state reaction route. Conventional solid-state route was employed as sodium oxalate is soluble in water. Stoichiometric amounts of raw materials were weighed and ball milled in IPA for 2h. The dried mixed powder was finally calcined at 1000°C for 6h for all the compositions with intermediate heating and grinding steps at 800°C and 900°C for 4h.

3.2.5 Synthesis of $BaBi_4Ti_{4-x}(Nb_{x/2}Al_{x/2})O_{15}$ (x = 0.1, 0.2, 0.3)

Nb_2O_5 (Alfa Aesar, Assay >99%) and $Al(NO_3)_3.9H_2O$ (Merck, India Ltd., Assay >99%) raw materials were used in addition to those in Section 3.2.1 for the synthesis. $Al(NO_3)_3.9H_2O$ was dissolved in aqueous solution of barium nitrate. Nb_2O_5 was dispersed in oxalic acid solution along with TiO_2 and rest of the process was as described in Section 3.2.1. The dried precursor powders were finally calcined at 1000°C for 4h with intermediate heating and grinding steps at 800°C and 900°C for 4h. Composition with $x = 0.3$ was calcined two times at 1000°C for 4h as secondary phases were observed in the composition.

3.2.6 Synthesis of $Ba_{1-x}Na_xBi_4Ti_{4-x}Nb_xO_{15}$ (x = 0.1, 0.2, 0.3, 0.4, 0.5, 0.6)

For the synthesis of these compositions, conventional solid state route was used. Nb_2O_5 (Alfa Aesar, Assay >99%) was used in addition to the raw materials used in section 3.2.4. Stoichiometric amounts of raw materials were weighed and ball milled in IPA for 2h. The mixed powders were finally calcined at 900°C and 1050°C for 4h with intermediate heating and grinding steps at 800°C.

3.2.7 Synthesis of $BaBi_{3.8}M_{0.2}Ti_{3.8}Nb_{0.2}O_{15}$ ($M = Mg^{2+}, Ca^{2+}, Sr^{2+}, Ba^{2+}$)

$Mg(NO_3)_2.6H_2O$ (Merck, India Ltd., Assay >99%), $Ca(NO_3)_2.4H_2O$ (Merck, India Ltd., Assay >99%), $Sr(NO_3)_2$ (Merck, India Ltd., Assay >99%), and Nb_2O_5 were used as raw materials in addition to those in Section 3.2.1. Aqueous solutions of the respective metal nitrates were added to barium nitrate aqueous solution. Similar to the above synthesis procedures, Nb_2O_5 was dispersed in TiO_2-oxalic acid suspension and rest procedures were followed as in Section 3.2.1. The dried precursor powders were finally calcined at 1000°C for 4h with intermediate heating and grinding steps at 800 and 950°C for 4h.

3.3 Characterization of powder

3.3.1 Differential Scanning Caloriemetry (DSC) and Thermo-gravimetric Analysis (TGA)

The dried precursor powder was characterized by DSC and TGA analysis using NETZSCH STA (Model No 409C) in an ambient atmosphere with a heating rate of 10°C/min using α-Al_2O_3 as a reference material. The reference material was chosen such that it itself does not undergo any transformation in the temperature range of interest. This characterization technique was used to analyze the dehydration and decomposition behaviour, the thermodynamics and phase formation behaviour of the precursor powder.

When a material is subjected to a temperature change, it absorbs or releases thermal energy owing to the various physical and chemical changes undergoing in the material. DSC device evaluates the difference in temperature of the sample with respect to the reference inert material (α-Al_2O_3) during heating or cooling. This temperature difference is measured by a differential thermocouple. A calibration constant, computed by the software provided, converts the amplified differential thermocouple voltage to energy per unit time (Watts) which is plotted in the DSC curve as the deviation from zero base line. Exothermic and endothermic changes are in the opposite directions of the baseline.

TGA is a simple analytical technique that measures the weight loss (or weight gain) of a material as a function of temperature. As materials are heated, they can lose weight due to drying or evolution of gases from chemical reactions taking place in the specimen. Some materials can gain weight by reacting with the atmospheric gases in the testing environment. The TGA plot identifies the temperature at which mass loss is maximum, corresponding to the DSC peak.

3.3.2 Phase analysis

X-ray diffraction is a powerful tool for material characterization. Various physical properties such as optical, ferroelectric, magnetic, electric, etc. depend on the atomic arrangement of the specimen and its chemical composition. X-ray diffraction pattern provides vital information such as: (i) qualitative phase composition of the sample, (ii) inter-planar spacing of different phases, (iii) intensities of diffraction peaks providing quantitative information of the phases, (iv) unit cell parameters and lattice type of different phases, (v) crystallite size of phases, and (vi) stress and strain present in the lattice.

Phase formation of raw and calcined powder samples was studied by powder X-ray diffraction, performed with a Philip's Diffractometer (Model: PW-1830, Philips, Netherlands). The source is Cu K_α with a wavelength of 1.541874 Å and equipped with Ni β-filter. To detect the diffracted X-rays, an electronic detector is placed on the other side of the sample from the X-ray tube and the sample was rotated through different Bragg's angles. The goniometer keeps track of the angle 2θ and the detector records the diffracted X-rays in units of counts/sec and sends this information to the computer. The parameters for carrying out the diffraction were; power controls of 40 kV and 35 mA, with a step size of 0.02^{o} and a count time in the range 2-6 s per step. The diffraction pattern of the sample was plotted as X-ray intensity (counts/sec) against the angle 2θ. The 2θ for each diffraction peak was converted to *d*-spacing, using the Bragg's law; $n\lambda = 2d \sin\theta$, where λ is the wave length of X-ray and n is order of diffraction.

Identification of different phases was carried out by Hanawalt method using Philips X-pert Highscore software. The powder pattern comprises of a set of peak positions 2θ and a set of relative peak intensities I. But the angular position of the peaks depends on the wavelength used and a more fundamental quantity is the spacing d of the lattice planes forming each peak. Each pattern is described by listing the d and I values of its diffraction peaks. Each substance is characterized by d values of its 3 strongest peaks. d values together with the relative intensities are sufficient to characterize the pattern of an unknown phase [154].

Lattice parameters were determined using following relationship for orthorhombic structure using the relation

$$\frac{1}{d^2} = \frac{h^2}{a^2} + \frac{k^2}{b^2} + \frac{l^2}{c^2} \tag{3.1}$$

where, a, b and c are the lattice parameters, d is the interplanar spacing and (hkl) are Miller indices and volume (V) of the unit cell was determined from the relation

$$V = a \times b \times c \tag{3.2}$$

3.3.3 Densification Study

Densification kinetics of powder compact was investigated by NETZSCH dilatometer model DIL 402 C, Germany. In the dilatometer, the specimen is kept in a specimen holder in the centre of the furnace. The linear dimensional change i.e. shrinkage or expansion of the specimen is transmitted through the push rod (pressed against the sample inside the furnace) to the measuring head. The inductive displacement transducer details the change in length and produces an analogue signal through a measuring amplifier. The digitally displayed signal is in analogue form on a recorder.

Samples were made in the form of rods having diameter 6 mm and length 20 mm for dilatometer experiment. The heating rate was maintained at 10^{o}C/min. The measurement was carried out from room temperature to 1150^{o}C in an air atmosphere.

3.4. Fabrication of pellet and Sintering

Calcined powder of each composition was granulated with 3 wt% polyvinyl alcohol (PVA). For the granules to be uniform and fine grained, the granulated powder was sieved through a 150 µm sieve. The remains after sieving were again ground in an agate mortar and passed through the sieve. This procedure was repeated till the granules were less than 150 µm in size. Powder was pressed into circular disks with a 15 mm die using stearic acid as a lubricant. The powder was compacted at a pressure of 220 MPa with a holding time of two minutes. The pellets were then sintered at different temperatures as stated in Table 3.2 depending on the compositions, and in a sealed alumina crucible to minimize bismuth volatilization.

Table 3.2. Sintering parameters for different compositions.

	Formulas	**Sintering temperatures**
1.	$BaBi_4Ti_4O_{15}$	1100^{o}C/1h to 4h.
2.	$BaBi_{4-x}La_xTi_4O_{15}$ (x = 0.1, 0.2, 0.3, 0.5, 1.0)	1100^{o}C/4h, 1100^{o}C/6h, 1110^{o}C/4h, 1120^{o}C/4h and 1145^{o}C/4h, respectively.
3.	$BaBi_4Ti_{4-x}Zr_xO_{15}$ (x = 0.1, 0.2, 0.3, 0.5)	1100, 1050, 1000, 950^{o}C and each for 4h, respectively.
4.	$Ba_{1-x}(Na_{x/2}La_{x/2})Bi_4Ti_4O_{15}$ (x = 0.25, 0.5, 0.75, 1.0)	1100^{o}C/6h
5.	$BaBi_4Ti_{4-x}(Nb_{x/2}Al_{x/2})O_{15}$ (x = 0.1, 0.2, 0.3)	1100^{o}C, 1110^{o}C and 1120^{o}C for 4h each, respectively.
6.	$Ba_{1-x}Na_xBi_4Ti_{4-x}Nb_xO_{15}$ (x = 0.1, 0.2, 0.3, 0.4, 0.5, 0.6)	1100^{o}C/4h, 3h, 2h, 1h, for x = 0.1, 0.2, 0.3 and 0.4, respectively and 1090 and 1080^{o}C for 2h, respectively for x = 0.5 and 0.6.
	$BaBi_{3.8}M_{0.2}Ti_{3.8}Nb_{0.2}O_{15}$ (M = Mg^{2+}, Ca^{2+}, Sr^{2+}, Ba^{2+})	1080^{o}C/2h (Ba), 1080^{o}C/4h (Sr), 1090^{o}C/4h (Ca), 1100^{o}C/2h (Mg).

3.4.1 Density measurements

Densities of sintered samples were measured using Archimedes principle. The basic procedure was as follows. The dry weight of the sintered samples was measured. The sintered samples were then immersed in water and kept under a vacuum of 4 mm of mercury for 5 hrs to ensure that water filled up the open pores completely. The suspended weight of the pellet was then measured in water. Then the soaked weight was measured by blotting the pellet with a wet paper towel and weighed. The apparent porosity and bulk densities were calculated as follows:

$$\%\ \mathrm{P_{App}} = \frac{W_s - W_d}{W_s - W_a} \times 100 \qquad (3.3)$$

$$\mathrm{D_{bulk}} = \frac{W_d}{W_s - W_a} \qquad (3.4)$$

where, W_d = Dry weight of the sample , W_s = Soaked weight of the sample, W_a = Suspended weight of the sample.

Relative densities of different sintered specimens were calculated from the bulk density and theoretical density as obtained from X-ray method. As the macroscopic specimen usually does carry minute cracks and pores, its bulk density based on the sample's weight and volume is usually less than and cannot exceed the X-ray density. The true porosity was calculated by comparing X-ray density with the bulk density of the sintered compacts. X-ray density is also called 'theoretical density'. However, it is not theoretical because it is determined experimentally. The base for the X-ray density for calculation is the single unit cell by defining the X-ray density equal to weight of atoms in unit cell per volume of unit cell, expressed [154]:

$$\rho = \frac{\Sigma A_w}{NV} \qquad (3.5)$$

where, ρ is the X-ray density (gm/cc), ΣA_w is the sum of the atomic weights of all the atoms in the unit cell, N is the Avogadro's number and V is the volume of unit cell (cc). Orthorhombic unit cell of $BaBi_4Ti_4O_{15}$ contains 4 formula units in one unit cell. Thus equation (3.5) can be written as:

$$\rho = \frac{4M_w}{N(a \times b \times c)} \tag{3.6}$$

where, M_w is the molecular weight of one formula unit and ‘a’, ‘b’ and ‘c’ are the lattice parameters of the unit cell. Percentage porosity is calculated as follows [155]:

$$\text{True Porosity \%} = \frac{\text{X - ray Density - Bulk Density}}{\text{X - ray Density}} \times 100 \tag{3.7}$$

3.4.2 Microstructural study

Microstructures of the sintered specimen were studied using JEOL-JSM840 Scanning electron microscope (SEM). In SEM, a hot tungsten filament electron gun under vacuum emits electron beam which passes through a series of electromagnetic lenses. The sample is then bombarded with the fine beam of electrons having acceleration potentials ranging from 1 to 30 kV. A part of the beam is reflected as back scattered electrons (BSE) along with low energy secondary electron emission (SE).

Images formed from the BSE beam were studied in the extrinsic mode of SEM. The images appeared very real as if photographed by ordinary means. The apparent illumination is a function of particle emission rather than radiation. The emitted back scattered electrons are detected and displayed on a scanning TV display. An image will be the result of high electron emission, while the primary influence on high emission is the surface structure of the specimen. The end result is therefore brightness associated with surface characteristics and an image which looks very much like a normally illuminated object.

The micrographs of the sintered samples were recorded without any coating. Images formed from the back scattered electrons were studied by SEM, in conjunction with EDX for elemental analysis. The grain size was determined using Image-J software. The grains of the samples are plate like in shape, possessing length, breadth and thickness. So, individual length, breadth and thickness of each grain were determined and their mean values were calculated.

3.4.3 Accurate lattice parameter determination and Quantitative phase estimation through Rietveld refinement

Lattice parameters can be accurately determined through full pattern Rietveld refinement considering all the diffraction peaks. Also the quantitative phase composition of a mixed specimen can be accurately determined through Rietveld method without using any internal standard.

The Rietveld method [156] extracts the detailed structural information from the powder diffraction data. The conventional profile fitting method uses integrated intensities of reflections whereas Rietveld method employs the entire powder diffraction pattern. In Rietveld method, each data point in the digitized intensity versus 2θ curve is considered as an independent observation. During the refinement procedure, structure parameters, background parameters and profile parameters are varied in least squares method until the simulated pattern matches well with experimental pattern for the proposed crystal structure model [157].

The principal goal of the Rietveld method is to refine the crystal structure and not profiles. In this method, parameters are refined in models provided for the crystal structure and for other factors and the instruments effects on the diffraction pattern. This methodology employs the least square refinement process, which is carried out until best fit is obtained between the entire observed powder diffraction pattern taken as a whole and the entire calculated pattern based on the simultaneously refined models for the crystal structures, diffraction optics effects, instrumental factors and other specimen characteristics i.e. lattice parameters as may be desired and can be modeled.

The Rietveld refinement was carried out using MAUDWEB (version 2.031) software [158]. This software is especially designed to refine simultaneously both the structural and microstructural parameters through a least-square fitting procedure. The peak shape was assumed to be pseudo-Voigt function with asymmetry. The background factor of each pattern was fitted to a polynomial of degree 5.

The simulation of the diffraction pattern requires some necessary initial structural information of the individual phases, which can be provided with the help of the graphical user interface of MAUD software. Initially, the positions of the peaks were corrected by successive refinements of zero-shift error. The integrated intensity of the peak was considered as a function of structural parameters only. The Marquardt least-squares procedure was adopted to minimize the difference between the observed and simulated patterns.

Rietveld refinement process will adjust the refineable parameters until the reliability index parameter (R) is minimized with some sense. The reliability index parameters are a measure between the observed and the simulated powder diffraction patterns and are commonly expressed by R_{wp} (weighted residual error), R_b (Bragg factor) and R_{exp} (expected error). These factors are calculated as follows:

$$R_b = 100\frac{\sum\left[I_i(obs)-I_i(calc)\right]}{\sum I_i(obs)} \tag{3.8}$$

$$R_{wp} = \left\{\frac{\sum W_i([I_i(obs)-I_i(calc)])^{2}}{\sum W_i(I_i(obs))^2}\right\}^{1/2} \tag{3.9}$$

$$R_{exp} = \left\{\frac{N-P}{\sum W_i(I_i(obs))^2}\right\}^{1/2} \tag{3.10}$$

where $I_i(obs)$ and $I_i(calc)$ are the observed and the calculated intensities, respectively, $W_i = 1/I_i(obs)$, N are the weight and number of experimental observations and P is the number of fitting parameters. Among all these R-factors, R_{wp} is the most meaningful as its numerator is the residual being minimized.

Another numerical criterion is the “goodness of fit” G, which is expressed as

$$G=\left(\frac{R_{wp}}{R_{exp}}\right) \tag{3.11}$$

Refinement continues till the convergence is reached with the minimum value of G that can be achieved.

Rietveld method can be applied to determine the quantitative phases of mixed phase materials [159-165]. There is a simple relationship between the individual scale factors determined, considering all refined structural parameters of individual phases of multiphase material and the phase concentration (volume/weight fraction) in the mixture. The weight fraction (W_i) for each phase was obtained from the following refinement relation:

$$W_i = \frac{S_j(ZMV)_i}{\sum_j S_j(ZMV)_j} \tag{3.12}$$

where, i is the value of j for a particular phase among the N phases present, S_j is the refined scale factor, Z is the number of formula units per cell, M is the atomic weight of the formula unit and V is the volume of the unit cell [158, 166].

3.4.4 Electroding and Electrical Property Measurements

3.4.4.1 Dielectric Measurements

For electrical measurements, both the surfaces of pellets were painted uniformly with a silver conductive paste (Alfa Aesar) and cured at 600^{o}C for half an hour. Thus a pellet with two parallel electrodes acts as a single layer capacitor.

The capacitance (C) of this disc capacitor and dielectric loss (tan δ) of the same were measured using a Solatron 1260 Impedance/Gain-Phase Analyzer, with the temperature ranging from room temperature to 650^{o}C depending on the composition. The temperature of the specimen was controlled using a furnace at a heating rate of 1^{o}C/min with platinum leads. Data were collected in the frequency range 1Hz – 5MHz. dc bias voltage of the instrument was zero. The instrument applies a sinusoidal voltage to the dielectric, and the magnitude and phase shift of the resultant current were measured.

The capacitance (C) of a dielectric capacitor is given by

$$C = \frac{\varepsilon\varepsilon_o A}{d'} \tag{3.13}$$

where, ε is the dielectric constant or permittivity of the capacitor, ε_o is the permittivity of free space (8.854 x 10^{-12} F/m), A is the area of the conducting electrodes and d' is the thickness of the disc capacitor. Dielectric constant is the ratio of the amount of electrical energy stored in an insulator relative to vacuum, when the dielectric is subjected to an electric field.

When a dielectric is subjected to an electric field, a current flows. This total current flowing in a dielectric is made up of two parts: (a) conduction current and (b) displacement current. The displacement current is the elastic response of the dielectric material to the applied electric field. When the amplitude of the electric field is increased, the additional displacement gets stored within the dielectric as potential energy. As the amplitude of the electric field is decreased, the dielectric releases some amount of its stored energy as the displacement current. This displacement current can be separated into a vacuum contribution and the other part as resulting from the dielectric by the relation:

$$D = \varepsilon_o E + P \qquad (3.14)$$

where, E is the electric field and P is the polarization of the dielectric.

The capacitance of a dielectric capacitor arises due to dielectric polarization. Dielectric polarization may be described as the separation of bound charges in a dielectric material into positive and negative charge entities when subjected to an electric field. There are different types of polarization occurring in a material. They are electronic, ionic, dipolar and space charge polarization. Of these, electronic, ionic and dipolar polarizations are dependent on the bound charges of the material whereas space charge is concerned with the free charge. When the material is placed in an electric field, the electron cloud of the atom is displaced slightly with respect to the nuclei, causing electronic polarization. Ionic polarization is concerned with the motion of positive and negative charges in an electric field. Dipolar polarization also known as ion jump polarization is the preferential occupation of equivalent or near equivalent lattice sites on application of an external field. The free charges capable of migrating that are trapped in the interface of the material give rise to space charge polarization. The total polarization of a material is the sum of all the four polarization.

The dielectric loss (tan δ) is the measure of energy dissipated in a dielectric on application of an electric field, which can be expressed as the ratio of resistive (loss) component of the current to the capacitive component of the current.

When a varying voltage $V = V_o e^{i\omega t}$ is applied, the total current in the dielectric is given by

$$I = \frac{dQ}{dt} = \frac{d(CV)}{dt} = jC\omega V = j\omega\varepsilon C_o V \qquad (3.15)$$

where C_o is the capacitance in vacuum. As ε is a complex quantity ($\varepsilon = \varepsilon' - j\varepsilon''$), so I can be written as

$$I = j\omega(\varepsilon' - j\varepsilon'')C_o V = j\omega\varepsilon' C_o V + \omega\varepsilon'' C_o V = I_c + I_l \qquad (3.16)$$

where I_c and I_l are the capacitive and loss component of the current, respectively.

The total current (I) through the capacitor can be resolved into two components; the capacitive or charging current (I_c) is 90° out-of-phase with the voltage in an ideal capacitor, and the loss or conductive current (I_l) is in-phase with the voltage. However, in a real capacitor, the current lags behind the applied voltage by an angle δ. This is represented as the dielectric loss of the material which is the measure of energy dissipated in dielectric on application of an electric field. Fig.3.2, shows the vector resolution of current (I) and the dielectric loss ($\tan\delta$) derived from it is given by,

$$\tan\delta = \frac{I_l}{I_c} = \frac{\varepsilon''}{\varepsilon'} \qquad (3.17)$$

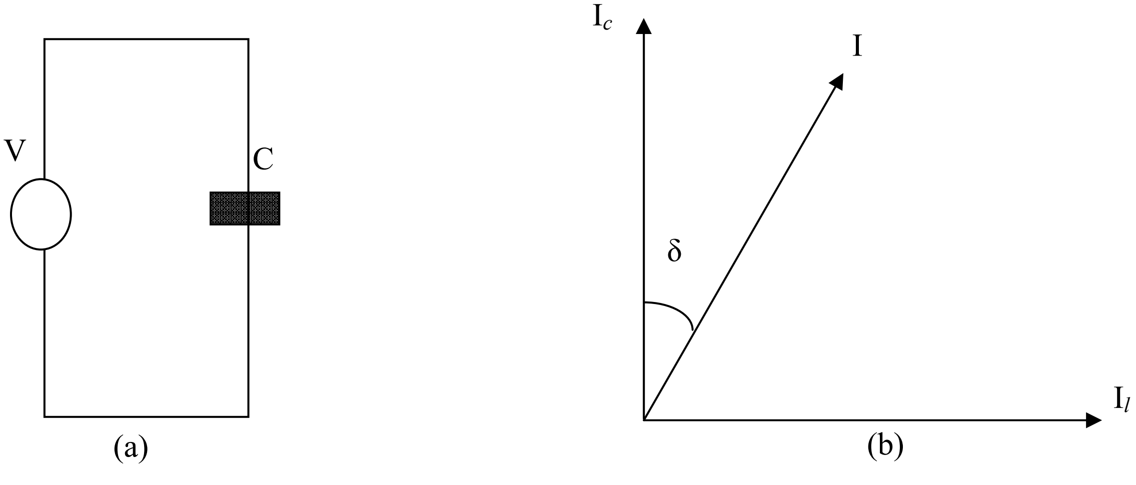

Fig.3.2. (a) ac voltage applied to the parallel plate dielectric capacitor, (b) Capacitive current (I_c) leads voltage by (90^o-δ).

3.4.4.2 Impedance Spectroscopy

Impedance spectroscopy is a powerful tool for investigation of complex electrical properties. The technique is advantageous in separating and determining the values of grain and grain boundary effects, and also helpful in correlation with the properties such as composition, microstructure, defects, dielectric properties, etc.

In impedance spectroscopy technique, impedance $|Z|$ and the phase difference (θ) between voltage and current are measured as a function of frequency. Analysis of the data and separation of the various phenomena are carried out by plotting the real part of impedance $Z' = |Z|\sin\theta$ versus $Z'' = |Z|\cos\theta$ called Cole-Cole plot. This impedance plot is used to examine the equivalent circuit representing it. The impedance plot of an ideal capacitor is represented by a straight line coinciding with the imaginary axis, while that of an ideal resistor is a point on the real axis. An equivalent circuit model consisting of parallel resistor (*R*) and capacitor (*C*) is shown in Fig.3.3. The following relation is used to represent a parallel *RC* equivalent circuit

$$Z^* = Z' - j\,Z'' \tag{3.18}$$

Simplifying the above relation,

$$\left(Z' - \frac{R}{2}\right)^2 + Z''^2 = \left(\frac{R}{2}\right)^2 \tag{3.19}$$

The resulting Eq. 3.19, represents the equation of a circle with a radius of *R*/2 and centre at (*R*/2,0). Thus it can be said that the plot of Z′ versus Z″ will be semicircular in shape with a radius of *R*/2. The time constant (τ) of the parallel *RC* is expressed as

$$\tau = RC = \frac{1}{\omega} = \frac{1}{2\pi f} \tag{3.20}$$

where *f* is the characteristic frequency lying at the peak of the semicircle. A typical Cole-Cole plot is shown in Fig.3.3. The high frequency arc corresponds to the bulk property or grain behaviour of the polycrystalline material, while the low frequency arc represents the grain boundary effect. Solatron 1260 was used for impedance measurements.

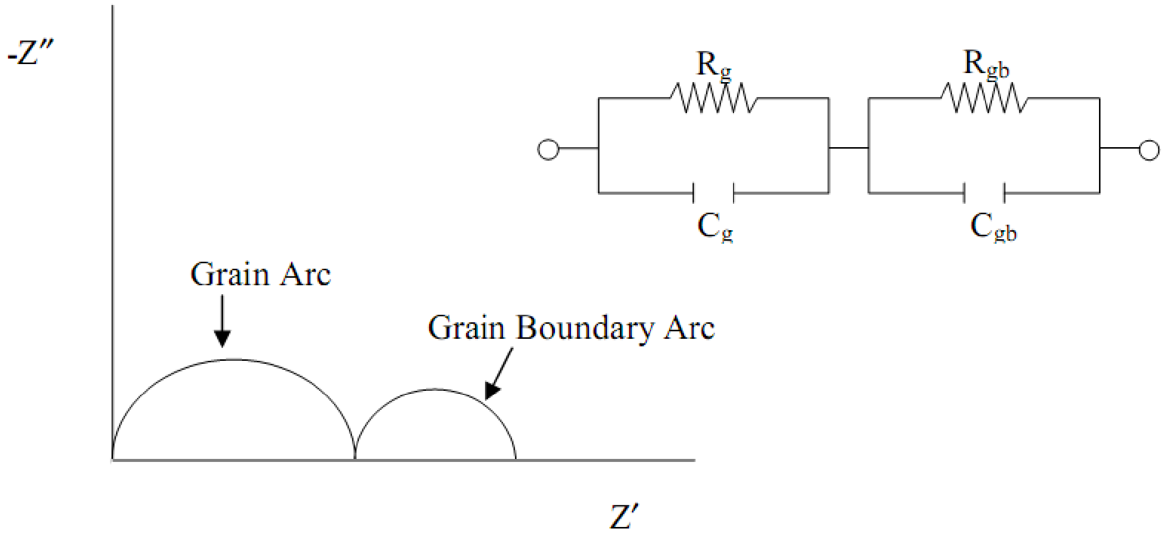

Fig.3.3. Cole-Cole plot showing grain and grain boundary effects and its equivalent circuit model consisting of parallel resistor and capacitor.

3.4.4.3 Polarization versus Electric field study

The hysteresis loop measurement was carried out by a *P-E* loop tracer (Marine India Electronics). For these measurements, the thickness of the pellets was reduced to ~0.4mm. The pellets were electroded with silver paint and cured at 550°C for 1h. All the measurements were carried out at room temperature.

Materials exhibiting ferroelectricity must be solids composed of crystallites and must also possess reversible spontaneous polarization which can be reversed on the application of an external electric field. Spontaneous polarization means a nonzero polarization value in the absence of an electric field and the direction of which can be reversed by an applied field in the opposite direction. Hysteresis is one of the prominent features of ferroelectricity exhibiting a non-linear relationship between the polarization P and applied field E.

The instrument is based on the Sawyer-Tower method [167, 168], as shown in Fig. 3.4. In the figure C is the ferroelectric capacitor and C_o is the standard reference capacitor. An *ac* signal voltage V of usually low frequency is applied across the capacitor C. However, the voltage applied should be adequate to bring saturation in polarization. So that V_o should be proportional to the polarization charge $V_o = AP/C_o$, where A is the area of the sample. Thus the applied field across the specimen is given by

$$F = \frac{V_c}{d} = \frac{(V - V_o)}{d} \tag{3.21}$$

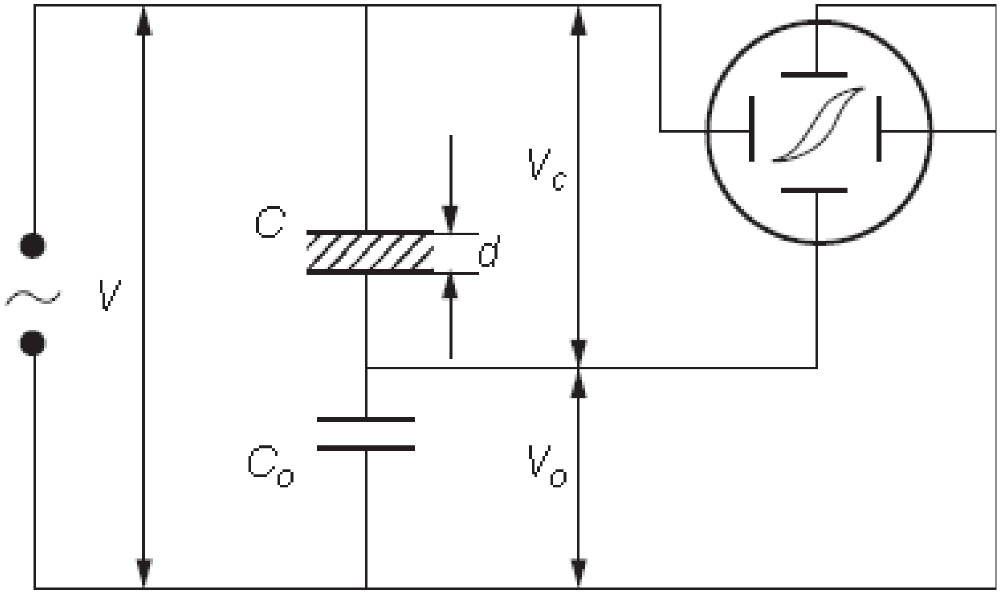

Fig.3.4. Sawyer-Tower method for polarization versus electric field measurement [168].

Fig. 3.5 shows a typical hysteresis plot. In portion *OA* of the graph, field induced polarization occurs on the application of a low field. On increasing the field strength, polarization increases non-linearly with the field as the domains start to align in the direction of applied field (portion *AB*). On further increase in the field strength, the polarization attains a saturation value (portion *BC*), where maximum domains are aligned in the field direction. On gradually decreasing the field strength, the polarization decreases following the path *CBD*. The extrapolation of the *CB* region to zero-field axis at *E*, gives the region *OE*, *i.e*, spontaneous polarization P_s and the region *OD* represents the remnant polarization P_r. P_r is always less than P_s, as some of the domains return to their original positions on reducing the field to zero. The electric field required to bring the polarization to zero is called the coercive field (E_c), shown in region *OR*. E_c depends on frequency, temperature and waveform applied.

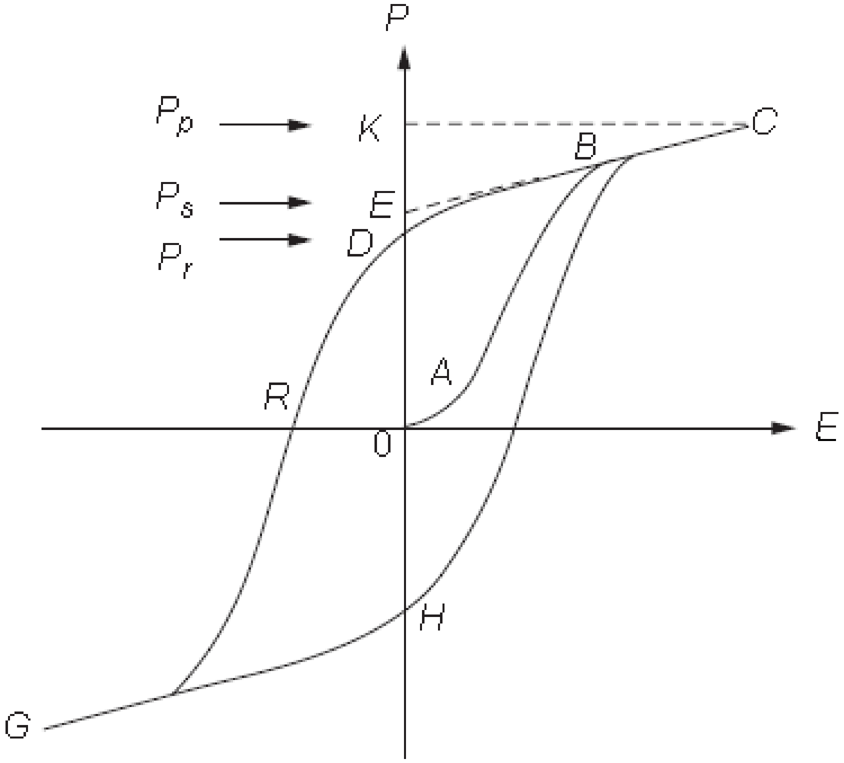

Fig.3.5. Schematic figure of a typical *P-E* hysteresis loop [168].

3.4.4.4 Piezoelectric study

Crystals which are formed of polar molecules with a non-centro-symmetric structure will exhibit piezoelectric effect. Thus when a mechanical stress is applied to such a sample, it gets polarized and hence a voltage is observed in it. So, piezoelectricity can be defined as the ability of certain crystalline materials to develop an electrical charge proportional to an applied mechanical stress [169]. This is called direct piezoelectric effect. A reverse stress direction will cause a polarity reversal and a voltage. Converse piezoelectric effect is also possible where an electric field is applied a mechanical stress is created in the material.

In general, piezoelectric properties of a material are dependent on orientation direction. Piezoelectric coefficients are usually denoted with two subscripts indicating the direction of properties. The first subscript gives the direction of the electric field and the second subscript gives the direction of mechanical stress. Mathematically, the tensor notations used to express the direct and converse piezoelectric effects are given by:

$$P_i = d_{ijk}\sigma_{jk} \quad \text{(direct piezoelectric effect)} \tag{3.22}$$

$$x_{ij} = d_{kij}E_k \quad \text{(converse piezoelectric effect)} \tag{3.23}$$

where P_i is the polarization generated along the i^{th} axis in response to the applied stress σ_{jk}, $d_{ijk} = d_{kij}$ is the piezoelectric coefficient, and x_{ij} is the strain generated in a particular orientation of the crystal on application of the electric field E_k along the k^{th} axis [170].

For the piezoelectric measurements, the pellet samples were first poled in silicon oil under an applied field of 30 kV/cm at 180°C for 20min. The d_{33} coefficients of the samples were then measured with a d_{33} meter (YE2730A d33 Meter, APC International Ltd.). A force of 0.25N is applied to the sample and the corresponding d_{33} coefficient is measured.

The convention is to define the poling direction as the 3-axis, as shown in Fig. 3.6 [171]. The shear planes are indicated by the subscripts 4, 5 and 6 and are perpendicular to the directions 1, 2 and 3, respectively. So, the piezoelectric coefficient d_{33} can be interpreted as both strain and field parallel to the polar axis.

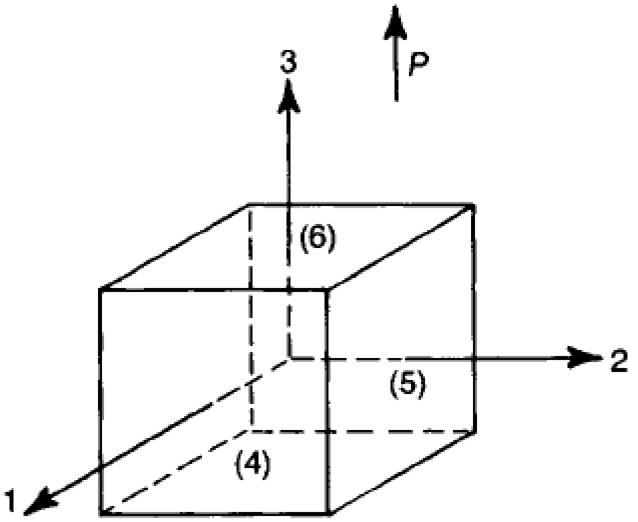

Fig.3.6. Labeling of reference axes and planes for piezoceramics [171].

Chapter IV

Results and Discussions

4.1 Synthesis of $BaBi_4Ti_4O_{15}$ through modified chemical route

4.1.1 Introduction

Several reports are available for the preparation of $BaBi_4Ti_4O_{15}$ (BBT) powders by conventional solid-state method [22, 28, 172] and a few reports using chemical methods [48, 54, 173]. This chapter presents the synthesis of BBT through a modified chemical route. The precursor for BBT synthesis was prepared by precipitating Bi- and Ba-oxalates in TiO_2 powder suspension. The thermal decomposition behaviour and phase formation during heat treatment of precursor powder were investigated. The synthesized BBT was characterized with respect to structural analysis, densification behaviour, dielectric and relaxor behaviour, ferroelectric hysteresis, d_{33} and impedance spectroscopic study.

4.1.2 Results and Discussions

4.1.2.1 Thermal decomposition and Phase formation behaviour

The raw precursor powder obtained after filtration and drying of the precipitate (Section 3.2.1) was used to study the thermal decomposition behaviour using differential scanning caloriemetry (DSC) and thermo-gravimetric (TG) analysis. Fig. 4.1 shows the decomposition behaviour of the precursor. The decomposition reaction proceeds mainly in three steps. The initial TG weight loss (~ 0.92%) up to 150^oC corresponds to the dehydration of the precursor. Next weight loss (~ 12.31%) in the temperature range $200\text{-}400^oC$ corresponds to the decarboxylation of oxalates, which results in an exothermic peak in the DSC curve at 289.9^oC. Further weight loss (~ 2.30%) in the temperature range $400\text{-}600^oC$ is due to the decomposition of residual Ba-oxalate with an exothermic peak at 487.7^oC. Lastly, the decomposition of Ba-carbonate occurs with associated weight loss of about 1.59% in the temperature range $700\text{-}900^oC$.

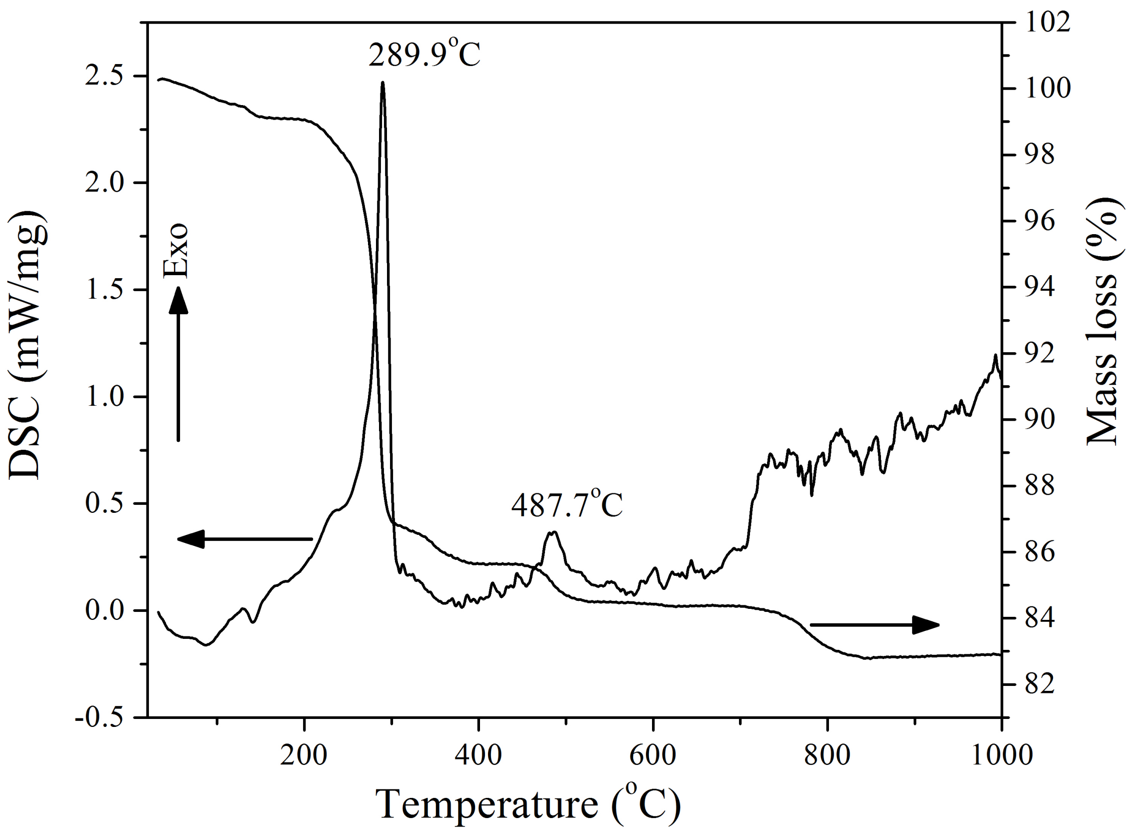

Fig.4.1. DSC/TG plot of precursor powder of $BaBi_4Ti_4O_{15}$ ceramic at a heating rate of 10°C/min in air atmosphere.

To understand the phase formation behaviour, the dried precursor powder was calcined in the temperature range 400 to 1000°C, at an interval of 100°C and each time the calcined powder was analyzed by XRD at room temperature. Fig. 4.2 shows the XRD pattern of raw precursor powder and the precursors after calcination at 400, 500 and 600°C. The phase identification revealed that the precursor powder contained bismuth-oxalate phase $Bi_2(C_2O_4)_3.7H_2O$, along with two different types of barium-oxalate phases ($BaC_2O_4.0.5H_2O$, and $BaC_2O_4.H_2O$) and TiO_2 phases. XRD pattern of sample calcined at 400°C (Fig. 4.2(b)) shows the presence of BaC_2O_4 and Bi_2O_3 phases along with TiO_2. This indicated that upon calcination, $Bi_2(C_2O_4)_3.7H_2O$ decomposed to form Bi_2O_3 as per reaction 4.1, and Ba-oxalate hydrates decomposed to form anhydrous Ba-oxalate as per decomposition reactions 4.2 and 4.3. The overall weight loss of these three reactions corresponded to a weight loss of ~12.3 % in TG curve (Fig. 4.1).

$$Bi_2(C_2O_4)_3.7H_2O \xrightarrow{400^\circ C} Bi_2O_3 + 6CO_2(\uparrow) + 7H_2O(\uparrow) \tag{4.1}$$

$$\mathrm{BaC_2O_4.0.5H_2O} \xrightarrow{400^\circ \mathrm{C}} \mathrm{BaC_2O_4} + 0.5\mathrm{H_2O}(\uparrow) \tag{4.2}$$

$$\mathrm{BaC_2O_4.H_2O} \xrightarrow{400^\circ \mathrm{C}} \mathrm{BaC_2O_4} + \mathrm{H_2O}(\uparrow) \tag{4.3}$$

Fig. 4.2(c) shows the XRD pattern of precursor after calcination at 500°C, where the BaC_2O_4 phase was absent and $BaCO_3$ phase appears. This was due to decarboxylation of anhydrous barium oxalate to $BaCO_3$ with an associated exothermic DSC peak at 487.7°C (Fig. 4.1) as per reaction 4.4. Figure 4.2(d) shows the appearance of BBT phase in the specimen calcined at 600°C with a decrease in the peak intensities of Bi_2O_3, TiO_2 and $BaCO_3$ phases in comparison with Fig. 4.2(c). Equation 4.5 represents the formation of BBT phase through the reaction between Bi_2O_3, TiO_2 and $BaCO_3$ phases.

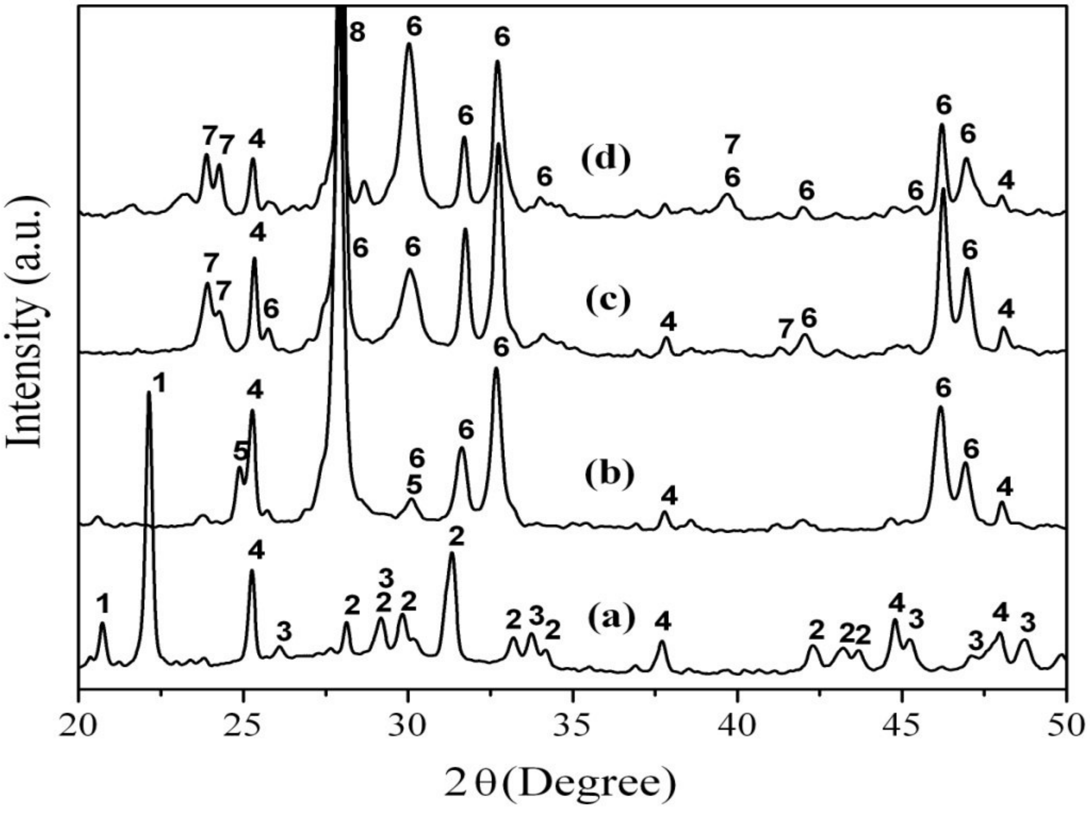

Fig.4.2. Room temperature XRD pattern of raw precursor powder (a) and precursor powder calcined at 400°C (b), 500°C (c), and 600°C (d). Major phases identified are marked as: (1) $BaC_2O_4.H_2O$; (2) $C_2BaO_4.0.5H_2O$; (3) $Bi_2(C_2O_4)_3.7H_2O$; (4) TiO_2; (5) BaC_2O_4; (6) Bi_2O_3; (7) $BaCO_3$; and (8) $BaBi_4Ti_4O_{15}$.

$$BaC_2O_4 + 0.5O_2 \xrightarrow{500^oC} BaCO_3 + CO_2(\uparrow) \quad (4.4)$$

$$BaCO_3 + 2Bi_2O_3 + 4TiO_2 \xrightarrow{600^oC} BaBi_4Ti_4O_{15} + CO_2(\uparrow) \quad (4.5)$$

The precursor powder was also calcined at 700, 800, 900 and 1000°C to study the intermediate phase formation and reaction mechanism. Fig. 4.3 shows the XRD patterns of precursors calcined at 700, 800, 900 and 1000°C. There was an evidence of the formation of a few intermediate phases during heat treatment of the precursor. In the temperature range of 600-700°C, Bi_2O_3 reacted with $BaCO_3$ resulting in the formation of an intermediate phase $BaBiO_3$ (along with BBT) as shown in Fig. 4.3(a) as per reaction 4.6. In 800°C, calcined specimen (Fig. 4.3(b)), no traces of TiO_2 was observed; instead two new intermediate phases $Bi_4Ti_3O_{12}$ and $BaTiO_3$ were detected in the samples (by reactions 4.7 and 4.8). XRD pattern of sample calcined at 900°C (Fig. 4.3(c)), shows presence of $Bi_4Ti_3O_{12}$ and $BaTiO_3$ mainly along with BBT phase.

$$Bi_2O_3 + BaCO_3 \xrightarrow{700^oC} BaBiO_3 + CO_2(\uparrow) \quad (4.6)$$

$$BaCO_3 + TiO_2 \xrightarrow{800^oC} BaTiO_3 + CO_2(\uparrow) \quad (4.7)$$

$$2Bi_2O_3 + 3TiO_2 \xrightarrow{800^oC} Bi_4Ti_3O_{12} \quad (4.8)$$

Fig. 4.3(d) shows the XRD pattern of the sample calcined at 1000°C for 4 hours. In the pattern no trace of $Bi_4Ti_3O_{12}$ and $BaTiO_3$ phases was observed, and instead BBT phase was formed due to reaction 4.9.

$$BaTiO_3 + Bi_4Ti_3O_{12} = BaBi_4Ti_4O_{15} \quad (4.9)$$

All the above equations showed the sequence of phase formation of BBT during the heat treatment steps.

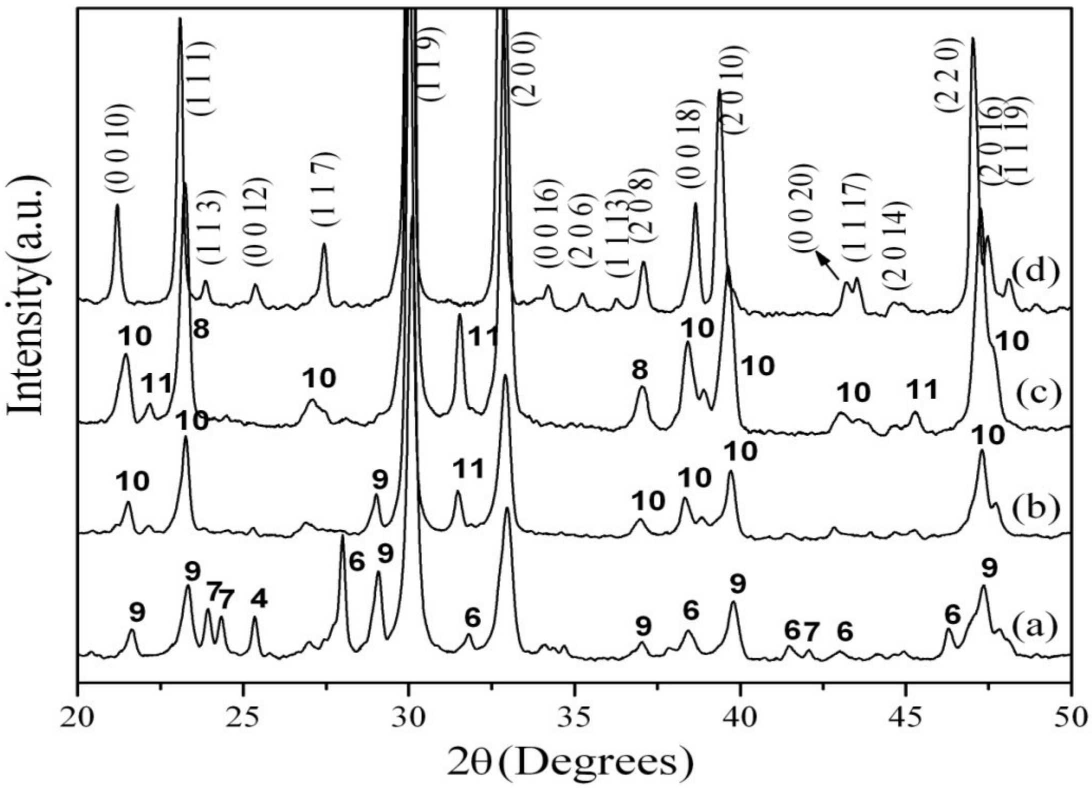

Fig.4.3. Room temperature XRD pattern of precursor powder calcined at (a) 700°C, (b) 800°C, (c) 900°C, and (d) 1000°C with 4 hours heating. Major phases identified are marked as: (4) TiO_2; (6) Bi_2O_3; (7) $BaCO_3$; (8) $BaBi_4Ti_4O_{15}$; (9) $BaBiO_3$; (10) $Bi_4Ti_3O_{12}$; and (11) $BaTiO_3$.

4.1.2.2 Structural Analysis

Full pattern Rietveld refinement was performed using MAUD Program [158]. Starting parameters for Rietveld refinement were taken from $BaBi_4Ti_4O_{15}$ as presented by *Kennedy et.al.* [29], with orthorhombic space group $A2_1am$ (No. 36) and initial cell parameters of a = 5.4697 Å, b = 5.4558 Å and c = 41.865 Å. Starting atomic coordinates and atomic displacements were also taken from the same reference. The refinement consisted of the parameters set including the modeling of background scale factor, lattice parameters, detector zero, point and profile parameters. Some constraints were imposed during the refinement to limit the no of refined parameters. Each constraint was systematically verified.

Fig.4.4 shows the Rietveld refinement output curve for BBT. Table 4.1 shows the refined lattice parameters, the R-factors and Sigma. The refined lattice parameters were observed to be *a* = 5.4656 Å, *b* = 5.452 Å, *c* = 41.8778 Å, respectively. These lattice parameters and *R*-factors obtained were similar to those obtained by other researchers [17, 29].

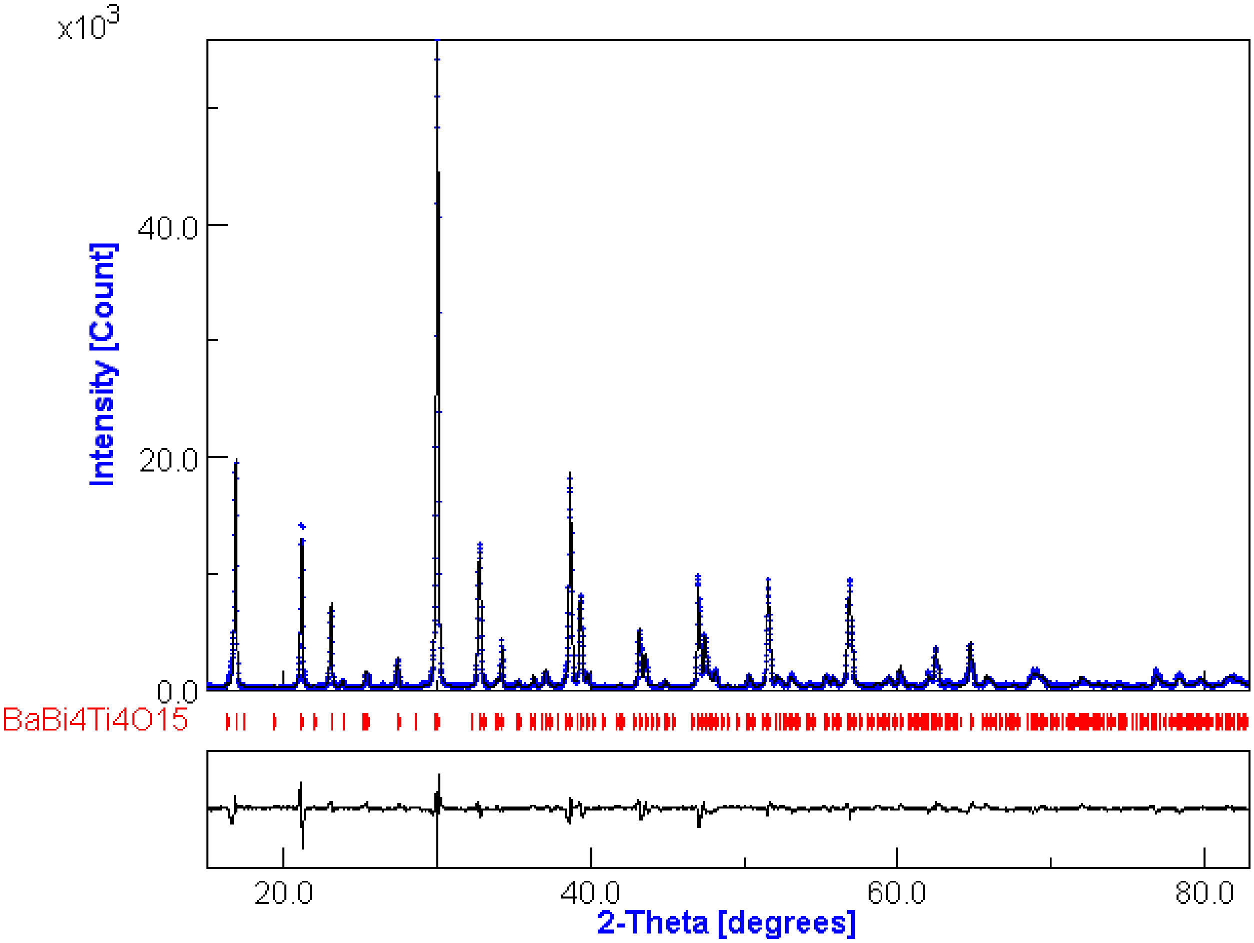

Fig.4.4. Rietveld refinement output of $BaBi_4Ti_4O_{15}$. The calculated and observed patterns are shown by the solid line and dots, respectively. The vertical marks in the middle show the positions calculated for Bragg reflections. The trace on the bottom is the plot of difference between calculated and observed intensities.

The lattice parameters demonstrate the structure to be orthorhombic. The orthorhombicity of the structure can be determined by the equation:

$$\text{Orthorhombicity} = \frac{2(a-b)}{(a+b)} \tag{4.10}$$

The orthorhombicity of the BBT was 0.0024.

Table 4.1. Symmetry, Space group, Refined lattice parameters '*a*', '*b*' and '*c*', *R*-factors, Sigma, Orthorhombicity of $BaBi_4Ti_4O_{15}$ ceramic.

Parameters	**Values**
Symmetry	Orthorhombic
Space group	$A2_1am$
a (Å)	5.4656(4)
b (Å)	5.4520(3)
c (Å)	41.8778(15)
R_w (%)	5.6
R_b (%)	3.92
Sigma	3.27
Orthorhombicity	0.0027

4.1.2.3 Densification Behaviour

Before the sintering of the ceramics the densification behaviour, *i.e.* the shrinkage behaviour with the increase in temperature is essential. BBT powder synthesized through this modified chemical route was studied for its densification behaviour. Fig. 4.5 shows the non-isothermal shrinkage behaviour of the BBT powder compact. It was evident that the shrinkage of the specimen started at about 1040°C and continued up to 1130°C. So a sintering schedule of 1100°C was selected. More than 96 % dense ceramics were obtained by sintering pellet at 1100°C for 4 hours. Heating above 1130°C caused the specimen to melt.

4.1.2.4 Microstructural Characteristics

Fig.4.6 shows the microstructure of BBT sintered at 1100°C for 1h. Microstructure showed plate like grains with random orientation of plate faces. The plate like grains has an edge length between 2-5 µm and a thickness of about 0.3 µm. The aspect ratio of the grains, which is the ratio between the largest to the smallest dimension, for the ceramics was in the range 6-9. The plate like grain formation is a typical characteristic of bismuth layer-structured ferroelectrics as they have highly anisotropic crystal structure. *Horn et al.* [8] have shown that the {0 0 1} plane of BLSF possesses lower surface energy, resulting in a rapid grain growth in the *a*-*b* plane during sintering and thus attaining a plate like morphology.

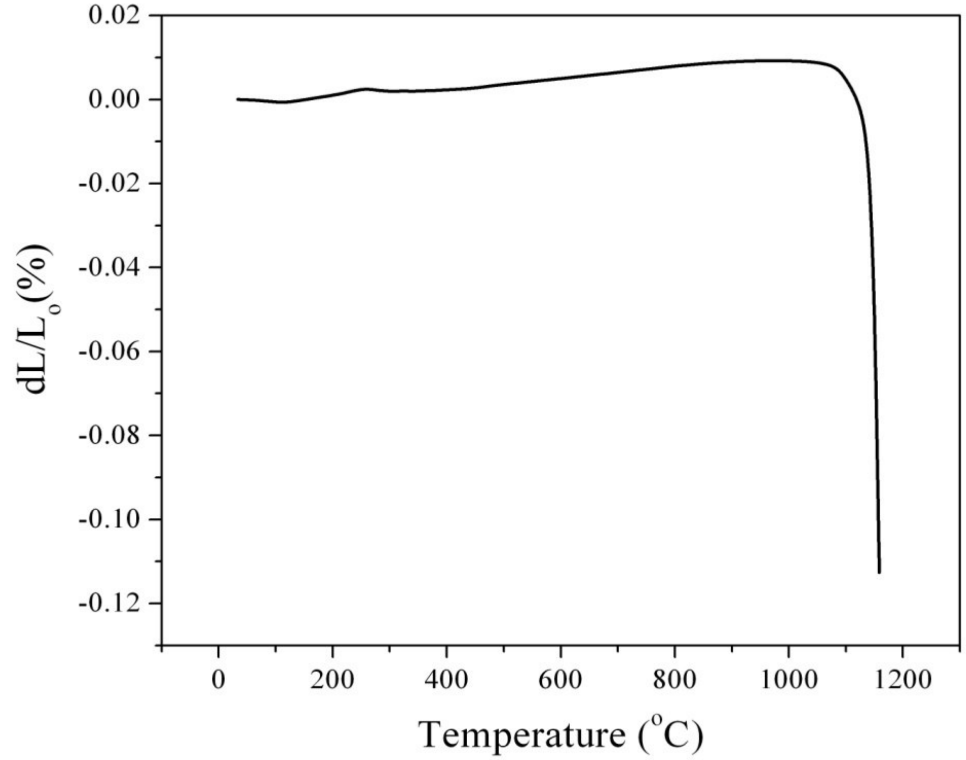

Fig.4.5. Non-isothermal sintering behaviour of $BaBi_4Ti_4O_{15}$ powder compact.

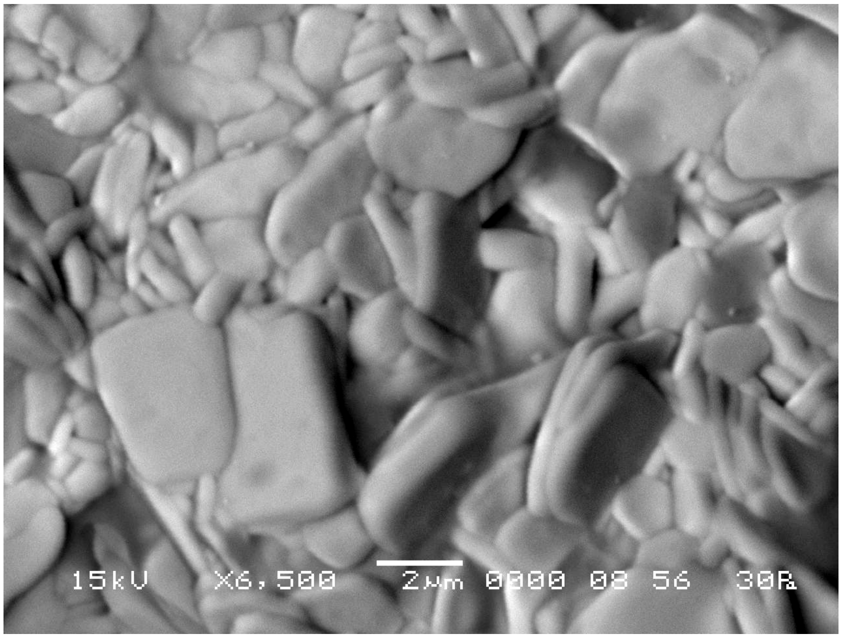

Fig.4.6. Microstructure of as-sintered specimen surface of $BaBi_4Ti_4O_{15}$ ceramic.

4.1.2.5 Dielectric and Diffuse Phase Transition Behaviour

Specimens with more than 96% sintered density were used for dielectric and other studies. Fig. 4.7 shows the temperature dependence of dielectric constant (ε') and dielectric loss (tan δ) for BBT ceramics at various frequencies. Broad peaks were observed in the ε' (T) and tan δ (T) versus temperature plots. The temperature T_m corresponding to the maximum value of ε', i.e. (ε_m') shifted to higher temperatures and ε_m' decreased with increase in frequency. T_m was 419 and 434°C at 1 kHz and 1 MHz, respectively. Table 4.2 summarizes the values of dielectric constant at room temperature (ε_{rm}), ε_m', T_m, tan δ at room temperature and tan δ_m for BBT ceramics. The temperature corresponding to tan δ maximum also increased with increase in frequency. The frequency and temperature dependence of both ε' and tan δ supported the relaxor behaviour of BBT as observed by earlier researchers [22, 106].

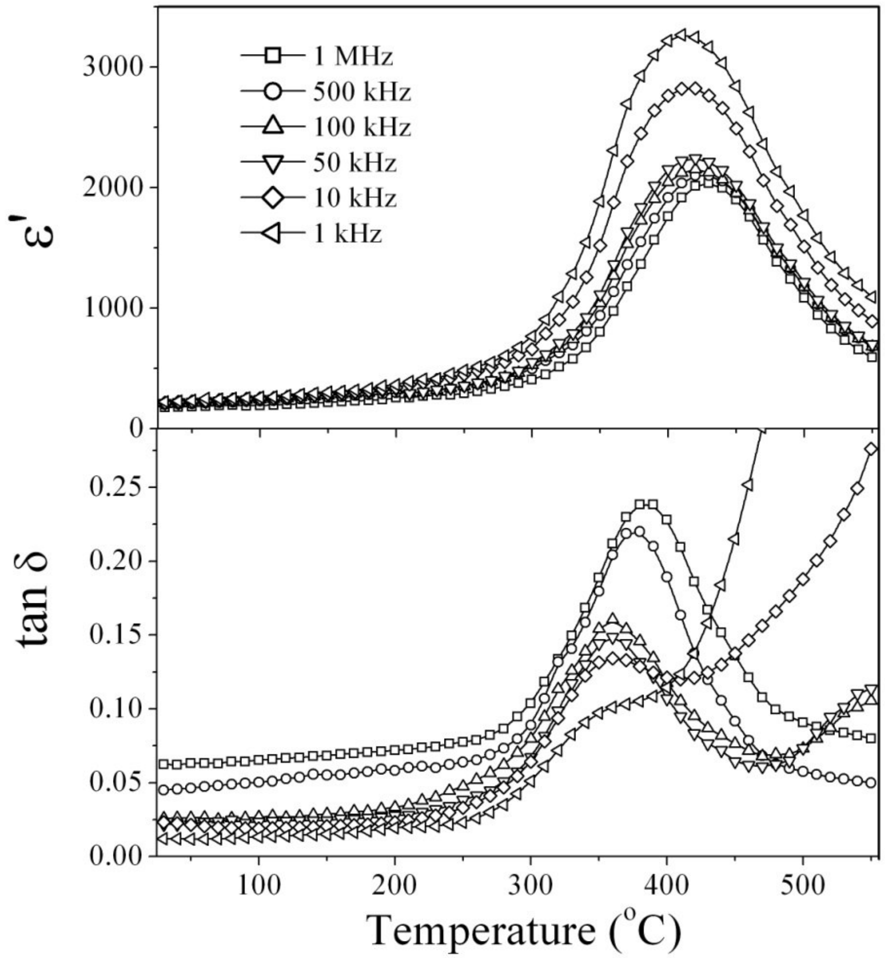

Fig.4.7. Temperature dependence of ε' and tan δ of $BaBi_4Ti_4O_{15}$ ceramic at various frequencies.

Table 4.2. Dielectric, ferroelectric, piezoelectric properties and activation energy (from impedance) of $BaBi_4Ti_4O_{15}$ ceramic.

Dielectric properties at 100 kHz	
Room temperature permittivity (ε_{rm})	211
Room temperature dielectric loss (tan δ)	0.026
Maximum permittivity (ε_m')	2150
Dielectric loss at peak (tan δ_m)	0.165
Maximum permittivity temperature (T_m)	400°C
Peak broadening parameter (δ)	139°C
Dielectric dispersion (γ)	1.88
Degree of relaxation (ΔT_m)	15°C
Vogel-Fulcher fitting parameters: E_{vf} (eV) = 0.0286	
T_f (°C) = 382	ν_o (Hz) = 1.03 x 10^9

Polarization hysteresis (electric field 38kV/cm)	
Remnant polarization ($2P_r$)	0.82 μC/cm^2
Coercive field ($2E_c$)	14.4 kV/cm
Piezoelectric coefficient d_{33}	11 pC/N
Impedance spectroscopy	
Activation energy E_a (relaxation time)	0.424 ± 0.01 eV
dc conductivity (σ_{dc}) at 550°C	9.77×10^{-7} Ω^{-1}cm^{-1}
Activation energy from Cole-Cole plot	
Below T_m = 0.45 eV	*Above* T_m = 0.073 eV

The degree of relaxation can be represented by [41]:

$$\Delta T_m = T\varepsilon_m'{}_{(1\ \mathrm{MHz})} - T\varepsilon_m'{}_{(1\ \mathrm{kHz})} \tag{4.11}$$

where, $T\varepsilon_m'{}_{(1\ \mathrm{MHz})}$ and $T\varepsilon_m'{}_{(1\ \mathrm{kHz})}$ is the maximum permittivity temperature at 1 MHz and 1 kHz respectively. ΔT_m was found to be 15°C for BBT which suggests BBT possess relaxor behaviour. Similar results concerning the relaxor behaviour of BBT are observed by *Hou et al.* [22].

Peak broadening may be quantified by the parameter δ, which is related with permittivity and temperature as follows [174]:

$$\frac{1}{\varepsilon'} - \frac{1}{\varepsilon_m'} = \frac{(T - T_m)^2}{2\varepsilon_m \delta^2} \tag{4.12}$$

δ parameter was calculated by fitting permittivity-temperature data at 100 kHz, as shown in Fig. 4.8. Value of δ for BBT was 139°C. Generally, the broadness arises because of the compositional fluctuations and structural disorderness present in the material when one or more cations occupy the same crystallographic sites. As already stated, the broadness arises in BBT because of the in-homogeneity in the material due to the mixed cation site occupancy of Ba^{2+} and Bi^{3+} in Bi_2O_3 layer.

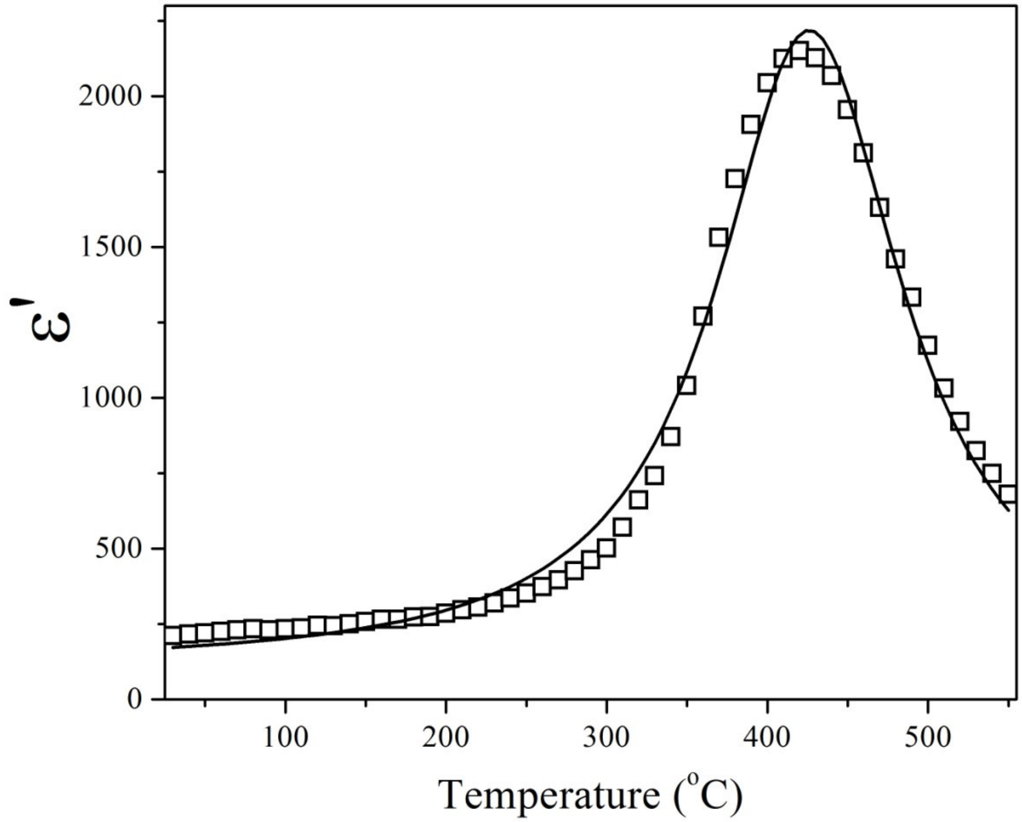

Fig.4.8. Dielectric constant versus temperature at 100 kHz for $BaBi_4Ti_4O_{15}$ ceramic. The symbols represent the experimental data and the solid line is the fitting to the law (Eq.4.12).

Generally, in a normal ferroelectric, dielectric constant follows the Curie-Weiss law above Curie temperature. The Curie-Weiss law is given by the following relation:

$$\varepsilon' = \frac{C}{T - T_\theta} \tag{4.13}$$

where C is the Curie-Weiss constant and T_θ is the Curie-Weiss temperature. Fig. 4.9 shows the dielectric constant data fitted with the Curie-Weiss law at a temperature higher than T_m at 100 kHz. From the figure, a deviation was observed from the Curie-Weiss law at a temperature T_d.

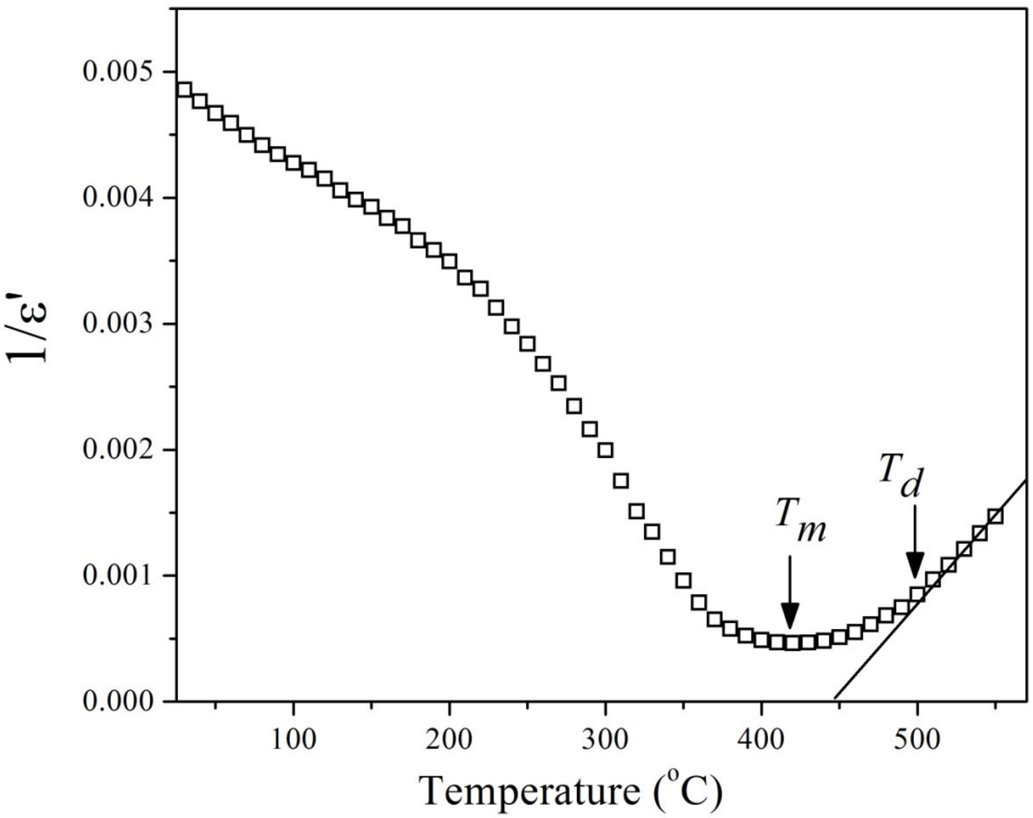

Fig.4.9. Inverse of dielectric constant versus temperature at a frequency of 100 kHz for $BaBi_4Ti_4O_{15}$ ceramic. The open symbols are the experimental data points and the solid line is the fit to Curie-Weiss law.

So, for relaxor ferroelectrics, a modified Curie-Weiss relationship has been proposed by Uchino and Nomura [175] to study the relaxor behaviour of a ferroelectric phase transition and is given by:

$$\frac{1}{\varepsilon'}-\frac{1}{\varepsilon'_m}=\frac{(T-T_m)^{\gamma}}{C_1} \quad \text{, for } (T > T_m) \tag{4.14}$$

where C_1 is the modified Curie-Weiss constant and γ indicates the degree of diffuseness of the relaxor. The value of γ lies in the range $1 \leq \gamma \leq 2$, *i.e.* in case of normal ferroelectric, γ=1 and for ideal relaxors, γ=2. Fig. 4.10 shows the plot of log ($1/\varepsilon'-1/\varepsilon_m'$) as a function of log ($T$-$T_m$) for 100 kHz data. The value of γ calculated from the slope of the curve was found to be 1.88, which revealed the near-relaxor nature of BBT ceramics.

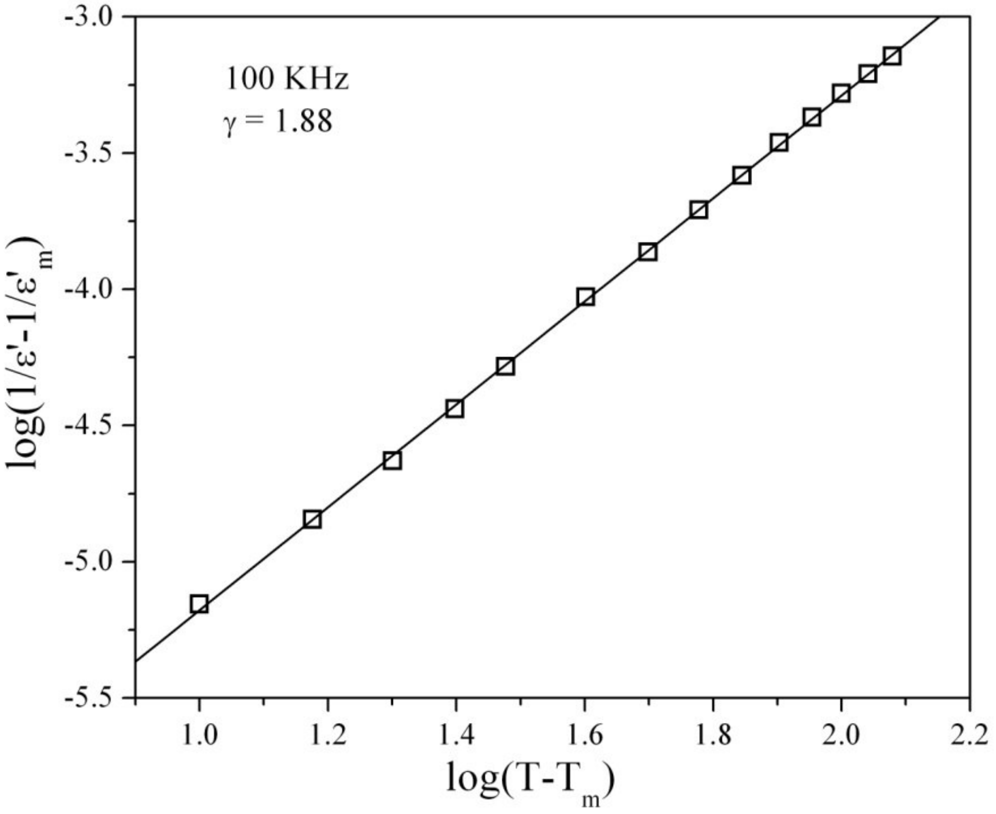

Fig.4.10. Plot of log (1/ ε' - 1/ ε_m') versus log (T - T_m) at 100 kHz frequency for $BaBi_4Ti_4O_{15}$ ceramic.

An empirical Vogel-Fülcher relationship was used to account for the dielectric relaxation nature in relaxor ferroelectrics. The variation of frequency of ac field with T_m is given [176] as:

$$\nu = \nu_o \, exp\left[\frac{-E_{vf}}{k_B\left(T_m - T_f\right)}\right] \tag{4.15}$$

where ν_0 is the Debye frequency, E_{vf} is the activation energy (i.e., the energy barrier between two equivalent polarization states), k_B is the Boltzmann's constant, T_f is the static freezing temperature (i.e., the temperature at which dynamic reorientation of the dipolar cluster polarization can no longer be thermally activated). Fig. 4.11 shows the plot of ln (ν) as a function of 1000/T_m where the symbols represent the experimental data points and the continuous line is a fit to Eq. 4.15. The analysis of the Vogel- Fülcher model yielded E_{vf} = 0.0286 ± 0.002 eV, ν_0 = 1.03×10^9 Hz, and T_f = 382°C.

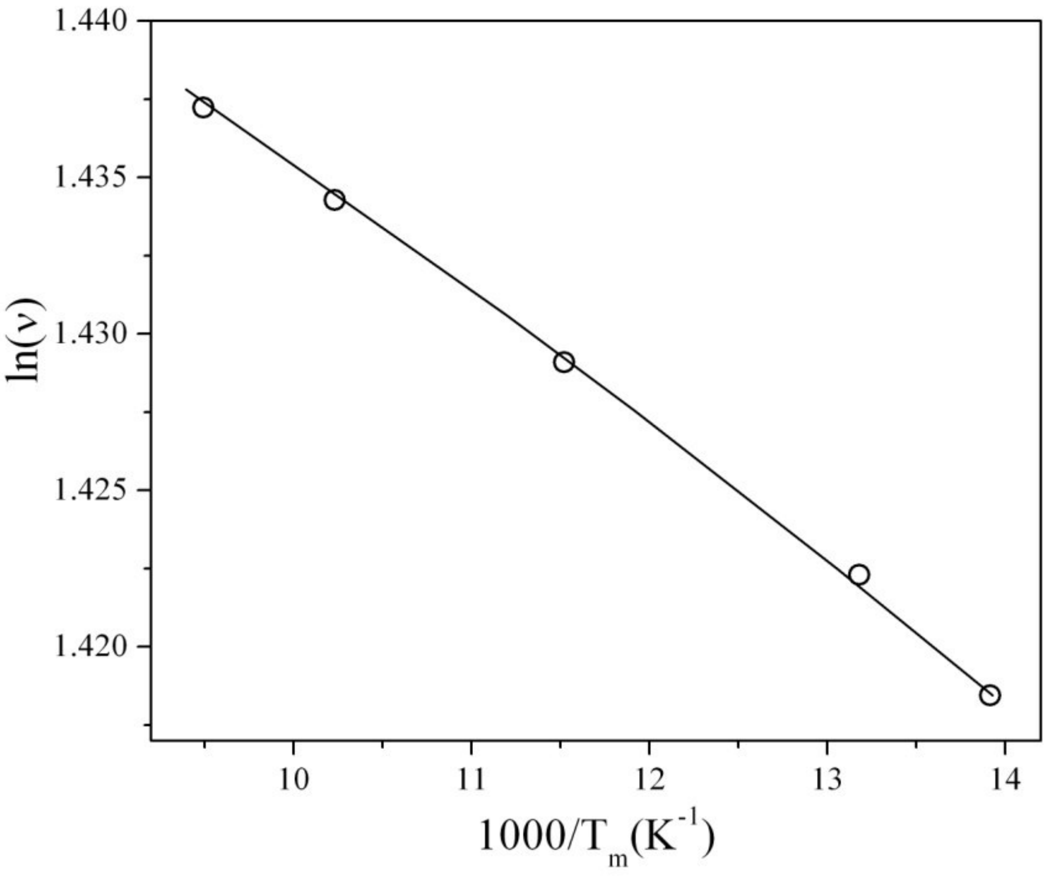

Fig.4.11. Frequency dependence of T_m for $BaBi_4Ti_4O_{15}$ ceramic. The symbols and solid line indicate experimental data points and fit to Vogel–Fülcher relationship, respectively.

BBT possesses orthorhombic structure below T_m and has stable spontaneous polarization due to the displacement of atoms along polar *a*-axis [28]. The shifting of T_m with measuring frequency suggests the existence of polar cluster in BBT. Single crystal X-Ray diffraction of BBT suggested cation distribution in the perovskite *A*-site and bismuth-site in the $(Bi_2O_2)^{2+}$ layer [17], *i.e.* *A*-site Ba^{2+} cation partially occupies the Bi^{3+} site in the Bi_2O_2 layer. This cation distribution is related to the existence of shearing-defects due to mismatch between the Bi_2O_2 layer and perovskite lattice. To compensate for this shearing Ba^{2+} occupies the Bi_2O_2 layer. The replacement of Ba^{2+} for Bi^{3+} in the Bi_2O_2 layer creates excess positive point charges leading to the formation of a random electric field. This random field results in formation of some polar clusters existing in the macrodomains of the material. But it is not strong enough, compared with the mean electric field, to destroy completely the long range electric ordering in the material [28]. That is why relaxor behaviour can be observed in BBT.

4.1.2.6 Polarization Hysteresis Characteristics

To study ferroelectricity of BBT ceramic, polarization versus electric field measurement on the ceramic was performed at room temperature. Fig. 4.12 shows the polarization versus electric field hysteresis loop for BBT. A remnant polarization (P_r) of 0.41μC/cm^2 with a coercive field (E_c) of 7.2kV/cm was shown by the ceramic under an applied electric field of 38kV/cm. Saturated *P-E* was not achieved at room temperature with the applied field stated. To saturate the polarization either higher field strength or measurement at elevated temperatures are usually applied. Unfortunately, there was no provision for high temperature measurement in the equipment and the maximum field achieved for the specimen after making it thin was ~38 to 40 kV/cm. P_r and E_c values obtained for these parameters were comparable to that reported in the literature for the polycrystalline BBT material [48].

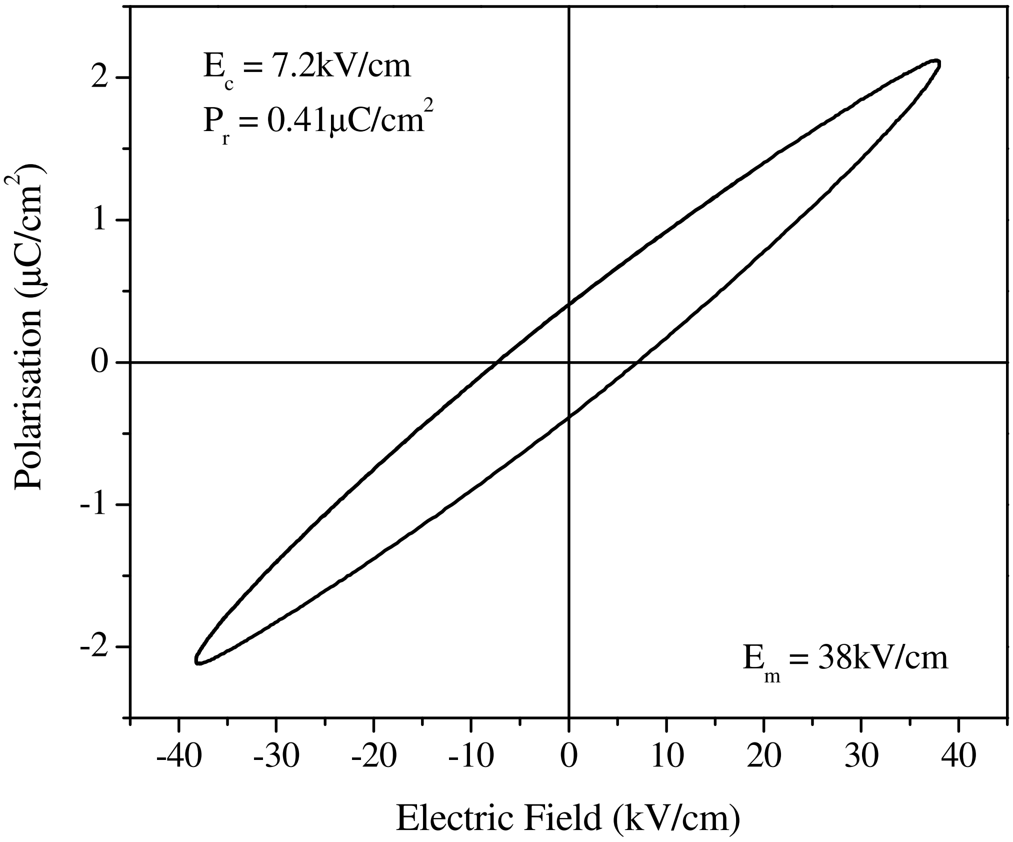

Fig.4.12. Polarization versus electric field (*P-E*) hysteresis loop recorded for $BaBi_4Ti_4O_{15}$ ceramic at room temperature.

4.1.2.7 Piezoelectric Properties

d_{33} coefficient of BBT was found to be 11 pC/N after poling the specimen under a dc field of 30 kV/cm at a temperature of 180^{o}C. *Subbarao* [14] reported a d_{33} coefficient of 12 pC/N that was poled under a dc field of 20-50 kV/cm at 200-250^{o}C. In comparison to the lead based materials like PZT, PMN etc., BLSF possesses low room temperature d_{33} coefficients. The low d_{33} coefficients are due to two-dimensional orientation restriction of its spontaneous polarization and high coercive field [18]. As reported by Subbarao, the five layer member of BLSF possesses the highest d_{33} coefficient among all members followed by the four layered members. Among the four layered members, $PbBi_4Ti_4O_{14}$ has the highest d_{33} of 23 pC/N while $CaBi_4Ti_4O_{14}$ do not possess any d_{33} and $SrBi_4Ti_4O_{14}$ exhibits the same d_{33} as that of BBT. The other members such as $Na_{0.5}Bi_{4.5}Ti_4O_{15}$ and $K_{0.5}Bi_{4.5}Ti_4O_{15}$ display a d_{33} ~10 pC/N. This has already been mentioned that piezoelectric coefficient of BLSFs can be enhanced by *A* and/or *B*-site substitutions in the structure. The following chapters represent the nature of change in piezoelectric coefficient of BBT by such a few substitutions.

4.1.2.8 Impedance Spectroscopy

Fig. 4.13 shows the variation of real part of impedance Z′ with frequency measured at various temperatures. The figure shows a decrease in the magnitude of Z′ with increase in frequency as well as temperature, indicating an increase in the *ac* conductivity of the system with increase in frequency and temperature. The Z′ plots appear to merge in the high frequency from 10 kHz. The reason for such behaviour may be the release of space charge due to reduction in the potential barrier of the material with rise in temperature [177]. This may be responsible for increase in the *ac* conductivity of the material. At low frequency, values of Z′ decreases with rise in temperature suggesting the negative temperature coefficient (NTCR) type of behaviour. Before the plots merge in the high frequency zone, a dip was observed. The height of the dip decreased with increase in temperature and this may be associated with charge carrier hopping.

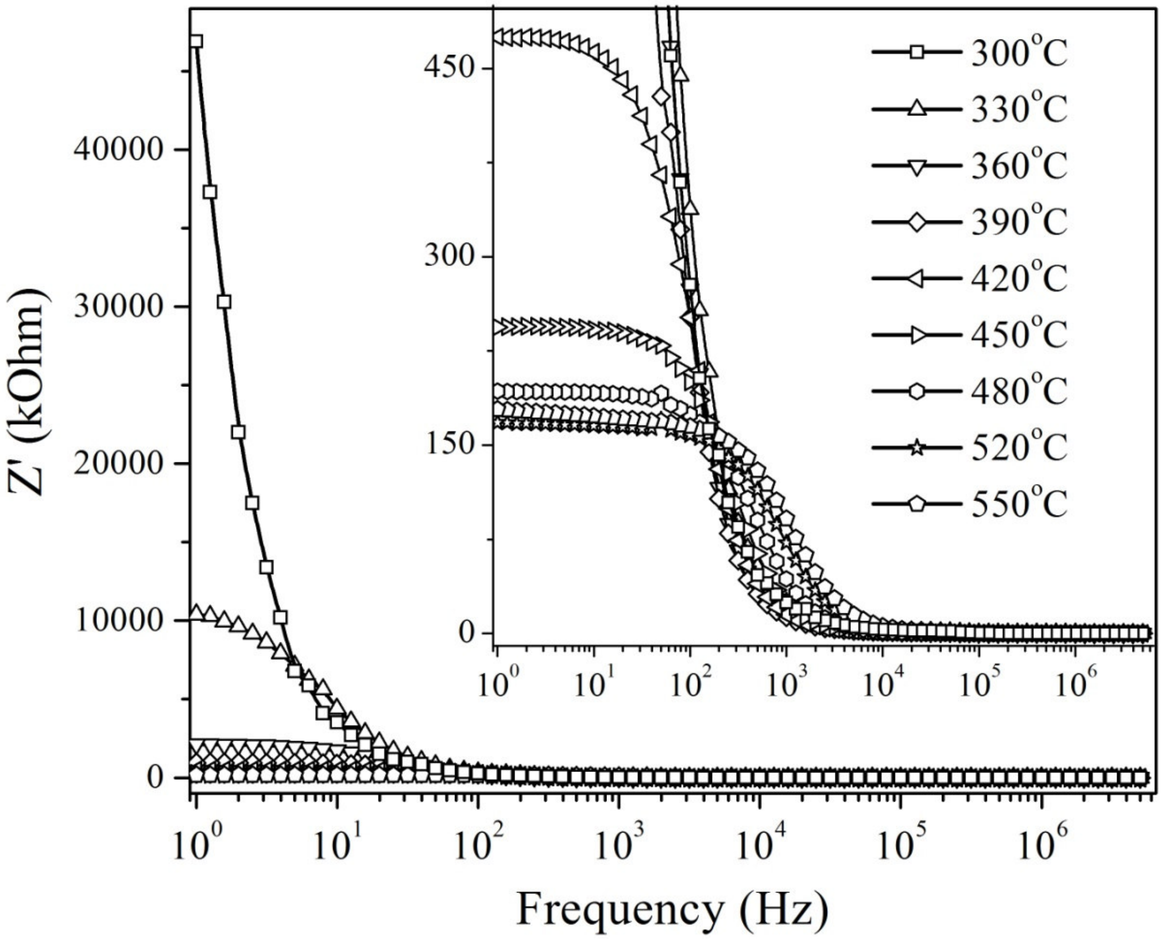

Fig.4.13. Variation of Z′ with frequency at various temperatures for $BaBi_4Ti_4O_{15}$.

Fig.4.14 shows the variation of imaginary part of impedance Z″ with frequency at various temperatures. The Z″ peaks appear above 300°C, at a characteristic frequency depending on the type and intensity of the electrical relaxation phenomena of the material. These Z″ peaks shifted to higher temperatures with increasing frequency implying an existence of distribution of relaxation time with temperature. Thus it may be said that the present system possesses temperature dependent relaxation process, indicating non-Debye behaviour. The peaks were asymmetric in nature suggesting the material to be consisting of electrical processes with a spread of relaxation time.

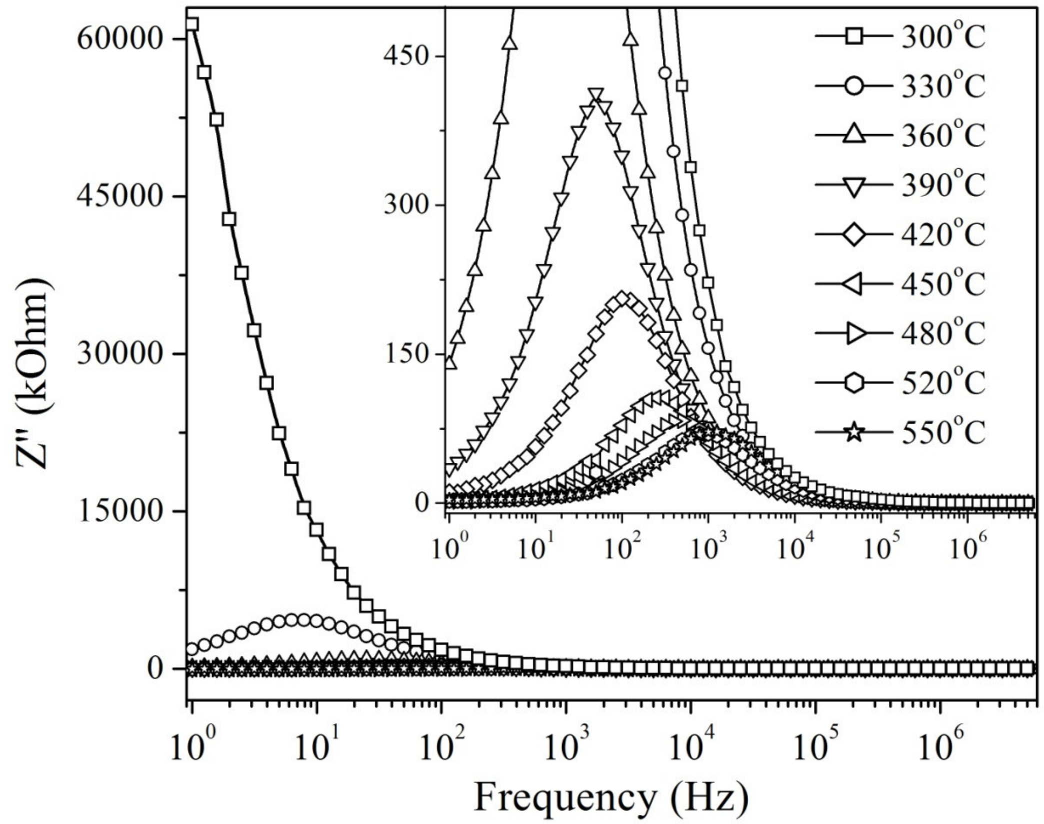

Fig.4.14. Variation of Z″ with frequency at various temperatures for $BaBi_4Ti_4O_{15}$.

The relaxation time is calculated using the relation:

$$\tau = \frac{1}{\omega} = \frac{1}{2\pi f_{\max}} \tag{4.16}$$

where τ is the relaxation time, ω is the angular frequency and $f_{\max}$ is the peak frequency or relaxation frequency. τ was calculated from the above equation using $f_{\max}$ from the Z″ versus log frequency plot (Fig.4.14). The value of τ decreased with the increase in temperature. The activation energy (E_a) related of the compound is calculated based on the relation:

$$\tau = \tau_o \exp\left(\frac{-E_a}{k_B T}\right) \tag{4.17}$$

Where, E_a is the energy associated with the relaxation process, τ_0 is the pre-exponential factor, T is the absolute temperature and k_B is the Boltzmann constant. Fig. 4.15 shows the plot of log τ versus 1000/T. From the slope of the linear fit to the experimental data points E_a was evaluated and was found to be 0.424 ± 0.004 eV for BBT.

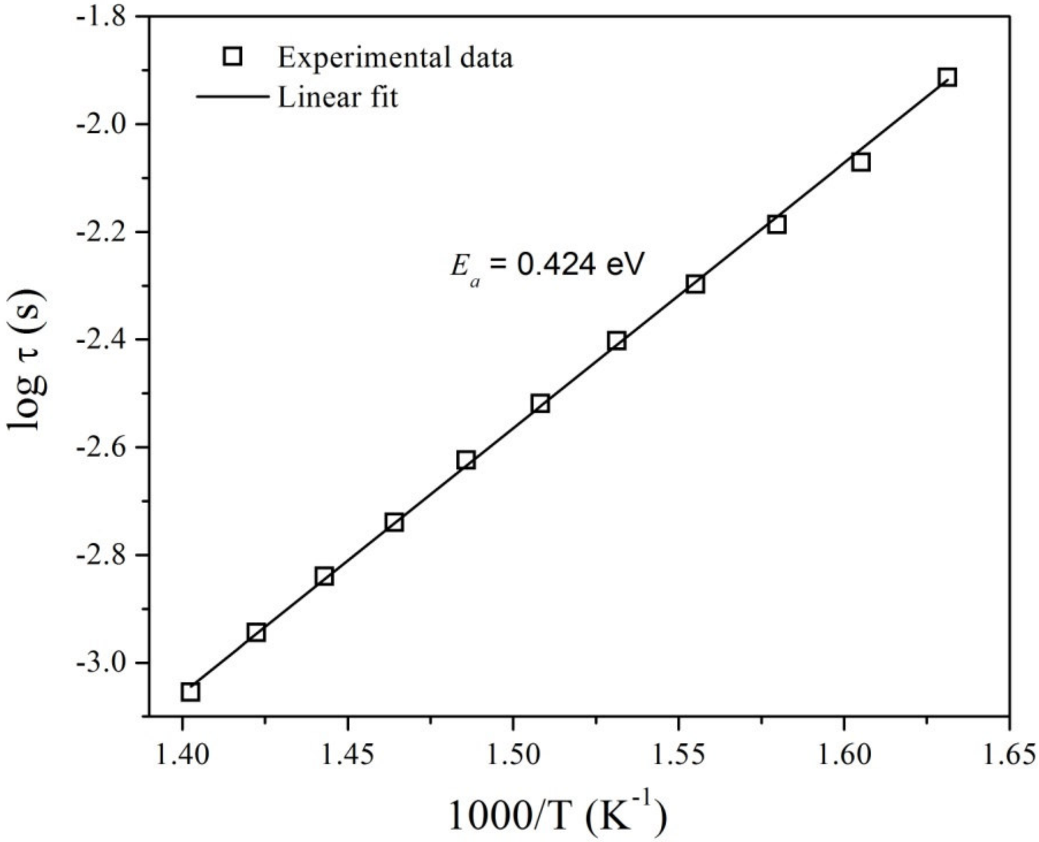

Fig.4.15. log τ versus 1000/T for $BaBi_4Ti_4O_{15}$.

Fig.4.16 shows the temperature dependence of complex impedance spectrum at different temperatures. A single semicircular was attributed to transport mechanism through the bulk of the material including grain and grain boundary of the system. It was observed that with increase in temperature the curve was suppressed and the intercept decreased with increase in temperature. The centre of the arc was found to lie below the Z′ axis, rather than on the axis indicating a distribution of relaxation time. The curve was fitted to the circuit consisting of parallel resistor (R) and capacitor (C) unit using ZView software. The inset of the figure shows the fitted curve to the experimental data at 550°C. ZView gives the value of R_{tot} and total capacitance C.

The capacitance values associated with R_{tot}, were found to increase with increase in temperature and attaining maximum capacitance in the temperature range 410-430°C. With further increase in temperature, the capacitance decreased. Further, these R_{tot} values were used to determine the *dc* conductivity of the sample, based on the following relation

$$\sigma_{dc} = \frac{t}{R_{tot} A} \tag{4.18}$$

where t is the thickness of the pellet and A is the overlapping electrode area. σ_{dc} at 350 and 550°C was found to be 4.89×10^{-8} and 9.77×10^{-7} $\Omega^{-1}\text{cm}^{-1}$, respectively. *Kumar et al.* reported the σ_{dc} of BBT at 350°C to be 1.18×10^{-5} $\Omega^{-1}\text{cm}^{-1}$ prepared by conventional solid state synthesis [106]. This depicted that sample prepared by the present modified chemical route possessed three orders of magnitude lower conductivity than the ceramics prepared through conventional solid state process.

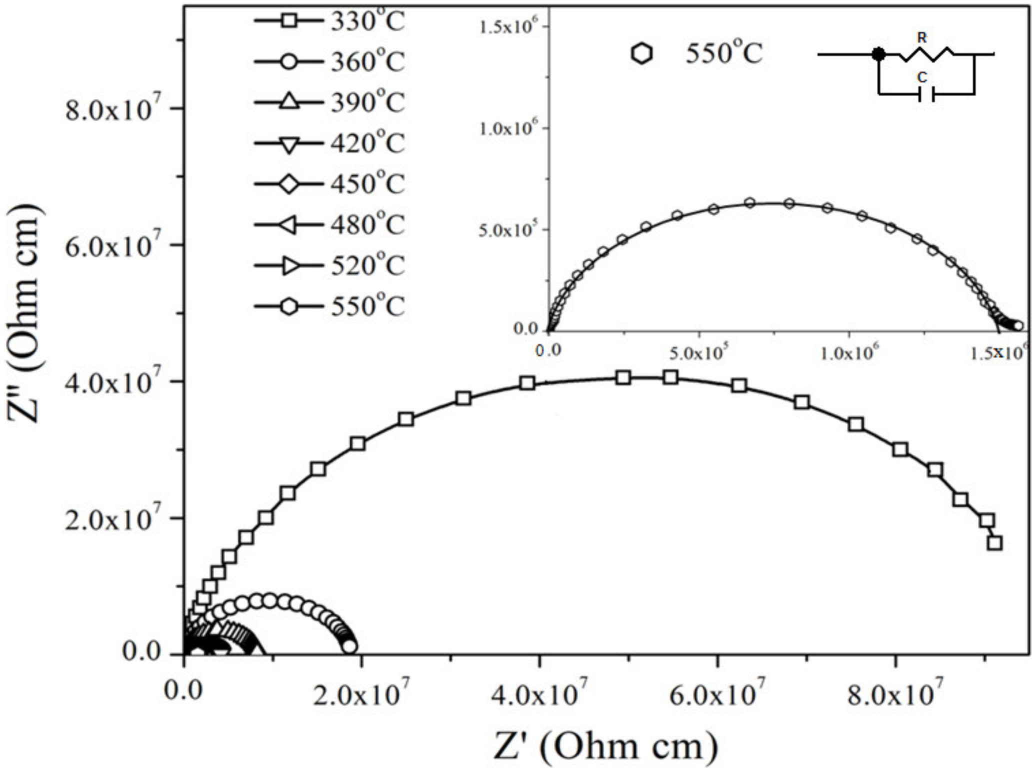

Fig.4.16. Complex plane impedance plot of $BaBi_4Ti_4O_{15}$ at different temperatures.

The activation energy (E_{dc}) for the *dc* conductivity can be calculated from the Arrhenius equation given by:

$$\sigma_{dc} = \sigma_o \, exp\left(\frac{-E_{dc}}{k_B T}\right) \tag{4.19}$$

E_{dc} is the activation energy for the formation and hopping of defects. E_{dc} can be calculated from slope of the plot of log σ_{dc} versus inverse of temperature as is shown in Fig. 4.17. Different slopes were observed in different temperature regimes indicating presence of different dominant conductivity mechanisms. It was observed that with increase in temperature E_{dc} decreased, indicating an increase in the conductivity of BBT. Similar values of E_{dc} were obtained by *Kumar et al.* above and below T_m [106]. In BLSF, conductivity at low temperatures is due to extrinsic defects and at high temperatures it is due to the thermally activated oxygen vacancies [20]. The ionization of these oxygen vacancies form conduction electrons, the formation of which can be described by Kroger-Vink notation [178]. Excess oxygen vacancies and electrons are formed through the reduction reaction:

$$\mathrm{O_O^X} \rightarrow \frac{1}{2}\mathrm{O_2}(\uparrow) + \mathrm{V_O^{\bullet\bullet}} + 2\mathrm{e}' \tag{4.20}$$

These oxygen vacancies act as trapping sites for charge carriers and the free electrons generated may bond with $\mathrm{Ti^{4+}}$ and convert them to $\mathrm{Ti^{3+}}$ by:

$$\mathrm{Ti^{4+}} + \mathrm{e}' \rightarrow \mathrm{Ti^{3+}} \tag{4.21}$$

Thus these two effects, i.e. generation of oxygen vacancies and the electrons, lead to a rise in the conductivity of BLSF by the hopping mechanism between the available sites.

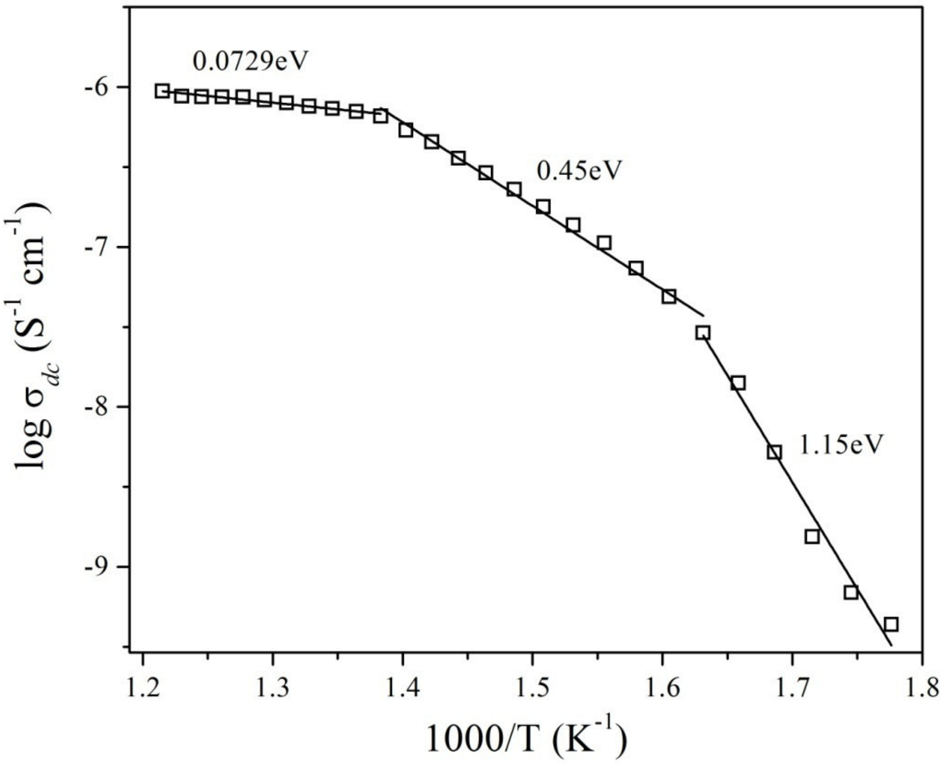

Fig.4.17. Arrhenius plot of log σ_{dc} versus inverse of temperature for $BaBi_4Ti_4O_{15}$.

4.1.3 Conclusions

$BaBi_4Ti_4O_{15}$ powder was synthesized by a modified chemical route. The precursor powder, a mixture of Bi-oxalate, Ba-oxalate and TiO_2, was calcined at 1000°C to produce a pure phase BBT. Better homogeneity of the precursor and exothermic decomposition of oxalates had facilitated the formation of BBT phase at 600°C onwards. The microstructure of sintered specimen showed the formation of randomly oriented plate like grains in the ceramics. The temperature dependence of dielectric constant at various frequencies explained the relaxor behaviour of the sample. The value of critical exponent γ (= 1.88) obtained from the modified Curie-Weiss law, confirmed the same. The frequency dependence of T_m was modeled using Vogel-Fülcher relation. All these observations clearly suggest that BBT is a relaxor ferroelectric. The P_r of BBT was ~0.41 μC/cm^2 under an applied field of 38 kV/cm and the d_{33} coefficient was ~11 pC/N. These values were in good agreement with the values reported earlier by other researchers. The variation of Z″ with frequency shows asymmetric nature of the peaks confirming BBT to possess non-Debye relaxation behaviour. The activation energy for the movement of defects was calculated using relaxation time and dc conductivity.

4.2 La^{3+} substitution for Bi^{3+} in $BaBi_4Ti_4O_{15}$

4.2.1 Introduction

Substitution of La^{3+} for Bi^{3+} in many BLSF has been found to play multifaceted effects. It plays an effective role in improving properties of many BLSFs [69, 106, 179, 181], especially of $Bi_4Ti_3O_{12}$ [182, 183]. The substitution resulted in a transition from ferroelectric to relaxor behaviour in $SrBi_4Ti_4O_{15}$ and $Bi_4Ti_3O_{12}$ [22, 181, 183]. The substitution was also helpful in increasing remnant polarization and decreasing coercive field of many BLSFs [22, 62, 184, 185]. Concentration of Bi ion vacancies and associated oxygen vacancies were reported to decrease by La^{3+} substitution. That is the La^{3+} doping increases the stability of the BO_6 octahedra of the system [71]. This chapter describes the effect of this substitution on the properties of $BaBi_4Ti_4O_{15}$.

La^{3+} substituted BBT compositions; $BaBi_{4-x}La_xTi_4O_{15}$ (x = 0.1, 0.2, 0.3, 0.5, 1.0) were synthesized through modified chemical route. The precursor powder was calcined in the temperature range 900-950°C and pure phase materials were sintered in the range 1100-1145°C; depending on the composition. The effect of La^{3+} substitution on the change in microstructure, dielectric relaxor behaviour, ferroelectric hysteresis, piezoelectric properties and impedance spectroscopy of the ceramics were investigated. Rietveld analysis of the structure was also performed to examine the site selectivity of La^{3+} in the structure.

4.2.2 Results and Discussion

4.2.2.1 Structural Analysis

Fig.4.18 shows X-ray diffraction patterns of $BaBi_{(4-x)}La_xTi_4O_{15}$ ceramics. Diffraction patterns of all compositions matched with standard $BaBi_4Ti_4O_{15}$ phase (JCPDS Card No. 35-0757). No other secondary phase was detected in the compositions. Thus La^{3+} shows complete solid solution formation in BBT for the compositions $x \leq 1.0$. The strongest diffraction peak (1 1 9) was consistent with the (1 1 2m+1) highest diffraction peak for BLSF phase [186]. Inset of figure (4.18) shows (1 1 9) peak. The peak shifted to higher 2θ for the compositions $0.1 \leq x \leq$

0.5, indicating a decrease in the *d*-spacing, while for x = 1.0 composition, the peak shifted slightly to lower 2θ, with an increase in *d*-spacing.

Lattice parameters were evaluated through Rietveld analysis using MAUD [158] program considering orthorhombic $A2_1am$ space group. Fig. 4.19 shows the Rietveld output plot for all the compositions. A good fit was obtained for all the compositions. Table 4.3 summarizes the refined lattice parameters (a, b and c), volume, R-factors and sigma. Fig. 4.20 shows the change in lattice parameter with lanthanum substitution (x). All the three lattice parameters decreased nominally up to x = 0.5. This may be due to the occupancy of La^{3+} in pseudo-perovskite layer and associated changes in $Ti\text{-}O_6$ octahedral tilting in the unit cell [187, 188]. A slight increase in the lattice parameters near x = 1.0, may be due to the occupancy of La^{3+} in Bi_2O_2 layer over and above perovskite layer occupancy. It was found through Raman studies [179] that La^{3+} began to occupy the Bi-site in Bi_2O_2 layers of $Bi_{3-x}La_xTiNbO_9$ when $x > 0.50$. The figure also shows the change of orthorhombic structure to pseudo-tetragonal around x = 0.5. The orthorhombicity of the structure was evaluated using Eq. 4.10 and is listed in Table 4.3. Orthorhombicity of the structures decreased with increase in substitution and was pseudo-tetragonal for $x \geq 0.5$.

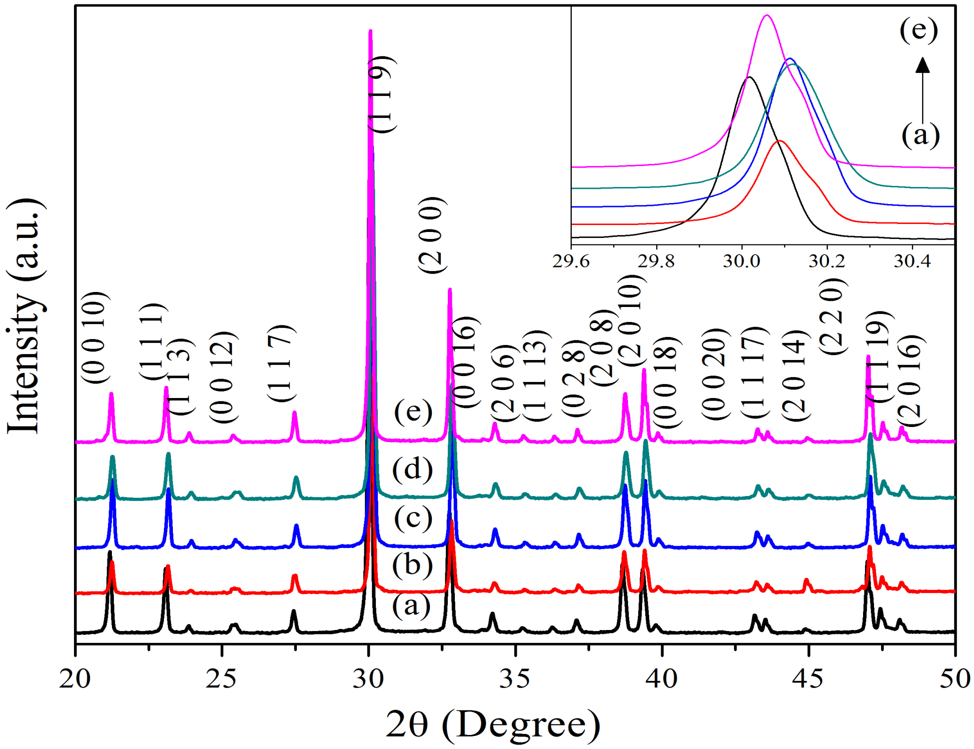

Fig.4.18. XRD patterns of $BaBi_{(4-x)}La_xTi_4O_{15}$ ceramics (a) x=0.1, (b) 0.2, (c) 0.3, (d) 0.5, (e) 1.0.

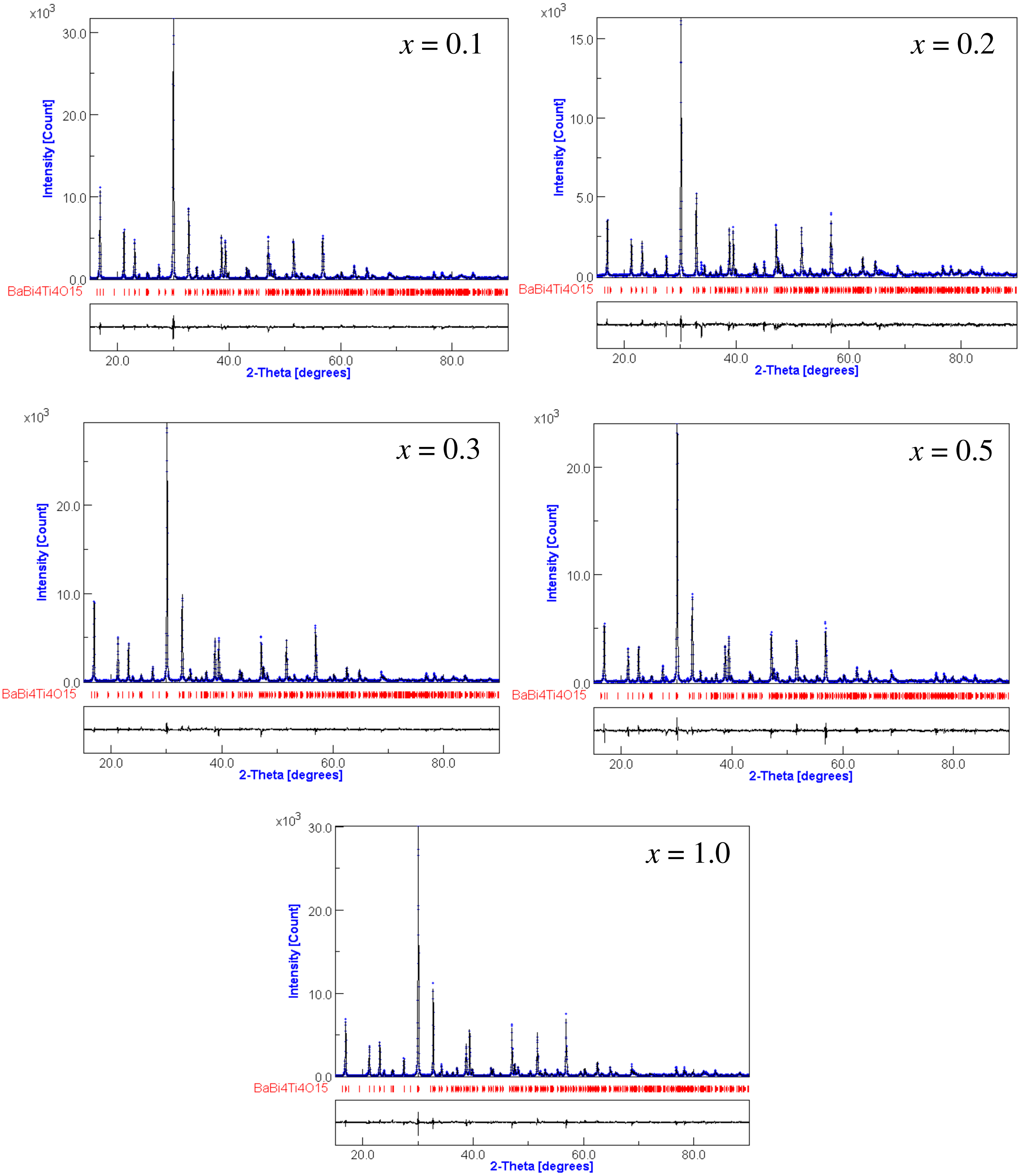

Fig.4.19. Final Rietveld plots for $BaBi_{4-x}La_xTi_4O_{15}$ (x = 0.1, 0.2, 0.3, 0.5, 1.0) ceramics.

It was also observed that the degree of *a*-axis orientation (α) increased with increasing La^{3+} content. α can be represented [64]:

$$\alpha = I(2\ 0\ 0) / [I(2\ 0\ 0) + I(1\ 1\ 9)] \tag{4.22}$$

where I(1 1 9) and I(2 0 0) denote the XRD intensities of (1 1 9) and (2 0 0) reflections. The α values are 0.21, 0.24, 0.25, 0.26, and 0.27 respectively for compositions serially from x = 0.1 to 1.0. This increasing trend of α could be explained by the fact that the crystal structure changes from orthorhombic to tetragonal.

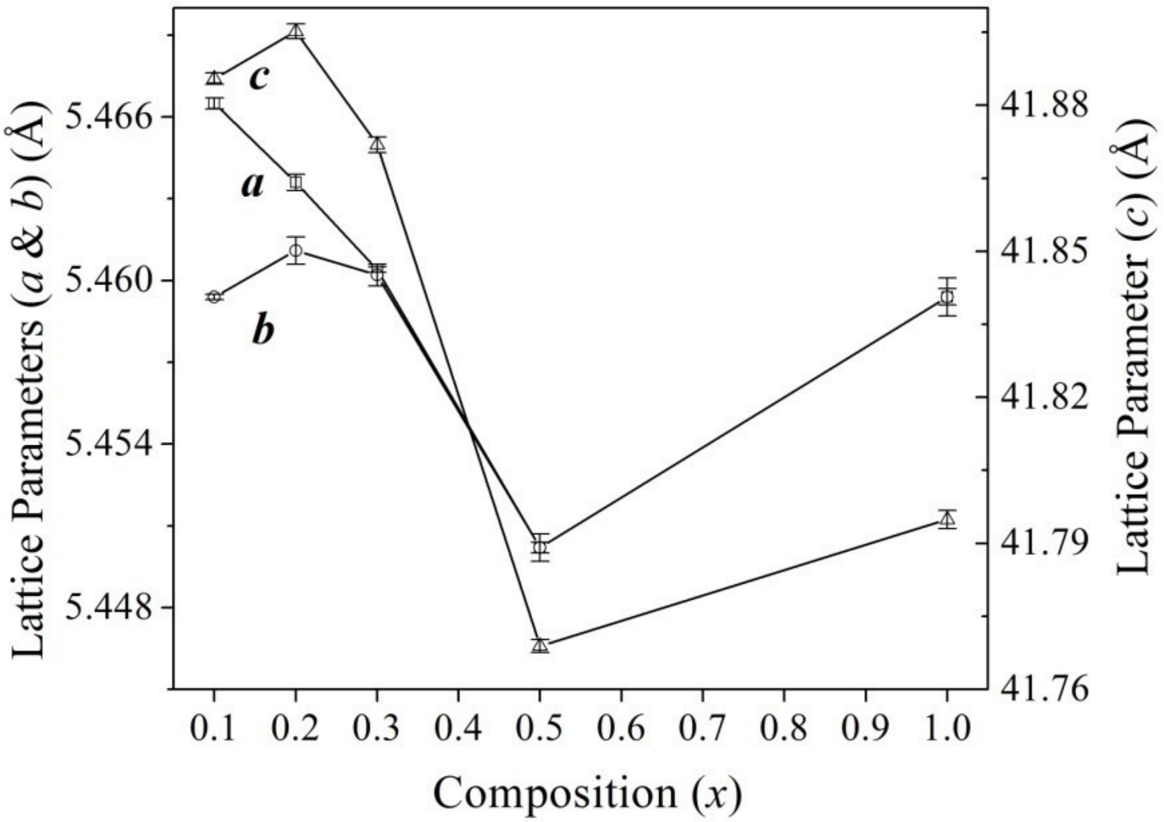

Fig.4.20. Lattice parameters of $BaBi_{4-x}La_xTi_4O_{15}$ ceramics as a function of La^{3+} concentration (x).

Table 4.3. Refined lattice parameters (*a*, *b* and *c*), Volume of unit cell, *R*-factors, Sigma, Orthorhombicity and Grain Size of $BaBi_{4-x}La_xTi_4O_{15}$ ($x = 0.1, 0.2, 0.3, 0.5, 1.0$) ceramics.

Formula	$x = 0.1$	$x = 0.2$	$x = 0.3$	$x = 0.5$	$x = 1.0$
a (Å)	5.4665(2)	5.4636(3)	5.4604(1)	5.4502(5)	5.4594(7)
b (Å)	5.4594(1)	5.4611(5)	5.4602(4)	5.4502(2)	5.4594(3)
c (Å)	41.8855(12)	41.8952(15)	41.8719(16)	41.7689(13)	41.7949(19)
Volume $(Å)^3$	1250.02	1250.03	1248.40	1240.73	1245.69
R_w (%)	5.15	6.57	5.08	6.91	5.44
R_b (%)	4.02	4.67	3.85	5.17	4.17
Sigma	1.72	1.92	1.67	2.22	1.72
Orthorhombicity	0.0013	4.57E-4	3.66E-5	0	0

4.2.2.2 Densification and Microstructural Characteristics

Table 4.4 shows % theoretical density as a function of sintering temperature and time for all La^{3+} substituted BBT ceramics. $BaBi_{(4-x)}La_xTi_4O_{15}$ ceramics required higher sintering temperature with the increase in La^{3+} substitution from 1100°C for $x = 0.1$ composition to 1145°C for $x = 1.0$. It indicated that with increase in La^{3+} substitution, the ceramics required higher temperature or time to achieve more than 90% theoretical density. The increase in sintering temperature with increase in La^{3+} may be due to the difficulty in diffusion of bigger size La^{3+} compared to Bi^{3+} for which La^{3+} was substituted.

Fig.4.21 shows the SEM micrograph of all the substituted ceramics. Ceramics were composed of randomly oriented plate-like grains. With increase in substitution, the plate-like grains showed a transformation towards circular shaped grains with rounded edges. The grain size decreased with increase in La^{3+} substitution (Table 4.3). This indicated that La^{3+} ions act as grain growth inhibitor. Grain growth occurs through diffusion of material. So the grain growth was suppressed due to difficulty in diffusion of bigger La^{3+} cation.

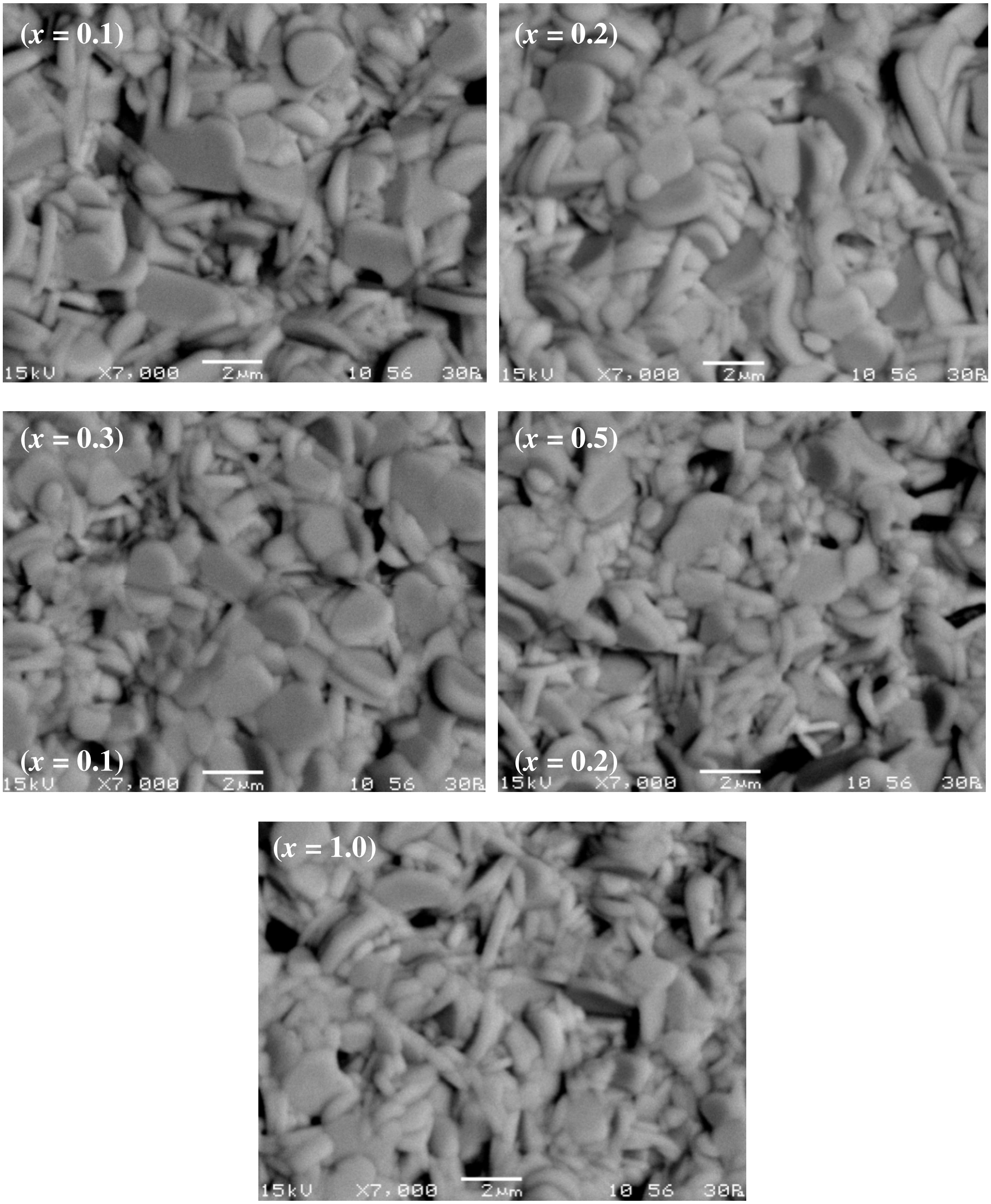

Fig.4.21. Micrograph of $BaBi_{(4-x)}La_xTi_4O_{15}$ ($x = 0.1, 0.2, 0.3, 0.5, 1.0$) ceramics.

Table 4.4. %Theoretical density with Sintering temperature/time and Grain Size of $BaBi_{4-x}La_xTi_4O_{15}$ (x = 0.1, 0.2, 0.3, 0.5, 1.0) ceramics.

Formula	**x = 0.1**	**x = 0.2**	**x = 0.3**	**x = 0.5**	**x = 1.0**
Sintering temperature and time	**% Theoritical density**				
1100^{o}C/4h	95	89	-	-	-
1100^{o}C/6h	-	94	89	-	-
1110^{o}C/4h	-	-	92	83	-
1120^{o}C/4h	-	-	-	92	81
1130^{o}C/4h	-	-	-	-	86
1145^{o}C/4h	-	-	-	-	93
Grain Size					
Length (μm)	1.44	1.38	1.24	1.16	1.12
Breadth (μm)	0.83	0.68	0.66	0.66	0.63
Thickness (μm)	0.28	0.24	0.23	0.23	0.22

4.2.2.3 Dielectric and Diffuse Phase Transition Behaviour

Fig.4.22 displays the temperature dependence of ε' and tan δ of $BaBi_{(4-x)}La_xTi_4O_{15}$ ceramics at a frequency of 100 kHz. ε_m', T_m and ε_{rm} are shown in Table 4.5. It was noted that ε_{rm} increased with increasing substitution, which was due to the shifting of ε_m' peak towards room temperature. However, ε_m' decreased with increasing substitution. This may be due to the decreased lattice parameter '*a*' and associated relaxation in structural distortion. Smaller the lattice parameter, lower will be polarization as ferroelectricity in BLSFs arises by the *A*-type cation displacement along *a*-axis direction [180, 189].

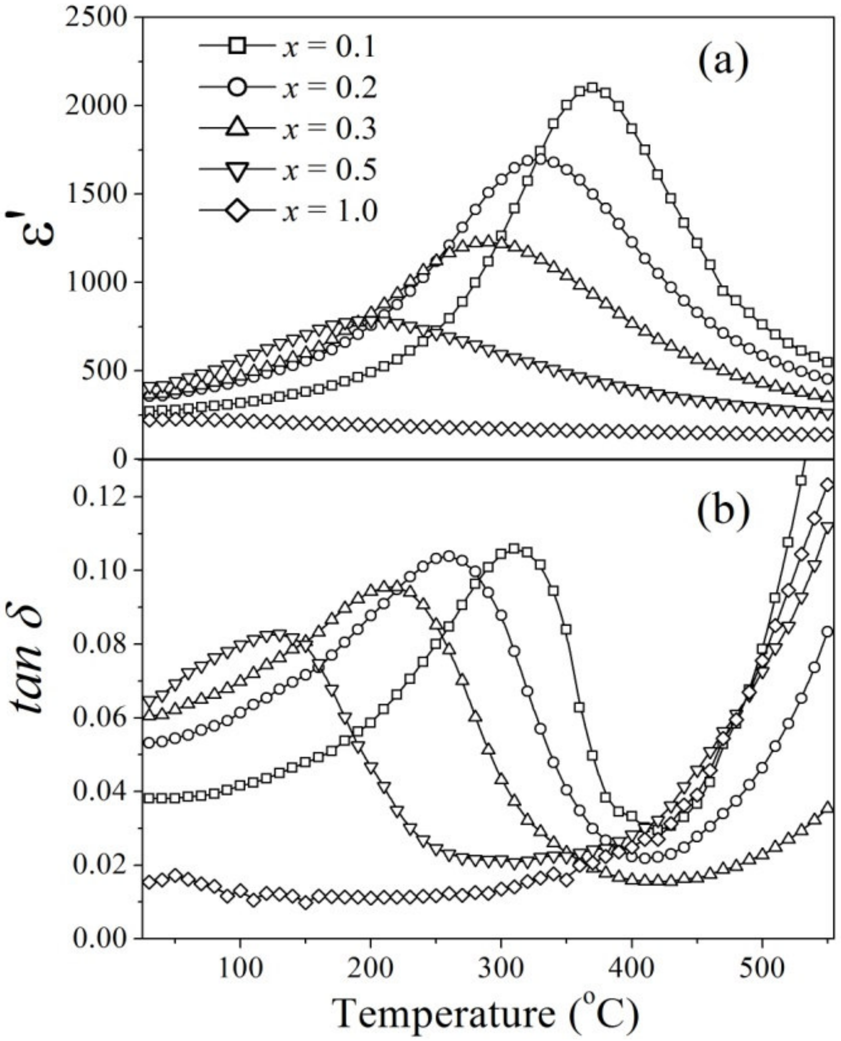

Fig.4.22. Temperature dependence of ε' and tan δ of $BaBi_{(4-x)}La_xTi_4O_{15}$ (x = 0.1, 0.2, 0.3, 0.5, 1.0) ceramics at a frequency of 100 kHz.

Dielectric dispersion was more pronounced in tan δ versus temperature plot shown in Fig. 4.22(b). The loss decreased with increasing substitution. In general, oxygen vacancies are responsible for the dielectric losses in BLSFs, which are formed as a result of Bi^{3+} volatilization [190]. In the present system, La^{3+} was substituted for volatile Bi^{3+}. So the substitution suppressed the formation of *A*-site vacancies as well as oxygen vacancies. Also the La-O bonds are much stronger than the Bi-O bonds. So the perovskite unit is much more stabilized. This eventually leads to a decreased dielectric loss with substitution.

T_m was observed to shift to lower temperature with La^{3+} substitution. This was due to the increase in size of A-site cation [14]. Further, the decrease of T_m can be explained on the basis of tolerance factor t given by:

$$t = \frac{R_A + R_B}{\sqrt{2(R_B + R_O)}} \tag{4.23}$$

where R_A, R_B and R_O are the effective ionic radii for A-site, B-site and oxygen ion, respectively. The tolerance factor of BBT was 0.9886. Table 4.5 summarizes the tolerance factor for the La^{3+} substituted BBT ceramics. As the tolerance factor t increases, the structural distortion and hence the Curie temperature decreased [191]. The ionic radius of La^{3+} is larger than that of Bi^{3+} [192]. So, the substitution increased the tolerance factor and T_m decreased.

All compositions exhibited a broad permittivity maximum with temperature. The broadness increased with increasing substitution. Peak broadening may be quantified by the parameter δ, which is related with permittivity and temperature (Fig. 4.22(a)) as described in Eq. 4.12. δ parameters of different compositions were calculated by fitting permittivity-temperature data to Eq. 4.12 and its values are listed in Table 4.5. The broadening increased significantly with La^{3+} substitution. It is well accepted that the broadness in relaxor originates from the compositional fluctuation and disorder in crystallographic sites when one or more cations occupy the same site in the structure [17]. La^{3+} exaggerates the compositional fluctuation in BBT. This results in the formation of small clusters possessing different Curie temperature. As a result broadness increases due to the presence of local Curie points.

Fig. 4.23 shows the temperature dependence of permittivity for x = 0.1 to 0.5 at different frequencies. A significant frequency dispersion of permittivity was observed with increasing substitution. This indicated that La^{3+} substitution enhanced the relaxor behaviour in BBT.

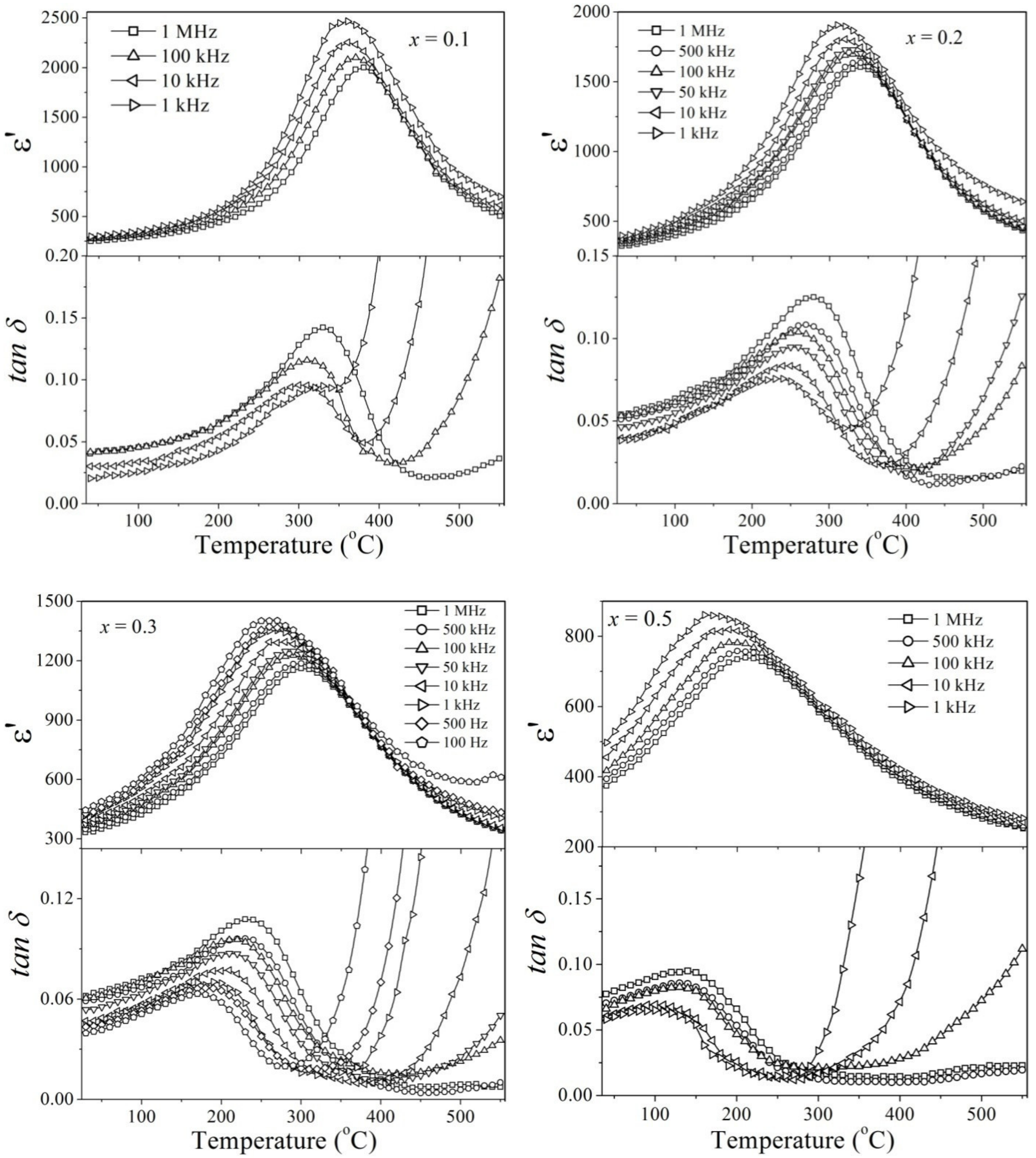

Fig.4.23. Temperature and frequency dependence of ε' and *tan* δ of $BaBi_{4-x}La_xTi_4O_{15}$ (x = 0.1, 0.2, 0.3, 0.5) ceramics.

The diffusivity (γ) parameter was applied to characterize the relaxor behaviour and it was expressed by a modified Curie-Weiss law [175], described by Eq.4.14. Fig.4.24 shows the plot of log $(1/\varepsilon' - 1/\varepsilon_m')$ versus log $(T - T_m)$ at a frequency of 100 kHz. γ

values for different compositions were calculated from the plot. It was evident that γ increased with increase in La^{3+}. That is the degree of diffuseness or relaxor behaviour increased with La^{3+} substitution.

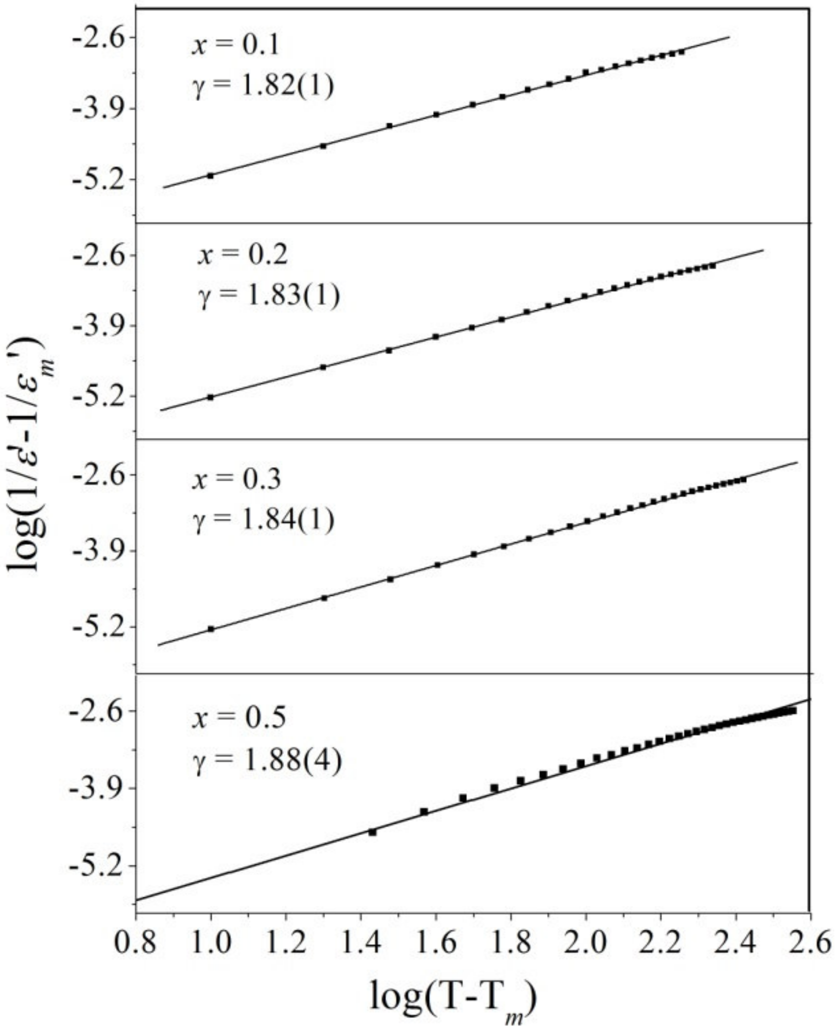

Fig.4.24. Plot of log ($1/\varepsilon' - 1/\varepsilon_m'$) versus log ($T - T_m$) for different $BaBi_{(4-x)}La_xTi_4O_{15}$ ($x = 0.1$, 0.2, 0.3, 0.5) ceramics at frequency of 100 kHz.

The frequency dispersion ΔT_m in relaxors are listed in Table 4.5 for different compositions, described by Eq. 4.11. ΔT_m increased from 20°C (for $x = 0.1$) to 50°C (for $x = 0.5$). These results indicated that the substitution of La^{3+} enhanced the frequency dispersion or relaxor behaviour in these ceramics.

In relaxor ferroelectrics, dielectric relaxation is expressed by Vogel-Fulcher relationship described by Eq. 4.15. Fig.4.25 shows the plot of $1000/T_m$ versus log ν for $x = 0.1$ to 0.5 compositions. Open symbols represent the experimental data points and the line gives the fit to Eq. 4.15. T_m shows a good fit to Vogel-Fulcher law and confirmed them to possess relaxor characteristics. The values for fitting parameters ν_0, E_{vf} and T_{f} are listed in Table 4.5. E_{a} increased with increase in La^{3+} concentration confirming the strengthening in the relaxation behaviour [106]. As stated above, E_{vf} represents the energy barrier between two equivalent polarization states under ac field. As energy increases, polarization becomes more dependent on frequency, which is one of the major characteristics of relaxor. The static freezing temperature was also found to decrease with increasing La^{3+} substitution.

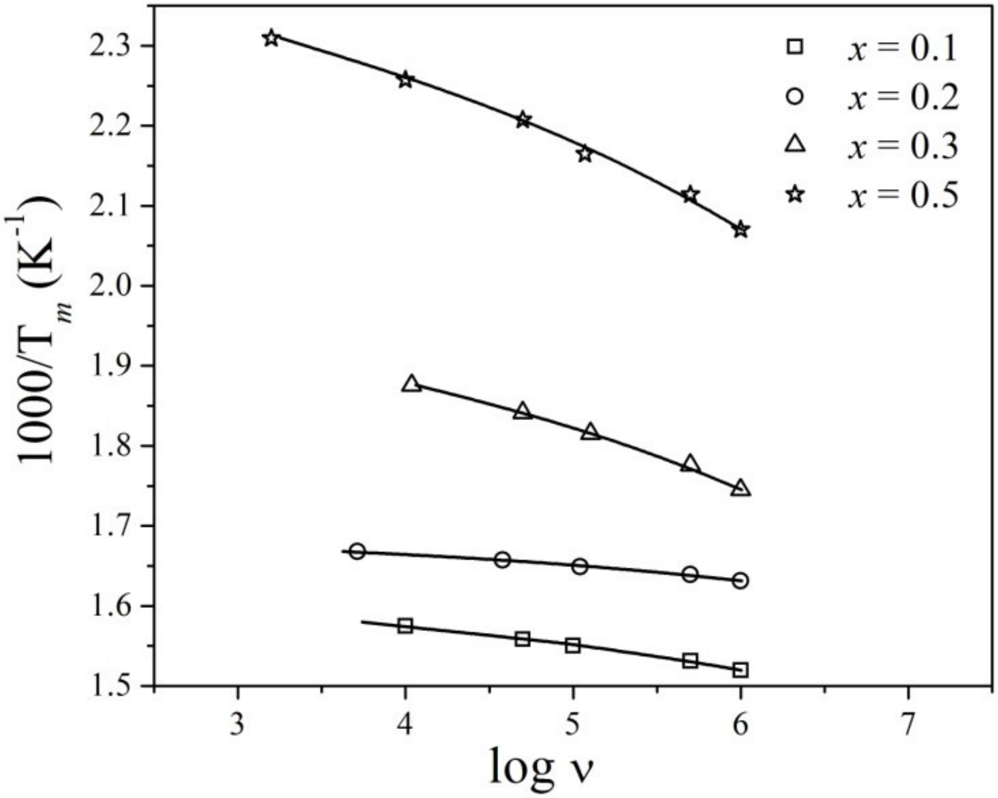

Fig.4.25. Frequency dependence of T_m for different $BaBi_{(4-x)}La_xTi_4O_{15}$ (x = 0.1, 0.2, 0.3, 0.5) ceramics. The symbols and solid line indicate data points and fit to Vogel–Fulcher relationship, respectively.

The introduction of La^{3+} ions in the system exaggerated the already existing cation disorder between the Ba^{2+} and Bi^{3+} sites, leading to an increase in the relaxor behaviour. The driving force behind this cation disorder can be explained on the basis of tolerance factor argument. That is the size mismatch between the Bi_2O_2 layer and perovskite-like layer competes with the preference of Ba^{2+} for occupying the Bi_2O_2 layer [144]. From Table 4.5, it is visible that the tolerance factor increased with increase in La^{3+} concentration. The increase in tolerance factor implies the increase in mismatch among the two layers, thus implying an increase in driving force for cation disorder. Thus with an increase in cation disorder the relaxor behaviour was observed to increase. Also, La^{3+} weakens the coupling of electric dipoles in a system by disrupting the translational symmetry in the material [22]. As a result the ferroelectricity of the material decreased due to the decrease in coupling and concentration of dipoles. So the Curie temperature was lowered and short range polar clusters appeared along with long range ordering, leading to increased relaxor behaviour. Such results were also observed by La^{3+} substitution in other members of BLSF [22, 181, 183].

Table 4.5. Room temperature relative permittivity (ε_{rm}), maximum relative permittivity (ε_m'), maximum permittivity temperature (T_m), degree of diffuseness (δ) at 100 kHz and degree of frequency dispersion (ΔT_m), tolerance factor (t), fitting parameters from Vogel Fulcher relation (E_{vf}, T_f and ν_0) for different $BaBi_{(4-x)}La_xTi_4O_{15}$ (x = 0.1, 0.2, 0.3, 0.5) ceramics.

Formula	***x* = 0.1**	***x* = 0.2**	***x* = 0.3**	***x* = 0.5**	***x* = 1.0**
ε_{rm}	270	356	366	411	221
ε_m'	2102	1697	1227	780	--
T_m (°C)	370	330	290	200	--
ΔT_m (°C)	20	30	40	50	--
δ (°C)	158 (1)	196 (1)	232 (2)	280 (3)	--
t	0.9894	0.9901	0.9908	0.9922	0.9957
E_{vf} (eV)	0.067 (1)	0.066(3)	0.098(2)	1.002 (3)	--
T_f (°C)	310	307	177	100	--
ν_0 ($\times 10^{10}$ Hz)	3.34	9.91	1.08	1.18	--

4.2.2.4 Polarization Hysteresis Characteristics

Fig. 4.26 shows the ferroelectric hysteresis loop of $BaBi_{(4-x)}La_xTi_4O_{15}$ ceramics obtained under a maximum applied electric field of 30 kV/cm. Though the loops were far from saturation due to the limitation of the experimental setup, the data can still be used for comparison purpose as they are taken at the same electric field for different compositions. This can provide an overview on the variation of remnant polarization and coercive field with La^{3+} substitution. *P-E* loop for all the compositions were recorded at room temperature and at a frequency of 100 Hz. The values of remnant polarization ($2P_r$) and coercive field ($2E_c$) are listed in Table 4.6. With increase in La^{3+} substitution, $2P_r$ increased up to $x = 0.3$. Composition with $x = 0.3$ also showed highest $2P_r$ among all and a lower $2E_c$ than BBT [48].

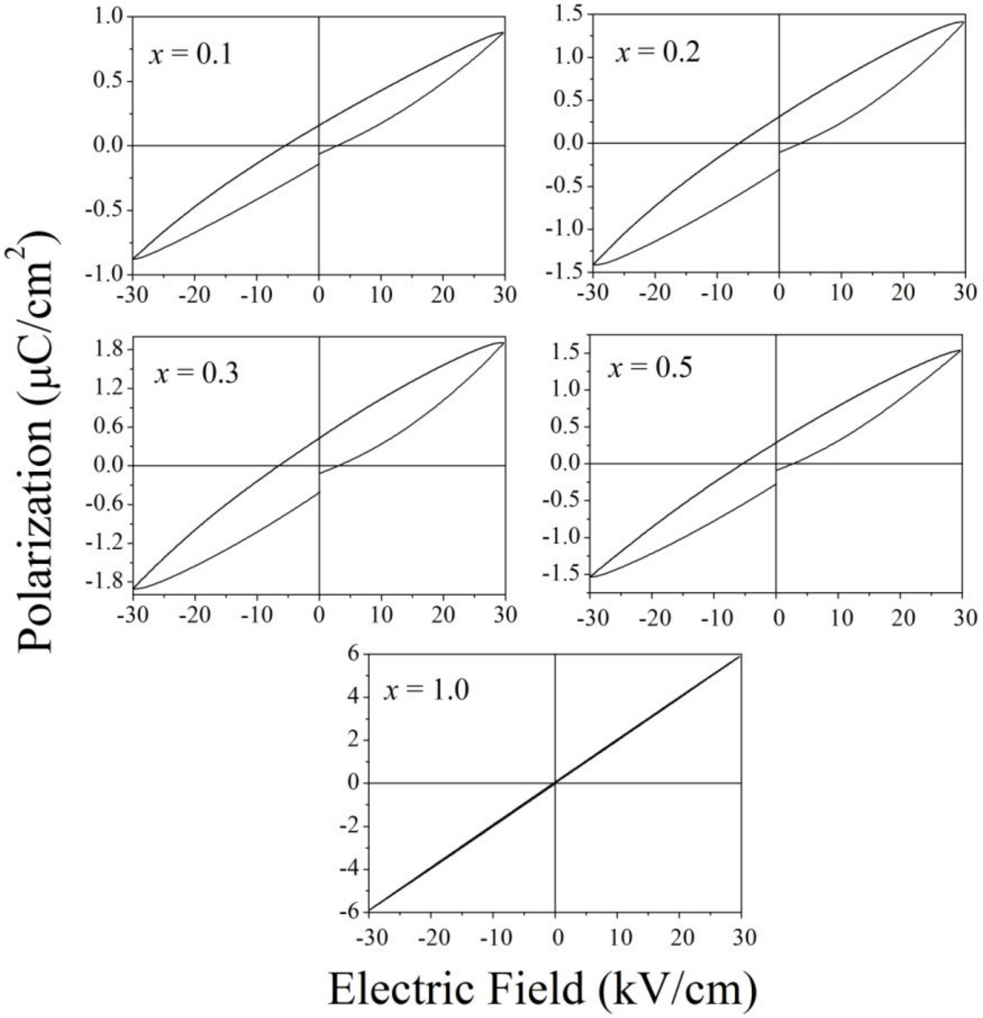

Fig.4.26. Plot of ferroelectric hysteresis loop measured at room temperature for different $BaBi_{(4-x)}La_xTi_4O_{15}$ ($x = 0.1, 0.2, 0.3, 0.5$) ceramics.

The initial increase in $2P_r$ may be due to decrease in concentration of oxygen vacancies in the system. As a result, the domain pinning effect gets decreased, enhancing $2P_r$. In general, Bi_2O_2 layers of BLSF plays the role of an insulating layer by compensating the space charge effect and refraining the oxygen vacancies from accumulating at the domain walls, thus pinning the domains [2]. With increase in La^{3+} substitution, La^{3+} ions get incorporated in the Bi_2O_2 layers. Thus, role of Bi_2O_2 layer was weakened and it was unable to prevent the collection of oxygen vacancies at domain walls, thus resulting in a decreased $2P_r$.

4.2.2.5 Piezoelectric Properties

Fig. 4.27 shows the variation of piezoelectric d_{33} coefficients as a function of composition. The d_{33} coefficients are also listed in Table 4.6. The d_{33} was found to be maximum for $x = 0.1$ ($d_{33} = 22$) and was also quite high compared to BBT (Section 4.2.1.5). This increase in d_{33} may be due to the decrease in oxygen vacancy with increase in La^{3+} concentration as discussed earlier. It is well known that the oxygen vacancies pin down the domain walls. So a decrease in oxygen vacancy facilitates the movement of the domain walls, thus increasing the d_{33} coefficient. With further increase in La^{3+} concentration, the room temperature d_{33} values decreased. This was in good agreement with the outcome that with an increase in the La^{3+} concentration, relaxor behaviour enhanced. Similar results were also observed by *Zhou et. al.* [179].

The compositions with $x = 0.5$ and 1.0, showed almost negligible piezoelectricity. Their near room temperature T_f may be responsible for their absence of piezoelectricity. Similar enhancement was observed for La^{3+} modified $K_{0.5}Bi_5Ti_4O_{15}$ [113]. A few reports concerning the d_{33} coefficients of some modified four layers members are also available, the compositions namely, CeO_2 modified $K_{0.5}Bi_5Ti_4O_{15}$, $K_{0.5}La_{0.5}Bi_4Ti_4O_{15}$ and CeO_2 modified $K_{0.5}La_{0.5}Bi_4Ti_4O_{15}$ [112, 113, 193]. Amidst all these compositions, a maximum value of 28 pC/N was reported for CeO_2 modified $K_{0.5}Bi_5Ti_4O_{15}$ and $K_{0.5}La_{0.5}Bi_4Ti_4O_{15}$.

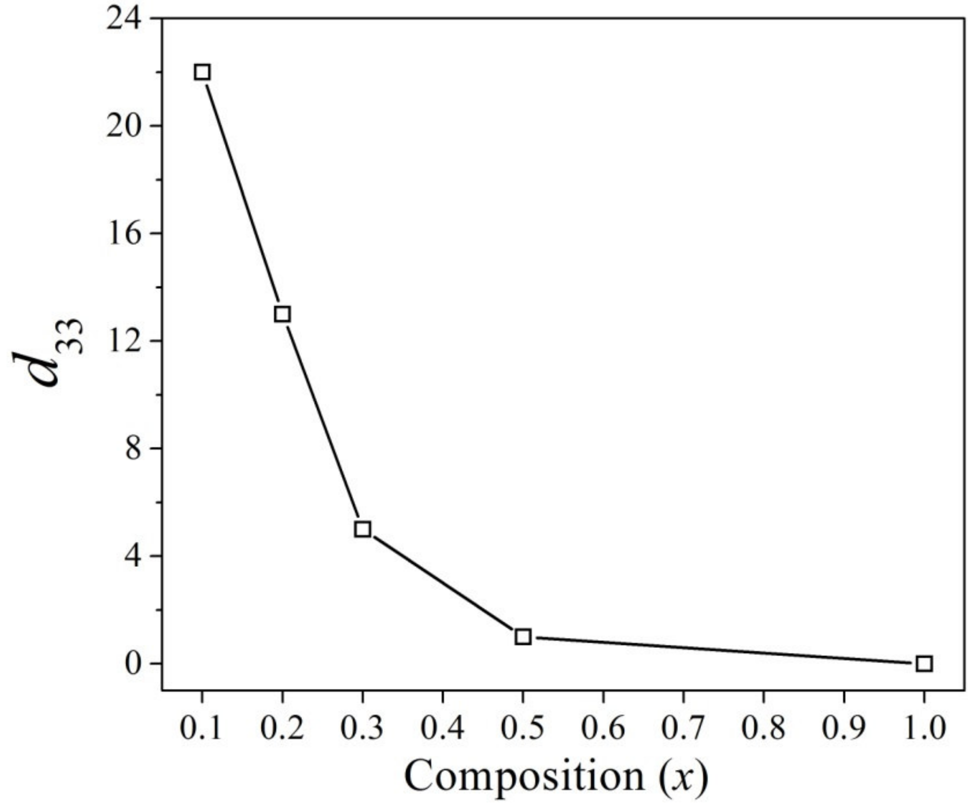

Fig.4.27. Variation of d_{33} as a function of $BaBi_{(4-x)}La_xTi_4O_{15}$ ($x = 0.1, 0.2, 0.3, 0.5$) composition.

Table 4.6. Room temperature Remnant polarization ($2P_r$), Coercive field ($2E_c$), and Piezoelectric Coefficient d_{33} values for different $BaBi_{(4-x)}La_xTi_4O_{15}$ ($x = 0.1, 0.2, 0.3, 0.5$) ceramics.

Formula	**$x = 0.1$**	**$x = 0.2$**	**$x = 0.3$**	**$x = 0.5$**	**$x = 1.0$**
$2P_r$ (μC/cm^2)	0.295	0.61	0.834	0.556	0.055
$2E_c$ (kV/cm)	8.35	9.87	9.53	8.08	0.37
d_{33} (pC/N)	22	13	5	1	0

4.2.2.6 Impedance Spectroscopy

Fig. 4.28 shows the variation of Z′ (inset) and Z″ as a function of log of frequency at various temperatures for all the La^{3+} substituted BBT samples. The height of Z′ plots decreased with increase in frequency as well as temperature, indicating an increase in the *ac* conductivity of the system. Z′ plots appear to merge in the high frequency from 10 kHz. The reason for such behaviour may be the release of space charge and reduction in the barrier properties of the material [177]. At low frequency, Z′ plots decreased with rise in temperature suggesting the negative temperature coefficient (NTCR) type of behaviour. The upper limit of Z′ values increased with increase in La^{3+} from 0.1 to 0.3. However, on further increase in La^{3+}, values of Z′ decreased.

The Z″ peaks appear at ~330°C and the characteristic frequencies for the appearance of peaks for different compositions were different. For all the samples, the peaks shifted to higher frequency side with increase in temperature along with suppression in the peak height. The peaks were also asymmetric in shape indicating a spread of relaxation time, confirming them to possess non-Debye behaviour.

The spread of relaxation time was confirmed from the Z″ versus log frequency plot and can be calculated based on the relation 4.16. For all compositions, τ decreased with rise in temperature. Fig. 4.29 shows the plot of log τ versus inverse of temperature for all compositions. The linear fit to the slope of the curve based on Eq. 4.17 gives the E_a for the compositions and is listed in Table 4.7. E_a values increased for $x = 0.1$ to 0.3 compared to BBT, but with further increase in x, i.e. for $x \geq 0.5$, E_a decreased and was in the same range as that of BBT. As already explained in section 4.2.2.1, La^{3+} occupies the *A*-site of perovskite block for $x \leq 0.5$, which stabilizes the oxygen vacancies in the structure, while for $x \geq 0.5$, La^{3+} occupies Bi_2O_2 layer, degrading its insulating nature and resulting in an decrease in impedance of the system.

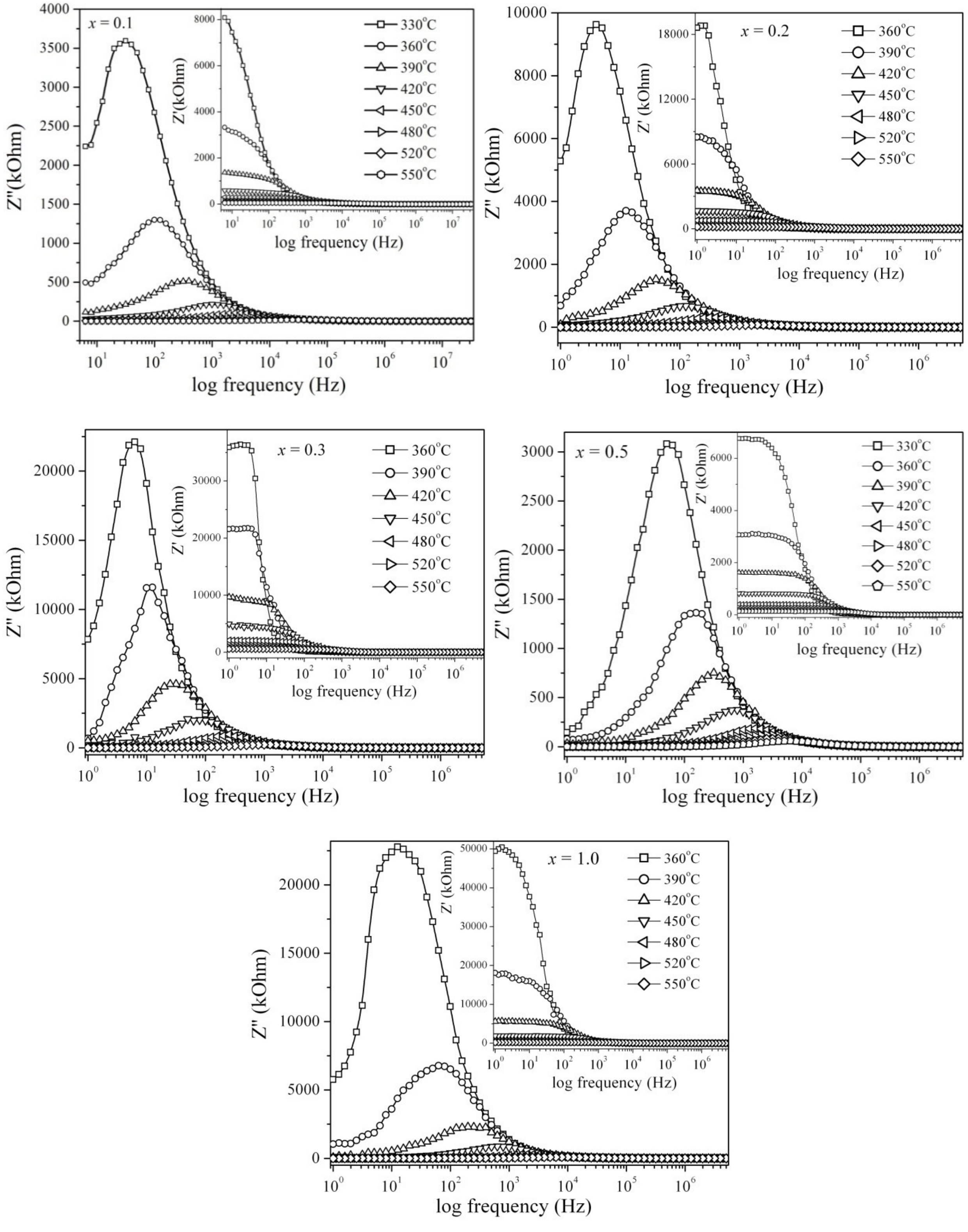

Fig.4.28. Variation of Z′ and Z″ with frequency at various temperatures for $BaBi_{(4-x)}La_xTi_4O_{15}$ (x = 0.1, 0.2, 0.3, 0.5) ceramics.

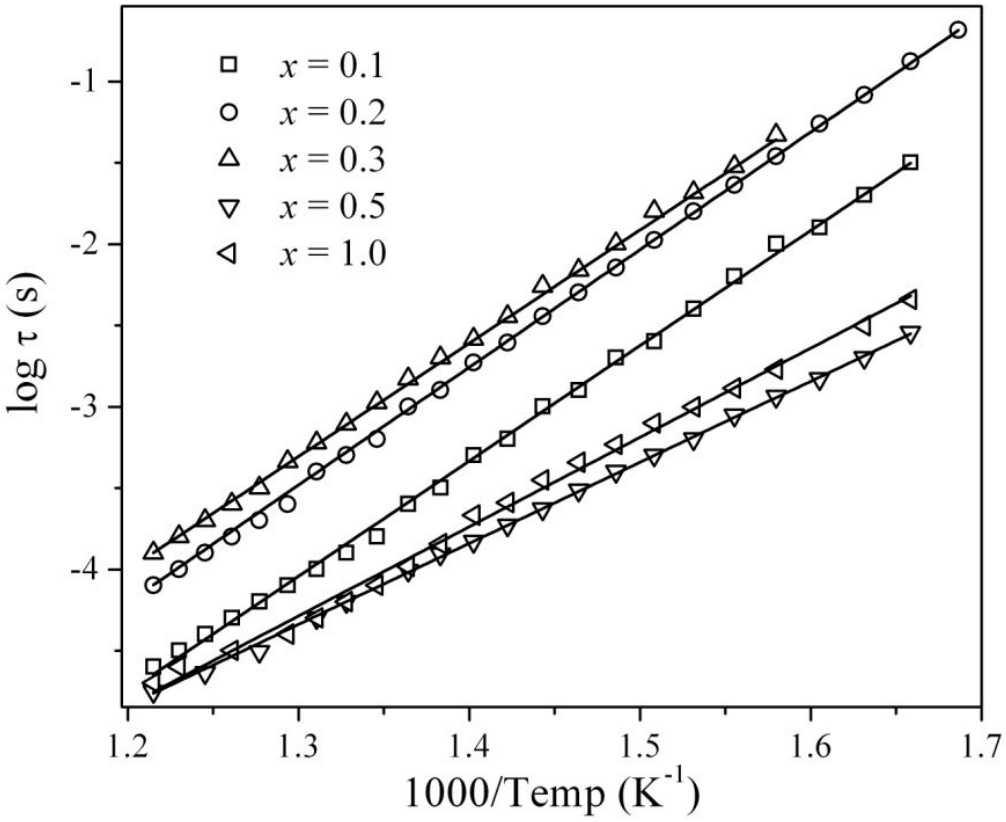

Fig.4.29. log (τ) versus 1000/T for different $BaBi_{(4-x)}La_xTi_4O_{15}$ (x = 0.1, 0.2, 0.3, 0.5, 1.0) ceramics.

Cole-Cole plots obtained from impedance spectra are shown in Fig.4.30. To extract resistance (*R*) and capacitance (*C*) values, an equivalent circuit comprising of two parallel resistor-capacitor (*RC*) elements connected in series was used to model the electrical response. *R* and *C* values were determined**.** At low temperatures, a single arc was observed for all compositions which can be attributed to the contribution from the bulk of the ceramics including grain and grain boundary. However, at high temperatures from ~450°C, a tail to the low frequency side of the arc was observed. This tail could be attributed to the electrode effect and it was not taken into account. The intercepts of the high frequency arc gives the total resistance (R_{tot}). Using the R_{tot}, *dc* conductivity of bulk can be evaluated using Eq. 4.18. The *dc* conductivity of different compositions at 550°C are listed in Table 4.7. Conductivity decreased with substitution due to the same reason of decreased oxygen vacancies as stated above.

Composition with $x = 0.3$ showed the lowest *dc* conductivity among all and was lower even compared to that of pure BBT. The activation energy for *dc* conductivity of all the compositions was calculated from the temperature dependence of the *dc* conductivity using the Arrhenius relation Eq. 4.19. The values of E_{dc} are listed in Table 4.7. In comparison to pure BBT ceramics, La^{3+} substituted ceramics displayed single slope. In the present case, the activation energy due to the ionization of the oxygen vacancy as described by Kroger-Vink notation (Eq. 4.20) was only obtained.

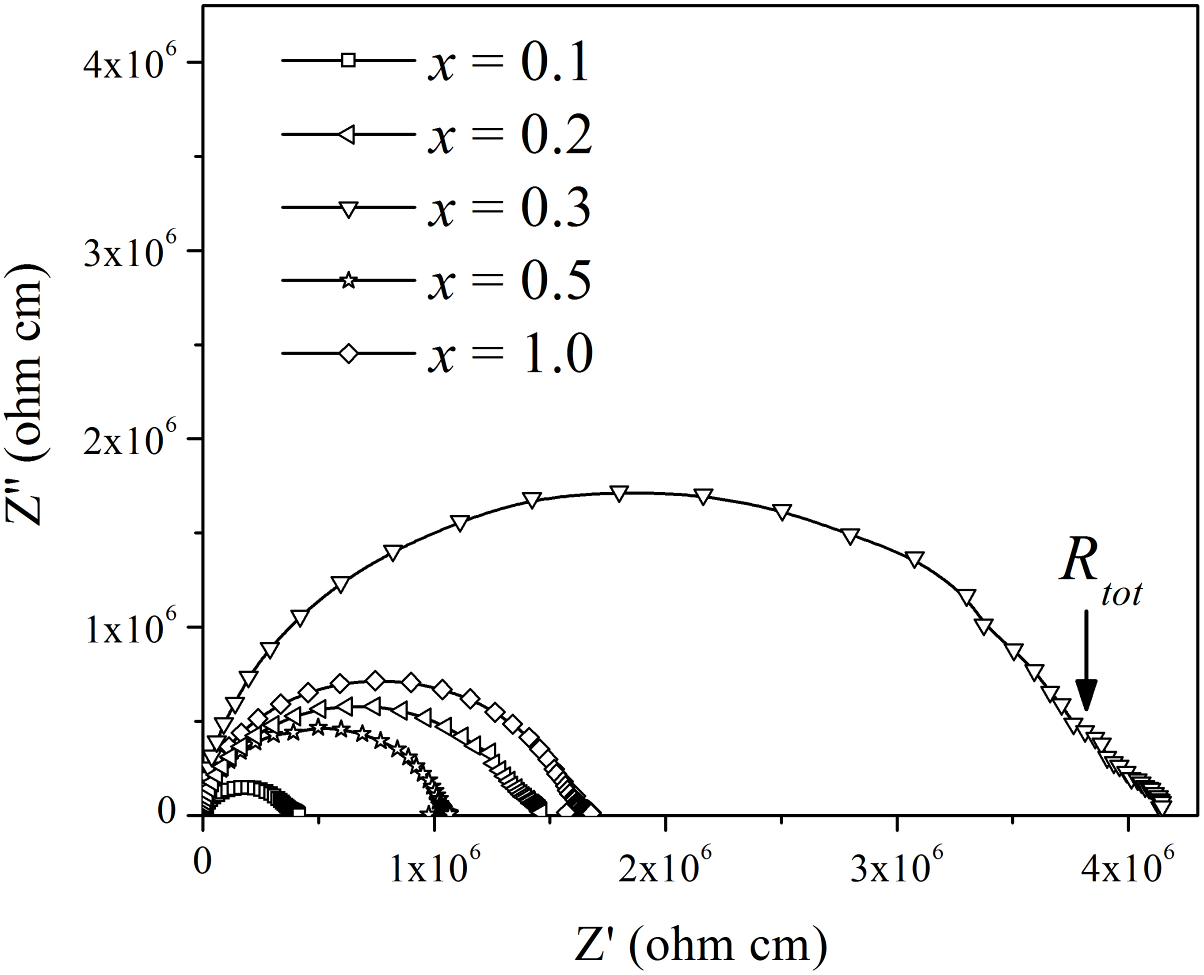

Fig.4.30. Complex impedance plot of $BaBi_{4-x}La_xTi_4O_{15}$ ($x = 0.1, 0.2, 0.3, 0.5$) ceramics at 550°C.

Table 4.7. Activation energy from τ (E_a), Activation energy (E_{dc}), *dc* conductivity for bulk (σ_{dc}) at 550°C for different $BaBi_{(4-x)}La_xTi_4O_{15}$ (x = 0.1, 0.2, 0.3, 0.5) ceramics.

Formula	x **= 0.1**	x **= 0.2**	x **= 0.3**	x **= 0.5**	x **= 1.0**
E_a (eV)	0.611 ± 0.02	0.624 ± 0.02	0.6 ± 0.01	0.429 ± 0.03	0.473 ± 0.02
σ_{dc} ($\Omega^{-1}cm^{-1}$)	2.9×10^{-6}	7.41×10^{-7}	2.77×10^{-7}	9.8×10^{-7}	6.48×10^{-7}
E_{dc} (eV)	0.218 ± 0.01	0.273 ± 0.02	0.355 ± 0.02	0.213 ± 0.01	0.261 ± 0.01

4.2.3 Conclusions

La^{3+} substitution for Bi^{3+} in $BaBi_4Ti_4O_{15}$ ceramics was successfully prepared through modified chemical route. Single phase $BaBi_{4-x}La_xTi_4O_{15}$ solid solution was observed for $x \leq 1.0$. La^{3+} ions were found to occupy the Bi_2O_2 layer for $x \geq 0.5$. The sintering temperature increased accompanied with a decrease in grain size with increase in La^{3+} concentration. Temperature of the dielectric maximum was lowered and the dielectric loss decreased with La^{3+} substitution. A significant increase in the diffuseness and relaxor behaviour was observed with increasing x. The increase in the relaxor behaviour can probably be attributed to the compositional fluctuation induced by La^{3+}, partly in perovskite and partly in Bi_2O_2 layers. The dielectric relaxation shows a sufficiently good fit with the Vogel Fulcher relationship. The freezing temperature T_f was noted to decrease from 310 to 100°C with increasing x from 0.1 to 0.5. Composition with x = 0.3 showed the highest $2P_r$ among all and a lower $2E_c$ than BBT. The incorporation of La^{3+} ions also resulted in a significant reduction in the *dc* conductivity in x = 0.3 composition. The increased activation energies and decreased *dc* conductivities confirms the decrease in oxygen vacancy concentration with La^{3+} substitution.

4.3 Zr^{4+} substitution for Ti^{4+} in $BaBi_4Ti_4O_{15}$

4.3.1 Introduction

In BLSF compounds, it is very difficult to substitute cations at *B*-site other than those with a d^0 electronic configuration e.g. Ti^{4+}, Nb^{5+}, W^{6+} [42]. It has been observed that the maximum solid solubility of Ga^{3+} in $BaBi_4Ti_{4-x}Ga_xO_{15}$ was around x~0.2 [42]. The solid solubility in the system $Bi_4Ti_{3-x}B_xO_{12}$ (B = Ge^{4+}, Sn^{4+}, Zr^{4+}, Hf^{4+}) were very low (<2%) [194]. It is therefore interesting to study the substitution of Zr^{4+} in $BaBi_4Ti_{4-x}Zr_xO_{15}$ with respect to its solid solubility and relaxor characteristic.

$BaBi_4Ti_{4-x}Zr_xO_{15}$ with $x = 0.1$, 0.2, 0.3 and 0.5 ceramics were synthesized via modified chemical route. The structural, densification, microstructural, relaxor characteristics, ferroelectric, piezoelectric and impedance spectroscopic properties of these ceramics were investigated.

4.3.2 Results and Discussion

4.3.2.1 Solid Solubility Limit and Structural Analysis

Fig.4.31 shows X-ray diffraction patterns of $BaBi_4Ti_{4-x}Zr_xO_{15}$ ($x = 0.1$, 0.2, 0.3 and 0.5) ceramics. The major phase of each pattern was identified to match with the standard pattern of $BaBi_4Ti_4O_{15}$ (JCPDS #35-0757). Patterns of ceramics with $x = 0.1$ and 0.2 show the presence of pure single phase BBT. However, presence of minor amounts of Bi_2O_3 and ZrO_2 containing phases was detected in the compositions $x = 0.3$ and 0.5. The figure also shows that there was a shifting of diffraction peaks with Zr^{4+} substitution indicating the dissolution of Zr^{4+} in the structure and also a change in the lattice parameters.

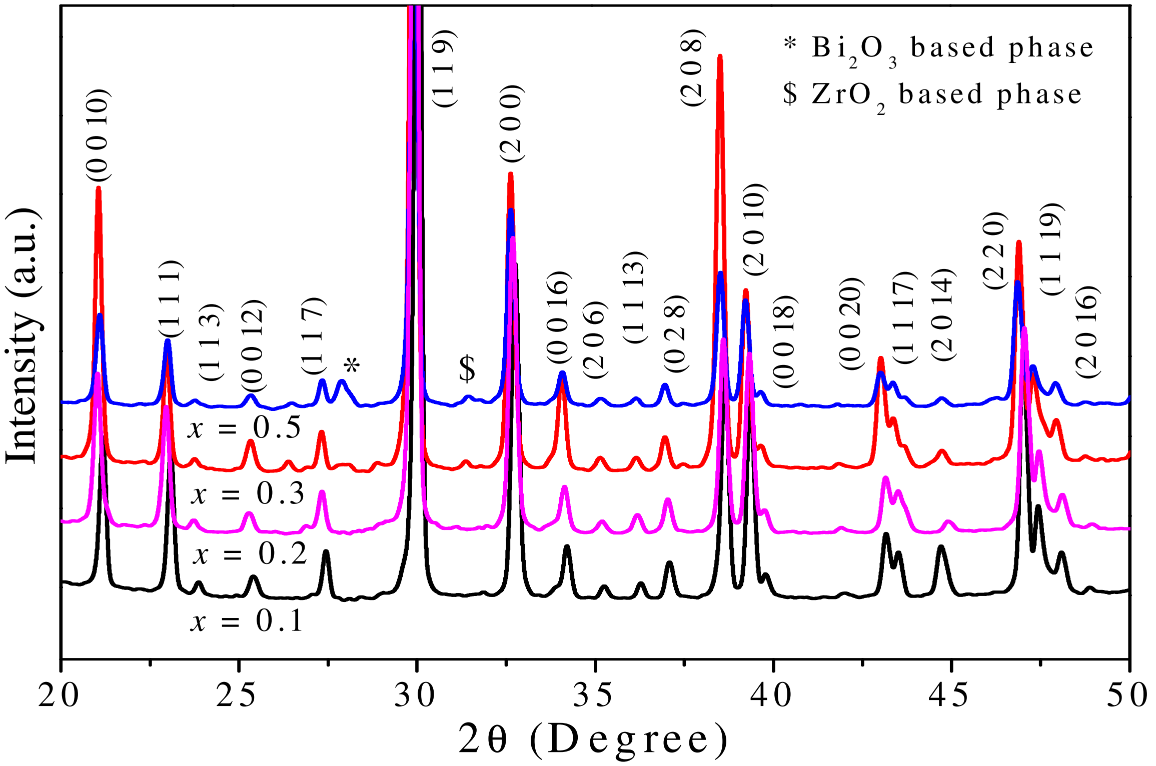

Fig.4.31. XRD patterns of $BaBi_4Ti_{4-x}Zr_xO_{15}$ (x = 0.1, 0.2, 0.3, 0.5) ceramics.

To evaluate the effect of Zr^{4+} substitution on lattice parameters, full pattern Rietveld refinement was performed using MAUD Program [158]. Starting parameters for Rietveld refinement were taken from $BaBi_4Ti_4O_{15}$ as presented by *Kennedy et.al.* [29], with orthorhombic space group $A2_1am$ (No. 36) and cell parameters a = 5.4697 Å, b = 5.4558 Å and c = 41.865 Å. Some constraints were imposed during the refinement to limit the no of refined parameters. Each constraint was systematically verified by comparison with result previously obtained on $BaBi_4Ti_4O_{15}$ (x = 0). The set of refined parameters obtained for x = 0 specimen were used as starting parameters for refinement in x = 0.1 and so on.

Table 4.8 presents a summary of the refinement for different compositions. Fig.4.32 shows the fitted output pattern of all compositions. The patterns of the compositions with x = 0.3 and 0.5 are shown after the refinement based on three phases; BBT, Bi_2O_3 and ZrO_2. No attempt was made to model the true stoichiometry of these three phases, although we assume that all may contain Zr^{4+}. Based on this assumption, lattice parameters for each were allowed to vary. It may be noted that the Rietveld fits for x = 0.3 and 0.5 samples were much improved as demonstrated by the final goodness-of-fit indices, sigma (Table 4.8), when three phase refinement was considered. The lattice parameters *a*, *b* and *c* increase with increasing Zr^{4+} substitution as shown in Fig. 4.33(a). This may be due to the fact that ionic radius of Zr^{4+} is larger than Ti^{4+} [192]. The volume of the unit cell also increased with the substitution as shown in Fig. 4.33(b). The orthorhombic distortion of the structure was calculated using the relation 4.10.

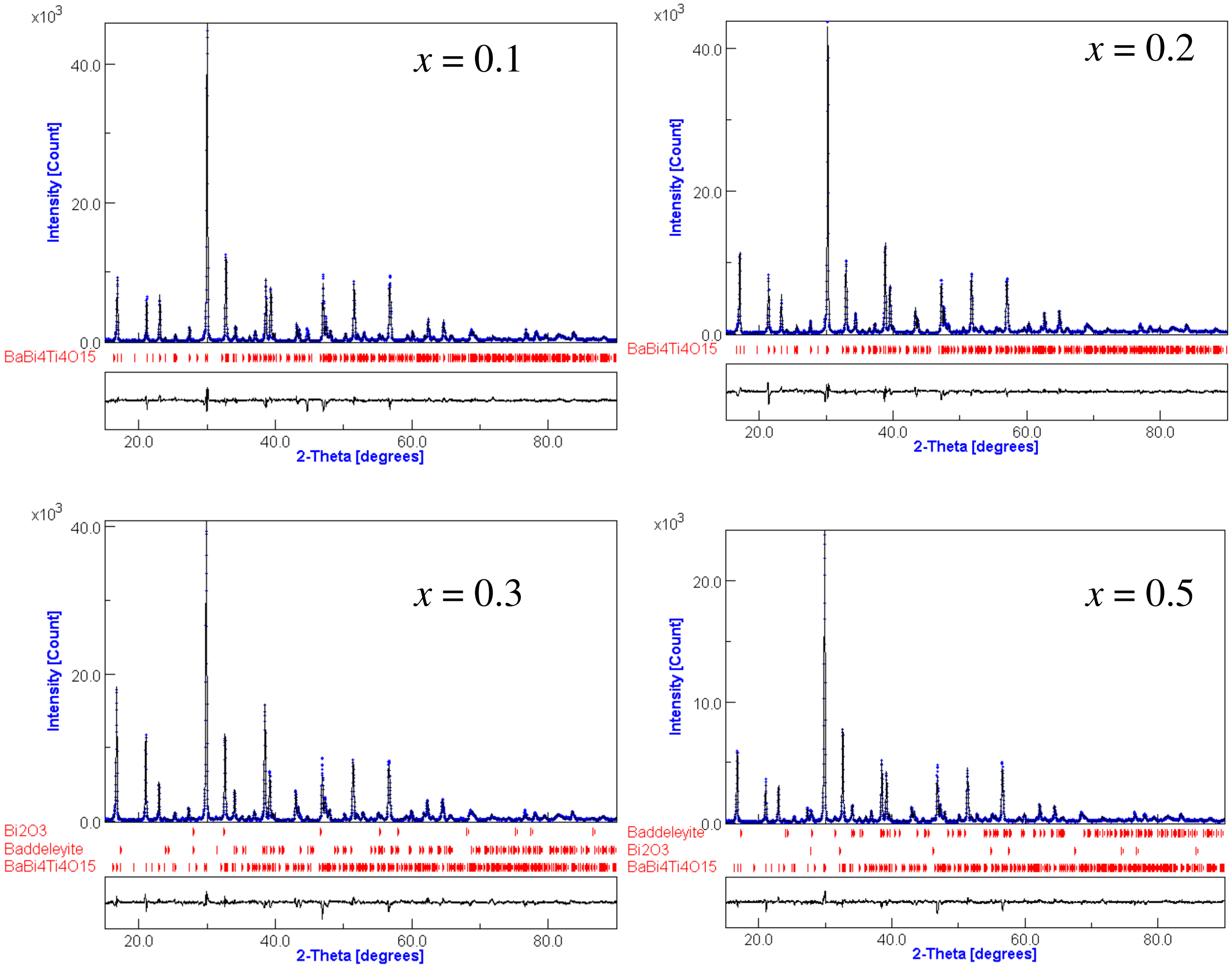

Fig.4.32. Final Rietveld fit for $BaBi_4Ti_{4-x}Zr_xO_{15}$ ($x = 0.1, 0.2, 0.3, 0.5$) ceramics.

Effect of Zr^{4+} substitution on orthorhombic distortion was evaluated and is shown in Fig. 4.33(b). This result shows that Zr^{4+} substitution has a tendency to change the orthorhombic crystal structure of BBT to a structure with more tetragonality or to pseudo tetragonal. To verify the tetrogonality of $x = 0.5$ specimen, Rietveld refinement was tried considering the tetragonal space group *I4/mmm*, with a = 3.8936 Å and c = 42.2914 Å as proposed by *Kennedy et.al.* [28] for $BaBi_4Ti_4O_{15}$ at 1000 K. However, the *R*-factors and sigma for the refinement did not much improve as compared to orthorhombic $A2_1am$ based model.

The increase in lattice parameter with Zr^{4+} substitution apparently indicated that Zr^{4+} has solid solubility in the substitution range studied here. However, the presence of Bi_2O_3 and ZrO_2 based phases in $x = 0.3$ and 0.5 compositions indicated that Zr^{4+} has solid solubility limit up to 0.2. Table 4.8 shows the quantitative estimation of different phases those found after Rietveld refinement for each specimen. The results showed that the amount of ZrO_2 and Bi_2O_3 based phases increased with increase in Zr^{4+} above $x = 0.2$. This again supports the solubility limit at 'B' site of 4-layer BLSF being around $x = 0.2$.

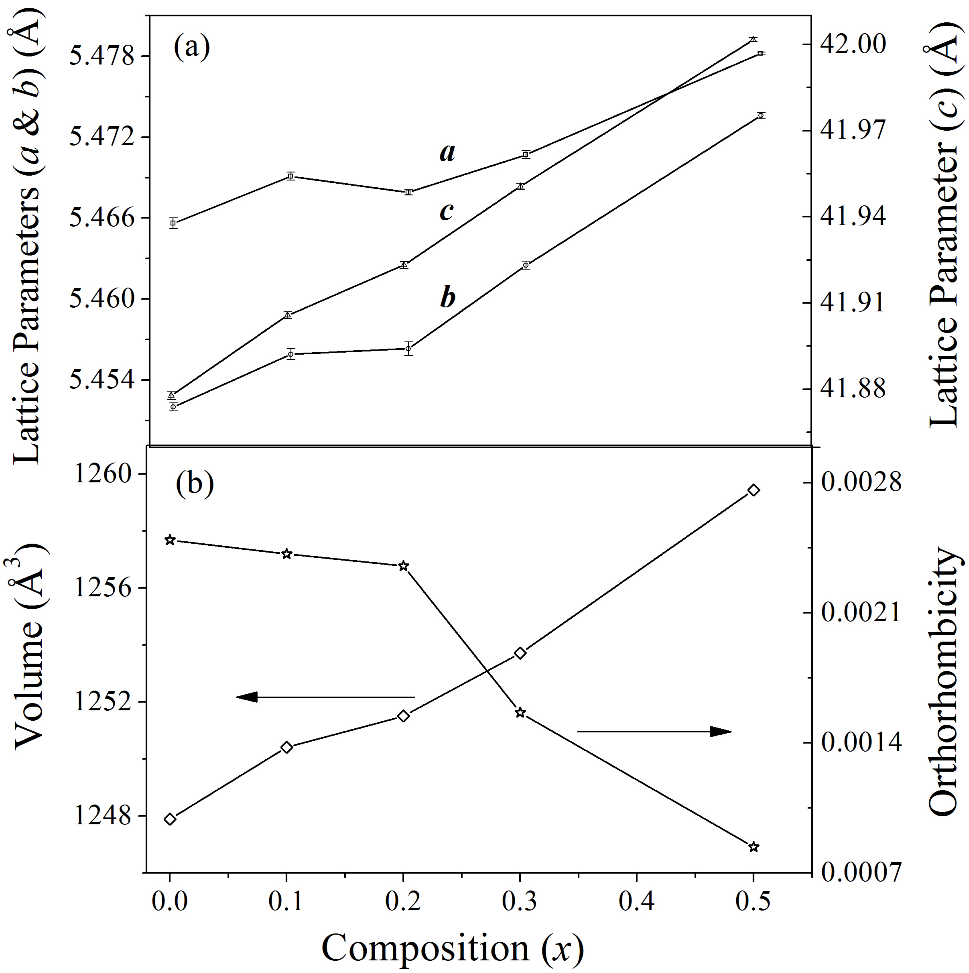

Fig.4.33. Lattice parameters, volume and orthorhombicity of $BaBi_4Ti_{4-x}Zr_xO_{15}$ (x = 0.1, 0.2, 0.3, 0.5) ceramics as a function of Zr^{+4} substitution.

As the solid solubility limit of zirconia is considered to be ~0.2, then an explanation is required as to why the volume of the unit cell increased above $x = 0.2$, i.e., for $x = 0.3$ and 0.5. The refinement showed an increase in lattice parameters as well as increase in ZrO_2 and Bi_2O_3 based phase content (Table 4.8) from $x = 0.3$ to 0.5. It may be due to the effect of increased solid solubility in presence of excess zirconia containing phase at the grain boundary of the ceramics. This increased Zr^{4+} solubility can be supported by the fact that maximum permittivity temperature position (T_m) shifted from 410°C for $x = 0.3$ to 390°C for $x = 0.5$ as discussed further.

Table 4.8. Refined lattice parameters (*a*, *b* and *c*), Volume, Phase constituents, *R*-factors, Sigma and Orthorhombicity for $BaBi_4Ti_{4-x}Zr_xO_{15}$ (x =0.1, 0.2, 0.3, 0.5) ceramics.

Formula	$\boldsymbol{x = 0.1}$	$\boldsymbol{x = 0.2}$	$\boldsymbol{x = 0.3}$	$\boldsymbol{x = 0.5}$
Cell parameters				
a (Å)	5.4691(3)	5.4679(2)	5.4707(3)	5.4782(1)
b (Å)	5.4559(4)	5.4563(5)	5.4625(3)	5.4736(2)
c (Å)	41.9057(12)	41.9232(12)	41.9506(11)	42.0016(7)
Volume (Å)^3	1250.41	1251.51	1253.71	1259.43
Phase constitution (weight %)				
$BaBi_4Ti_4O_{15}$	100	100	98	88.2
Bi_2O_3	---	---	0.3	1.9
ZrO_2	---	---	1.7	9.9
R_w (%)	5.1	5.1	5.1	4.9
R_b (%)	3.6	3.6	3.8	3.7
Sigma	2.76	2.74	2.84	1.96
Orthorhombicity	0.00242	0.00235	0.00156	0.00084

4.3.2.2 Densification and Microstructural Characteristics

Table 4.9 tabulates the sintering temperature and time of the Zr^{4+} substituted ceramics versus their %theoretical density. Sintering temperature decreased with increase in zirconium substitution. The sintering temperature decreased from 1100°C for $x = 0.1$ to 1000°C for $x = 0.5$. The major reason of decrease in sintering temperature could be the presence of grain boundary impurity phase Bi_2O_3, which has a low melting temperature of ~815°C. As stated above, the grain boundary impurity phase Bi_2O_3 has been found for x=0.3 and 0.5 compositions.

Fig. 4.34 shows SEM micrograph for the Zr^{4+} substituted BBT ceramics. Microstructures have randomly oriented plate like grains which decreased with increase in Zr^{4+} content. Table 4.9 lists the grain size of the substituted ceramics. The decrease in grain size with Zr^{4+} substitutions seems to be related with the lower grain-growth rate induced by slow diffusion of Zr^{4+} ion which has a larger ionic radius than Ti^{4+} [195]. Micrograph for $x = 0.5$ composition shows some dark coloured grains along grain boundaries of whitish big grains. The dark colored grains are assigned for Bi_2O_3 and ZrO_2 based impurity phases, which have been detected by XRD analysis.

Table 4.9. %Theoritical density with Sintering temperature/time and Grain Size for $BaBi_4Ti_{4-x}Zr_xO_{15}$ (x =0.1, 0.2, 0.3, 0.5) ceramics.

Formula	***x* = 0.1**	***x* = 0.2**	***x* = 0.3**	***x* = 0.5**
Sintering temperature and time	**% Theoritical density**			
1100°C/4h	92	Partial melting	-	-
1050°C/4h	-	95	Partial melting	-
1000°C/4h	-	-	93	Partial melting
950°C/4h	-	-	-	89
Grain Size (μm)				
Length	1.67	1.73	1.31	1.23
Breadth	0.96	0.99	0.89	0.87
Thickness	0.44	0.35	0.27	0.24

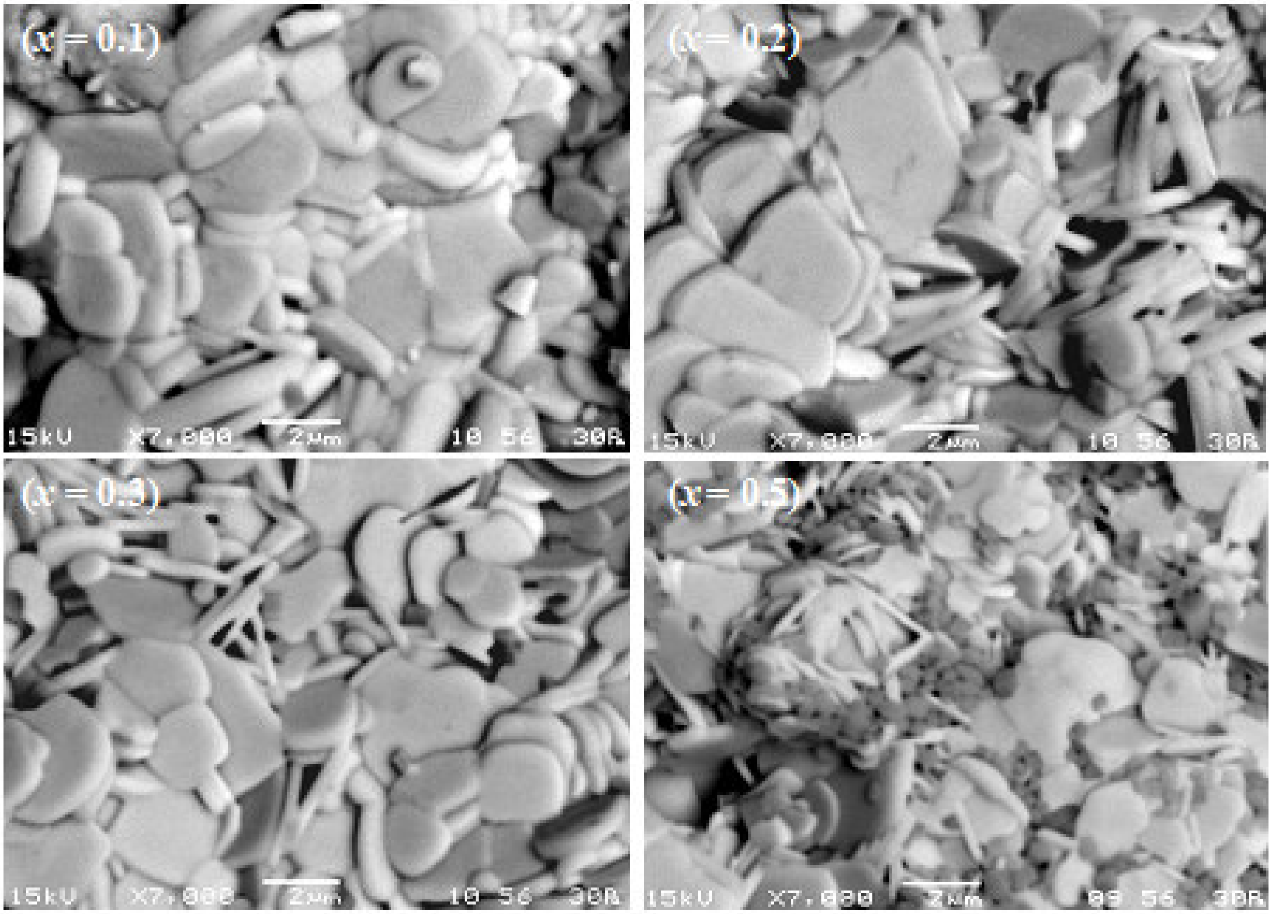

Fig.4.34. Scanning electron micrograph of $BaBi_4Ti_{4-x}Zr_xO_{15}$ (x =0.1, 0.2, 0.3, 0.5) ceramics.

4.3.2.3 Dielectric and Diffuse Phase Transition Behaviour

The dielectric properties of BBT ceramics doped with various amount of Zr^{4+} were studied. Fig. 4.35 shows the temperature dependence of the relative permittivity (ε') and dielectric loss (tan δ) measured at 100 kHz for different Zr^{4+} substituted BBT ceramics. Table 4.10 lists ε_m', dielectric loss at maxima (tan δ_m) and T_m for different compositions. ε_m' values of x = 0.1, 0.2 and 0.3 remained almost same as that of BBT. But ε_m' for x = 0.5 was much lower than others due to the combined effect of decreased orthorhombicity and presence of increased amount of non-ferroelectric Bi_2O_3 and ZrO_2 based phases.

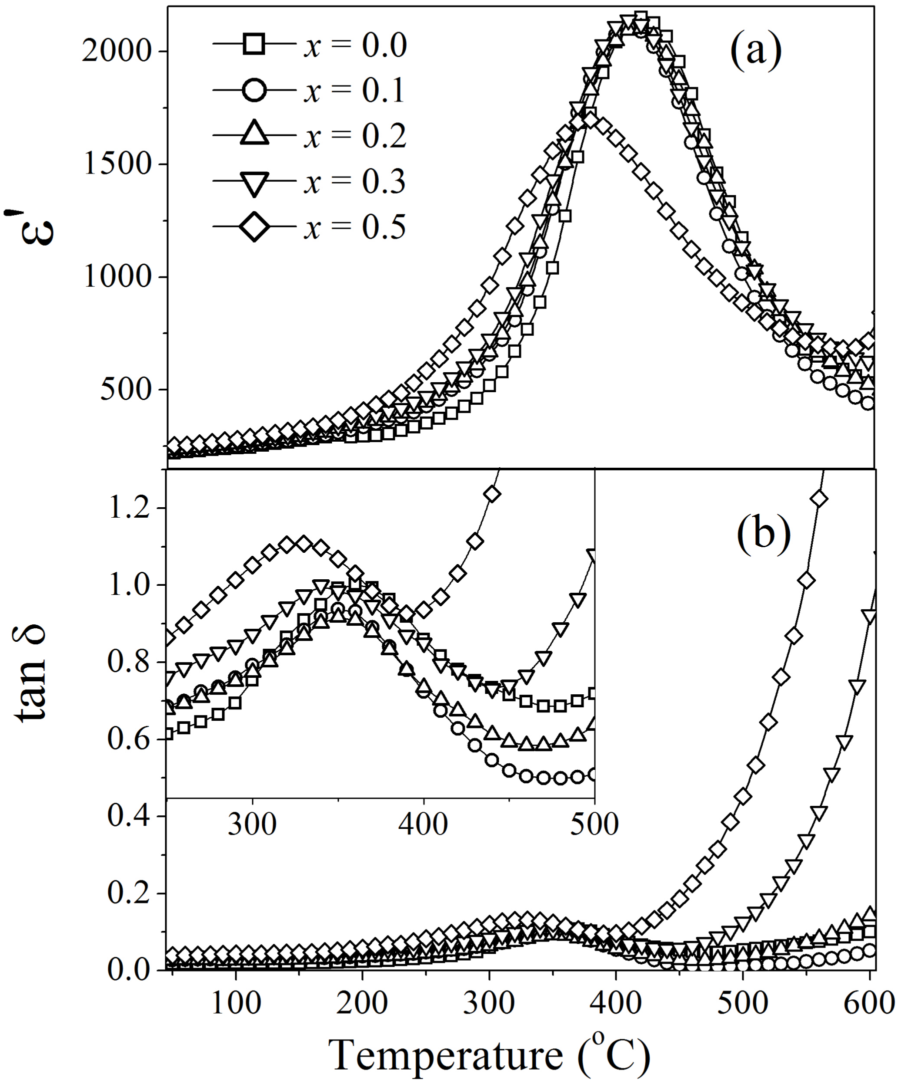

Fig.4.35. Temperature dependence of the relative permittivity and tan *δ* for different $BaBi_4Ti_{4-x}Zr_xO_{15}$ ($x = 0.1$, 0.2, 0.3 and 0.5) ceramics at 100 kHz.

A nominal shifting of T_m (~10°C) towards lower temperature was observed for Zr^{4+} substitution upto $x = 0.3$. However, the T_m of $x = 0.5$ was shifted by 30°C. This could be assigned to the increased Zr^{4+} solid solubility in $x = 0.5$. The unit cell volume of $x = 0.5$ was maximum (Fig. 4.33 (b)) due to the increased solubility of Zr^{4+} in presence of ZrO_2-rich grain boundary phase as stated above. The shifting of T_m towards lower temperature may be due to the decrease in the rattling space of the BO_6 octahedra by the Zr^{4+} substitution as the ionic radius of Zr^{4+} is greater than that of Ti^{4+} ion [192].

Fig. 4.35(b) shows the temperature dependence of dielectric loss for different compositions. The dielectric loss decreased for $x = 0.1$ and 0.2 compositions compared to BBT at room temperature as well as at high temperature (Table 4.10), whereas, it was higher for $x = 0.3$ and 0.5. In BBT, the conduction mechanism of the leakage current involves; (a) a space charge limited conduction related to oxygen vacancies [106] and (b) a field-assisted conduction by polaron hopping between Ti^{4+} and Ti^{3+}. Hence, the reason behind lowering of loss in $x = 0.1$ and 0.2 may be attributed to the lowering of Ti^{4+} concentration by Zr^{4+} substitution. With further increase in Zr^{4+} concentration ($x > 0.2$, i.e., > 5 at. %), the loss was found to increase due to the presence of grain boundary secondary phases, especially Bi_2O_3, which is known to be conducting in nature [196]. This also correlated the highest tan δ of $x = 0.5$ as it contained largest amount of Bi_2O_3 amongst these.

One important characteristic of a relaxor is the relaxation frequency which is measured from the degree of relaxation parameter. The degree of relaxation ΔT_m is represented by Eq. 4.11 and is shown in Table 4.10. ΔT_m was in the range 10-15°C for substitutions upto $x = 0.3$. However, the ΔT_m parameter for $x = 0.5$ was found to be zero. This highlighted the fact that relaxor behaviour was suppressed at $x = 0.5$ substitution.

Another important parameter; dielectric dispersion is frequently used for relaxor characterization. An empirical relation as stated in Eq. 4.14 was used to calculate the dielectric dispersion denoted by γ. Fig. 4.36 shows the plot of log $(1/\varepsilon' - 1/\varepsilon_m')$ versus log $(T - T_m)$ for different compositions at 100 kHz and respective γ values. The γ values were found to decrease with increasing Zr^{4+} substitution from 1.89 for $x = 0.1$ to 1.52 for $x = 0.5$. This may be due to the decrease in relaxor phenomena as stated above. The low γ value 1.52 of $x = 0.5$ ceramics suggest to possess more of ferroelectrics characteristic than that of a relaxor.

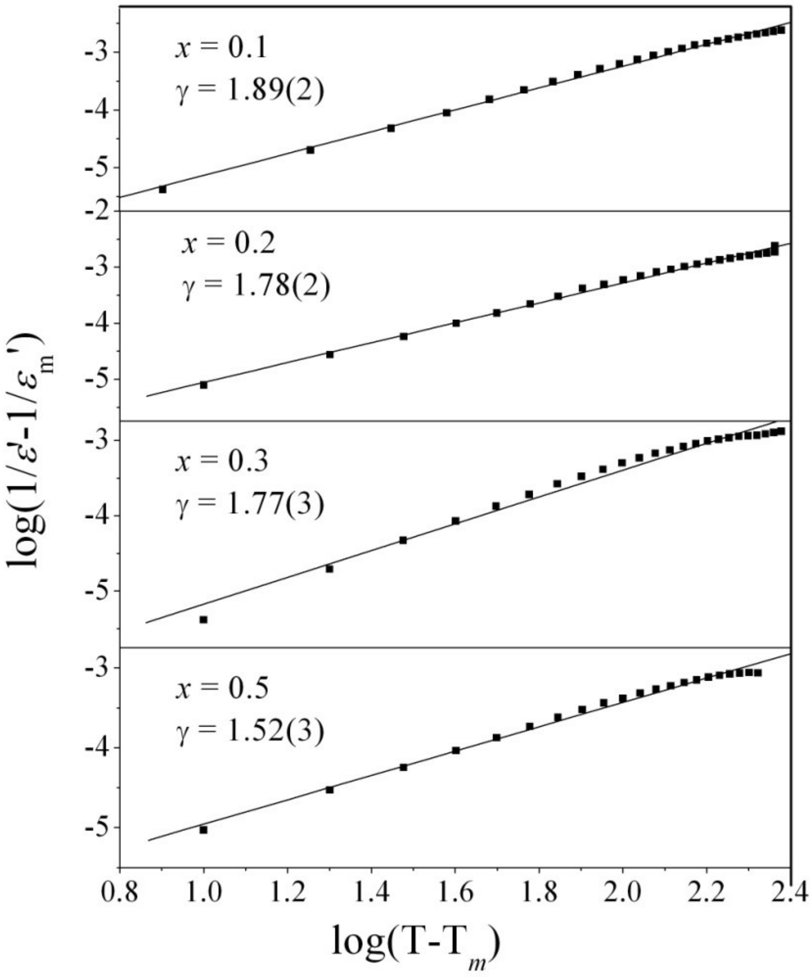

Fig.4.36. Plot of log (1/ε′ – 1/ε$_m$′) versus log (T – T_m) at 100 kHz for different $BaBi_4Ti_{4-x}Zr_xO_{15}$ (x = 0.1, 0.2, 0.3, 0.5) ceramics.

It was interesting to note that the broadening of permittivity versus temperature curve increased with Zr^{4+} substitutions, although the relaxor nature was suppressed. Peak broadening, i.e., diffusiveness is generally expressed by a parameter δ which is related with permittivity and temperature as described by Eq. 4.12. The δ parameters of different compositions were calculated by fitting permittivity-temperature data (Fig.4.35(b)) and are shown in Table 4.8. The result showed the degree of diffusiveness increased with increase in Zr^{4+} substitution. The compositional fluctuations and structural disorder in the crystallographic sites gave rise to the broadness or diffusiveness of the peak suggesting microscopic heterogeneity with different local Curie points. In the present compositions, Ti^{4+} cation was replaced by Zr^{4+} for *B*-site of BLSF structure. Compositional heterogeneity with respect to these two dissimilar cations may be responsible for this broadening behaviour.

The dielectric relaxation behaviour for relaxor ferroelectrics can be modeled by Vogel-Fulcher relationship, described by Eq. 4.15. Fig.4.37 shows the plot of $1000/T_m$ versus log ν for $x = 0.1$ and 0.2 compositions. Open symbols represent the experimental data points and the line gives the fit to Eq. 4.15. Values of T_m show a good fit to the theoretical Vogel-Fulcher law. The values of ν_0, E_a and T_f obtained by fitting Eq. 4.15 to the experimental values are listed in Table 4.10. The composition with $x = 0.2$ and 0.3, show the same fitting parameters as both the samples show same frequency dispersion in the same frequency zone.

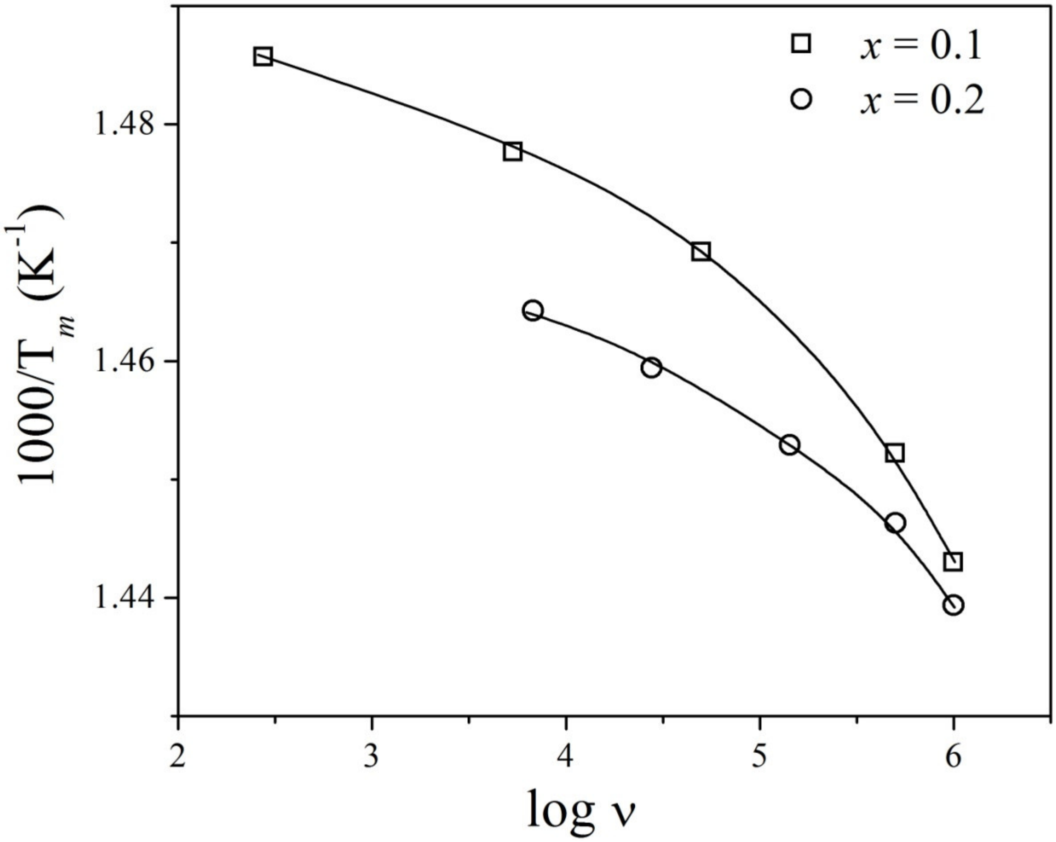

Fig.4.37. Frequency dependence of T_m for different $BaBi_4Ti_{4-x}Zr_xO_{15}$ ($x = 0.1$ and 0.2) ceramics. The symbols and solid line indicate data points and fit to Vogel–Fulcher relationship, respectively.

Hence it was observed that Zr^{4+} substitution for Ti^{4+} in BBT resulted in a decrease in the relaxor behaviour. As previously stated, relaxor behaviour of BBT was known to arise due to occupancy of Ba^{2+} cations in the Bi_2O_2 layer. This occurs in order to release the excess strain generated in the structure by the large size of Ba^{2+}. So the decrease in relaxor behaviour in the present case implied a decrease of cation disorder between the Ba^{2+} and Bi^{3+} cations in the Bi_2O_2 layer. As the ionic radius of Zr^{4+} is larger than Ti^{4+}, it increased the unit cell volume (Table 4.8). Thus it may be assumed that this increase in volume may permit more of the bigger Ba^{2+} cations to occupy the perovskite block and decrease the driving force for cation disorder. As a result decrease in cation disorder decreased the relaxor behaviour.

Table 4.10. Maximum relative permittivity (ε_m'), dielectric loss (tan δ_m), maximum permittivity temperature (T_m), degree of diffuseness (δ) at 100 kHz, degree of relaxation (ΔT_m), fitting parameters from Vogel Fulcher relation (E_{vf}, T_f and ν_0) for different $BaBi_4Ti_{4-x}Zr_xO_{15}$ (x = 0.1, 0.2, 0.3, 0.5) ceramics.

Formula	**$x = 0.1$**	**$x = 0.2$**	**$x = 0.3$**	**$x = 0.5$**
ε_m'	2108	2102	2138	1696
tan δ_m	0.09	0.09	0.11	0.13
T_m	410	410	410	390
ΔT_m (°C)	15	10	10	---
δ (°C)	146	160	164	199
E_{vf} (eV)	0.011	0.053	0.053	--
ν_o (Hz)	$6.35x10^7$	$4.32x10^7$	$4.32x10^7$	--
T_f (°C)	390	380	380	--

4.3.2.4 Polarization Hysteresis Characteristics

Fig. 4.38 shows the ferroelectric hysteresis loop of $BaBi_4Ti_{4-x}Zr_xO_{15}$ ceramics obtained under a maximum applied electric field of 30 kV/cm. P-E loops for all the compositions were recorded at room temperature and at a frequency of 100 Hz. The values of remnant polarization ($2P_r$) and coercive field ($2E_c$) are listed in Table 4.11. The $2P_r$ value was maximum for $x = 0.2$ and with further increase in x, it decreased. This decrease in $2P_r$ values from $x = 0.3$ may be a result of the presence of the secondary phases in the material matrix. $2P_r$ of $x = 0.2$ was high and also had lower $2E_c$ compared to that of BBT. The decrease in loss of the material with Zr^{4+} substitution may be responsible for its slightly higher $2P_r$ and lower $2E_c$.

4.3.2.5 Piezoelectric Properties

d_{33} coefficients for Zr^{4+} substituted BBT ceramics are given in Table 4.11. The d_{33} coefficients for $x = 0.1$ and 0.2 were found to be in the same range to that of BBT. However, with further increase in Zr^{4+} content, for $x = 0.3$ and 0.5, decrease in the d_{33} coefficients was observed. The decrease in d_{33} coefficients may be a result of the presence of Bi_2O_3 and ZrO_2 based secondary phases which increased the loss of the samples.

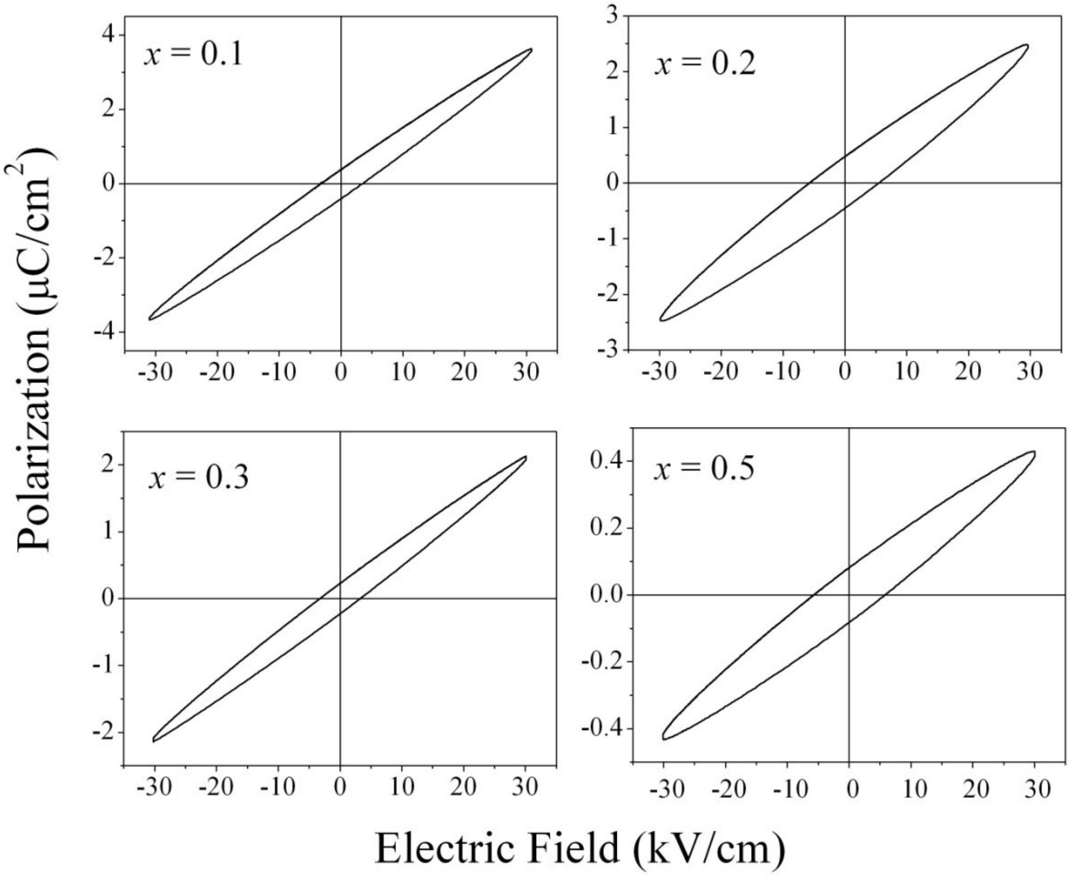

Fig.4.38. Plot of ferroelectric hysteresis loop measured at room temperature for different $BaBi_4Ti_{4-x}Zr_xO_{15}$ ($x = 0.1, 0.2, 0.3, 0.5$) ceramics.

Table 4.11. Remnant polarization ($2P_r$), coercive field ($2E_c$) and piezoelectric coefficient (d_{33}) for different $BaBi_4Ti_{4-x}Zr_xO_{15}$ (x = 0.1, 0.2, 0.3, 0.5) ceramics.

Formula	***x* = 0.1**	***x* = 0.2**	***x* = 0.3**	***x* = 0.5**
$2P_r$ (μC/cm^2)	0.8	0.93	0.44	0.14
$2E_c$ (kV/cm)	6.64	11.22	6.78	11.3
d_{33} (pC/N)	11	11	8	7

4.3.2.6 Impedance Spectroscopy

Variation of Z′ with log of frequency for the Zr^{4+} substituted ceramics exhibited behaviour similar to that of BBT. The curves were found to merge around a frequency of 10 kHz and also displayed NTCR type of behaviour. Fig. 4.39 shows the variation of Z″ with log of frequency at various temperatures typically for x = 0.2. Similar behaviour of the plots were observed for the other Zr^{4+} based compositions as well (not shown here). Similar to BBT and La^{3+} substituted BBT ceramics, the peaks were found to be suppressed and shifted to higher frequency with increase in temperature. This again indicated the system to be non-Debye. The inset of Fig. 4.39 shows Z″ versus log of frequency plot at 390°C for x = 0.1, 0.2, 0.3 and 0.5. The asymmetric nature of the graphs for all the compositions confirmed the existence of spread of relaxation time.

The relaxation time for the systems was calculated using Eq. 4.16. Similar to the La^{3+} substituted BBT ceramics, τ decreases with increase in temperature. Fig. 4.40 shows the plot of log τ versus inverse of temperature for all the compositions. The linear fit to the slope of the curve based on Eq. 4.17 gives E_a, for the compositions and is listed in Table 4.12. E_a values increased with Zr^{4+} content and was maximum at x = 0.3 and was greater than BBT. This increase in E_a may be due to the decrease in the concentration of oxygen vacancies of the system. Oxygen vacancies are generated in a system to maintain the charge imbalance due to volatilization of Bi^{3+}. Also, the replacement of Ti^{4+} by Zr^{4+} reduced the probability of hopping between the Ti^{4+} and Ti^{3+} states. Hence, as the hopping probability between the two titanium states decreased in the present case, a decrease occurred in the concentration of charge carriers, thus increasing E_a. Though x = 0.3 possessed impure phases, E_a was found to be maximum. So it may be stated that the suppression of oxygen vacancy by Zr^{4+} substitution was dominant over the presence of impurity phases. However, for $x = 0.5$, E_a decreased. As already stated, this composition has secondary phase mainly Bi_2O_3. Bi_2O_3 is conducting in nature, thus it contributes in increasing the loss of the system, increasing E_a.

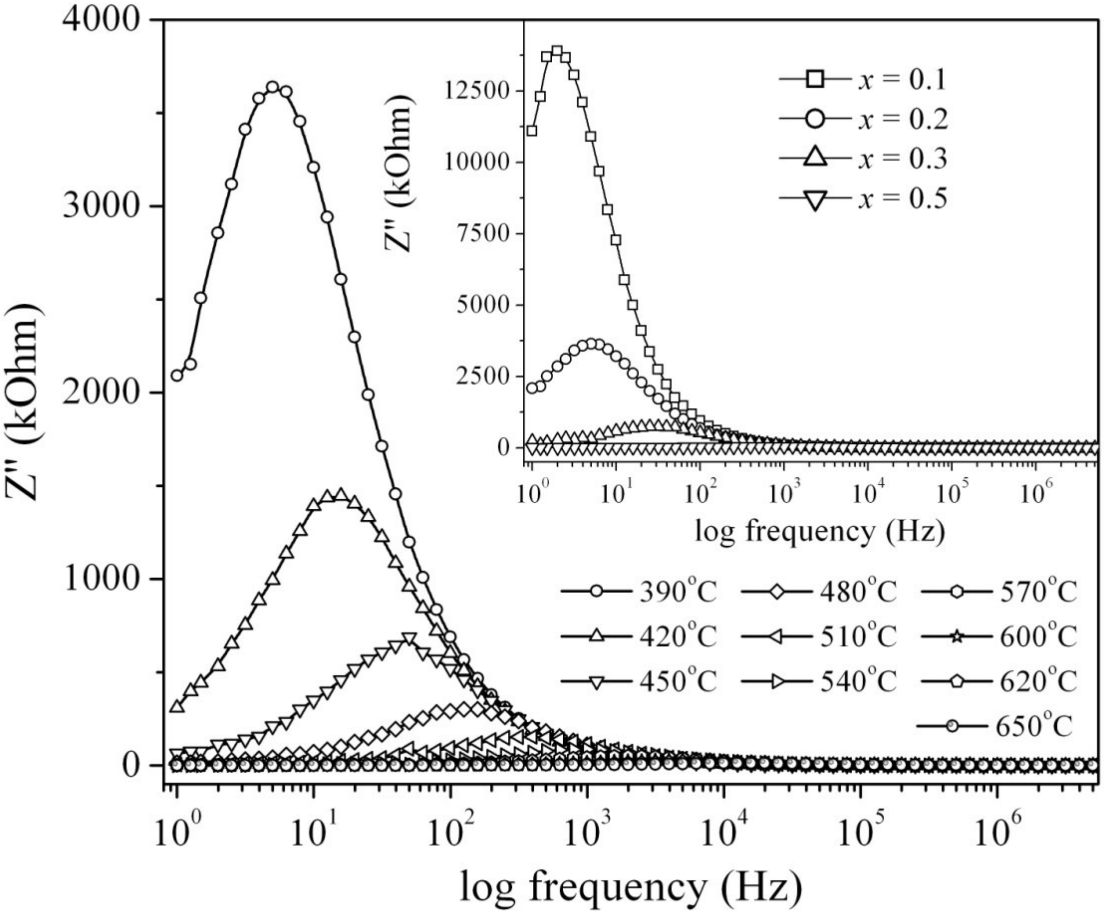

Fig.4.39. Variation of Z″ with frequency at various temperatures for $x = 0.2$. (Inset) Variation of Z″ with frequency at 390°C for $x = 0.1$, 0.2, 0.3 and 0.5 for $BaBi_4Ti_{4-x}Zr_xO_{15}$ ceramics.

Cole-Cole plots obtained from impedance spectra at a temperature of 550°C are shown in Fig. 4.41. The equivalent model used to fit these arcs was a parallel resistance and capacitor circuit, indicating the bulk contribution. Similar to the previous chapters, the total resistances and capacitances were calculated. Based on the above grain resistances and using Eq. 4.18, the *dc* conductivities of the samples at various temperatures were determined. Table 4.12 shows the value of *dc* conductivities at 550°C. Compositions with $x = 0.1$ and 0.2 exhibited the lowest order of *dc* conductivity. The *dc* conductivity for these two compositions was of the same order as that of La^{3+} substituted BBT ceramics. The *dc* conductivity increased with further increase in Zr^{4+} concentration. The presence of Bi_2O_3 secondary phase was detected in compositions 0.3 and 0.5. Bi_2O_3 is known to be a conducting material, and thus it may be said that it was responsible for the increase in conductivity of the 0.3 and 0.5 ceramics.

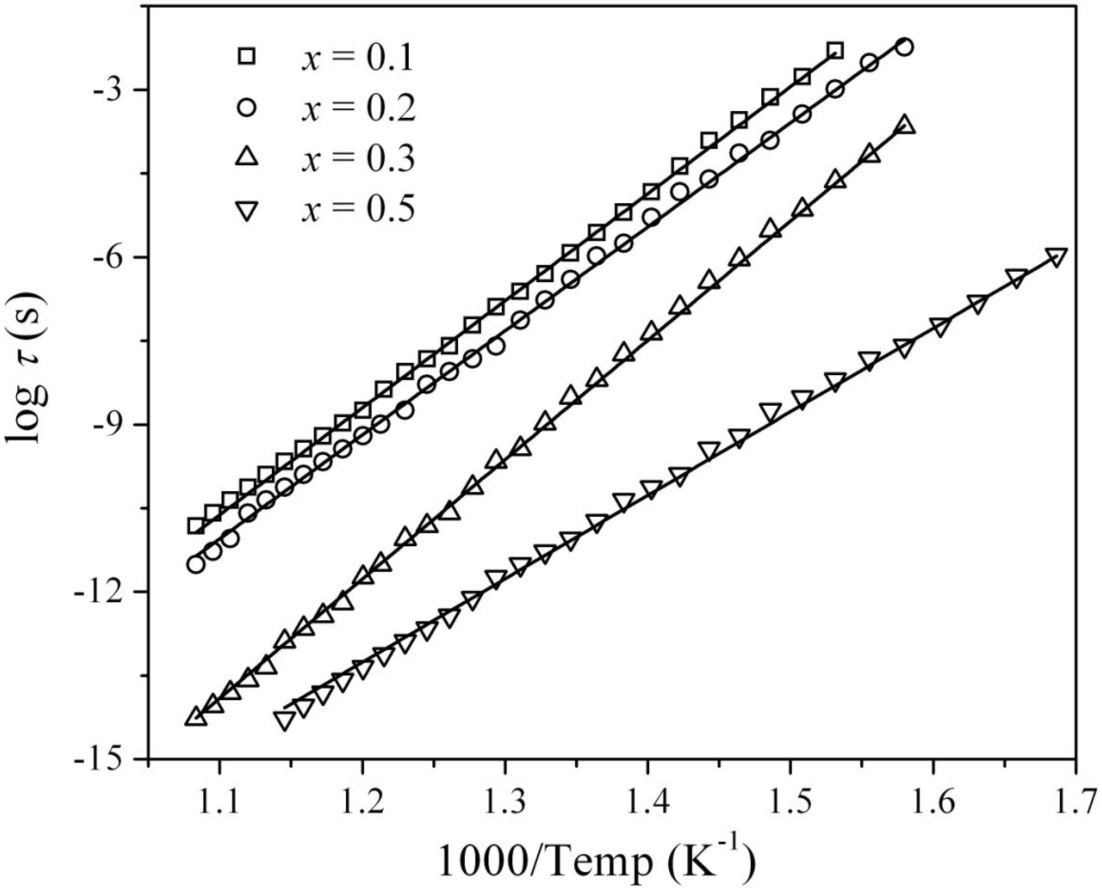

Fig.4.40. log (τ) versus 1000/T for different $BaBi_4Ti_{4-x}Zr_xO_{15}$ ($x = 0.1, 0.2, 0.3, 0.5$) ceramics.

The temperature dependence of the *dc* conductivity for bulk was plotted for all the compositions and the plots were found to obey the Arrhenius law. Based on the Arrhenius relation as stated in Eq. 4.19, E_{dc} values were calculated. The E_{dc} values are listed in Table 4.12. The E_{dc} values for $x = 0.1$, 0.2 and 0.3 were in the same range ~0.5 eV.

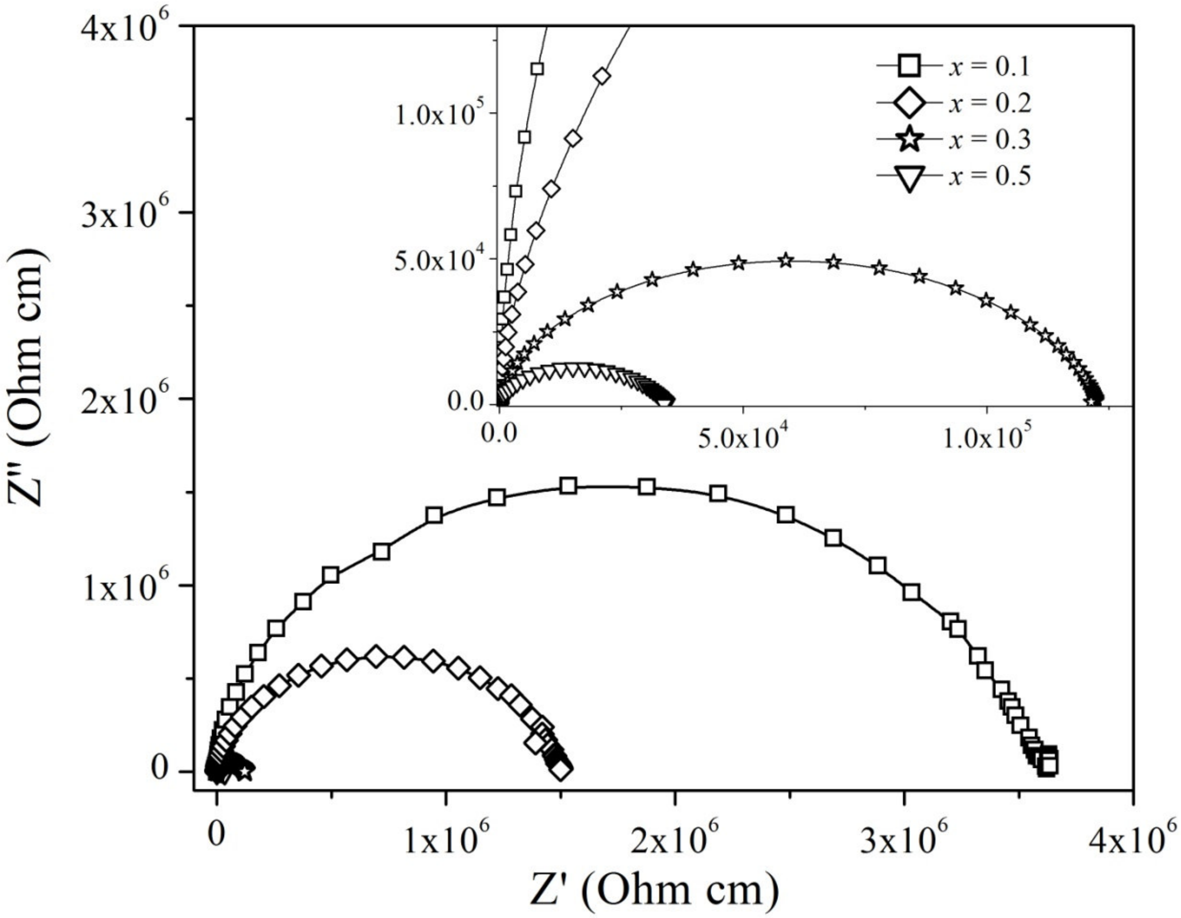

Fig.4.41. Complex impedance plot of $BaBi_4Ti_{4-x}Zr_xO_{15}$ (x = 0.1, 0.2, 0.3, 0.5) ceramics at 550°C.

Table 4.12. Activation energy from relaxation time (E_a), Activation energy (E_{dc}), *dc* conductivity at 550°C for different $BaBi_4Ti_{4-x}Zr_xO_{15}$ (x = 0.1, 0.2, 0.3, 0.5) ceramics.

Formula	***x* = 0.1**	***x* = 0.2**	***x* = 0.3**	***x* = 0.5**
E_a (eV)	1.65	1.61	1.843	1.28
σ_{dc} ($\Omega^{-1}cm^{-1}$)	2.86×10^{-7}	6.69×10^{-7}	8.11×10^{-6}	2.89×10^{-5}
E_{dc}(eV)	0.558	0.514	0.589	0.411

4.3.3 Conclusions

Zr^{4+} cation was substituted for Ti^{4+} cation in the four layer Aurivillius compound $BaBi_4Ti_4O_{15}$. XRD phase analysis revealed that the solid solubility limit for Zr^{4+} seemed to be $x = 0.2$ in $BaBi_4Ti_{(4-x)}Zr_xO_{15}$ because, ZrO_2 and Bi_2O_3 based impurity phases were detected for $x = 0.3$ and 0.5. It was interesting to note that the lattice parameters of $BaBi_4Ti_{(4-x)}Zr_xO_{15}$ increased up to $x = 0.5$ that is beyond the solid solubility limit. Increased lattice parameters may be attributed to the increased solubility of Zr^{4+} in presence of grain boundary ZrO_2 containing phases. This phenomena can be confirmed by the shifting of permittivity temperature peak towards room temperature by an amount of 30°C in the composition $x = 0.5$. Dielectric studies demonstrated that the relaxor nature decreased with substitution and vanishes at $x = 0.5$ composition. However, a significant broadening of permittivity-temperature peak was found at $x = 0.5$. The dielectric loss decreased upto $x = 0.2$ and increased for 0.3 and 0.5 compositions due to the presence of Bi_2O_3 phase. The E_a of the compositions for the oxygen vacancy as established from relaxation time was found to be maximum for $x = 0.3$.

4.4 Na^+ and La^{3+} substitution for Ba^{2+} in $BaBi_4Ti_4O_{15}$

4.4.1 Introduction

La^{3+} was substituted for *A*-site, i.e., Bi^{3+} in BBT. As stated in Section 4.2, the introduction of La^{3+} for Bi^{3+} improved the relaxor behaviour and also the *dc* conductivity. There is another *A*-site cation Ba^{2+} in the structure. The objective of the present study was to replace the *A*-site Ba^{2+} cation by La^{3+}. The excess charge thus introduced was compensated by replacing again Ba^{2+} by Na^+. The Curie temperature of $CaBi_2Nb_2O_9$ was reported to shift to higher temperature with Na^+ substitution [103], which is advantageous for its high temperature application.

$(Ba_{1-x}Na_{x/2}La_{x/2})Bi_4Ti_4O_{15}$ with $x = 0.25$, 0.5, 0.75 and 1.0 ceramics were synthesized via conventional solid-oxide route. The structural, relaxor characteristics, ferroelectric, piezoelectric and impedance spectroscopic behaviour of the ceramics were investigated.

4.4.2 Results and Discussion

4.4.2.1 Structural Analysis

Fig. 4.42 shows X-ray diffraction patterns of $(Ba_{1-x}Na_{x/2}La_{x/2})Bi_4Ti_4O_{15}$ ceramics with $x =$ 0.25, 0.5, 0.75 and 1.0. All the patterns matched with the parent BBT phase (JCPDS # 35-0757). No secondary phase was identified in the patterns, confirming complete solid solubility of Na^+ and La^{3+} in the structure. The inset figure shows the (119) peak for all the compositions. The peaks shifted towards higher 2θ with increase in Na^+ and La^{3+} substitution implying a decrease in *d*-spacing and lattice parameters. Though the peaks matched with standard BBT pattern, the relative peak intensities were different than standard pattern. This may be due to the preferred orientation of the grains.

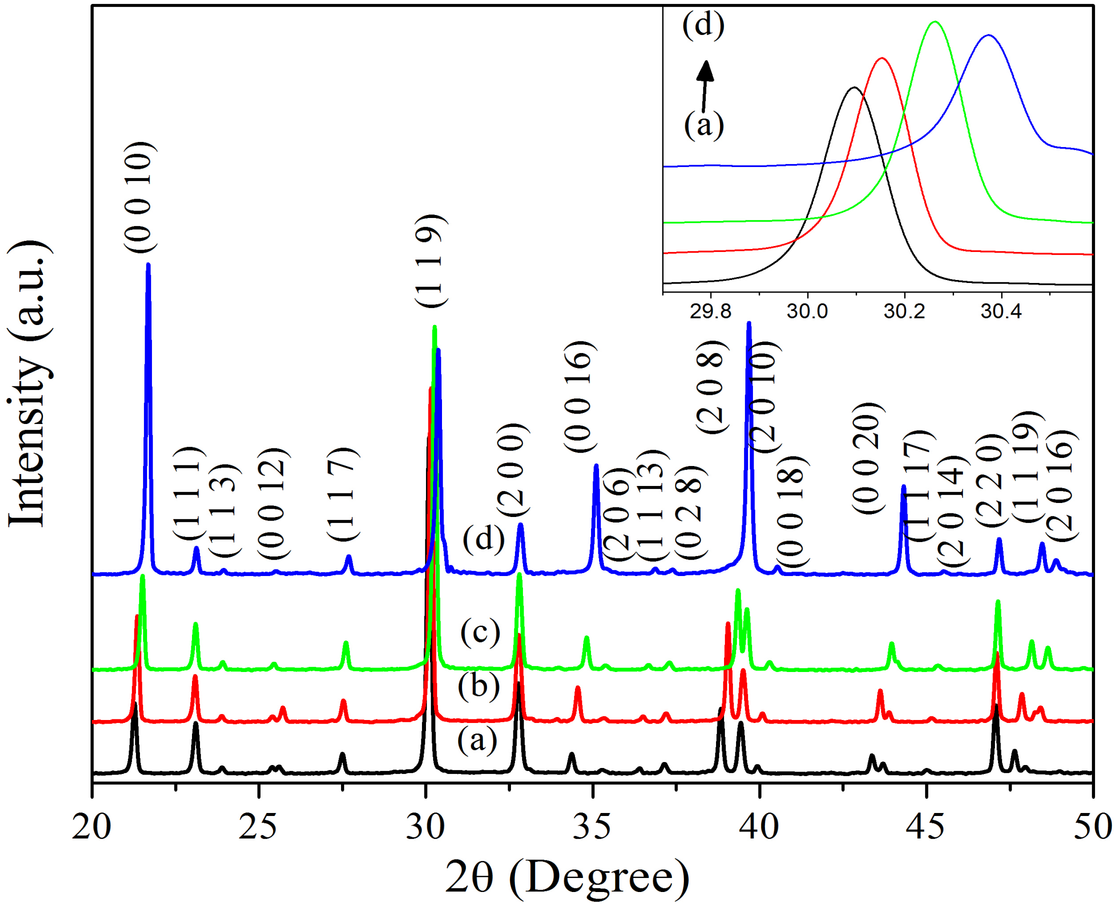

Fig.4.42. XRD patterns of $(Ba_{1-x}Na_{x/2}La_{x/2})Bi_4Ti_4O_{15}$ ceramics for x = (a) 0.25, (b) 0.5, (c) 0.75 and (d) 1.0.

To evaluate the effect of Na^+ and La^{3+} substitution on lattice parameters, full pattern Rietveld refinement was performed. The refined lattice parameters, *R*-factors, sigma, volume and orthorhombicity of the ceramics are given in Table 4.13. Composition with x = 1.0 was near to tetragonal. Fig. 4.43 shows variation of lattice parameters, volume and orthorhombicity as a function of substituent's concentration 'x'. It was observed that the lattice parameters and volume decreased with increase in Na^+ and La^{3+} concentration, indicating a contraction in the unit cell. The average ionic radii of Na^+ and La^{3+} is 1.38Å which was quite less as compared to the ionic radius of Ba^{2+}, 1.61Å [192]. Thus the substitution of Na^+ and La^{3+} for Ba^{2+} resulted in decrease of cell parameters. The orthorhombic distortion calculated from Eq.4.10 (Table 4.13) was also found to decrease. The contraction in the unit cell size may be the reason behind the decrease in orthorhombic distortion of the structure.

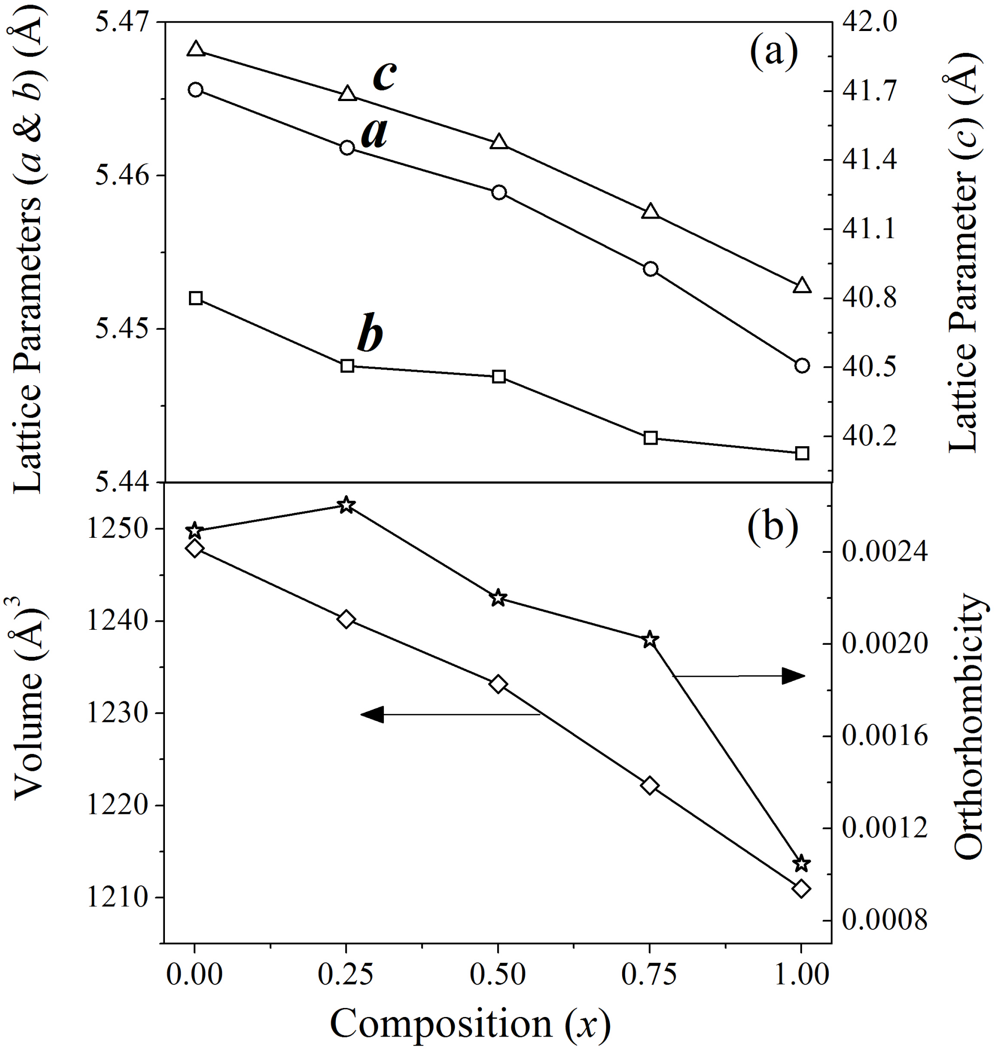

Fig.4.43. Variation of lattice parameters, volume and orthorhombicity as a function of composition (x) for $(Ba_{1-x}Na_{x/2}La_{x/2})Bi_4Ti_4O_{15}$ ($x = 0.25, 0.5, 0.75, 1.0$) ceramics.

4.4.2.2 Densification and Microstructural Characteristics

Table 4.14 lists sintering temperature and time of the substituted ceramics versus % theoretical density. More than 90% densification was obtained for all the ceramics at 1100°C/6h sintering temperature. Fig. 4.44 shows the micrograph of $(Ba_{1-x}Na_{x/2}La_{x/2})Bi_4Ti_4O_{15}$ ceramics. The grain size of the ceramics is listed in Table 4.14. The micrograph showed an increase in grain size with increase in substituent concentration. In addition to the increase in grain size a change in morphology of the grains was also observed. Na^+ and La^{3+} substituted ceramics showed more circular shape grains compared to typical plate like grains of BBT. Increased grain size indicated that Na^+ and La^{3+} substitution help in grain growth of the ceramics may be due to their smaller radius than Ba^{2+} and associated easy diffusion.

Table 4.13. Refined unit cell parameters (*a*, *b* and *c*), *R*-factors, Volume and Orthorhombicity of $(Ba_{1-x}Na_{x/2}La_{x/2})Bi_4Ti_4O_{15}$ (x = 0.25, 0.5, 0.75, 1.0) ceramics.

Formula	**x = 0.25**	**x = 0.50**	**x = 0.75**	**x = 1.0**
a (Å)	5.4618	5.4589	5.4539	5.4476
b (Å)	5.4476	5.4469	5.4429	5.4419
c (Å)	41.6831	41.4742	41.1717	40.8494
R_w (%)	4.35	10.0	9.75	12.17
R_b (%)	4.3	6.9	6.8	8.82
Sigma	1.91	3.4	3.3	4.38
Volume $(Å)^3$	1240	1233	1222	1210
Orthorhombicity	0.0026	0.0022	0.00202	0.00105

Table 4.14. %Theoretical density with Sintering temperature/time and Grain Size for $(Ba_{1-x}Na_{x/2}La_{x/2})Bi_4Ti_4O_{15}$ (x = 0.25, 0.5, 0.75, 1.0) ceramics.

Formula	**x = 0.25**	**x = 0.5**	**x = 0.75**	**x = 1.0**
Sintering temperature and time	**% Theoretical density**			
1100°C/4h	89	-	-	-
1100°C/6h	94	93	96	94
Grain Size (µm)				
Length	1.4	1.78	1.89	3.8
Breadth	0.9	1.23	1.3	1.5
Thickness	0.23	0.41	0.43	0.67

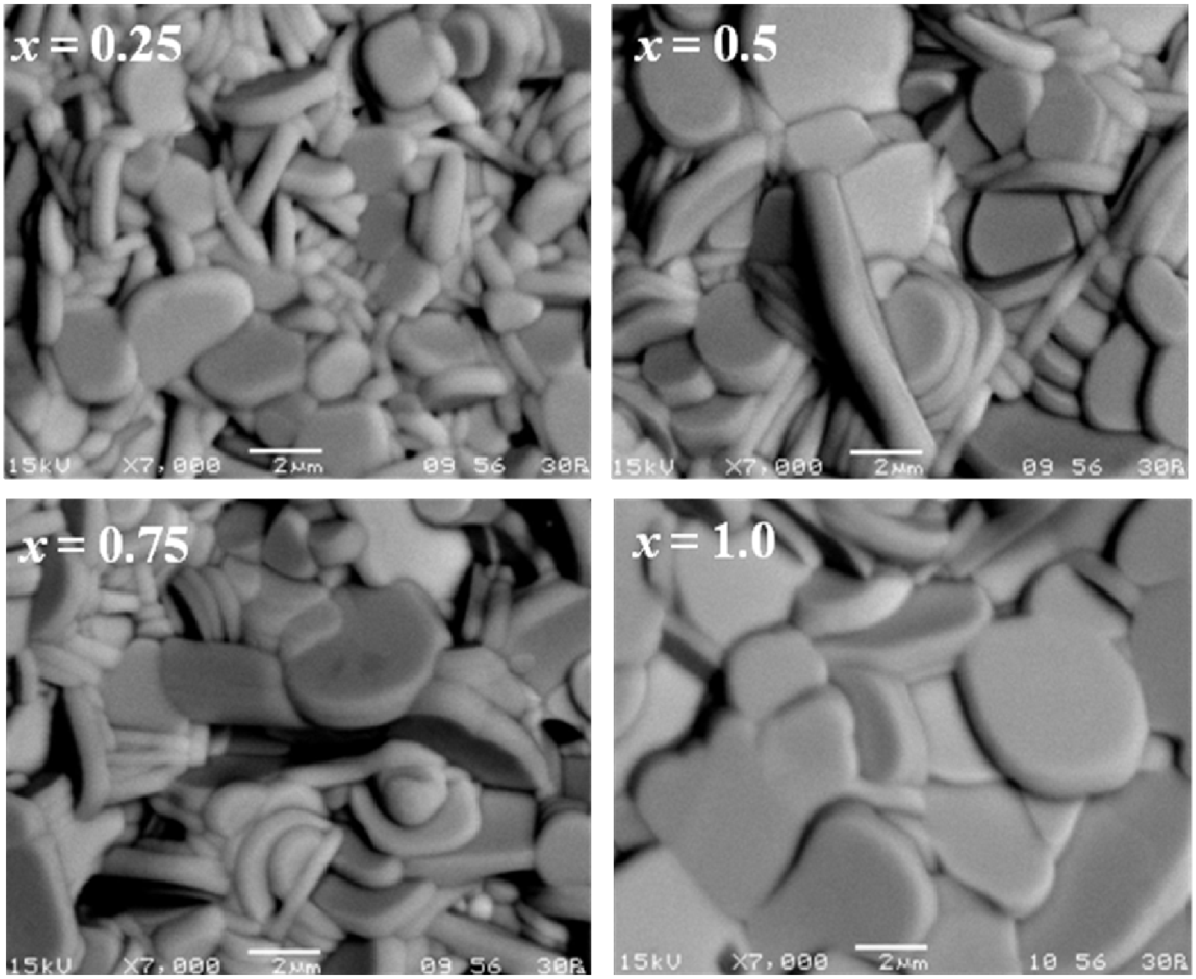

Fig.4.44. Scanning electron micrograph of $(Ba_{1-x}Na_{x/2}La_{x/2})Bi_4Ti_4O_{15}$ (x = 0.25, 0.5, 0.75, 1.0) ceramics.

4.4.2.3 Dielectric and Diffuse Phase Transition Behaviour

Fig. 4.45 shows temperature dependence of $(Ba_{1-x}Na_{x/2}La_{x/2})Bi_4Ti_4O_{15}$ at various frequencies. Table 4.15 lists ε_m', T_m, dielectric loss at room temperature (tan δ_{rm}) and at peak (tan δ_m) for the compositions. Composition with x = 0.25, showed the highest ε_m' among all compositions. The increased ε_m' may be due to the better sinterability of the samples and a slight increase in the orthorhombicity (0.0026) of the composition compared to pure BBT (0.0024). The increase in orthorhombicity implied an increase in the distortions which are prevalent in the orthorhombic symmetry, favoring the increase in ferroelectricity. However, ε_m' decreased with a further increase in x, i.e., for x = 0.5, 0.75 and 1.0 compositions. This decrease may be a consequence of the decrease in cell parameters which decreased the orthorhombicity of the unit cell. The decrease in the orthorhombicity caused the decrease in ferroelectricity. It is known that ferroelectricity of BLSF arises due to their distortions such as, tilting and rotation from *a*- and *c*-axes and a displacement of the *A*-site cation in the orthorhombic symmetry. A reduction in the orthorhombicity may lead to a decrease in the above stated distortions. As a consequence the ferroelectricity of the ceramics decreased.

The dielectric loss at room temperature decreased with increase in Na^+ and La^{3+} substitution. Compared to BBT, the dielectric loss at peak was also low for $x = 0.25$. This decrease in loss may be due to decrease in defects in the structure, which may be due to the following two reasons. It is well known that Bi_2O_2 layer acts as an insulating layer in BLSF. So, as Ba^{2+} gets replaced from the system, the loss was decreased due to the decrease in cation disorder between the Ba^{2+} and Bi^{3+} site in the Bi_2O_2 layer enhancing its insulating property and thus decreasing the loss of the ceramics. Secondly, the electro-negativities of Ba^{2+} (0.89), Na^+ (0.93) and La^{3+} (1.1) ions show that the Na-O and La-O have stronger bond strength than Ba-O bond. The presence of these strong bonds stabilized the perovskite structure to a greater extent, decreasing the loss.

T_m of the compositions was observed to increase with increase in substitution. T_m increased due to the decrease in ionic radii of *A*-site [14]. This increase in T_m can also be explained on the basis of tolerance factor *t*. The tolerance factors of the compositions can be calculated using Eq. 4.23. The *t* of the compositions is listed in Table 4.15. It was observed that *t* decreased from 0.982 to 0.961 with increase in substitution. Decrease in *t* implies an increase in the Curie temperature [191].

It was observed from Fig.4.45 that the dielectric dispersion with frequency decreased with increase in substitution, thus displaying a relaxor to ferroelectric like transition. The frequency dispersion (ΔT_m) of relaxor, as explained in Chapter 4.1, was evaluated by Eq.4.11. The ΔT_m values for different composition are listed in Table 4.15. ΔT_m decreased to 10°C for $x = 0.25$ and finally to 0°C for $x = 0.75$, indicating a decrease in the relaxor behaviour and transition to normal ferroelectrics.

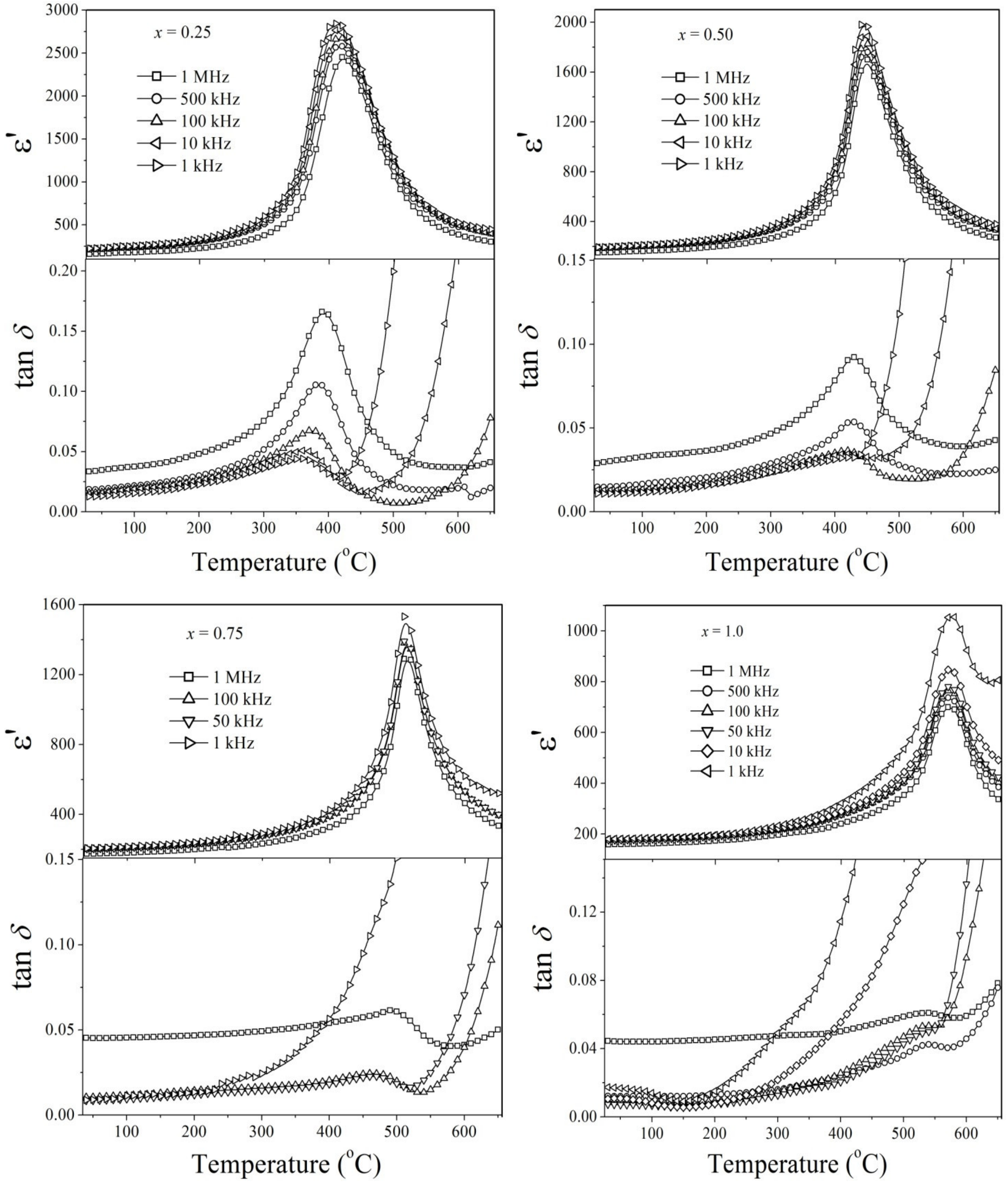

Fig.4.45. Temperature dependence of ε_m' and tan δ of $(Ba_{1-x}Na_{x/2}La_{x/2})Bi_4Ti_4O_{15}$ (x = 0.25, 0.5, 0.75, 1.0) ceramics at various frequencies.

The diffusivity parameter (γ) was evaluated from modified Curie-Weiss law [175] using Eq. 4.14. Table 4.15 lists the γ values for different compositions, and was observed to decrease from 1.7 (for $x = 0.75$) to 1.16 (for $x = 1.0$). This decrease of γ indicated them to transform to a normal ferroelectric. So the relaxor behaviour decreased with increase in substitution.

The relaxor behaviour in BBT, as discussed earlier is a consequence of the cation re-distribution among the Ba^{2+} and Bi^{3+} crystallographic sites. The cation disorder occurs in order to release the excess strain created in the structure due to the large ionic radii of Ba^{2+}. For the present ceramics, smaller average ionic radii Na^{+} and La^{3+} ions substitute Ba^{2+}, which may lead to a decrease in the structural strain, thus decreasing the cation disorder in Bi_2O_3 layer. This may be the reason behind the decrease in relaxor behaviour of the ceramics with increase in Na+ and La3+ ions substitution.

4.4.2.4 Polarization Hysteresis Characteristics and Piezoelectric Properties

The ferroelectric hysteresis loop for $x = 0.25$ composition of (Ba1-xNax/2Lax/2)Bi4Ti4O15 ceramics is shown in Fig.4.46. The ferroelectric hysteresis loop was obtained under a maximum applied electric field of 20 kV/cm, but was far from saturation. The experimental constraints (such as room temperature measurements, low electric field) and the high Curie temperature hindered the loop formation.

Composition with $x = 0.25$ shows d_{33} of 11 pC/N similar to BBT. d_{33} coefficient decreased to 6, 4 and 7 for $x = 0.5$, 0.75 and 1.0 compositions, respectively. As stated earlier, the decreased size of the unit cell decreased the polarizability, thus reducing the d_{33} coefficient.

Table 4.15. Dielectric loss at room temperature (tan δ_{rm}), Maximum relative permittivity (ε_m'), Dielectric loss at peak (tan δ_m), Maximum permittivity temperature (T_m), and Degree of diffuseness (γ) at 100 kHz, degree of relaxation (ΔT_m), tolerance factor (t) for $(Ba_{1-x}Na_{x/2}La_{x/2})Bi_4Ti_4O_{15}$ (x = 0.25, 0.5, 0.75, 1.0) ceramics.

Formula	***x* = 0.25**	***x* = 0.5**	***x* = 0.75**	***x* = 1.0**
tan δ_{rm}	0.015	0.007	0.01	0.009
tan δ_m	0.066	0.034	0.024	0.053
ε_m'	2672	1825	1381	894
T_m	420	450	510	570
t	0.9817	0.9748	0.9679	0.961
ΔT_m (°C)	10	10	0	0
γ	1.71(1)	1.38(1)	1.58(3)	1.16(5)

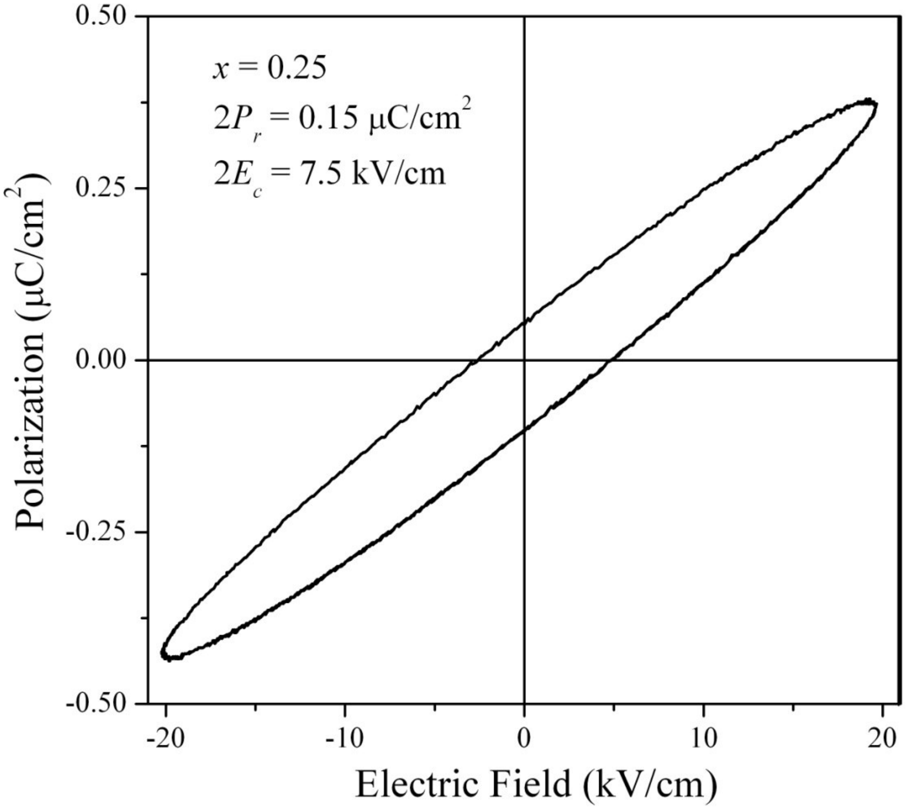

Fig.4.46. Plot of ferroelectric hysteresis loop measured at room temperature for $(Ba_{1-x}Na_{x/2}La_{x/2})Bi_4Ti_4O_{15}$ (x = 0.25).

4.4.2.5 Impedance spectroscopy

Fig. 4.47 inset shows the variation of Z″ with frequency for $(Ba_{1-x}Na_{x/2}La_{x/2})Bi_4Ti_4O_{15}$ (x = 0.25, 0.5, 0.75, 1.0) compositions at 400°C. The main figure shows the plot of Z′′ versus frequency at various temperatures for composition x = 0.25. The figure shows that Z′′ peaks were shifted to higher frequency with increase in temperature accompanied by suppression in its peak value. Similar nature of Z′′ plots were also observed for the other compositions.

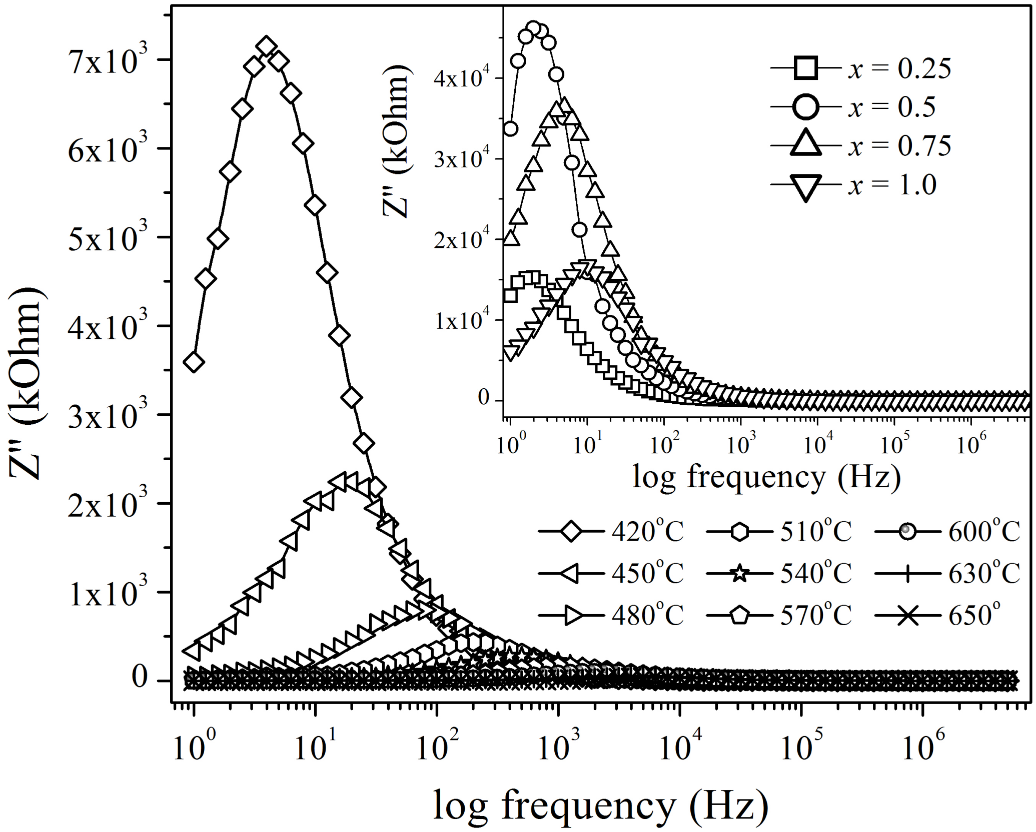

Fig.4.47. Variation of Z″ with frequency and temperature for x=0.25 composition of $(Ba_{1-x}Na_{x/2}La_{x/2})Bi_4Ti_4O_{15}$ and for x = 0.25, 0.5, 0.75, 1.0 ceramics at 400°C (Inset).

The increase in resistivity of the system can also be evaluated on the basis of activation energy derived from the relaxation time. The relaxation time of the systems can be calculated using Eq. 4.16. The value of τ decreased with increase in temperature, indicating an increase in conductivity of the system with temperature. Fig. 4.48 shows the plot of log τ versus 1000/T for all the samples. A linear fit was obtained to the curve based on Eq. 4.17. The slopes of the curves give E_a values for the compositions. E_a values of the compositions increased with increase in the concentration of Na^+ and La^{3+} ions in the system. This result also supported the decrease in the loss of the system may be due to decrease in Bi_2O_3 layer ionic disorder. For all the compositions two different regions were visible depending on the Curie temperature. Similar observation has been made by other researchers in these BLSF materials [106]. The change in slope above Curie temperature depicts a change in activation energy E_a. This may suggest different conduction mechanisms are in play in different temperature zones. In the low temperature region, the extrinsic defects are responsible for the conduction mechanism. While in the high temperature zone, the thermally activated oxygen vacancies are responsible for the conduction mechanism.

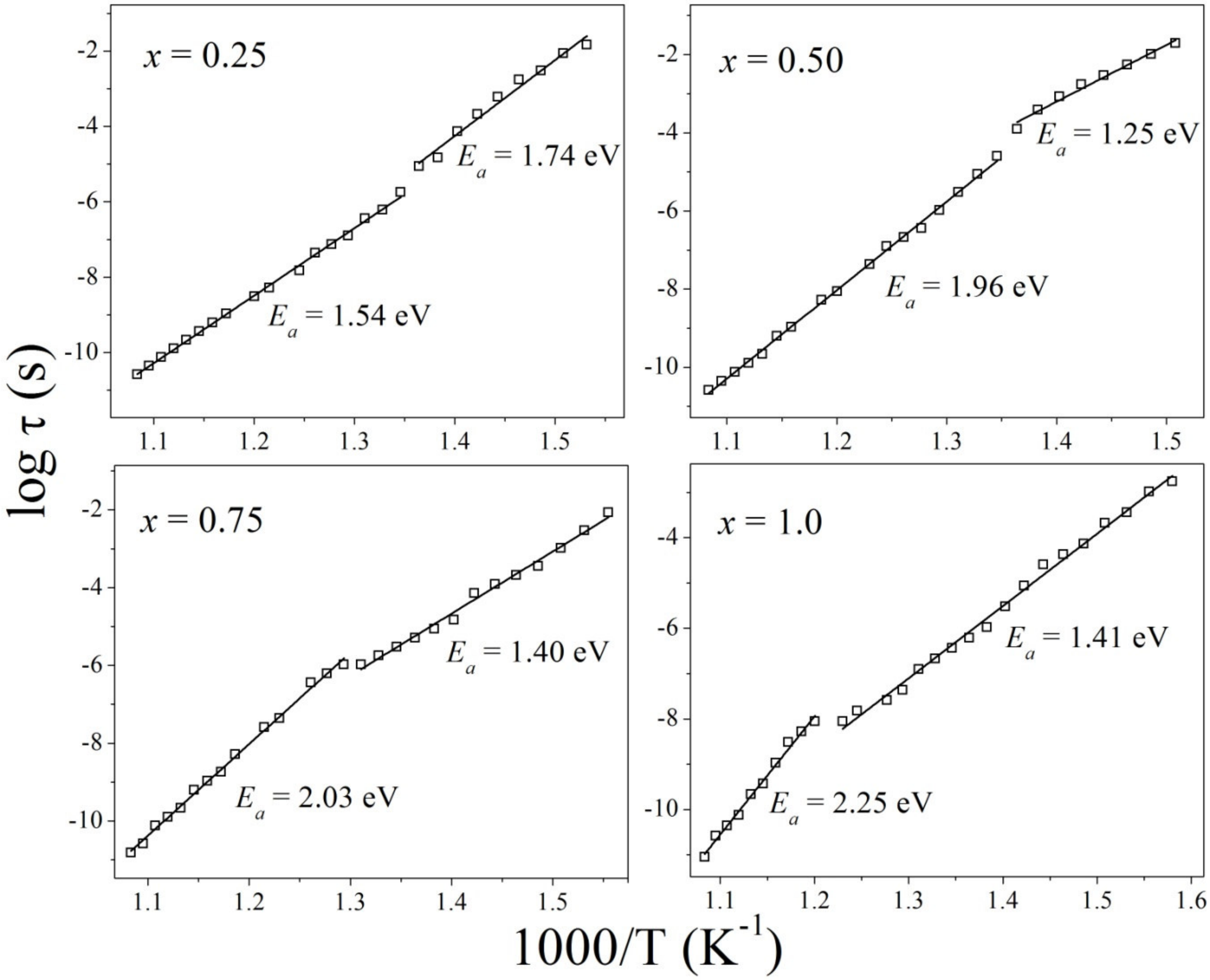

Fig.4.48. log (τ) versus 1000/T for $(Ba_{1-x}Na_{x/2}La_{x/2})Bi_4Ti_4O_{15}$ ($x = 0.25, 0.5, 0.75, 1.0$) ceramics.

Fig. 4.49 shows the complex impedance plot of the ceramics at 550^{o}C. The plot shows a single semicircular arc attributed to the contribution mainly from the bulk. An equivalent circuit comprising of parallel resistance and capacitance were used to fit these arcs using ZView software. To determine the R_{tot} and C parameters, similar procedure was adopted as stated in the previous chapters. The R_{tot} and C were calculated and are summarized in Table 4.16 for 550^{o}C. Using Eq. 4.18, *dc* conductivities of the samples at various temperatures were calculated based on R_{tot}. *dc* conductivities (σ_{dc}) of the ceramics at 550^{o}C are listed in Table 4.16. Unlike the other systems, these samples show their *dc* conductivities to be in the order 10^{-7}.

Based on the Arrhenius relation in Eq. 4.19, E_{dc} were calculated from the log of *dc* conductivity versus inverse of temperature plot. For all the samples, two regions were visible around T_m. The E_{dc} values (high and low temperatures) are given in Table 4.16. The activation energy obtained shows a similar range of values for different compositions. However, compared to the previous systems, the E_{dc} values were high.

Table 4.16. Total resistance (R_{tot}), Capacitance (C) and *dc* conductivity at 550^{o}C, Activation energy (E_{dc}) at high and low temperatures for different $(Ba_{1-x}Na_{x/2}La_{x/2})Bi_4Ti_4O_{15}$ (x = 0.25, 0.5, 0.75, 1.0) ceramics.

Formula	***x* = 0.25**	***x* = 0.5**	***x* = 0.75**	***x* = 1.0**
R_{tot} (Ω)	4.57×10^{5}	8.56×10^{5}	5.95×10^{5}	4.52×10^{5}
C (Farad)	5.39×10^{-10}	5.17×10^{-10}	7.49×10^{-10}	7.44×10^{-10}
σ_{dc} ($\Omega^{-1}cm^{-1}$)	2.56×10^{-7}	1.39×10^{-7}	2.0×10^{-7}	2.52×10^{-7}
E_{dc} (eV) (high temperature)	0.492 ± 0.01	0.617 ± 0.02	0.594 ± 0.01	0.664 ± 0.03
E_{dc} (eV) (low temperature)	0.644 ± 0.02	0.606 ± 0.04	0.694 ± 0.01	0.545 ± 0.02

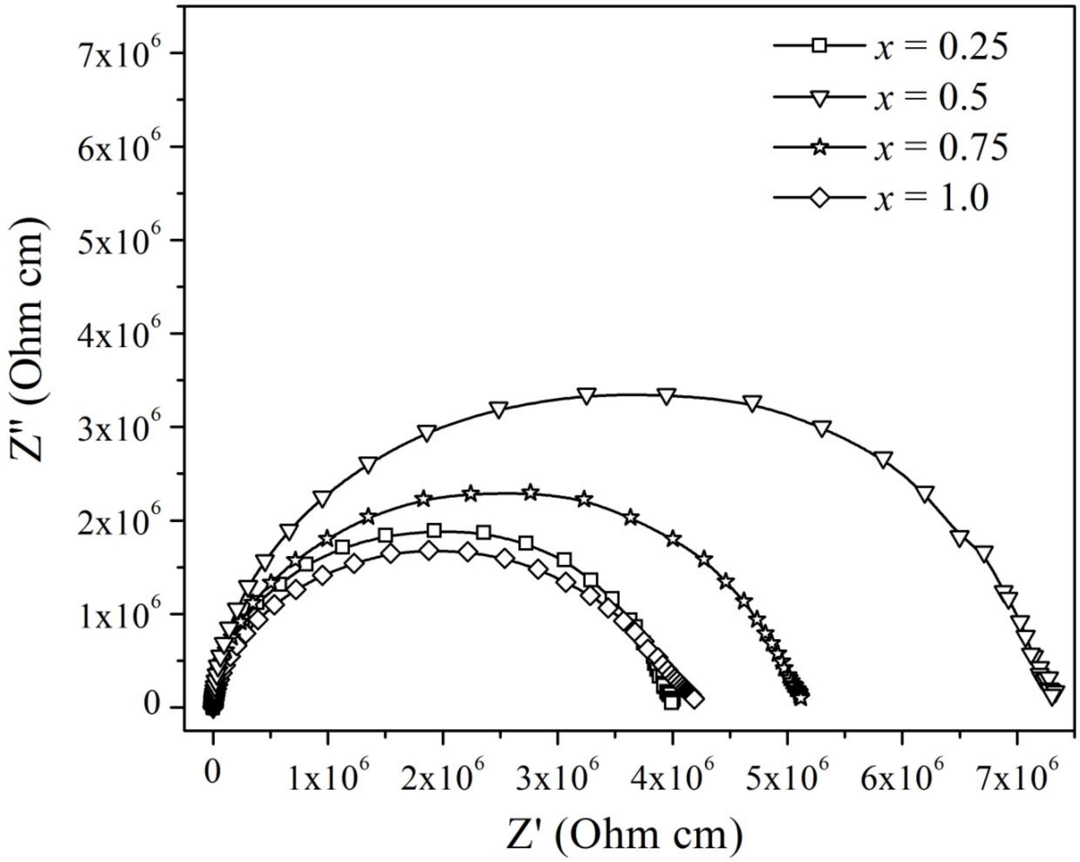

Fig.4.49. Complex impedance plot of $(Ba_{1-x}Na_{x/2}La_{x/2})Bi_4Ti_4O_{15}$ (x = 0.25, 0.5, 0.75, 1.0) ceramics at 550°C.

4.4.3 Conclusions

In summary, Na^+ and La^{3+} were substituted for Ba^{2+} in the Aurivillius compound $BaBi_4Ti_4O_{15}$. The ceramics obtained were single phase indicating complete solid solubility. XRD analysis revealed that the lattice parameters decreased with increase in substitution due to the introduction of smaller ionic radii Na^+ and La^{3+} cation in place of Ba^{2+}. Orthorhombicity decrease with increase in substitution and the $x = 1.0$ composition was near to tetragonal system. The grain size of the ceramics increased with increasing substitution. T_m increased due to the decrease in tolerance factor with the substitution. These substitutions provide a low loss BBT, although the relaxor behaviour decreased. This material could be applicable for high frequency application where low loss is required.

4.5 Nb^{5+} and Al^{3+} substitution for Ti^{4+} in $BaBi_4Ti_4O_{15}$

4.5.1 Introduction

Substitution of Nb^{5+} for Ti^{4+} in BLSF was found to improve the ferroelectric, piezoelectric properties and resistivity of the ceramics [7, 150, 94]. For the present investigation, Nb^{5+} is substituted for Ti^{4+} and the charge has been compensated by Al^{3+} substitution for Ti^{4+}. It has been reported that Al^{3+} has some solid solubility in BLSF compound [194]. The co-substitution at *A* and *B*-site significantly increased the remnant polarization and lowered the coercive field in many BLSFs [197, 198]. However, no detailed reports are available about the effect of Nb^{5+} and Al^{3+} donor-acceptor co-substitution at *B*-site.

$BaBi_4Ti_{4-x}(Nb_{x/2}Al_{x/2})O_{15}$ ceramics with x = 0.1, 0.2 and 0.3 were synthesized via modified chemical route. The structural, microstructural, relaxor characteristics, ferroelectric, piezoelectric properties and impedance spectroscopic study of the ceramics was investigated. This chapter describes the results and discussion of the investigations.

4.5.2 Results and Discussion

4.5.2.1 Solid Solubility Limit and Structural Analysis

Fig. 4.50 shows the X-ray diffraction patterns of calcined $BaBi_4Ti_{4-x}(Nb_{x/2}Al_{x/2})O_{15}$ ceramics. The patterns of all the compositions matched with the parent BBT phase (JCPDS # 35-0757). However, the composition with $x = 0.3$ shows the presence of small amount of secondary phase. These phases were identified to be of Bi_2O_3 based composition. This indicated the solid solubility limit of Nb^{5+} and Al^{3+} substitution for Ti^{4+} was ~0.2. This result supported the previous report (Section 4.3) of solid solubility limit of Zr^{4+} (of ~0.2) for Ti^{4+}. Though in the case of Zr^{4+} its larger ionic radii was a restriction to its further substitution, in the present case the charge of Al^{3+} cation can be the deciding factor for this limit. As the *B*-site of BLSFs is a highly charged cationic site, the substitution of lower charge trivalent Al^{3+} cation could not be made to a larger extent [14].

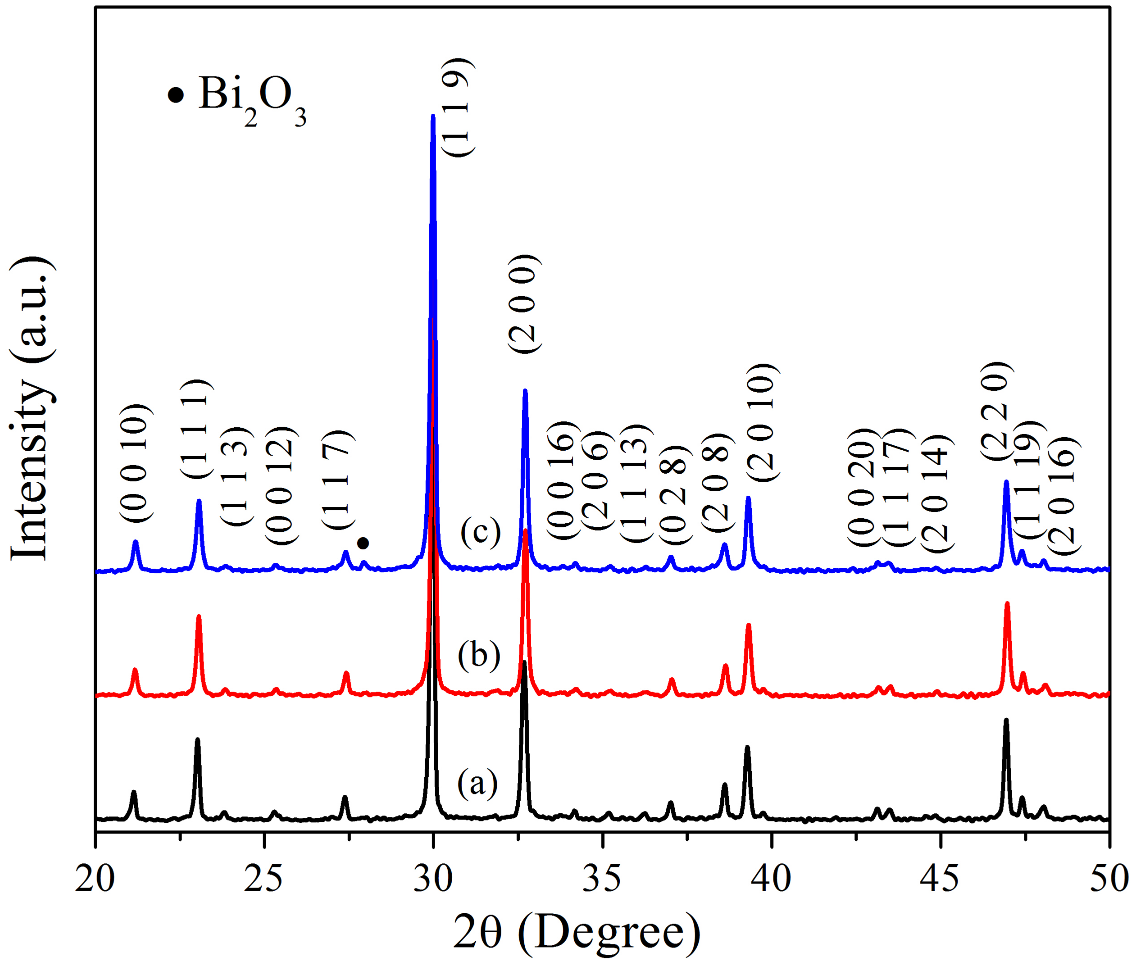

Fig.4.50. XRD patterns of $BaBi_4Ti_{4-x}(Nb_{x/2}Al_{x/2})O_{15}$ (x = 0.1, 0.2, 0.3) ceramics.

Full pattern Rietveld refinement was performed. Fig. 4.51 shows the experimental and calculated refined patterns of all compositions. The refined lattice parameters, R-factors, sigma, volume and orthorhombicity of the ceramics are given in Table 4.17. The lattice parameters *'a'*, '*b'* and '*c*' did not show a significant change for x = 0.1 and 0.2. This highlighted the fact that the substitution of Nb^{5+} and Al^{3+} for Ti^{4+} did not affect the structure to a greater extent. One of the reasons may be the small difference in their ionic radii. The ionic radii of Ti^{4+} being 0.605 Å and average ionic radii of Nb^{5+} and Al^{3+} is 0.57 Å [192]. This was also visible from the volume of the unit cell. The volume was same for x = 0.1 and 0.2. This result was similar to that obtained in case of Zr^{4+} substitution for Ti^{4+} as reported in Chapter 4.3.

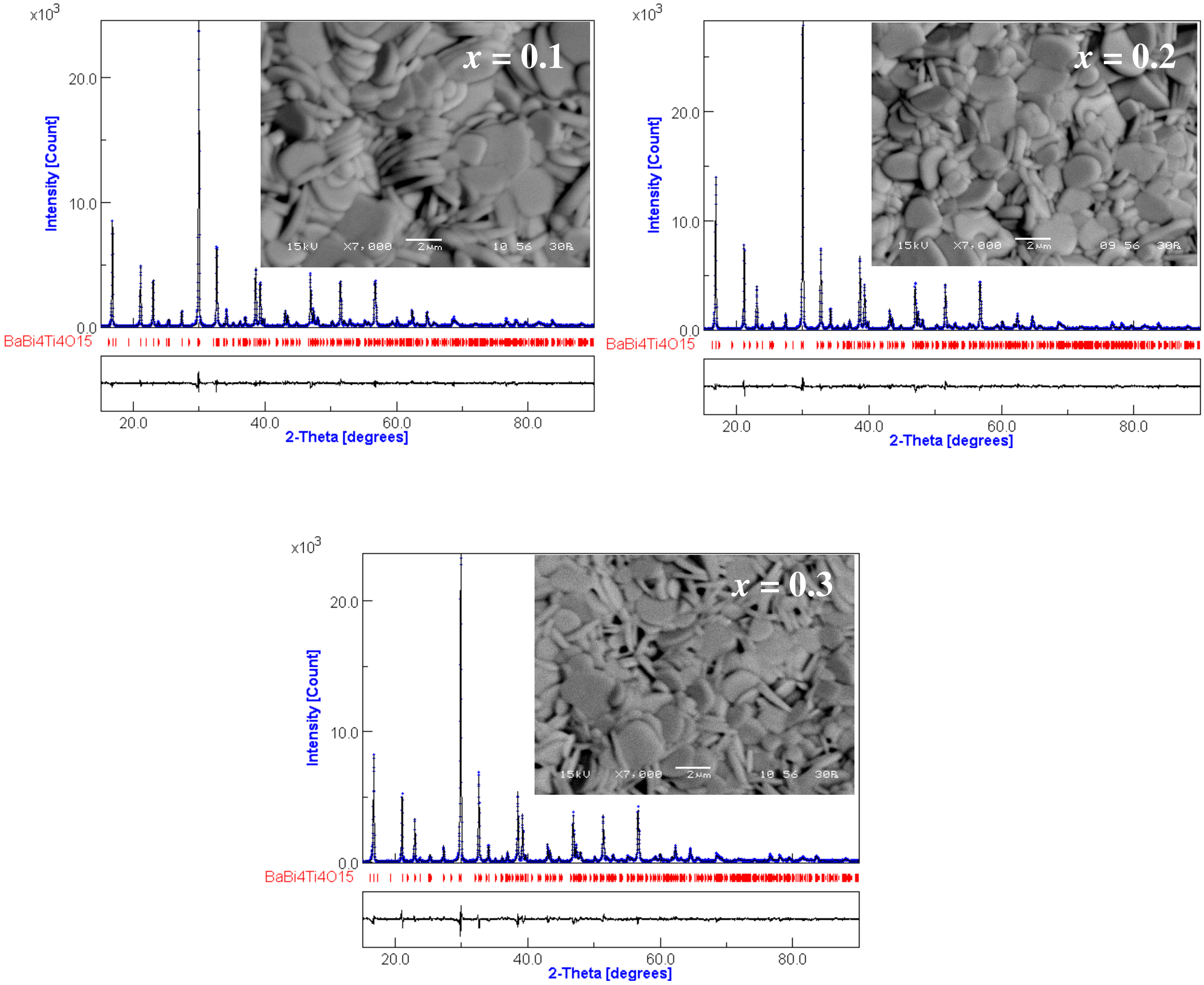

Fig.4.51. Rietveld output plot showing the experimental and calculated patterns of $BaBi_4Ti_{4-x}(Nb_{x/2}Al_{x/2})O_{15}$ (x = 0.1, 0.2, 0.3) ceramics.. The inset of the figure shows the micrographs of the corresponding of the samples.

Table 4.17. Refined unit cell parameters (*a*, *b*, *c*), *R*-factors, Volume and Orthorhombicity of $BaBi_4Ti_{4-x}(Nb_{x/2}Al_{x/2})O_{15}$ ($x = 0.1, 0.2, 0.3$) ceramics.

Formula	**x = 0.1**	**x = 0.2**	**x = 0.3**
Cell parameters			
a (Å)	5.4709	5.4681	5.4691
b (Å)	5.4604	5.4621	5.4652
c (Å)	41.9047	41.9051	41.9309
Rw (%)	4.8	4.9	6.3
Rb (%)	3.8	3.8	4.7
Sigma	1.55	1.7	1.98
Volume $(Å)^3$	1251.83	1251.59	1253.30
Orthorhombicity	0.0019	0.0011	7.13E-4

Table 4.18 lists %theoritical density as a function of sintering temperature and time. The sintering temperature increased with increase in substituent concentration to achieve %theoritical density >90%. The inset of Fig. 4.51 shows the scanning electron micrograph of the respective ceramics. The micrographs show the grain size remained almost the same (Table 4.18). However, a slight change was observed in the morphology of the grains which transformed to round shape from plate like.

Table 4.18. %Theoritical density with Sintering temperature/time and Grain Size for $BaBi_4Ti_{4-x}(Nb_{x/2}Al_{x/2})O_{15}$ ($x = 0.1, 0.2, 0.3$) ceramics.

Formula	***x* = 0.1**	***x* = 0.2**	***x* = 0.3**
Sintering temperature and time	**% Theoritical density**		
1100°C/4h	96	85	
1110°C/4h		94	86
1120°C/4h			96
Grain Size (μm)			
Length	1.2	1.24	1.22
Breadth	0.56	0.52	0.6
Thickness	0.13	0.11	0.12

4.5.2.2 Dielectric and Diffuse Phase Transition Behaviour

Fig. 4.52 shows the temperature dependence of relative permittivity (ε') and dielectric loss ($\tan \delta$) at various frequencies for $BaBi_4Ti_{4-x}(Nb_{x/2}Al_{x/2})O_{15}$ ceramics. A dielectric dispersion with frequency and diffuse phase transition was visible from these plots, displaying a relaxor like behaviour. The room temperature permittivity (ε_{rm}), room temperature dielectric loss ($\tan \delta_{rm}$) maximum relative permittivity (ε_m'), maximum dielectric loss ($\tan \delta_m$) and maximum permittivity temperature (T_m) at 100 kHz are tabulated in Table 4.19.

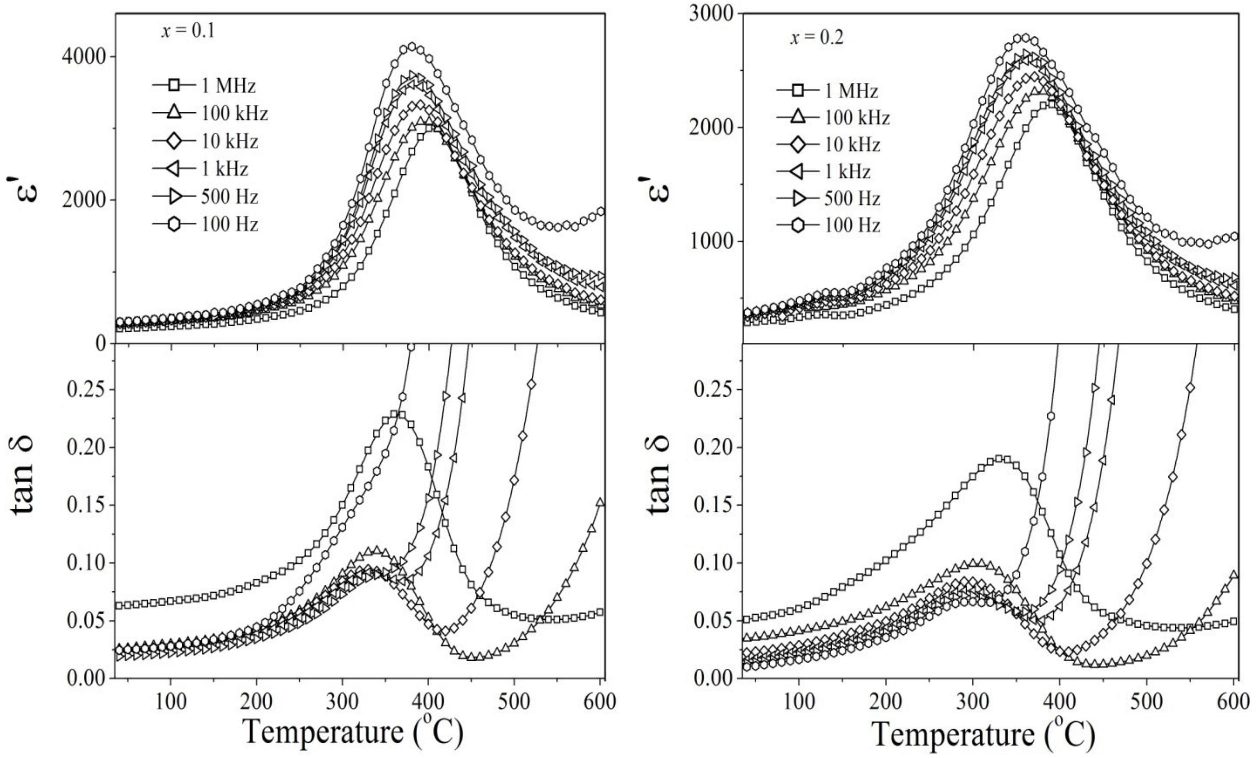

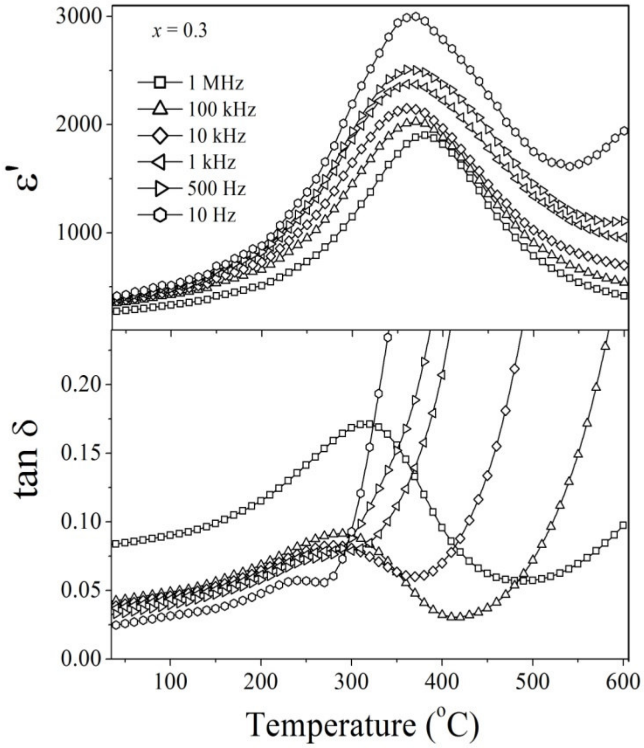

Fig.4.52. Temperature dependence of ε_m' and tan δ of $BaBi_4Ti_{4-x}(Nb_{x/2}Al_{x/2})O_{15}$ ($x = 0.1, 0.2, 0.3$) ceramics at various frequencies.

ε_{rm} of all the substituted ceramics were high compared to that of BBT and was highest for $x = 0.2$, almost double than ε_{rm} of BBT. tan δ_{rm} of $x = 0.1$ was almost same as that of BBT. It was found to increase slightly for $x = 0.2$ and 0.3. In addition to these results, a shifting of the T_m toward room temperature was also observed. This explains that the increase of ε_{rm} may be due to the shifting of the T_m towards room temperature to 380 and 360°C for $x = 0.1$ and 0.2, respectively. A similar behaviour for ε_m' was also observed. That is, ε_m' was highest for $x = 0.1$. Compared to BBT, ε_m' was quite high for $x = 0.1$ and 0.2. This increase in ε_m' may be due to introduction of more ferroelectrically active Nb^{5+} than Ti^{4+}. The decrease in ε_m' for $x = 0.3$ may be due to the combined effect of decrease in orthorhombicity (Table 4.17) and presence of secondary phase in the system. However, tan δ_m for all the compositions was less as compared to tan δ_m of BBT. Decrease in loss of these ceramics may be due to decrease in defects in the structure. This decrease may be due to the difference in the electronegativities of the cations. The electronegativity of Nb^{5+} and Al^{3+} is ~1.61 compared to that of ~1.53 for Ti^{4+}. These values of electronegativities convey that the Nb-O and Al-O will possess higher bond strength than that of Ti-O. Also, as the concentration of Ti^{4+} ion decreases with increase in substituent's concentration, the probability of polaron hopping between the Ti^{4+} and Ti^{3+} states decreases, thus contributing to decrease in loss of the ceramics. Similar results were obtained for $(Ba_{1-x}Na_{x/2}La_{x/2})Bi_4Ti_4O_{15}$ ceramics due to increase in electronegativity of the substituting cations.

The decrease in T_m was due to the increase in tolerance factor (t) (Eq. 4.23) listed in Table 4.19. The tolerance factor increased with increase in the substituent's concentration. An increase in tolerance factor implied a decrease in structural distortion and hence a decrease in T_m, which also supported the decrease in orthorhombicity of the structure.

The relative permittivity versus temperature plots for all the compositions show a broad peak (Fig. 4.52). This peak broadening may be quantified by the parameter δ. The δ values of the compositions were calculated by fitting permittivity-temperature data to Eq. 4.12 and summarized in Table 4.19. δ values were observed to increase with increase in Nb^{5+} and Al^{3+} amount. These values of δ were high compared to those of BBT. It has already been stated that compositional fluctuation and disorder in crystallographic sites are responsible for the broad permittivity versus temperature peak. So it may be assumed that the introduction of Nb^{5+} and Al^{3+} adds to the inhomogeneity and compositional fluctuation of the system. This created local Curie points in the material, increasing the broadness of the peak.

Fig. 4.52 shows frequency dispersion for all the three ceramics and the amount of frequency dispersion can be established from the following parameters.

The parameter ΔT_m representing the frequency dispersion for relaxor, was calculated using Eq. 4.11. The value of ΔT_m is given in Table 4.19. ΔT_m was same 20°C for all the compositions. However, a slight change in ΔT_m was observed for $x = 0.2$. This indicates the substitution did not affect the relaxor behaviour.

The diffusivity parameter (γ) was quantified from modified Curie-Weiss law (Eq.4.14). Fig. 4.53 shows the plot of log $(1/\varepsilon' - 1/\varepsilon_m')$ versus log $(T - T_m)$ for all the compositions. The γ value as determined from the slope of the graph is given in the figure. γ remained almost the same for all. So this parameter also highlights the fact that there was no major change in the relaxor behaviour of the ceramics.

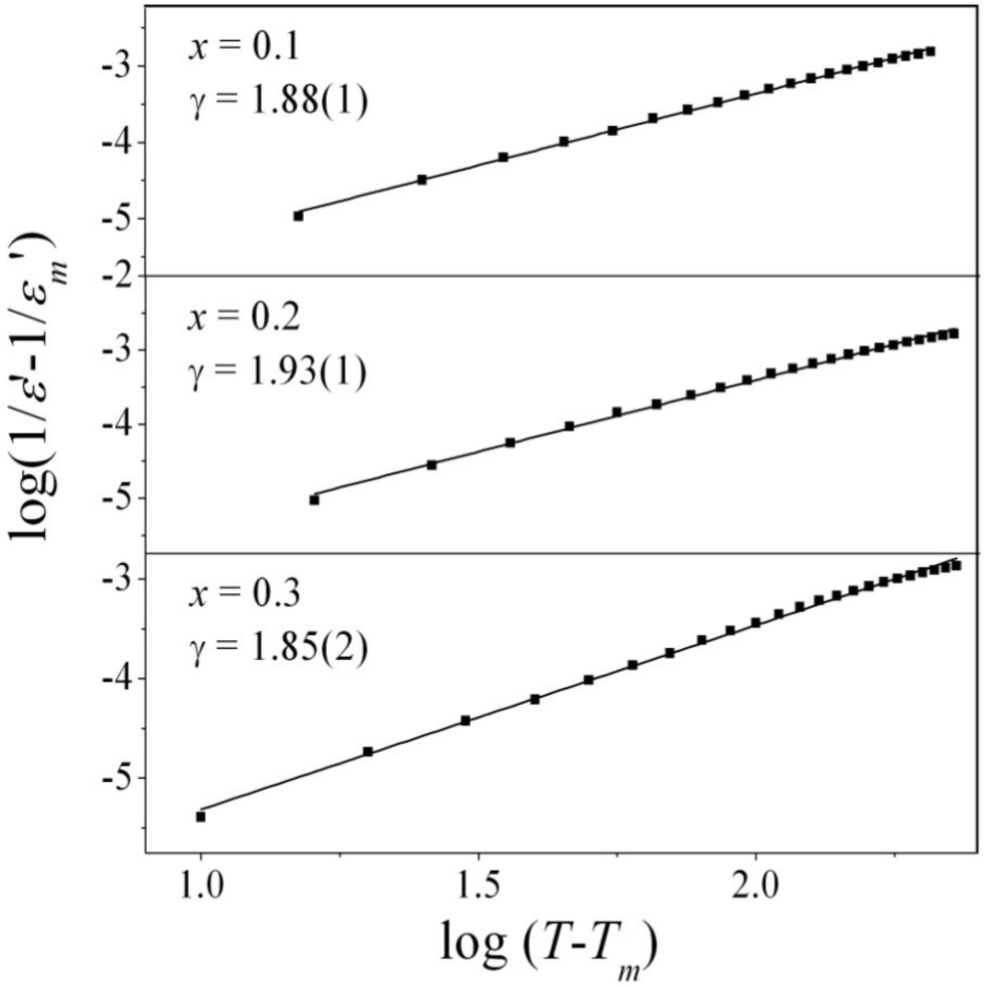

Fig.4.53. Plot of log (1/ε′ – 1/ε_m') versus log (T – T_m) at 100 kHz for $BaBi_4Ti_{4-x}(Nb_{x/2}Al_{x/2})O_{15}$ (x = 0.1, 0.2, 0.3) ceramics.

As discussed earlier, the relaxor behaviour of BBT is a result of cation re-distribution among the Ba^{2+} and Bi^{3+} crystallographic sites, that is disorder is created as Ba^{2+} ions occupy the Bi^{3+} sites in the Bi_2O_2 layer. From the results of the above parameters used to quantify the relaxor behaviour, it may be said that it remained almost the same as that of BBT. This may be justified with the reasoning that, as the concentration of the Ba^{2+} ion in this system remains same, so the disorder of the Ba^{2+} ions in the Bi_2O_2 layer was retained. Thus the relaxor behaviour was not affected.

Table 4.19. Room temperature permittivity (ε_{rm}), Dielectric loss at room temperature (tan δ_{rm}), Maximum relative permittivity (ε_m'), Dielectric loss at peak (tan δ_m), maximum permittivity temperature (T_m) at 100 kHz, degree of relaxation (ΔT_m), and tolerance factor (t), for $BaBi_4Ti_{4-x}(Nb_{x/2}Al_{x/2})O_{15}$ (x = 0.1, 0.2, 0.3) ceramics.

Formula	***x* = 0.1**	***x* = 0.2**	***x* = 0.3**
ε_{rm}	272	390	341
ε_m'	3095	2315	2025
tan δ_{rm}	0.025	0.034	0.042
tan δ_m	0.110	0.099	0.091
T_m (°C)	380	360	360
t	0.9888	0.9891	0.9893
δ (°C)	145	168	207
ΔT_m (°C)	20	30	20

4.5.2.3 Polarization Hysteresis Characteristics

Fig. 4.54 shows the ferroelectric hysteresis loop of $BaBi_4Ti_{4-x}(Nb_{x/2}Al_{x/2})O_{15}$ ceramics obtained under a maximum applied electric field of 40 kV/cm. The loops observed were far from saturation, but these may be utilized for comparison purpose. $2P_r$ and $2E_c$ values are listed in Table 4.20 and were found to increase with increase in Nb^{5+} - Al^{3+} concentration. The remnant polarization of the ceramics with x = 0.2 and 0.3 shows a value of 1.45 and 2.29 μC/cm^2 compared to $2P_r$ of 0.82 μC/cm^2 for BBT at the same applied electric field. This increase may be due to decrease in loss of the ceramics. The loss in BLSF mainly arises due to the oxygen vacancies. These oxygen vacancies pin down the domains, hampering its alignment with the applied field. As the concentration of these oxygen vacancies decreases, the domain pinning effect gets decreased [106]. Hence an increase in $2P_r$ values of these ceramics was observed. The introduction of more ferroelectrically active Nb^{5+} may increase ferroelectricity of the system. This may also play a contributing role in the increase of $2P_r$ values of the ceramics.

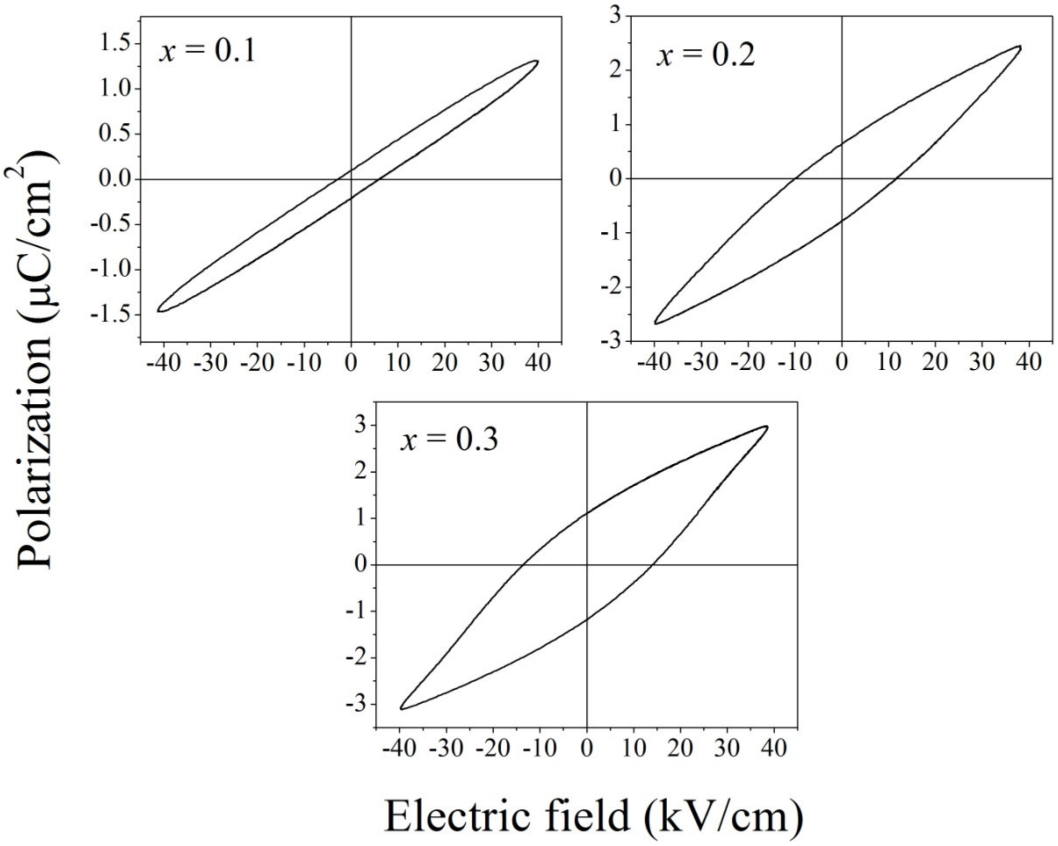

Fig.4.54. Plot of ferroelectric hysteresis loop measured at room temperature for $BaBi_4Ti_{4-x}(Nb_{x/2}Al_{x/2})O_{15}$ (x = 0.1, 0.2, 0.3) ceramics.

4.5.2.4 Piezoelectric Properties

d_{33} coefficients of $BaBi_4Ti_{4-x}(Nb_{x/2}Al_{x/2})O_{15}$ ceramics are listed in Table 4.20. d_{33} coefficients of these ceramics increased with substitution and was maximum for x = 0.2 with a value of 19 pC/N. This result contradicted the polarization behaviour of the ceramics, where it was found to be maximum for x = 0.3. But, this is acceptable as there is no direct relation between the ferroelectric and piezoelectric properties. The spontaneous polarization of ferroelectric ceramics originates from the alignment of the ferroelectric domains parallel to the applied electric field. On the other hand, piezoelectric properties are controlled by the contributions from the movement of non-180^o domain walls [199]. So the increase in d_{33} coefficients for x = 0.1 and 0.2 ceramics may be due to their decreased loss. However, the decrease in d_{33} for x = 0.3 was the outcome of presence of impurity phase in the ceramics.

Table 4.20. Room temperature Remnant polarization ($2P_r$), Coercive field ($2E_c$), and Piezoelectric d_{33} coefficients for $BaBi_4Ti_{4-x}(Nb_{x/2}Al_{x/2})O_{15}$ ($x = 0.1, 0.2, 0.3$) ceramics.

Formula	**$x = 0.1$**	**$x = 0.2$**	**$x = 0.3$**
$2P_r$ (μC/cm^2)	0.307	1.45	2.29
$2E_c$ (kV/cm)	9.18	22.16	28.1
d_{33} (pC/N)	17	19	11

4.5.2.5 Impedance Spectroscopy

In similarity to the previous systems, the relaxation time (τ) was calculated from the Z″ versus log of frequency plot using Eq. 4.16. The value of τ was estimated at various temperatures and was found to decrease with increase in temperature. Fig. 4.55 shows the plot of log τ versus 1000/T for all the compositions. A linear fit was obtained to the curve based on Eq. 4.17 and the slope of the curve gives the E_a values. The E_a values are given in Table 4.21. It was observed that E_a for all the compositions were ~1.4 eV. These values were high in comparison to that of BBT (~0.42 eV), indicating that the conductivity of the system decreased or resistivity increased, supporting the outcome of decrease in loss of the ceramics.

Fig. 4.56 shows the complex impedance plot of $BaBi_4Ti_{4-x}(Nb_{x/2}Al_{x/2})O_{15}$ ceramics at 550°C. The figure shows the presence of a single arc which was attributed to the contribution from the bulk of the ceramics. In order to determine the R_{tot} and C parameters, an equivalent circuit of parallel resistance and capacitance was found. In accordance with the previous chapters, the total resistances and capacitances were calculated. Using Eq. 4.18, the *dc* conductivities of the samples at various temperatures were determined based on the above calculated R_{tot}. *dc* conductivities of the ceramics at 550°C are given in Table 4.21. *dc* conductivity for $x = 0.2$ was of the order $10^{-7}\ \Omega^{-1}cm^{-1}$, which was lowest as compared to the other two compositions of the order of $10^{-6}\ \Omega^{-1}cm^{-1}$. The increase in conductivity for $x = 0.3$, may be because of the presence of the Bi_2O_3 secondary phase. As already stated, Bi_2O_3 increases the conductivity of the ceramics as it is known to be conducting in nature.

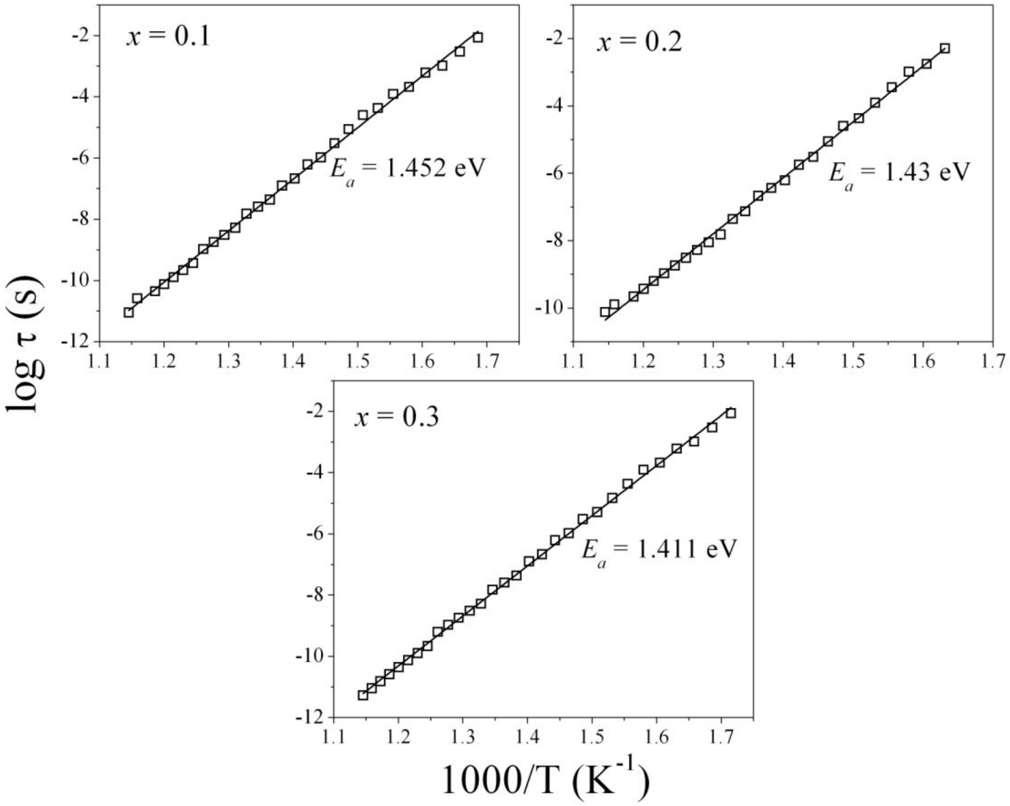

Fig.4.55. log (τ) versus 1000/T for $BaBi_4Ti_{4-x}(Nb_{x/2}Al_{x/2})O_{15}$ (x = 0.1, 0.2, 0.3) ceramics.

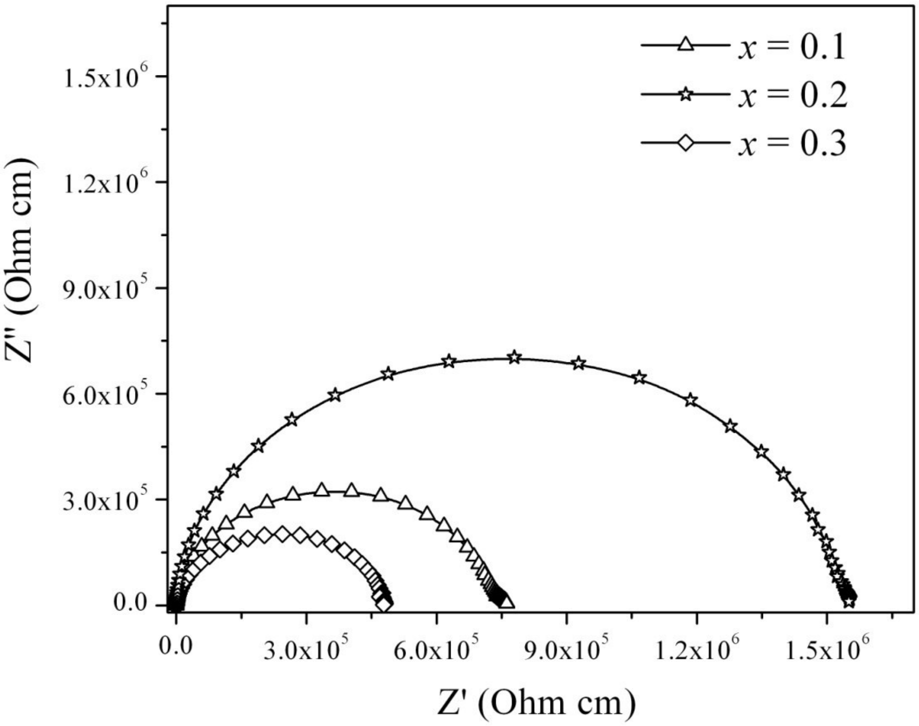

Fig.4.56. Complex impedance plot of $BaBi_4Ti_{4-x}(Nb_{x/2}Al_{x/2})O_{15}$ (x = 0.1, 0.2, 0.3) ceramics at 550°C.

The activation energy (E_{dc}) as computed from the plot of log of *dc* conductivity versus inverse of temperature using Arrhenius Eq. 4.19 is given in Table 4.21. The plot shows the presence of two different temperature regimes, implying the presence of different conduction mechanisms, as explained in previous chapter. From the values of E_{dc} it was observed that these ceramics also show about the same activation energy as that of other previous systems studied, but possess higher value compared to BBT.

Table 4.21. Activation energy from τ (E_a), *dc* conductivity (σ_{dc}), Activation energy (E_{dc}) at 550°C for different $BaBi_4Ti_{4-x}(Nb_{x/2}Al_{x/2})O_{15}$ (x = 0.1, 0.2, 0.3) ceramics.

Formula	**x = 0.1**	**x = 0.2**	**x = 0.3**
E_a (eV)	1.452	1.43	1.411
σ_{dc} ($\Omega^{-1}cm^{-1}$)	1.37×10^{-6}	6.50×10^{-7}	2.07×10^{-6}
E_{dc} (eV) (high temperature)	0.368	0.411	0.45
E_{dc} (eV) (low temperature)	0.585	0.478	0.437

4.5.3 Conclusions

Nb^{5+} and Al^{3+} cation was substituted for Ti^{4+} in the $BaBi_4Ti_4O_{15}$. The lattice parameters show only a slight variation with the substitution and the volume increased slightly for x = 0.3. The orthorhombicity of the structure decreased. An increase in the sintering temperature was observed. The permittivity increased significantly accompanied by a decrease in dielectric loss of the ceramics. This decreased loss was due to the stabilization of the octahedra because of the presence of stronger bonds like Nb-O and Al-O than Ti-O. Along with these, the polarization and the piezoelectric coefficients of the ceramics also increased significantly.

4.6 Na^+ substitution for Ba^{2+} and Nb^{5+} for Ti^{4+} in $BaBi_4Ti_4O_{15}$

4.6.1 Introduction

As stated in the previous chapter, replacement of Ti^{4+} by Nb^{5+} in BLSF improved its ferroelectric properties, piezoelectric properties and resistivity [7, 150, 94]. In that substitution, the charge was compensated at *B*-site. In this study, the charge was compensated at *A*-site. As the substitution of Nb^{5+} for Ti^{4+} creates charge imbalance in the system, the excess charge was compensated by the replacement of Ba^{2+} by Na^+.

$Ba_{(1-x)}Na_xBi_4Ti_{(4-x)}Nb_xO_{15}$ ceramics with x = 0.1, 0.2, 0.3, 0.4, 0.5 and 0.6 were synthesized via conventional solid-oxide route. The solid solubility limit and structural, microstructural, dielectric characteristics, ferroelectric, piezoelectric properties and impedance spectroscopic study of the ceramics were done. This chapter describes the results and discussion of the above characterizations.

4.6.2 Results and Discussion

4.6.2.1 Solid Solubility Limit and Structural Analysis

Fig. 4.57 shows X-ray diffraction patterns of $Ba_{(1-x)}Na_xBi_4Ti_{(4-x)}Nb_xO_{15}$ with x = 0.1, 0.2, 0.3, 0.4, 0.5 and 0.6 ceramics. The diffraction patterns for the compositions, $0.1 \leq x \leq 0.5$ matched with standard $BaBi_4Ti_4O_{15}$ phase (JCPDS Card No. 35-0757), while for composition x = 0.6, some minor amount of secondary impurity peaks in addition to the standard BBT pattern were detected as shown in the figure. The secondary phases were identified as Bi_2O_3 and $Na_2Ti_3O_7$. The inset of the figure shows a shifting in (1 1 9) peak towards higher 2θ degree indicating decrease in *d*-spacing with increase in x. This peak shifting indicated a change in the lattice parameters.

Lattice parameters were evaluated through Rietveld analysis (MAUD [158]) considering orthorhombic $A2_1am$ space group. The refined lattice parameters, *R*-factors, sigma, volume and orthorhombicity of the ceramics are given in Table 4.22. Fig.4.58 shows variation of lattice parameters with composition (*x*). Lattice parameter '*a*' remained almost same while '*b*' and '*c*' decreased with increase in '*x*'. An overall decrease was observed in the volume of the unit cell. This decrease in lattice parameter may be due to the replacement of Ba^{2+} by Na^+, as the ionic radii of Na^+ (r_{Na^+} = 1.39Å) is much smaller in comparison to Ba^{2+} ($r_{Ba^{2+}}$ = 1.61Å) [192]. The orthorhombicity of the structure was determined from Eq. 4.10 showed the same range of values for $x = 0.1$ to 0.5, while a slight increase was observed for $x = 0.6$.

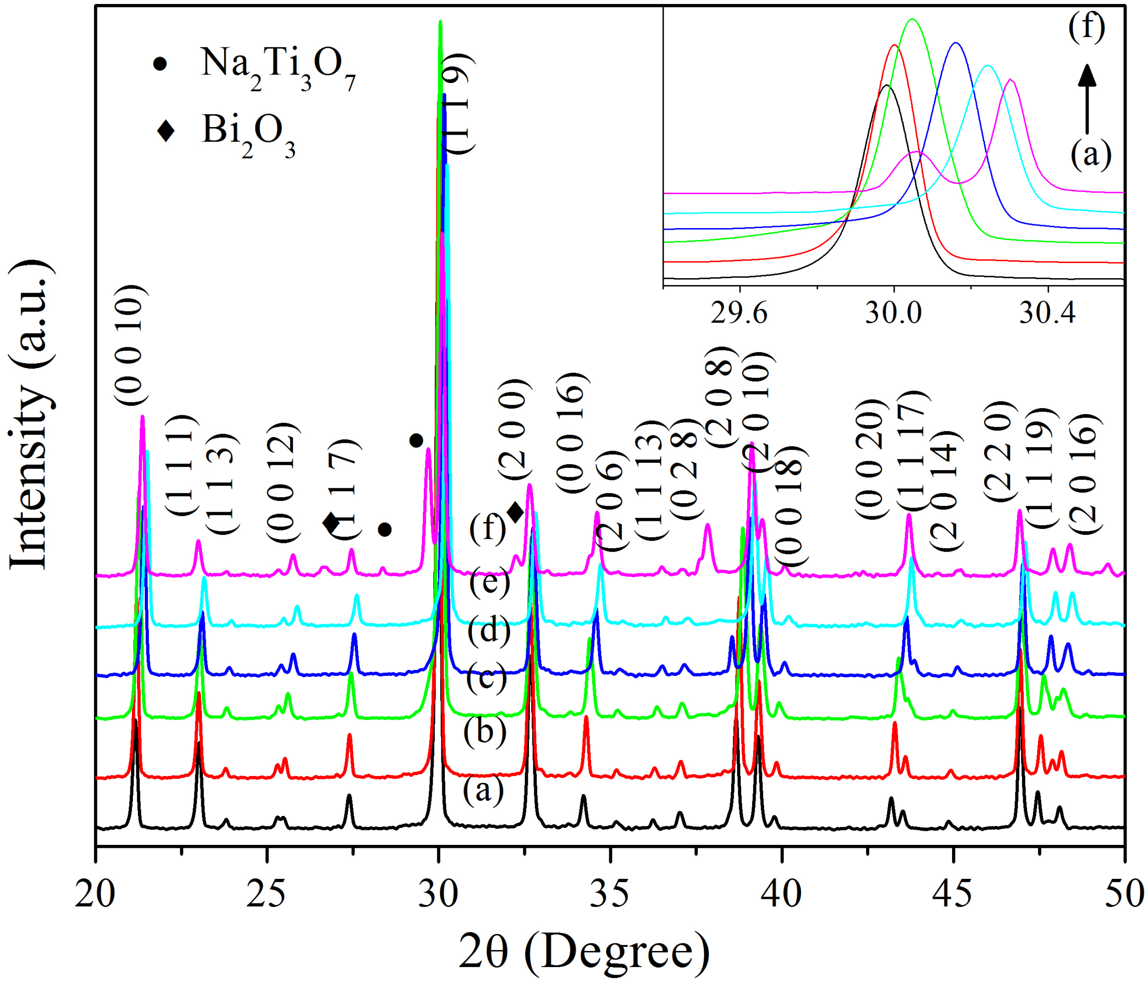

Fig.4.57. XRD patterns of $Ba_{(1-x)}Na_xBi_4Ti_{(4-x)}Nb_xO_{15}$ with x = (a) 0.1, (b) 0.2, (c) 0.3, (d) 0.4, (e) 0.5 and (f) 0.6 ceramics.

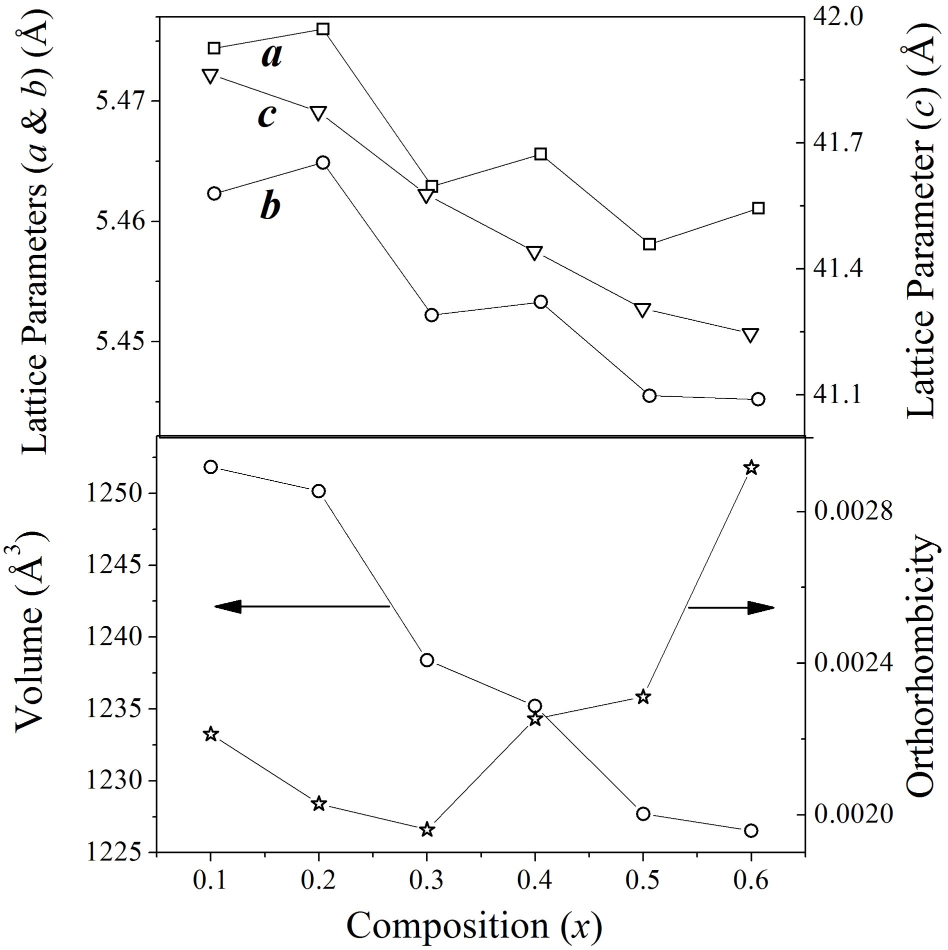

Fig.4.58. Variation of lattice parameters, volume and orthorhombicity for $Ba_{(1-x)}Na_xBi_4Ti_{(4-x)}Nb_xO_{15}$ (x = 0.1, 0.2, 0.3, 0.4, 0.5, 0.6) ceramics with composition 'x'.

Table 4.22. Refined lattice parameters (*a*, *b* and *c*), Volume, *R*-factors, Sigma and Orthorhombicity for $Ba_{(1-x)}Na_xBi_4Ti_{(4-x)}Nb_xO_{15}$ (x = 0.1, 0.2, 0.3, 0.4, 0.5, 0.6) ceramics.

Formula	***x* = 0.1**	***x* = 0.2**	***x* = 0.3**	***x* = 0.4**	***x* = 0.5**	***x* = 0.6**
a (Å)	5.4744	5.476	5.4629	5.4656	5.4581	5.4611
b (Å)	5.464	5.4649	5.4522	5.4533	5.4455	5.4452
c (Å)	41.8638	41.7751	41.5782	41.4422	41.3061	41.2463
Volume (Å)^3	1251.84	1250.15	1238.40	1235.20	1227.70	1226.53
R_{wp} (%)	7.52	10.78	6.44	7.66	7.58	15.73
R_b (%)	5.48	7.54	4.64	5.12	5.55	9.47
Sigma	2.49	3.64	2.13	2.66	2.96	3.04
Orthorhombicity	0.0022	0.0020	0.002	0.0023	0.0023	0.0024

Table 4.23. %Theoritical density with Sintering temperature/time and Grain Size for $Ba_{(1-x)}Na_xBi_4Ti_{(4-x)}Nb_xO_{15}$ (x = 0.1, 0.2, 0.3, 0.4, 0.5, 0.6) ceramics.

Formula	***x* = 0.1**	***x* = 0.2**	***x* = 0.3**	***x* = 0.4**	***x* = 0.5**	***x* = 0.6**
Sintering temperature and time	**% Theoretical density**					
1100°C/4h	96	Partial melting	-	-	-	-
1100°C/3h	-	96	Partial melting	-	-	-
1100°C/2h	-	-	95	Partial melting	-	-
1100°C/1h	-	-	-	96	Partial melting	-
1090°C/2h	-	-	-	-	93	Partial melting
1080°C/2h	-	-	-	-	-	94
Grain Size (μm)						
Length	1.51	1.57	1.62	1.69	1.86	1.92
Breadth	0.85	0.9	0.89	0.95	1.1	1.2
Thickness	0.3	0.28	0.3	0.4	0.51	0.56

4.6.2.2 Densification and Microstructural Characteristics

Table 4.23 lists the %theoritical density of the ceramics versus sintering temperature and time. The sintering temperature of the ceramics decreased with increase in x. Fig. 4.59 shows the micrograph of $Ba_{(1-x)}Na_xBi_4Ti_{(4-x)}Nb_xO_{15}$ ceramics. The micrographs of the ceramics show an increase in grain size with increase in substitution (x) (Table 4.23). This increase in grain size may be due to the effect of Na^+. Thus the sinterablity of the ceramics increased with increase in concentration of Na^+ in the system. Similar increase in grain size was observed by the substitution of Na^+ and La^{3+} for Ba^{2+}.

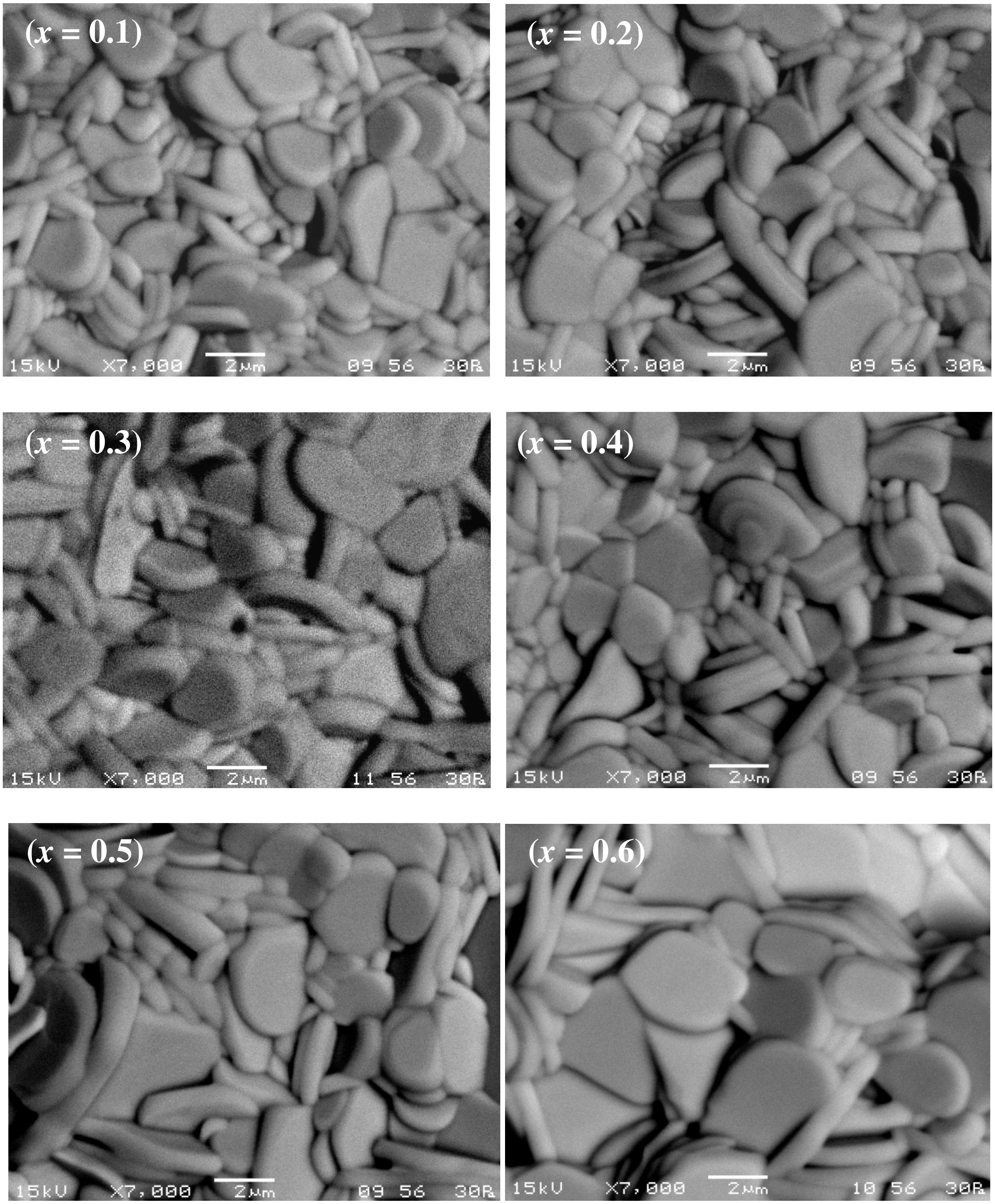

Fig.4.59. Scanning electron micrograph of $Ba_{(1-x)}Na_xBi_4Ti_{(4-x)}Nb_xO_{15}$ (x = 0.1, 0.2, 0.4, 0.5, 0.6) ceramics.

4.6.2.3 Dielectric and Diffuse Phase Transition Behaviour

Fig. 4.60 shows the temperature dependence of ε′ and tan δ at a frequency of 100 kHz for $Ba_{(1-x)}Na_xBi_4Ti_{(4-x)}Nb_xO_{15}$ ceramics. The room temperature permittivity (ε_{rm}), maximum relative permittivity (ε_m') and maximum permittivity temperature (T_m) at 100 kHz are summarized in Table 4.24. ε_m' increased for the compositions $x = 0.1$ and 0.2 compared to BBT, but with further increase in substitution it decreased, that is from $x \geq 0.3$. Although the lattice parameters slightly decreased in case of $x = 0.1$ and 0.2, ε_m' increased due to effect of ferroelectrically active Nb^{5+}, which tends to go an off-centre displacement. The decrease in ε_m' from $x \geq 0.3$ may be a result of the decrease in the volume of the unit cell. The decrease in unit cell dimension squeezes the lattice decreasing its rattling space, resulting in decrease of the displacement of the cations (*A*- and *B*-site cation), thus decreasing the ε_m'. From the table it was observed that the room temperature permittivity (ε_{rm}) exhibited a similar trend to that of ε_m'.

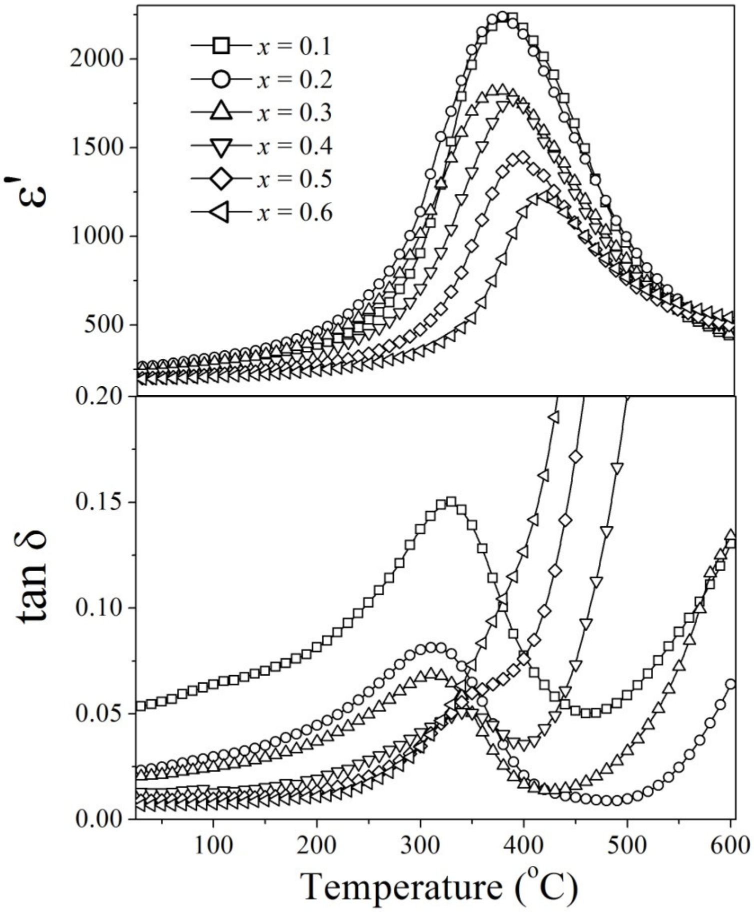

Fig.4.60. Temperature dependence of ε′ and tan δ at a frequency of 100 kHz for $Ba_{(1-x)}Na_xBi_4Ti_{(4-x)}Nb_xO_{15}$ ($x = 0.1, 0.2, 0.4, 0.5, 0.6$) ceramics.

Room temperature dielectric loss (tan δ_{rm}) and maximum dielectric loss (tan δ_m) of all the samples are given in Table 4.24. A decrease in loss was observed. So it may be said that an increase in ε_{rm} and ε_m' and a decreased loss were observed for $x = 0.1$ and 0.2, which may be favorable for its commercial FRAM applications. Similar to the previous explanations, this decrease in loss may be the outcome of two phenomenona. Firstly, based on the electronegativities of the cations, it may be said that the Na-O and Nb-O bonds are much stronger than Ba-O and Ti-O, respectively, increasing the stability of perovskite block. Also, the BO_6 octahedron was more stabilized due to the presence of Nb-O bonds thus decreasing the probability of oxygen vacancy formation. Secondly, as the concentration of Ti^{4+} ion decreased with increase in Nb^{5+} concentration, the probability of polaron hopping between the Ti^{4+} and Ti^{3+} states decreases, thus contributing to decrease in loss of the ceramics.

T_m for the compositions $x = 0.1$, 0.2 and 0.3 was ~390^{o}C. However, for the higher substituted compositions, T_m was observed to be ~420^{o}C for $x = 0.6$. The orthorhombicity as shown in Fig. 4.58 remained almost same, increasing slightly for $x = 0.6$. So, it may be said that as the distortion remains same, T_m also remains unaffected, increasing only slightly for $x = 0.6$. The tolerance factor 't' was calculated from Eq. 4.23 (Table 4.24) and it was found to decrease slightly. The decrease in t implies an increase in T_m.

The peak broadening (δ) factor determined (Eq. 4.12) from the temperature dependence of ε', was maximum for $x = 0.2$, about 265^{o}C. However, the δ for the other compositions was also high when compared to that of BBT. This highlighted the fact that degree of inhomogeneity of the ceramics was exaggerated by the introduction of Na^+ and Nb^{5+} in the system, creating more local Curie points in the material.

Fig. 4.61 shows frequency dispersion of the ceramics with $x = 0.1$ and 0.4 and the amount of frequency dispersion can be established from the following parameters. The parameter ΔT_m representing the frequency dispersion for relaxor can be determined using Eq. 4.11. The value of ΔT_m is given in Table 4.24. ΔT_m was found to remain the same ~20^{o}C for the compositions $0.1 \leq 0.3$, while from $x \geq 0.4$, ΔT_m was found to be zero.

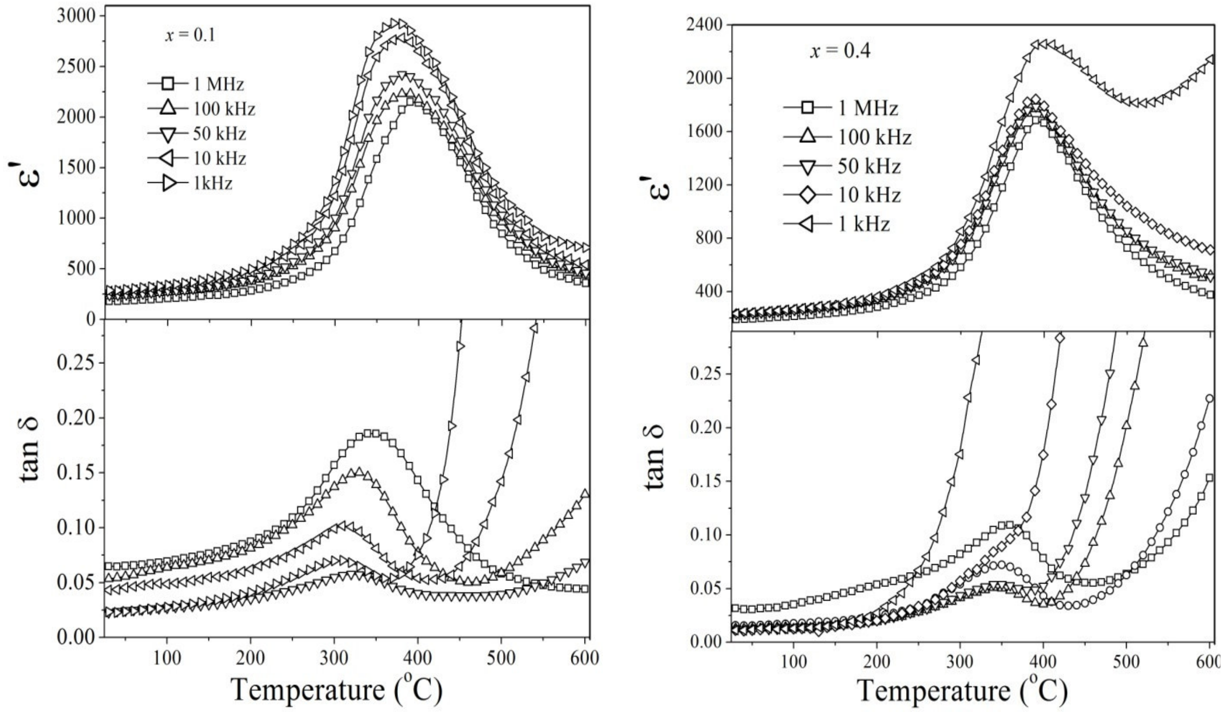

Fig.4.61. Temperature dependence of *ε*′ and tan δ at various frequencies for $Ba_{(1-x)}Na_xBi_4Ti_{(4-x)}Nb_xO_{15}$ ($x = 0.1$ and 0.4) ceramics.

The diffusivity parameter (γ) was determined from the Curie-Weiss law based by Eq. 4.14. γ which quantifies the relaxor behaviour was determined from the modified law. The γ value was determined from the slope of the graph (Fig.4.62) between log ($1/\varepsilon' - 1/\varepsilon_m'$) versus log ($T - T_m$) given in the Table 4.24. As excepted, γ of $0.1 \leq x \leq 0.3$ compositions were ~1.78, while with increase in substituent's concentration, γ decreased approaching the value of ~1.38, showing them to be normal ferroelectrics.

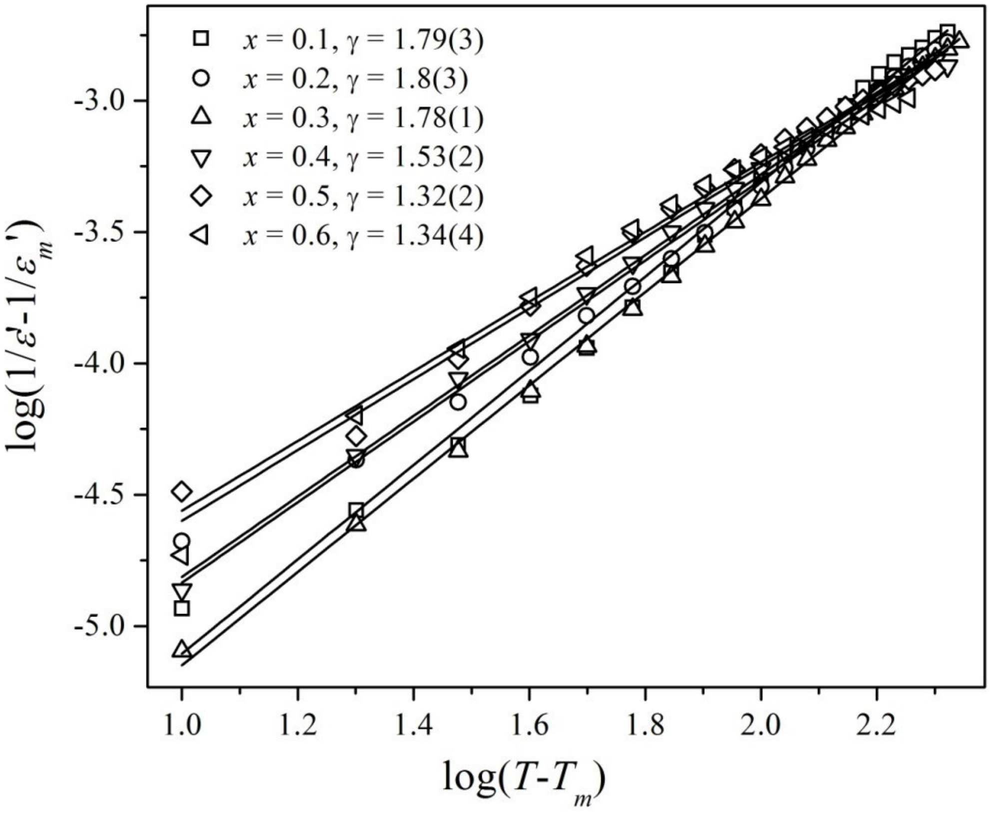

Fig.4.62. Plot of log(1/ε' – 1/ ε_m') versus log(T – T_m) at 100 kHz for $Ba_{(1-x)}Na_xBi_4Ti_{(4-x)}Nb_xO_{15}$ (x = 0.1, 0.2, 0.3, 0.4, 0.5, 0.6) ceramics.

The relaxor behaviour of the compositions $0.1 \leq x \leq 0.3$ was modeled using Vogel-Fulcher law described by Eq. 4.15. A fit between the experimental data points to the calculated ones, a plot represented by log frequency versus inverse of T_m was obtained for the compositions x = 0.1, 0.2 and 0.3. As the range of T_m and frequency was the same for these three compositions, the fitting parameters activation energy (E_{vf}), attempt frequency (ν_o) and freezing temperature (T_f) were same and are given in Table 4.24.

As explained in the earlier chapters, the origin of relaxor behaviour of BBT was the cation disorder of Ba^{2+} in Bi^{3+} site of the Bi_2O_2 layer. The decrease in the relaxor behaviour was associated with the decrease in the concentration of Ba^{2+} ions, as it decreases the cation disorder in the system. Hence the relaxor behaviour decreases.

Table 4.24. Room temperature permittivity (ε_{rm}), dielectric loss at room temperature (tan δ_{rm}), maximum relative permittivity (ε_m'), dielectric loss at peak (tan δ_m), maximum permittivity temperature (T_m), diffusivity parameter (γ) at 100 kHz, degree of relaxation (ΔT_m), Vogel-Fulcher fitting parameters (E_{vf}, ν_o and T_f) and tolerance factor (t), for $Ba_{(1-x)}Na_xBi_4Ti_{(4-x)}Nb_xO_{15}$ (x = 0.1, 0.2, 0.4, 0.5, 0.6) ceramics.

Formula	**x = 0.1**	**x = 0.2**	**x = 0.3**	**x = 0.4**	**x = 0.5**	**x = 0.6**
ε_{rm}	239	265	247	228	200	195
$\varepsilon_m{'}$	2231	2239	1820	1770	1542	1223
tan δ_{rm}	0.053	0.023	0.02	0.013	0.01	0.006
tan δ_m	0.15	0.081	0.068	0.05	0.021	--
T_m (^{o}C)	390	390	390	390	410	420
t	0.9856	0.9826	0.9796	0.9766	0.9736	0.9706
δ (^{o}C)	163	178	188	161	158	155
ΔT_m (^{o}C)	20	20	20	0	0	0
γ	1.79	1.80	1.77	1.53	1.50	1.34
E_{vf} (eV)	0.038	0.038	0.038	--	--	--
ν_o (Hz)	1.63×10^{10}	1.63×10^{10}	1.63×10^{10}	--	--	--
T_f (^{o}C)	325	325	325	--	--	--

4.6.2.4 Polarization Hysteresis Characteristics

Fig. 4.63 shows the ferroelectric hysteresis loop of $Ba_{(1-x)}Na_xBi_4Ti_{(4-x)}Nb_xO_{15}$ ceramics obtained under a maximum applied electric field of 40 kV/cm. Because of the high T_m of these compositions, their saturated hysteresis loop could not be traced. Slim hysteresis loops were observed for the ceramics. Table 4.25 lists the $2P_r$ and $2E_c$ for all ceramics. Both $2P_r$ and $2E_c$ decreases with the increase in substitution. The reduced lattice parameter limits the displacement of *A*-type cation along the *a*-axis which is responsible for its ferroelectricity, thus reducing the ferroelectricity of the system.

4.6.2.5 Piezoelectric Properties

Table 4.20 lists the d_{33} coefficients for different compositions. The coefficients were found to show a similar trend to that of $2P_r$. That is, the d_{33} of x = 0.1 was observed to remain almost same and with further increase in x, it decreased. Thus it may be said that these observations support the above argument that the ferroelectricity decreased due to the reduced lattice parameters.

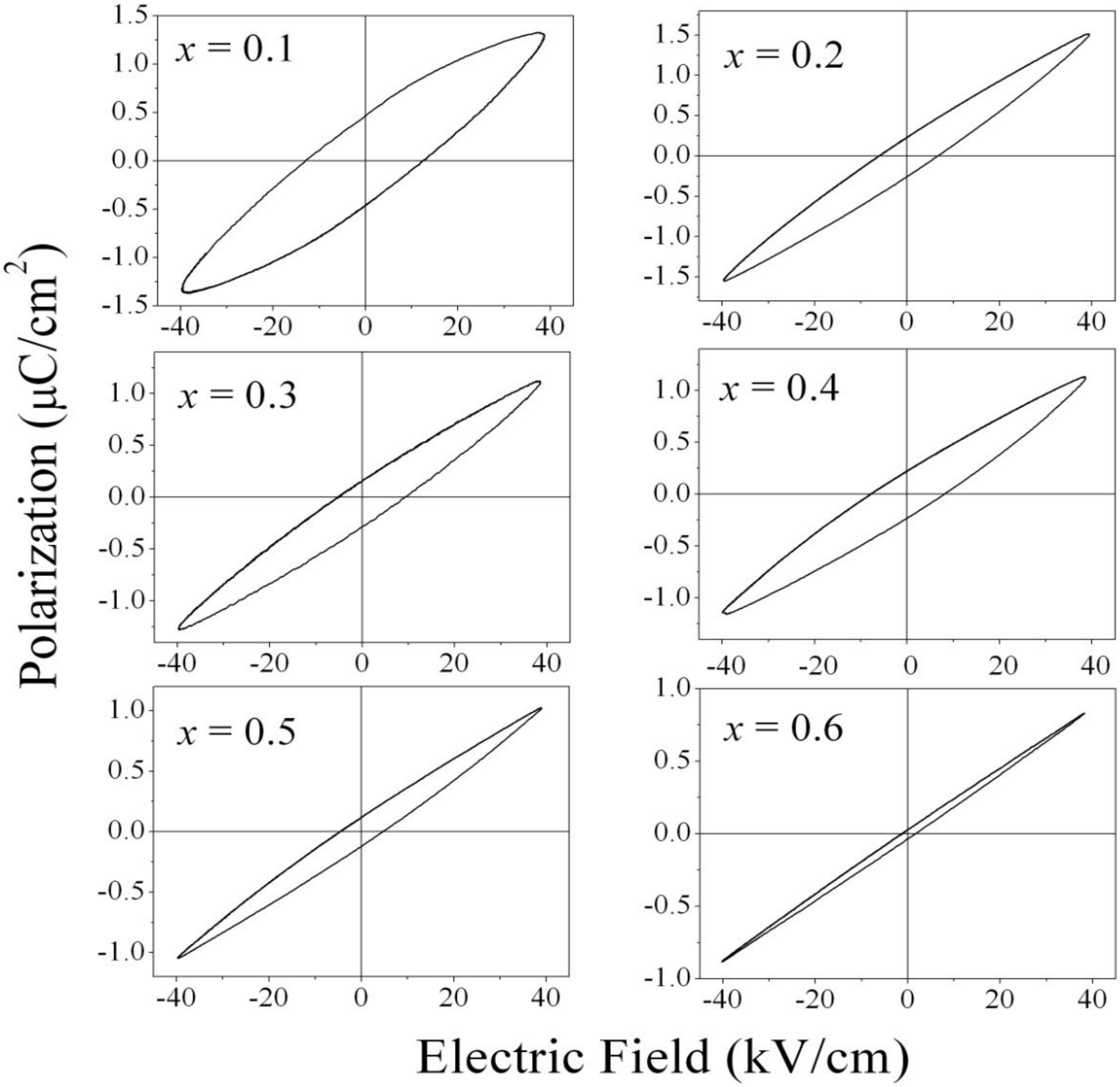

Fig.4.63. Ferroelectric hysteresis loop measured at room temperature for different $Ba_{(1-x)}Na_xBi_4Ti_{(4-x)}Nb_xO_{15}$ ($x = 0.1, 0.2, 0.4, 0.5, 0.6$) ceramics.

Table 4.25. Remnant polarization ($2P_r$), Coercive field ($2E_c$), and Piezoelectric d_{33} coefficients for $Ba_{(1-x)}Na_xBi_4Ti_{(4-x)}Nb_xO_{15}$ ($x = 0.1, 0.2, 0.4, 0.5, 0.6$) ceramics.

Formula	***x* = 0.1**	***x* = 0.2**	***x* = 0.3**	***x* = 0.4**	***x* = 0.5**	***x* = 0.6**
$2P_r$ (μC/cm^2)	0.912	0.478	0.45	0.455	0.245	0.062
$2E_c$ (kV/cm)	25.8	12.73	14.605	15.397	9.255	2.822
d_{33} (pC/N)	12	9	8	7	4	4

4.6.2.6 Impedance Spectroscopy

In analogy with the earlier chapters, the relaxation time (τ) was calculated from the Z″ versus log of frequency plot using Eq. 4.16. A linear fit was obtained to τ versus 1000/T plot (Eq. 4.17). The slopes of the curves give the E_a values and are given in Table 4.26. E_a values for all the compositions were in the range 1.4 to 1.8 eV which was well above BBT (0.42 eV). This indicated that high activation energy is requiring for conduction, which also supports decreased loss of the ceramics as stated above.

Fig. 4.64 shows the Cole-Cole plot for $Ba_{(1-x)}Na_xBi_4Ti_{(4-x)}Nb_xO_{15}$ ceramics measured at 550°C. The complex impedance plot of insulating ceramics results from the contribution of three components: grains, grain boundaries and sample/electrode interfaces. From the figure two semicircular curves were observed with the high frequency side passing through the origin. In analogy to the previous chapters, the semicircle through the high frequency side was ascribed to the contribution from the bulk while the semicircles towards the low frequency side to the sample/electrode interface. The *R* and *C* values were estimated from the plot at various temperatures. The total resistance (R_{tot}) at 550°C is summarized in Table 4.26. It was observed that the composition with $x = 0.2$ was the most resistive ceramic among all the compositions. *dc* conductivity (σ_{dc}) of the ceramics was calculated from the resistances using Eq. 4.18 and are summarized in Table 4.26. Thus the activation energy (E_{dc}) was calculated (Eq. 4.19) as described in the previous chapters. Table 4.26 lists the E_{dc} values for the compositions.

Table 4.26. Activation energy from relaxation time (E_a), Total resistance (R_{tot}), *dc* conductivity (σ_{dc}) at 550°C, *dc* Activation energy (E_{dc}) for $Ba_{(1-x)}Na_xBi_4Ti_{(4-x)}Nb_xO_{15}$ (x = 0.1, 0.2, 0.4, 0.5, 0.6) ceramics.

Formula	$x = 0.1$	$x = 0.2$	$x = 0.3$	$x = 0.4$	$x = 0.5$	$x = 0.6$
E_a (eV)	1.52	1.54	1.44	1.8	1.18	0.98
R_{tot} (Ω)	1.04×10^5	1.75×10^5	1×10^5	11099	6868	3653
σ_{dc} ($\Omega^{-1}cm^{-1}$)	9.83×10^{-7}	6.15×10^{-7}	1.15×10^{-6}	1.06×10^{-5}	2.15×10^{-5}	3.09×10^{-5}
E_{dc} (eV)	0.54	0.51	0.52	0.48	0.47	0.48

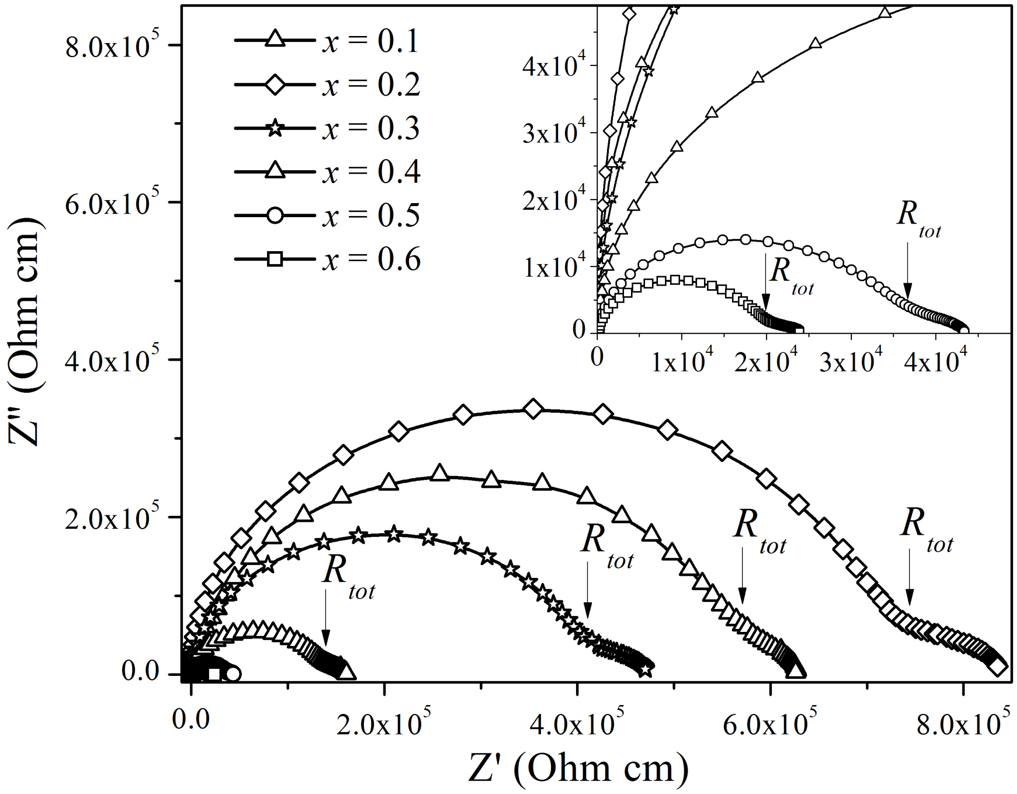

Fig.4.64. Cole-Cole plot for $Ba_{(1-x)}Na_xBi_4Ti_{(4-x)}Nb_xO_{15}$ (x = 0.1, 0.2, 0.4, 0.5, 0.6) ceramics at 550°C.

4.6.3 Conclusions

$Ba_{(1-x)}Na_xBi_4Ti_{(4-x)}Nb_xO_{15}$ ceramics were successfully prepared through solid-oxide route. Solid solution was obtained in the composition range $0.1 \leq x \leq 0.5$. Composition with $x = 0.6$, showed presence of secondary phases like Bi_2O_3 and $Na_2Ti_3O_7$. Lattice parameters decreased with an increase in orthorhombicity. The grain size of the ceramics increased with increase in substituent's concentration. The maximum dielectric constant increased initially accompanied with a decrease in loss. The analysis of the impedance spectra showed the composition with x = 0.2 to be the most resistive ceramics.

4.7 $Mg^{2+}/Ca^{2+}/Sr^{2+}/Ba^{2+}$ substitution for Bi^{3+} and Nb^{5+} for Ti^{4+} in $BaBi_4Ti_4O_{15}$

4.7.1 Introduction

As stated in the previous chapters, substitution of Nb^{5+} for Ti^{4+} in BLSF improved the ferroelectric, piezoelectric properties and resistivity of the ceramics [7, 150, 94]. In Chapter 4.6, it was established that the composition with Nb^{5+} concentration with x~0.2, depicted a better result among all. Therefore, to the study of effect of Nb^{5+} on various properties of the ceramics, Nb^{5+} concentration ~0.2 was chosen. To compensate the excess charge introduced in the system, divalent cation was substituted for Bi^{3+}.

$BaBi_{3.8}M_{0.2}(Ti_{3.8}Nb_{0.2})O_{15}$ with M = Mg, Ca, Sr and Ba (abbreviated as BBTN-Mg, BBTN-Ca, BBTN-Sr and BBTN-Ba) ceramics were synthesized via modified chemical route. The structural, dielectric characteristics, ferroelectric, piezoelectric properties of the ceramics were investigated. This chapter describes the results and discussions of the above characterizations.

4.7.2 Results and Discussion

4.7.2.1 Structural Analysis and Microstructural Characteristics

Rietveld refinement was performed using MAUD Program [158] in accordance with the previous chapters. The refined lattice parameters a, b and c, and R-factors are summarized in Table 4.27. Fig. 4.65 shows the refined patterns of BBTN-Mg, BBTN-Ca, BBTN-Sr and BBTN-Ba compounds. X-ray diffraction patterns for all the compounds matched with the standard BBT pattern (JCPDS Card no. 35-0757) and no extra peak for impurity phases were detected. This indicated the substituting cations form a solid solution in BBT.

The inset of Fig. 4.65 shows the microstructure of each ceramic. All the ceramics exhibited plate-like morphology due to the anisotropic growth of the ceramics in the a-b plane. For BBTN-Sr and BBTN-Ba ceramics, the grains show more round shaped morphology, indicating a grain growth.

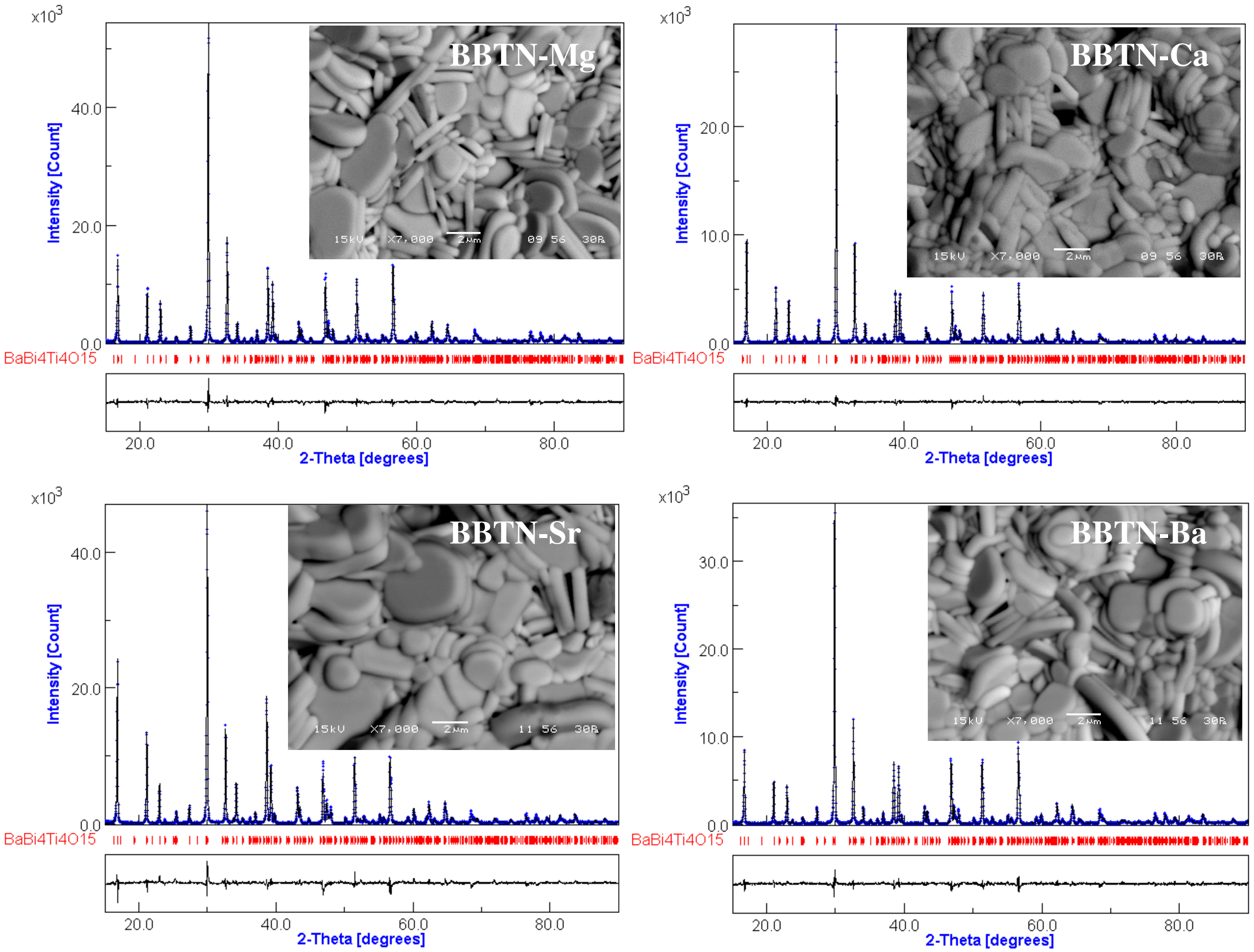

Fig.4.65. Observed and calculated X-ray diffraction profiles of BBTN-Mg, BBTN-Ca, BBTN-Sr and BBTN-Ba ceramics. Inset of the figure shows the corresponding scanning electron micrograph.

Fig. 4.66 shows that lattice parameters of BBTN-Mg increased compared to that of BBT (Table 4.27), while the parameters decreased for BBTN-Ca. Then the lattice parameters again increased for BBTN-Sr and BBTN-Ba compounds due to the increase in radii of cations. The ionic radii of Bi^{3+} ($r_{Bi}{}^{3+}$ = 1.36 Å) is larger than that of Mg^{2+} ($r_{Mg}{}^{2+}$ = 0.72 Å) and Ca^{2+} ($r_{Ca}{}^{2+}$ = 1.34 Å) and smaller compared to Sr^{2+} ($r_{Sr}{}^{2+}$ = 1.44 Å) and Ba^{2+} ($r_{Ba}{}^{2+}$ = 1.61 Å) [29]. As Ca^{2+} was substituted at *A*-site of perovskite block and is smaller than Bi^{3+}, it brings about a decrease in the lattice parameter of BBTN-Ca. The increase of same for BBTN-Sr and BBTN-Ba was due to the increase in radii of the substituting cation occupying *A*-site of the perovskite block. The figure also shows that the structure of BBTN-Ca, BBTN-Sr and BBTN-Ba are pseudo-tetragonal. It is known that the structure of BBT is orthorhombic as the *A*-site cations are too small for the holes in the perovskite unit. With the increase in the radii of the substituting *A*-site cation, the lattice mismatch in the perovskite layer as well as the structural distortion decreases. This decrease in the structural distortion was responsible for the transformation of the crystal structure to pseudo-tetragonal.

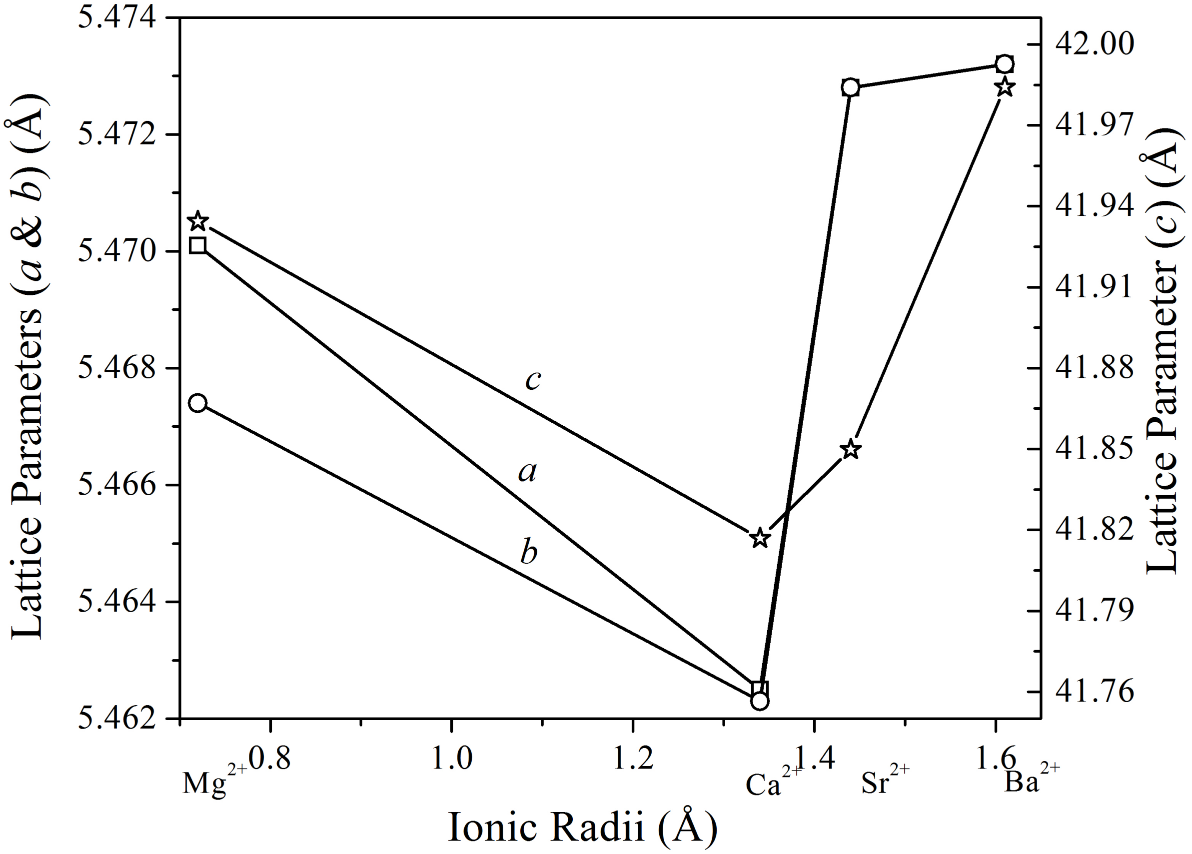

Fig.4.66. Variation of lattice parameters as a function of ionic radius of substituting cation for BBTN-Mg, BBTN-Ca, BBTN-Sr and BBTN-Ba ceramics.

The ionic radius of Mg^{2+} is much smaller compared to that of Bi^{3+} [192]. Thus one would expect the lattice parameters to decrease with Mg-substitution. However, the lattice parameter of

BBTN-Mg was higher than BBT and the structure remained orthorhombic. Thus an anomaly may be present regarding the occupancy of Mg^{2+} in the perovskite block.

Mg^{2+} usually prefers a 6 coordinated site due to its smaller ionic radius [200]. The *A*-site of BBT structure is 12 coordinated. Therefore, a possibility arises that the Mg^{2+} ions will prefer to enter the 6 coordinated Bi^{3+} site in Bi_2O_2 layer, rather than *A*-site of perovskite unit. It was observed from the Rietveld refinement that the occupancy of Bi site of Bi_2O_2 layer was 5.70 for BBTN-Mg, while that for BBTN-Ca, BBTN-Sr and BBTN-Ba were 5.96, 5.93 and 5.99, respectively. So the amount of Bi^{3+} in Bi_2O_2 layer of BBTN-Mg was less, which may be due to the presence of Mg^{2+} in this layer. Mg^{2+} has lower scattering factor than Bi^{3+} requiring a resultant lower occupancy factor at that site. As Mg^{2+} prefers to substitute in the Bi_2O_2 layer, the perovskite unit in BBTN-Mg remains almost similar to that of BBT. For this reason the structure of BBTN-Mg was orthorhombic. As stated earlier, the lattice parameters of BBTN-Mg was observed to be larger compared to BBT. It is known that the Bi_2O_2 layer is under tensile stress [201]. As Mg^{2+} is incorporated in Bi_2O_2 layer, its tensile stress may reduce, which may be one of the reasons for increase in its lattice parameters. Similar increase in lattice parameters was observed in an earlier case when La^{3+} was substituted for Bi^{3+} in BBT and for other BLSFs [69, 186].

Table 4.27. Lattice parameters (*a*, *b* and *c*), *R*-factors and Sigma for BBTN-Mg, BBTN-Ca, BBTN-Sr and BBTN-Ba ceramics.

Formula	**BBTN-Mg**	**BBTN-Ca**	**BBTN-Sr**	**BBTN-Ba**
a (Å)	5.4701(2)	5.4625(4)	5.4728(2)	5.4723(5)
b (Å)	5.4674(3)	5.4623(5)	5.4728(6)	5.4723(5)
c (Å)	41.9344(11)	41.8169(13)	41.8498(14)	41.9842(12)
R_{wp} (%)	4.18	4.68	4.92	3.98
R_b (%)	3.14	3.58	3.50	3.02
Sigma	2.35	1.57	2.80	1.96

4.7.2.2 Dielectric and Diffuse Phase Transition Behaviour

Fig.4.67 shows the temperature dependence of relative permittivity (ε') and dielectric loss (tan δ) at a frequency of 100 kHz for all the ceramics. Table 4.28 summarizes the room temperature permittivity (ε_{rm}), maximum permittivity (ε_m') and maximum permittivity temperature (T_m) at a frequency of 100 kHz for all compounds. ε_{rm} of these compositions increased in the order Mg <Ca <Sr <Ba based composition. This increase was due to the shifting of ε_m' peak towards room temperature. T_m decreased with increase in ionic radii of the substituting cation in the order Mg> Ca> Sr> Ba. This decrease may be explained considering the orthorhombicity of the structure. The orthorhombicity of the BBTN-Mg decreased compared to that of BBT. The other three compositions were pseudo-tetragonal and tetragonality increases in the order stated above. This resulted in the decrease of T_m for these compositions.

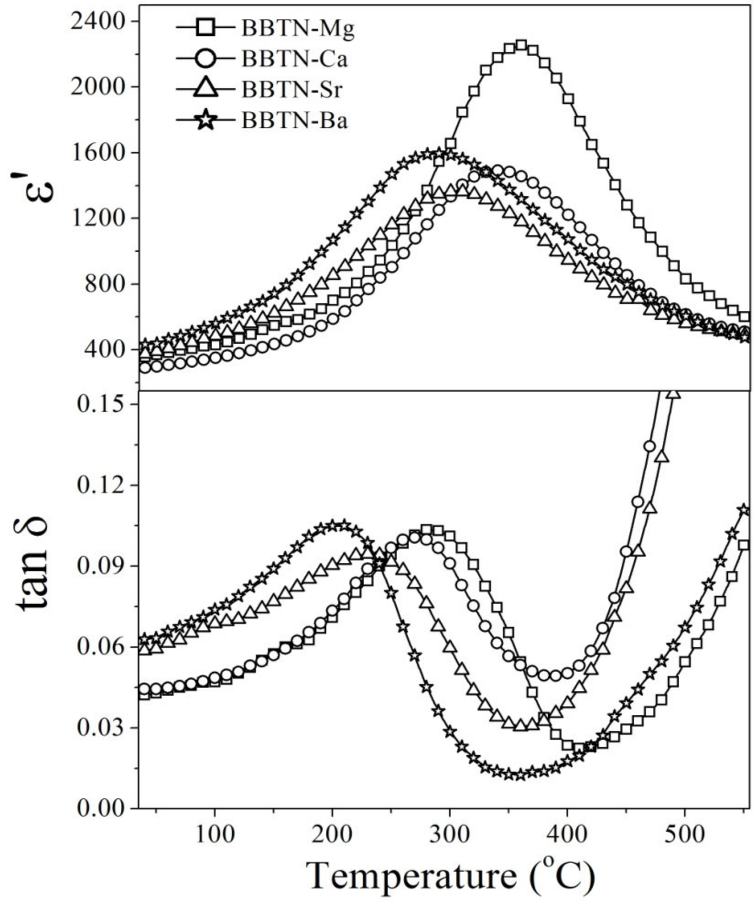

Fig.4.67. Temperature dependence of ε' and tan δ for BBT, BBTN-Mg, BBTN-Ca, BBTN-Sr and BBTN-Ba ceramics measured at 100 kHz frequency.

It was interesting to note from Fig.4.67 that the maximum permittivity (ε_m') of BBTN-Mg was higher than BBT, while that of other three compositions was lower. In BBTN-Mg, the perovskite unit remains unchanged (i.e. orthorhombic) except for the partial substitution of Ti^{4+} by Nb^{5+}. Nb^{5+} is more ferro-electrically active and thus ε_m' increased. On the other hand, the low ε_m' of BBTN-Ca, BBTN-Sr and BBTN-Ba may be due the change of structure from orthorhombic to pseudo-tetragonal. It is already stated that ferroelectricity in BLSF arises due to their structural distortions such as, tilting and rotation of oxygen octahedral from *a*- and *c*-axes and a displacement of the *A*-site cation in the orthorhombic symmetry. Hence the change in the structure may decrease these distortions reducing their ferroelectricity.

The tan δ (Fig.4.67) of the ceramics decreased. This may be due to the decrease in the concentration of oxygen vacancies. Bi^{3+} volatilization during sintering of BLSFs leads to the formation of oxygen vacancies, which are responsible for their loss. As a result of the substitution of Bi^{3+} by non-volatile cations (Mg, Ca, Ba etc.), concentration of oxygen vacancies decreases. Additionally, substitution of Ti^{4+} by Nb^{5+} may also plays a role in decreasing the loss [7, 126, 127]. One way of arising losses in Ti-based ceramics is the field-assisted conduction by polaron hopping between Ti^{4+} and Ti^{3+}. So the reduction in concentration of Ti^{4+} reduced the probability of hopping thus reducing loss.

Fig. 4.68 shows the temperature and frequency dependence of dielectric constant (ε') and dielectric loss (tan δ) for all compositions. A frequency dispersion of ε' was observed for all. T_m shifts to a higher temperature and ε_m' decreases with increase in frequency. This behaviour indicates the ceramics to retain relaxor behaviour. Relaxation behaviour was more prominent from the tan δ plot. BBTN-Ba seems to show the maximum relaxor behaviour among all.

The relaxor behaviour can be characterized by parameters such as degree of frequency dispersion (ΔT_m), critical exponent (γ), etc. ΔT_m has been expressed by Eq. 4.11. The ΔT_m of all compositions are listed in Table 4.28. For BBTN-Mg, BBTN-Ca, BBTN-Sr and BBTN-Ba, the ΔT_m equals 20^o, 20^o, 30^o and 40^oC, respectively. So BBTN-Ba showed maximum relaxor behaviour.

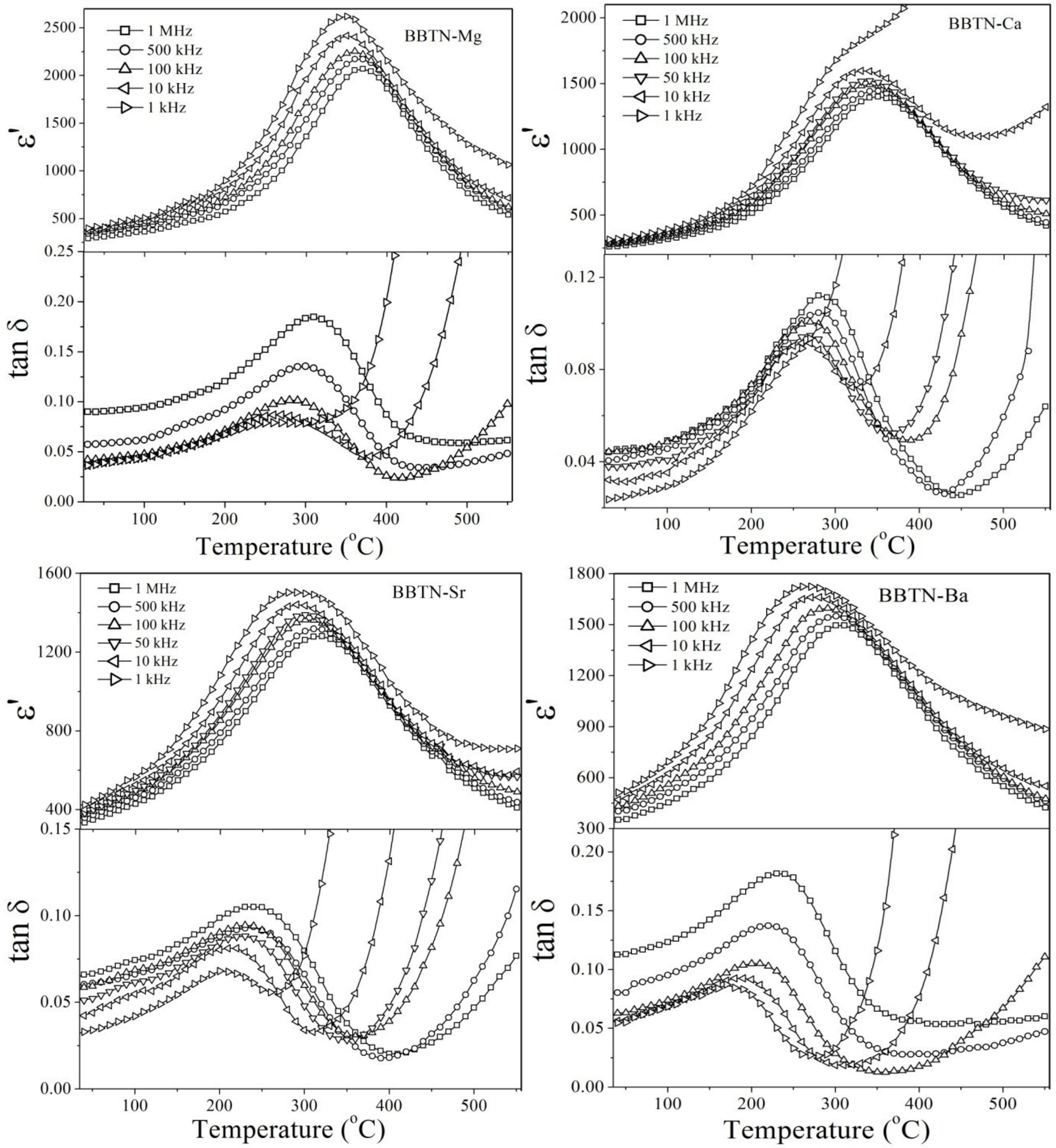

Fig.4.68. Temperature and frequency dependence of ε' and tan δ for BBTN-Mg, BBTN-Ca, BBTN-Sr and BBTN-Ba ceramics.

The critical exponent γ [175] may be calculated on basis of Eq. 4.14. Fig. 4.69 shows the plot of log $(1/\varepsilon' - 1/\varepsilon_m')$ versus log $(T - T_m)$. The γ increases from 1.81 to 1.86 in the order Mg<Ca<Sr<Ba based composition, again highlighting the fact that BBTN-Ba has the highest relaxor behaviour.

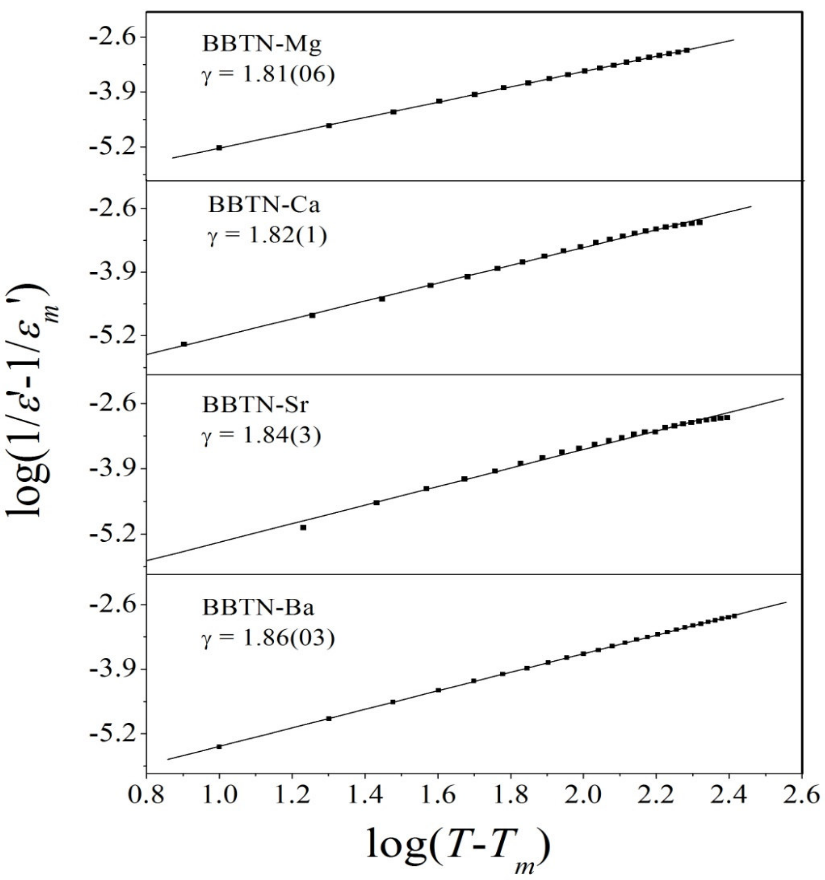

Fig.4.69. Plot of log(1/ε′ – 1/ε$_m$′) versus log(T – T_m) for BBTN-Mg, BBTN-Ca, BBTN-Sr and BBTN-Ba ceramics.

All compositions exhibit broad permittivity maximum with temperature (Fig.4.65). Peak broadening was quantified from the parameter δ [174], represented by Eq. 4.12. The δ parameters of different compositions were calculated by fitting permittivity-temperature data at 100 kHz and are presented in Table 4.28. δ increases from 194 for BBTN-Mg to 264 for BBTN-Ba, in the same order as stated above. The substituting cations create heterogeneous domains, which have their own local Curie temperatures. The distribution of the local Curie temperature was responsible for the broadness of the permittivity versus temperature peak.

All these results indicate that the relaxor behaviour increases in the order BBTN-Mg <BBTN-Ca <BBTN-Sr <BBTN-Ba. The relaxor behaviour in BBT was attributed to the partial occupancy of Ba^{2+} ions in the Bi_2O_2 layer [13]. This leads to the creation of local charge centre in the micro-domains. Along with it, a random electric field was created in the system as positive point charges are formed where Bi^{3+} replaces Ba^{2+} in the perovskite layer and negative charges

are created due to the substitution of Ba^{2+} at Bi^{3+} site in the Bi_2O_2 layer. This inner electric field destroyed the long range ordering resulting in the formation of some polar clusters in the system which gives rise to the relaxor behaviour in BBT [22]. For the present compositions, site mixing among the substituting and host cations may have occurred. So it may be assumed that Mg^{2+}, Ca^{2+}, Sr^{2+} and Ba^{2+} ions not only substitute Bi^{3+} ions but also affects the mixed occupancy in Bi_2O_2 layer. The relaxor behaviour of BBTN-Mg was similar to that of BBT. This may be due to the reason that as Mg^{2+} occupies the Bi_2O_2 layer and it does not affect the perovskite block as well as relaxor behaviour. The relaxor behaviour increased in the order BBTN-Ca<BBTN-Sr<BBTN-Ba. This may be due to the increased introduction of Ba^{2+} in the Bi_2O_2 layer, exaggerating the relaxor behaviour.

The relaxor behavior in ferroelectrics can be modeled by the Vogel-Fulcher relationship [176] given by Eq. 4.15. Fig. 4.70 shows the plot of inverse of T_m versus log of frequency. T_m showed a reasonably good fit to Vogel-Fulcher law for all. The fitted parameters ν_0, E_{vf} and T_f are listed in Table 4.28. T_f was found to decrease from 312 to 207°C in the same order Mg to Ba. This indicated that the interactions between the micro-polar regions with a short-range ferroelectric order decrease from Mg to Ba. E_{vf} of BBTN-Ba was highest in accordance with the fact that the relaxor behaviour was highest in this composition.

Table 4.28. Room temperature permittivity (ε_{rm}), Maximum relative permittivity (ε_m'), maximum permittivity temperature (T_m), degree of frequency dispersion (ΔT_m), degree of diffuseness (δ) at 100 kHz, fitting parameters from Vogel-Fulcher relation (E_{vf}, T_f and ν_0), for BBTN-Mg, BBTN-Ca, BBTN-Sr and BBTN-Ba ceramics.

Formula	**BBTN-Mg**	**BBTN-Ca**	**BBTN-Sr**	**BBTN-Ba**
ε_{rm}	356	290	374	432
ε_m'	2300	1491	1363	1617
T_m (°C)	360	340	300	280
ΔT_m (°C)	20	20	30	40
δ (°C)	194	220	248	264
E_{vf} (eV)	0.0433	0.0356	0.0397	0.0606
T_f (°C)	312	297	250	207
ν_0 (Hz)	5.9×10^9	2.46×10^9	7.40×10^8	9.2×10^8

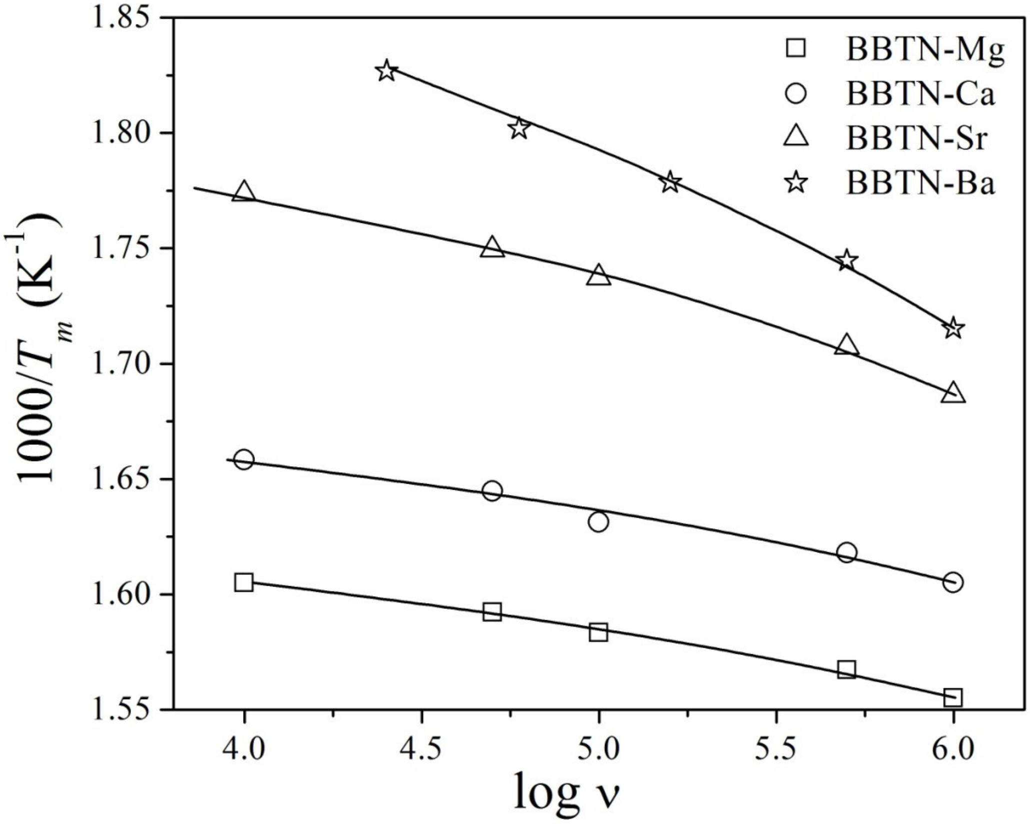

Fig.4.70. Plot of inverse of T_m with log of frequency for BBTN-Mg, BBTN-Ca, BBTN-Sr and BBTN-Ba ceramics.

4.7.2.3 Polarization Hysteresis Characteristics

Fig.4.71 shows the polarization versus electric field (*P*-*E*) hysteresis loop for all compositions under an applied electric field of 60 kV/cm. The $2P_r$ and $2E_c$ values are listed in Table 4.29. $2P_r$ increases from 2.4 to 6.49 μC/cm^2 in the order Mg< Ca< Sr< Ba and $2E_c$ were in the range 33 to 35 kV/cm. Large remnant polarization is usually related to higher distorted structure. Though there was a decrease in the distortion of the oxygen octahedra in the present compositions but the remnant polarization was observed to increase. This may be due to the shifting of T_m towards room temperature which resulted in the formation of a much more saturated hysteresis loop at room temperature. Additionally, the substitution of more ferroelectrically active Nb^{5+} for Ti^{4+} was responsible for the increase in $2P_r$ of these ceramics compared to BBT.

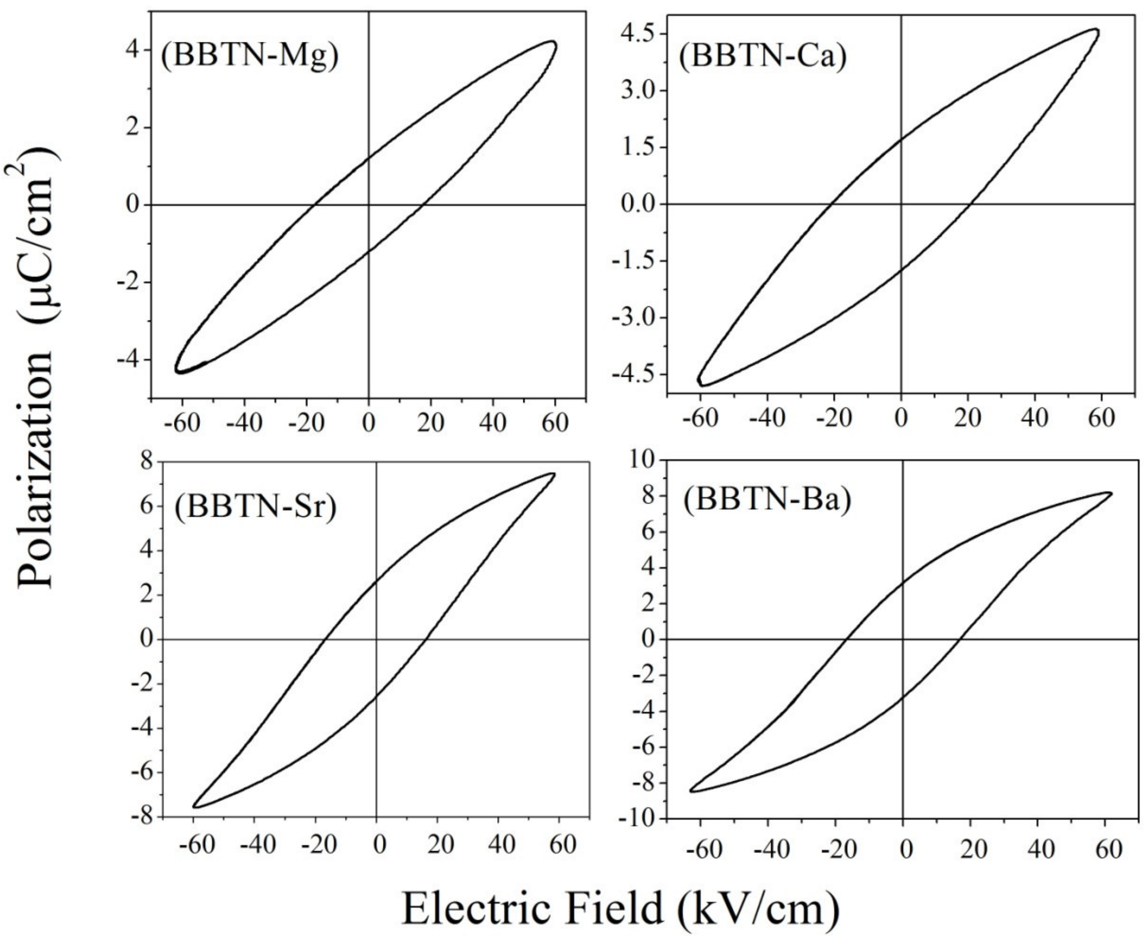

Fig.4.71. *P-E* loop for BBTN-Mg, BBTN-Ca, BBTN-Sr and BBTN-Ba ceramics.

4.7.2.4 Piezoelectric Properties

Table 4.29 shows the room temperature d_{33} coefficients of substituted ceramics. A significant increase of d_{33} co-efficient in BBTN-Mg was observed; with a value of 19 pC/N compared to 11 pC/N of BBT. As already stated, the perovskite unit of orthorhombic BBTN-Mg was affected at *B*-site where Ti^{4+} was replaced by Nb^{5+}. The introduction of more ferroelectrically active Nb^{5+} may be responsible for its increased d_{33}. For other substitutions (Ca^{2+}, Sr^{2+} and Ba^{2+}) the structure was pseudo-tetragonal and the tilting of TiO_6 octahedra decreased. This may result in a decrease of the d_{33} coefficients for others.

Table 4.29. Remnant polarization ($2P_r$), Coercive field ($2E_c$) and Piezoelectric coefficient (d_{33}), for BBTN-Mg, BBTN-Ca, BBTN-Sr and BBTN-Ba ceramics.

Formula	**BBTN-Mg**	**BBTN-Ca**	**BBTN-Sr**	**BBTN-Ba**
d_{33} (pC/N)	19	7	3	2
$2P_r$ (μC/cm^2)	2.4	3.42	5.27	6.49
$2E_c$ (kV/cm)	35	40	32	33

4.7.2.5 Impedance Spectroscopy

Fig. 4.72 shows the Cole-Cole plot for BBTN-Mg, BBTN-Ca, BBTN-Sr and BBTN-Ba ceramics at 550^{o}C. The plots for all the compositions show the presence of two distinct arcs. The bigger curve towards the high frequency side arises due to the contribution from the bulk (grain and grain boundary) and the low frequency curve was associated with the sample/electrode interface. To extract the resistance and capacitance values from the plot, similar methodology to the previous chapters were employed. From the resistance values thus obtained, *dc* conductivity was calculated from Eq. 4.18.

From the plot of log σ_{dc} versus inverse of temperature, E_{dc} was calculated based on Eq. 4.19 and are listed in Table 4.30. E_{dc} was maximum for BBTN-Ba. The difference in the morphology of the grains and their aspect ratio may be the reason behind such behaviour. E_{dc} values for the ceramics studied in the present case were quite high compared to that of the BBT, as the aspect ratio of all the compositions were less compared to BBT.

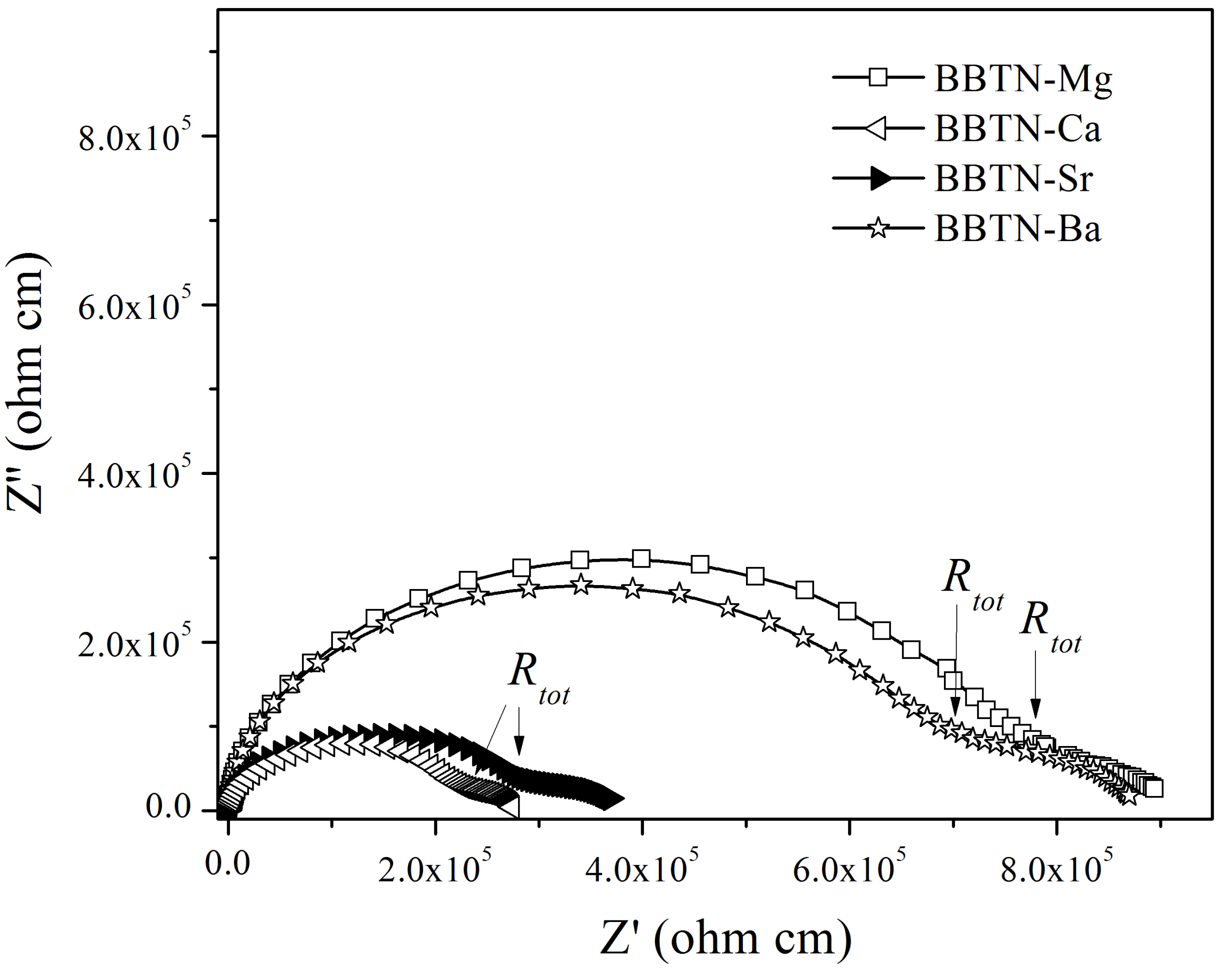

Fig.4.72. Cole-Cole plot for the complex plane at 550°C for BBTN-Mg, BBTN-Ca, BBTN-Sr and BBTN-Ba ceramics.

Table 4.30. *dc*-conductivity (σ_{dc}) at 550°C, Activation energy (E_{dc}) for BBTN-Mg, BBTN-Ca, BBTN-Sr and BBTN-Ba ceramics.

Formula	**BBTN-Mg**	**BBTN-Ca**	**BBTN-Sr**	**BBTN-Ba**
σ_{dc} ($\Omega^{-1}cm^{-1}$) grain	1.28 x 10^{-6}	4.22 x 10^{-6}	3.26 x 10^{-6}	1.41 x 10^{-6}
E_{dc} (eV)	0.477	0.474	0.485	0.619

4.7.3 Conclusions

$BaBi_{3.8}M_{0.2}Ti_{3.8}Nb_{0.2}O_{15}$ (M = Mg, Ca, Sr, Ba) ceramics were synthesized through the modified chemical route. Crystal structure was orthorhombic in case of Mg-based compound and that was tetragonal for Ca, Sr and Ba-based compounds. Rietveld analysis revealed that Mg^{2+} ions seemed to occupy the Bi-site in the Bi_2O_2 layer compared to the other cations occupying *A*-site of perovskite block. The room temperature permittivity increased substantially (~432) for Ba-based compound due to the shifting of T_m towards room temperature. An increased ε_m' (~2300) and d_{33} piezoelectric coefficient (~19 pC/N) were found in Mg-based compound. Relaxor behaviour increased in Ba-based compound due to the increased order of cation mixing in Bi_2O_2 layer. All the compositions displayed increased remnant polarization, with a maximum value of ~6 μC/cm^2 for Ba-based compound. The most significant finding of this study was the solubility of Mg^{2+} in BLSF structure.

Chapter V

Conclusions

5.1 Conclusions

The objective of present work was to study the effect of some isovalent and aliovalent substitutions on the structural, ferroelectric and piezoelectric properties of $BaBi_4Ti_4O_{15}$. The materials were synthesized through a modified chemical route. Following substitutions were investigated: (a) La^{3+} for Bi^{3+}, (b) Zr^{4+} for Ti^{4+}, (c) $(Na^{+}+La^{3+})/2$ for Ba^{2+}, (d) $(Nb^{5+}+Al^{3+})/2$ for Ti^{4+}, (e) Nb^{5+} for Ti^{4+} with compensation of Na^{+} for Ba^{2+}, (f) Ba^{2+} or Sr^{2+} or Ca^{2+} or Mg^{2+} for Bi^{3+} in combination with Nb^{5+} for Ti^{4+}.

Some of the significant findings are as follows:

(i) Pure and substituted $BaBi_4Ti_4O_{15}$ powders were synthesized by a modified chemical route. $BaBi_4Ti_4O_{15}$ phase was formed at 1000°C and the material was sintered to a dense body at ~1100°C.

(ii) La^{3+} was solid soluble in $BaBi_{4-x}La_xTi_4O_{15}$ in the range $0.1 \leq x \leq 1.0$. The diffuseness and relaxor behaviour of the ceramics were found to increase with increasing La^{3+} concentration. Composition with $x = 0.3$ showed highest $2P_r$ and lowest $2E_c$. The d_{33} coefficient of $x = 0.1$ composition was significantly high (~23 pC/N). A significantly low *dc* conductivity was observed at $x = 0.3$ composition.

(iii) The solid solubility limit for Zr^{4+} in $BaBi_4Ti_{(4-x)}Zr_xO_{15}$ was up to $x = 0.2$. However, the lattice parameters increased upto $x = 0.5$ due to the increased (super saturated) solubility of Zr^{4+} in presence of grain boundary ZrO_2 containing phases. Though relaxor behaviour decreased and vanished at $x = 0.5$, the permittivity-temperature peak broadened sufficiently. The dielectric loss of $x = 0.2$ composition was lowest.

(iv) The unit cell parameters decreased with increase in Na^{+} and La^{3+} substitution for Ba^{2+} in $(Ba_{1-x}Na_{x/2}La_{x/2})Bi_4Ti_4O_{15}$. The composition with $x = 0.25$, exhibited an enhanced permittivity. All the substituted compositions exhibited a significant decrease in dielectric loss and *dc* conductivity.

(v) The solid solubility limit for Nb^{5+} and Al^{3+} in $BaBi_4Ti_{4-x}Nb_{x/2}Al_{x/2}O_{15}$ was also $x = 0.2$. A significant increase in the peak permittivity and d_{33} coefficient was observed. The $x = 0.2$ composition displayed a significant reduction in the *dc* conductivity.

(vi) The maximum solubility of Nb^{5+} in $Ba_{(1-x)}Na_xBi_4Ti_{(4-x)}Nb_xO_{15}$ was x=0.5. The relative permittivity increased for the compositions upto $x = 0.2$. The d_{33} coefficient was maximum at $x = 0.1$ composition and the composition with $x = 0.2$ was most resistive.

(vii) $BaBi_{3.8}M_{0.2}Ti_{3.8}Nb_{0.2}O_{15}$ ($M = Mg^{2+}$, Ca^{2+}, Sr^{2+}, Ba^{2+}) ceramics displayed a change from orthorhombic structure to tetragonal with increase in *M*-cation radii. Rietveld analysis showed that the Mg^{2+} occupied the Bi-site in the Bi_2O_2 layer. A significant increase in peak permittivity ε_m' (~2300) and piezoelectric coefficient d_{33} (~19 pC/N) was observed for Mg^{2+} substituted ceramics. The relaxor behaviour increased in Ba^{2+} substituted composition. All compositions displayed an increased remnant polarization, and that was maximum for Ba^{2+} substituted ceramics (~6 $\mu C/cm^2$).

Overall Conclusion:

Prime intention of the work was to enhance the dielectric properties, relaxor behaviour, remnant polarization, piezoelectric coefficient and suppress loss of substituted $BaBi_4Ti_4O_{15}$.

a) In general, dielectric property of BBT can be increased by increasing orthorhombicity of the structure. The maximum probability of increasing the orthorhombicity is by substituting *A*-site cation by smaller ionic radii cation. The increase in orthorhombicity leads to an increase in tilting or distortion of the perovskite block, thus increasing the ferroelectricity of the system. The dielectric loss of the system can be decreased by substituting with cations which have higher bond strength compared to Ba-O, Bi-O and Ti-O bond. Dielectric loss can also be decreased by substituting Bi^{3+} by less volatile cation. This results in a decreased formation of Bi and oxygen vacancies, decreasing the loss.

b) Relaxor behaviour of BBT, in general, may be enhanced by substituting the *A*-site cation by Ba^{2+} or by rare earth cations with similar ionic radii. Relaxor behaviour of the ceramics is increased by increase in the mixed site occupancy of the Ba^{2+} and Bi^{3+} cation.

c) The piezoelectric coefficient of BBT may be enhanced by cation which decreases the oxygen vacancy of the system. The decrease in oxygen vacancy decreases the domain pinning caused by the presence of vacancies in the vicinity of the domains.

d) In BBT, substitution of Ti^{4+} by Nb^{5+} is observed to play a very promising role in increasing its ferroelectric and piezoelectric properties. Nb^{5+} tends to go an off-centre displacement, which may be responsible for increase in these properties.

5.2 Scope for Future Work

The scopes of the future works are:

a) The effect of simultaneous La^{3+} substitution for Bi^{3+} and ($Nb^{5+}Al^{3+}$) substitution for Ti^{4+} on the properties in $BaBi_4Ti_4O_{15}$.

b) Effect of La^{3+} substitution for Bi^{3+} on the relaxor properties of optimized $BaBi_{3.8}Ba_{0.2}Ti_{3.8}Nb_{0.2}O_{15}$ ceramics.

c) Effect of La^{3+} substitution for Bi^{3+} on the piezoelectric properties of optimized $BaBi_{3.8}Mg_{0.2}Ti_{3.8}Nb_{0.2}O_{15}$ ceramics.

d) A detailed investigation of the structure of substituted $BaBi_4Ti_4O_{15}$ with respect to above cation occupancies.

REFERENCES

[1] B. Aurivillius, Ark. Kemi 1 (1949) 463.

[2] C.A.P.de Araujo, J.D. Cuchiaro, L.D. McMillan, M. Scott, J.F. Scott, Nature 374 (1995) 627.

[3] B.H. Park, B.S. Kang, S.D. Bu, T.W. Noh, J. Lee, W. Joe, Nature 401 (1999) 682.

[4] S. Obregon Alfaro, A. Martinez-de la Cruz, Applied Catalysis A: General 383 (2010) 128.

[5] H. Yan, H. Zang, M.J. Reece, X. Dong, Appl. Phys. Lett. 87 (2005) 082911.

[6] F. Chu, D. Damjanovic, O. Steiner, N. Setter, J. Am. Ceram. Soc. 78 (1995) 3142.

[7] H.S. Shulman, M. Testorf, D. Damjanovic, N. Setter, J. Am. Ceram. Soc. 79 (1996) 3124.

[8] J.A. Horn, S.C. Zhang, U. Selvaraj, G.L. Messing, S. Trolier-McKinstry, J. Am. Ceram. Soc. 82 (1999) 921.

[9] S.K. Rout, E. Sinha, A. Hussain, J.S. Lee, C.W. Ahn, I.W. Kim, S.I. Woo, J. Appl. Phys. 105 (2009) 024105.

[10] S.H. Hong, S. Trolier-McKinstry, G. L. Messing, J. Am. Ceram. Soc. 83 (2000) 113.

[11] P. Goel, K.L. Yadav, Physica B 382 (2006) 245.

[12] R. Mazumder, A. Sen, H.S. Maiti, Mater. Lett. 58 (2004) 3201.

[13] J. Tellier, P. Boullay, D. B. Jennet, D. Mercurio, Solid State Sciences 10 (2008) 177.

[14] E.C. Subbarao, J. Phys. Chem. Solids 23 (1962) 665.

[15] H.C. Gupta, Archana, V. Luthra, J. Mol. Struct. 984 (2010) 204.

[16] M. Tripathy, R. Mani, J. Gopalakrishnan, Mater. Res. Bull. 42 (2007) 950.

[17] J. Tellier, Ph. Boullay, M. Manier, D. Mercurio, J. Solid State Chem. 177 (2004) 1829.

[18] R.E. Newnham, R.W. Wolfe, J.F. Dorrian, Mater. Res. Bull. 6 (1971) 1029.

[19] A.D. Rae, J.G. Thompson, R.L.Withers, Acta Crystallogr. Sect. B: Struct. Sci. 48 (1992) 418.

[20] S.K. Kim, M. Miyama, H. Yanagida, Mater. Res. Bull. 31 (1996) 121.

[21] M. Stachiotti, C. Rodriguez, C.A. Draxl, N. Christensen, Phys. Rev. B 61 (2000) 14434.

[22] R.Z. Hou, X.M. Chen, Y.W. Zeng, J. Am. Ceram. Soc. 89 (2006) 2839.

[23] C. Miranda, M.E.V. Costa, M. Avdeev, A.L. Kholkin, J.L. Baptista, J. Eur. Ceram. Soc. 21 (2001) 1303.

[24] M. Shimazu, J. Tanaka, K. Muramatsu, M. Tsukioka, J. Solid State Chem. 35 (1980) 402.

[25] C.M. Wang, L. Zhao, J.F. Wang, S. Zhang, T.R. Shrout, Phys. Status Solidi RRL 3 (2009) 7.

[26] M.V. Ramana, S.R. Kiran, N.R. Reddy, K.V.S. Kumar, V.R.K. Murthy, B.S. Murty, Mater. Chem. and Phys. 126 (2011) 295.

[27] L.E. Cross, Ferroelectrics 151 (1994) 437.

[28] B.J. Kennedy, Y. Kubota, B.A. Hunter, Ismunandar, K. Kato, Solid State Commun. 126 (2003) 653.

[29] B.J. Kennedy, Q. Zhou, Ismunandar, Y. Kubota, K. Kato, J. Solid State Chem. 181 (2008) 1377.

[30] K.M. Elsabawy, M.M. Sekkina, M.A. Asker, M.H. El-Newehy, Solid State Sciences 12 (2010) 1094.

[31] S. Jin, I.M. Salvado, Maria Elisabete V. Costa, Mater. Res. Bull. doi:10.1016/j.materresbull.2010.11.029.

[32] T. Takenaka, K. Sakata, Jpn. J. Appl. Phys. 19 (1980) 31.

[33] T. Takenaka, K. Sakata, Jpn. J. Appl. Phys. 55 (1984) 1092.

[34] L. Pardo, A. Castro, P. Millan, C. Alemany, R. Jimenez, B. Jimenez, Acta. Mater. 48 (2000) 2421.

[35] H.X. Yan, C.G. Li, J.G. Zhou, W.M. Zhu, L.X. He, Y.X. Song, Jpn. J. Appl. Phys. 39 (2000) 6339.

[36] H.X. Yan, C. Li, J.G. Zhou, W.M. Zhu, L.X. He, Y.X. Song, Y.H. Yu, Jpn. J. Appl. Phys. 40 (2001) 6501.

[37] H. Yan, H. Zhang, Z. Zhang, R. Ubic, M. J. Reece, J. Eur. Ceram. Soc. 26 (2006) 2785.

[38] M.E. Fuentes, A. Mehta, L. Lascano, H. Camacho, R. Chianelli, J.F. Fernandez, L. Fuentes, Ferroelectrics 269 (2002) 159.

[39] S.N. Achary, S.J. Patwe, A.K. Tyagi, Mater. Chem. Phys. 73 (2002) 186.

[40] S. Ahn, Y. Noguchi, M. Miyayama, T. Kudo, Mater. Res. Bull. 35 (2000) 825.

[41] M. Alga, A. Ammar, B. Tanouti, A. Outzourhit, F. Mauvy, R. Decourt, J. Solid State Chem. 178 (2005) 2873.

[42] A. Snedden, S.M. Blake, P. Lightfoot, Solid State Ionics 156 (2003) 439.

[43] A.Q. Jiang, H.G. Li, L.D. Zhang, J. Appl. Phys. 83 (1998) 4878.

[44] S.R. Dhage, Y.B. Khollam, S.B. Deshpande, V. Ravi, Mater. Res. Bull. 38 (2003) 1601.

[45] Y. Du, J. Fang, M. Zhang, J. Hong, Z. Yin, Q. Zhang, Mater. Lett. 57 (2002) 802.

[46] S.P. Gaikwad, S.B. Dhesphande, Y.B. Khollam, Violet Samuel, V. Ravi, Mater. Lett. 58 (2004) 3474.

[47] A.M. Umabala, M. Suresh, A.V. Prasadarao, Mater. Lett. 44 (2000) 175.

[48] A.V. Murugan, S.C. Navale, V. Ravi, Mater. Lett. 60 (2006) 1023.

[49] N.L. Amsei-Junior, A.Z. Simoes, L.S. Cavalcante, F. Moura, E. Longo, J.A. Varela, J. Alloys Compd. 461 (2008) 326.

[50] C. Belver, C. Adan, M. Fernandez-Garcia, Catalysis Today 143 (2009) 274.

[51] M.W. Chu, M.T. Caldes, Y. Piffard, A.M. Marie, E. Gautier, O. Joubert, M. Ganne, L. Brohan, J. of Solid State Chem. 172 (2003) 389.

[52] P. Duran, C. Moure, M. Villegas, J. Tartaj, A.C. Caballero, J.F. Fernandez, J. Am. Ceram. Soc. 83 (2000) 1029.

[53] M.J. Godinho, P.R. Bueno, M.O. Orlandi, E.R. Leite, E. Longo, Mater. Lett. 57 (2003) 2540.

[54] D. Xie, W. Pan, Mater. Lett. 57 (2003) 2970.

[55] P.C. Joshi, A. Mansingh, M. Nkanalasanan, S. Chandra, Appl. Phys. Lett. 59 (1991) 2390.

[56] L. Cui, Y.J. Hu, Physica B 404 (2009) 150.

[57] X.W. Dong, K.F. Wang, J.G. Wan, J.S. Zhu, J.M. Liu, J. Appl. Phys. 103 (2008) 094101.

[58] C.A. Randall, N. Kim, J.P. Kucera, W. Cao, Thomas R. Shrout, J. Am. Ceram. Soc. 81 (1998) 677.

[59] J.D. Bobic, M.M. Vijatovic, S. Greicius, J. Banys, B.D. Stojanovic, J. Alloys Compds. V 499 (2010) 221.

[60] S.N Achary, S.J Patwe, P.S.R. Krishna, A.B. Shinde, A.K. Tyagi, Pramana-J. Phys. 71 (2008) 935.

[61] C.W. Ahn, H.J. Lee, S.H. Kang, W. Kim, M.S. Choi, J.S. Lee, H.W. Kim, B.M. Jin, J. Electroceram. DOI 10.1007/s10832-007-9308-y.

[62] X.B. Chen, R. Hui, J. Zhu, W.P. Lu, X.Y. Mao, J. Appl. Phys. 96 (2004) 5697.

[63] Y. Li, S. Zhang, T. Sritharan, X. He, W. Fei, Thin Solid Films 517 (2009) 2633.

[64] F. Suhua, Z. Fengqing, W. Peiji, R. Yanxia, J. Rare Earths 26 (2008) 575.

[65] L. Sun, C. Feng, L. Chen, S. Huang, J. Am. Ceram. Soc. 90 (2007) 3875.

[66] Y.M. Sun, Y.C. Chen, J.Y. Gan, J.C. Hwang, Appl. Phys. Lett. 81 (2002) 3221.

[67] W. Li, D. Su, J. Zhu, Y. Wang, Solid State Commun. 131 (2004) 189.

[68] R.Z. Hou, X.M. Chen, J. Eur. Ceram. Soc. 26 (2006) 1379.

[69] S. Huang, C. Feng, M. Gu, Y. Li, J. Alloys Compd. 472 (2009) 262.

[70] P. Fang, H. Fan, J. Li, L. Chen, F. Liang, J. Alloys Compd. 497 (2010) 416.

[71] Y.Y. Yao, C.H. Song, P. Bao, D. Su, X.M. Lu, J.S. Zhu, Y.N. Wang, J. Appl. Phys. 95 (2004) 3126.

[72] D. Chakravarty, P. Singh, S. Singh, D. Kumar, Om Prakash, J. Alloys Compd. 438 (2007) 253.

[73] S.K. Patri, R.N.P. Choudhary, M.M. Raja, J. Alloys Compds. 478 (2009) 9.

[74] H. Lin, Z. Tong, T. Ming-Hua, D. Shui-Feng, Trans. Nonferrous Met. Soc. China 16 (2006) 1154.

[75] D. Guo, L. Zhang, M. Li, J. Liu, B. Yu, J. Am. Ceram. Soc. 91 (2008) 3280.

[76] S.S. Kim, W.J. Kim, Thin Solid Films 484 (2005) 303.

[77] Z.L. Liu, C.C. Wang, M. Chen, Y. Wang, K.L. Yao, Mater. Lett. 58 (2004) 3648.

[78] M.C. Kao, H.Z. Chen, S.L. Young, Mater. Lett. 62 (2008) 3243.

[79] M. Avdeev, A.L. Kholkin, M.E.V. Costa, J.L. Baptista, Key Eng. Mater. 595 (2002) 230.

[80] S. Huang, C. Feng, L. Chen, Q. Wang, J. Am. Ceram. Soc. 89 (2006) 328.

[81] H. Du , Y. Li, H. Li, X. Shi, C. Liu, Solid State Commun. 148 (2008) 357.

[82] H.L. Du, Piezoelect. Acoust. 32 (2009) 247.

[83] P. Fang, H. Fan, J. Li, X. Jia, F. Liang, Solid State Commun. 149 (2009) 2074.

[84] H. Ogawa, A. Yokoi, H. Taketani, Jpn J Appl Phys Part 1, 44 (2005) 7003.

[85] P. Huang, T. Xu, Rare Metal Mater. Eng. 8 (2005) 1226.

[86] Z. Liaoying, L. Guorong, Z. Wangzhong, C. Daren, Y. Qinrui, Mater. Sc. Eng. B 99 (2003) 363.

[87] L. Zheng, G. Li, Q. Yin, K.W. Kwok, J. Am. Ceram. Soc. 89 (2006) 1317.

[88] Z. Xu, R. Chu, J. Hao, Y. Zhang, Q. Chen, L. Zhao, G. Li, Q. Yin, J. Alloys Compds. 487 (2009) 585.

[89] D. Kajewski, Z. Ujma, K. Szot, M. Pawełczyk, Ceram. Inter. 35 (2009) 2351.

[90] L. Sun, C. Feng, L. Chen, S. Huang, X. Wen, Mater. Sc. Eng. B 135 (2006) 60.

[91] J. Hou, R.V. Kumar, Y. Qu, D. Krsmanovic, Scripta Mater. 61 (2009) 664.

[92] C. Karthik, K.B.R. Varma, Mater. Sc. Eng. B 129 (2006) 245.

[93] N. Yasuda, M. Miyayama, T. Kudo, Solid State Ionics 133 (2000) 273.

[94] N. Kumari, K.B.R. Varma, S.B. Krupanidhi, Mater. Sc. Eng. B 153 (2008) 36.

[95] S. R. Das, P. S. Dobal, B. Sundarakannan, R. R. Das, R. S. Katiyar, J. Raman Spectrosc. 38 (2007) 1077.

[96] C.L. Du, S.T. Zhang, G.X. Cheng, M.H. Lu, Z.B. Gu, J. Wang, Y.F. Chen, Physica B 368 (2005) 157.

[97] I.Y. Park, M. Miyayama, T. Kudo, J. Ceram. Soc. Jpn. 107 (1999) 527.

[98] V. Shrivastava, A.K. Jha, R.G. Mendiratta, Mater. Lett. 60 (2006) 1459.

[99] P. Fang, H. Fan, L. Liu, J. Chen, J. Li, J. Alloys Compds. 477 (2009) 828.

[100] I. Coondoo, A.K. Jha, Mater. Lett. 63 (2009) 48.

[101] D. Prasanta, D. Debasis, P. Kausikisankar, P. Panchanan, Solid State Sciences 10 (2008) 1936.

[102] C.M. Wang, S. Zhang, J.F. Wang, M.L. Zhao, C.L. Wang, Mater. Chem. Phys. 118 (2009) 21.

[103] X. Zhang, H. Yan, M. J. Reece, J. Am. Ceram. Soc. 91 (2008) 2928.

[104] K.S. Rao, D.M. Prasad, P.M. Krishna, B. Tilak, K.Ch. Varadarajulu, Mater. Sc. Eng. B 133 (2006) 141.

[105] M.S. Haluska, S.T. Misture, J. Solid State Chem. 177 (2004) 1965.

[106] S. Kumar, K.B.R. Varma, J. Phys. D: Appl. Phys. 42 (2009) 075405.

[107] R.E. Newnham, Mater. Res. Bull. 2 (1967) 1041.

[108] C.M. Wang, L. Zhao, J.F. Wang, L.M. Zheng, J. Du, M.L. Zhao, C.L. Wang, Mater. Sc. Eng. B 163 (2009) 179.

[109] E.V. Ramana, V.V. Kiran, T.B. Sankaram, J. Alloys Compds. 456 (2008) 271.

[110] Y. Noguchi, M.Suzuki, Y. Kitanaka, S. Teranishi, M. Miyayama, Appl. Phys. Lett. 93 (2008) 032904.

[111] C.M. Wang, J.F. Wang, J. Am. Ceram. Soc. 91 (2008) 918.

[112] C.M. Wang, J.F. Wang, C. Mao, X. Chen, X. Dong, Z.G. Gai, M.L. Zhao, J. Am. Ceram. Soc. 91 (2008) 3094.

[113] C.M. Wang, J.F. Wang, Z.G. Gai, M.L. Zhao, L. Zhao, J.X. Xua, N. Yin, C.J. Zhang, S.Q. Sun, G.Z. Zang, R.Q. Chu, Z.J. Xu, Mater. Chem. Phys. 110 (2008) 402.

[114] H. Yan, C. Li, J. Zhou, W. Zhu, L. He, Y. Song, Y. Yu, Jpn. J. Appl. Phys. Part 1 40 (2001) 6501.

[115] W. Wang, S.P. Gu, J. Zhu, X.B. Chen, Integ. Ferroelectr. 85 (2006) 85.

[116] J.Y. Choi, C.H. Choi, K.H. Cho, T.G. Seong, S. Nahm, C.Y. Kang, S.J. Yoon, J.H. Kim, Acta. Materialia 57 (2009) 2454.

[117] J. Qiu, G.Z. Liu, M. He, H.S. Gu, T.S. Zhou, Physica B 400 (2007) 134.

[118] Z. Zhou, X. Dong, H. Chen, H. Yan, J. Am. Ceram. Soc., 89 (2006) 1756.

[119] C. Ang, Z. Yu, Adv. Mater. 18 (2006) 103.

[120] S.Y. Moon, K.S. Choi, K.W. Jung, H. Lee, D. Jung, Bull. Korean Chem. Soc. 23 (2002) 1463.

[121] J.J. Shyu, C.C. Lee, J. Eur. Ceram. Soc. 23 (2003) 1167.

[122] E.I. Henriques, H.J. Kim, M.S. Haluska, D.D. Edwards, S.T. Misture, Solid State Ionics 178 (2007) 1175.

[123] A. Speakman, M.S. Haluska, C.A. Say, S.T. Misture, Solid State Ionics 176 (2005) 2617.

[124] J.K. Kim, T.K. Song, S.S. Kim, J. Kim, Mater. Lett. 57 (2002) 964.

[125] T. Jardiel, A.C. Caballero, M. Villegas, J. Eur. Ceram. Soc. 27 (2007) 4115.

[126] Z.H. Bao, Y.Y. Yao, J.S. Zhu, Y.N. Wang, Mater. Lett. 56 (2002) 861.

[127] A.Z. Simoes, E.C. Aguiar, A. Ries, E. Longo, J.A. Varela, Mater. Lett. 61 (2007) 588.

[128] N.L. Amsei Junior, A.Z. Simoes, R.F.C. Pianno, S.M. Zanetti, E. Longo, J.A. Varela, J. Alloys Compd. 458 (2008) 500.

[129] S.B. Desu, P.C. Joshi, X. Zhang, S.O. Ryu, Appl. Phys. Lett. 71 (1997) 1041.

[130] S. Kumar, K.B.R. Varma, Solid State Commun. 146 (2008) 137.

[131] Y. Noguchi, K. Yamamoto, Y. Kitanaka, M. Miyayama, J. Eur. Ceram. Soc. 27 (2007) 4081.

[132] D. Do, S.S. Kim, J.W. Kim, Appl. Surface Sc. 255 (2009) 4531.

[133] J. Zeng, Y. Li, Q. Yang, Q. Yin, Mater. Sc. Eng. B 117 (2005) 241.

[134] S. Zhang, N. Kim, T.R. Shrout, M. Kimura, A. Ando, Solid State Commun. 140 (2006) 154.

[135] T. Inoue, M. Kobune, J. Abe, T. Yazawa, Ceram. Trans. 196 (2006) 217.

[136] S. Kumar, K.B.R. Varma, Solid State Commun. 147 (2008) 457.

[137] D. Makovec, I. Pribosic, Z. Samardzija, M. Drofenik, J. Am. Ceram. Soc., 84 (2001) 2702.

[138] I. Pribosic, D. Makovec, M. Drofenik, J. Eur. Ceram. Soc. 21 (2001) 1327.

[139] M. Lei, Z. Kun, L. Jixia, W. Qi, Z. Minglei, W. Chunlei, J. Rare Earths 27 (2009) 496.

[140] P. Duran-Martin, B. Jimenez, P. Millan, A. Castro, J. Phys. Chem. Solids 61 (2000) 1423.

[141] B.J. Kalaiselvi, R. Sridarane, R. Murugan, Ceram. Inter. 32 (2006) 467.

[142] R. Sridarane, B.J. Kalaiselvi, B. Akila, S. Subramanian, R. Murugan, Physica B 357 (2005) 439.

[143] H. Du, S. Wohlrab, S. Kaskel, J. Phys. Chem. C 111 (2007) 11095.

[144] C. H. Hervoches, P. Lightfoot, J. Solid State Chem. 153 (2000) 66.

[145] D.B. Jennet, P. Marchet, M.E. Maaoui, J.P. Mercurio, Mater. Lett. 59 (2005) 376.

[146] H. Nagata, S. Matsuzawa, T. Tokutsu, S. Inai, M. Suzuki, Y. Hiruma, T. Takenaka, Ceram. Inter. 35 (2009) 163.

[147] Q.Y. Tanga, Y.M. Kan, Y.G. Li, G.J. Zhang, P.L. Wang, Solid State Commun. 142 (2007) 1.

[148] H. Nagata, T. Takahashi, Y. Yano, T. Takenaka, Key Eng. Mater. 214-215 (2002) 25.

[149] W. Sakamoto, Y. Mizutani, N. Iizawa, T. Yogo, T. Hayashi, S. Hirano, J. Eur. Ceram. Soc. 25 (2005) 2305.

[150] S.K. Singh, H. Ishiwara, Thin Solid Films 497 (2006) 90.

[151] D.H. Kuo, Y.W. Kao, Solid State Commun. 148 (2008) 279.

[152] H. Irie, M. Miyayama, T. Kudo, Key Eng. Mater. 214-215 (2002) 31.

[153] H. Irie, M. Miyayama, T. Kudo, Jpn. J. Appl. Phys. Part 1 40 (2001) 239.

[154] B. D. Cullity, ‘Elements of X-Ray Diffraction’, 2nd Ed, Addision-Wesley. INC (1978).

[155] S. Upadhyay, O. Parkash, D. Kumar, J. Alloys. Compd. 432 (2007) 258.

[156] H. M. Rietveld, J. Appl. Cryst. 2 (1969) 65.

[157] R.A. Young, Rietveld Method, International Union of Crystallography, Oxford University Press (1996).

[158] L. Lutterotti, MAUD version 2.031, 2005, http://www.ing.unitn.it/maud/.
[159] S. Bid, S.K. Pradhan, J. Appl. Cryst. 35 (2002) 517.
[160] S. Bid, S.K. Pradhan, Mater. Chem. Phys. 82 (2003) 27.
[161] S. Bid, S.K. Pradhan, Jpn. J. Appl. Phys. 43 (2004) 5455.
[162] S.K. Pradhan, S. Bid, M. Gateshki, V. Petkov, Mater. Chem. Phys. 93 (2005) 224.
[163] H. Toraya, J. Appl. Cryst. 31 (1998) 333.
[164] H. Toraya, J. Appl. Cryst. 33 (2000) 1324.
[165] S. Yamazaki, H. Toraya, J. Appl. Cryst. 32 (1999) 51.
[166] L. Lutterotti, P. Scardi, P. Maistrelli, J. Appl. Cryst. 25 (1992) 459.
[167] C.B. Sawyer and C.H. Tower, Phys. Rev. 35, 269 (1930).
[168] Y. Xu, Ferroelectric Materials and Their Applications, North-Holland Elsevier Sci. Publ., Amsterdam 1991.
[169] B. Jaffe, W. R. Cook, H. Jaffe, Piezoelectric Ceramics, London and New York 1971.
[170] J. F. Nye, Physical Properties of Crystals, Oxford University Press, Oxford 1957.
[171] A.J. Moulson, J.M. Herbert, Electroceramics: Materials, Properties, Applications. 2nd Edition. 2003 John Wiley & Sons.
[172] J. Tellier, Ph. Boullay, D. Ben Jennet, D. Mercurio, J. Eur. Ceram. Soc. 27 (2007) 3687.
[173] T. Kimura, Y. Yoshida, J. Am. Ceram. Soc. 89 (2006) 869.
[174] V.V. Kirillov, V.A. Isupov, Ferroelectrics 5 (1973) 3.
[175] K. Uchino, S. Nomura, Ferroelectrics 44 (1982) 55.
[176] D. Vielhand, S.J. Jang, L.E. Cross, J. Appl. Phys. 68 (1990) 2916.
[177] A.K. Jonscher, Nature 267 (1977) 673.
[178] C. Ang, Z. Yu, Z. Jing, P. Lunkenheimer, A. Loidl, Phys. Rev. B 61 (2000) 3922.
[179] Z. Zhou, X. Dong, S. Huang, H. Yan, J. Am. Ceram. Soc., 89 (2006) 2939.
[180] R.Z. Hou, X.M. Chen, Maters. Res. Bull. 38 (2003) 63.
[181] R.Z. Hou, X.M. Chen, Solid State Commun. 130 (2004) 469.
[182] S. Rachna, S. Bhattacharyya, S.M. Gupta, J. Phys. Chem. Solids 69 (2008) 822.
[183] V.B. Santos, J.C. M'Peko, M. Mir, V.R. Mastelaro, A.C. Hernandes, J. Eur. Ceram. Soc. 29 (2009) 751.
[184] H. Sun, X.B. Chen, J. Zhu, J.H. He, Y.F. Qian, H. Fang, J. Sol-Gel Sci Technol. 43 (2007) 125.

[185] A.Z. Simoes, C.S. Riccardi, F. Moura, A. Ries, N.L.A. Junior, M. A. Zaghete, B. Stojanovic, E. Longo, J.A. Varela, Mater. Lett. 58 (2004) 2842.

[186] S.M. Huang, C.D. Feng, L.D. Chen, X.W. Wen, Solid State Commun. 133 (2005) 375.

[187] J.A. Zavala, M.E. Villafuerte-Castrejon, F. Gonzalez, L. Bucio, O. Novelo-Peralta, R.Y. Sato-Berru, J. Ocotlan-Flores, Mater. Charact. 60 (2009) 219.

[188] A. Husur, J.H. Ko, S. Kojima, S.S. Lee, M.S. Jang, J. Korean Phys. Soc. 41 (2002) 763.

[189] Y. Shimakawa, Y. Kubo, Y. Tauchi, H. Asano, T. Kamiyama, F. Izumi, Z. Hiroi, Appl. Phys. Lett. 79 (2001) 2791.

[190] K.R. Kendall, C. Navas, J.K. Thomas, H.C. Zur Loye, Chem. Mater. 8 (1996) 642.

[191] D.Y. Saurez, I.M. Reaney, W.E. Lee, J. Mater. Res. 11 (2001) 3139.

[192] R.D. Shannon, Acta Cryst. A32 (1976) 751.

[193] C.M. Wang, L. Zhao, J.F. Wang, M.L. Zhao, Z.G. Gai, W.B. Su, J. Du, L.M. Zheng, Mater. Chem. Phys. 114 (2009) 1004.

[194] R.A. Armstrong, R.E. Newnham, Mater. Res. Bull. 7 (1972) 1025.

[195] J. Zhai, X. Yao, J. Shen, L. Zang, H. Chen, J. Phys. D: Appl. Phys. 37 (2004) 748.

[196] H.T. Martirena, J.C. Burfoot, Ferroelectrics 7 (1974) 151.

[197] S.T. Zhang, Y.F. Chen, J. Wang, G.X. Cheng, Z.G. Liu, N.B. Ming, Appl. Phys. Lett. 84 (2004) 3660.

[198] T.Y. Chiou, D.H. Kuo, Appl. Phys. Lett. 86 (2005) 032910.

[199] H. Wen, X. Wang, W. Zhao, H. Wang, L. Li, Z. Gui, J. Chinese Ceram. Soc. 34 (2006) 1367.

[200] J. Bernard, F. Belnou, D. Houivet, J.M. Haussonne, J. Eur. Ceram. Soc. 25 (2005) 2779.

[201] Y. Shimakawa, Y. Kubo, Y. Nakagawa, T. Kamiyama, H. Asano, F. Izumi, Appl. Phys. Lett. 74 (1999) 1904.

Publications resulting from the Ph. D. Work

1. **A. Chakrabarti**, J. Bera, T.P. Sinha, "*Dielectric properties of* $BaBi_4Ti_4O_{15}$ *ceramics produced by cost-effective chemical method*", **Physica B** 404 (2009) 1498.

2. **A. Chakrabarti**, J. Bera, "*Structure and relaxor behavior of* $BaBi_4Ti_{4-x}Zr_xO_{15}$ *ceramics*", **Current Applied Physics** 10 (2010) 574.

3. **A. Chakrabarti**, J. Bera, "*Effect of La-substitution on the Structure and Dielectric properties of* $BaBi_4Ti_4O_{15}$ *ceramics*", **Journal of Alloys and Compounds** 505 (2010) 668.

4. **A. Chakrabarti**, J. Bera, "*Structure and ferroelectric properties of* $Ba(Bi_{3.8}M_{0.2})Ti_{3.8}Nb_{0.2}O_{15}$ *(M = Mg, Ca, Sr and Ba) ceramics*", **Physica B: Condensed Matter** 406 (2011) 2891.

5. **A. Chakrabarti**, J. Bera, "*Structure and ferroelectric Properties of* $Ba_{1-x}(Na_{x/2}La_{x/2})Bi_4Ti_4O_{15}$ *Ceramics*", To be communicated.

6. **A. Chakrabarti**, J. Bera, "*Ferroelectric and Piezoelectric properties of Nb and Al substituted* $BaBi_4Ti_4O_{15}$" To be communicated.

7. **A. Chakrabarti**, J. Bera, "*Ferroelectric versus relaxor behaviour in Nb substituted* $BaBi_4Ti_4O_{15}$ *with compensation at Ba-site by Na*", To be communicated.

Curriculum Vitae

Arundhati Chakrabarti
D/O Mr.D.K. Chakrabarti,
BL-202, Basanti Colony, Rourkela-769012, INDIA.
Phone No: +91-9437605771 (M)
Email: arundhati.chakrabarti@gmail.com

Date of Birth: 03.05.1982

Education: Ph.D., M.Sc. (Physics)

Research Interest: Ferroelectric Relaxor Ceramic, Electro-Ceramic.

Technical Exposure: Publications: **7**, Conference: **4**

Publications:

1. **A. Chakrabarti**, J. Bera, T.P. Sinha, "*Dielectric properties of $BaBi_4Ti_4O_{15}$ ceramics produced by cost-effective chemical method*", **Physica B** 404 (2009) 1498.
2. **A. Chakrabarti**, J. Bera, "*Structure and relaxor behavior of $BaBi_4Ti_{4-x}Zr_xO_{15}$ ceramics*", **Current Applied Physics** 10 (2010) 574.
3. **A. Chakrabarti**, J. Bera, "*Effect of La-substitution on the Structure and Dielectric properties of $BaBi_4Ti_4O_{15}$ ceramics*", **Journal of Alloys and Compounds** 505 (2010) 668.
4. **A. Chakrabarti**, J. Bera, "*Structure and ferroelectric properties of $Ba(Bi_{3.8}M_{0.2})Ti_{3.8}Nb_{0.2}O_{15}$ (M = Mg, Ca, Sr and Ba) ceramics*", **Physica B: Condensed Matter** 406 (2011) 2891.
5. **A. Chakrabarti**, J. Bera, "*Structure and ferroelectric Properties of $Ba_{1-x}(Na_{x/2}La_{x/2})Bi_4Ti_4O_{15}$ Ceramics*", To be communicated.
6. **A. Chakrabarti**, J. Bera, "*Ferroelectric and Piezoelectric properties of Nb and Al substituted $BaBi_4Ti_4O_{15}$*" To be communicated.
7. **A. Chakrabarti**, J. Bera, "*Ferroelectric versus relaxor behaviour in Nb substituted $BaBi_4Ti_4O_{15}$ with compensation at Ba-site by Na*", To be communicated.

Research Presentations:

1. **A.Chakrabarti**, J.Bera, *"Synthesis of $BaBi_4Ti_4O_{15}$ through Modified Solid-oxide Route and its Characterization"*, National Conference on CMDAYS, 29th-31st August, 2007, Dept. of Physics, N.I.T. Rourkela, India.
2. **A.Chakrabarti**, J.Bera, "*Synthesis of $BaBi_4Ti_4O_{15}$ by novel chemical method and its ferroelectric relaxor behavior*", International Conference of Environmental Resaech (ICER-08) 18th – 20th Dec, 2008, BITs Pilani, Goa, India.
3. **A.Chakrabarti**, J.Bera, "*Relaxor ferroelectric behaviour of $BaBi_4Ti_4O_{15}$ synthesized through semi-oxalate method*", Socio-Economic: Challenges before women scientist, technologists and engineers, 2009, Dept. of Biotechnology, N.I.T., Rourkela, India.
4. **A.Chakrabarti**, J.Bera, "*Structure and Impedance Spectroscopy of $BaBi_{(4-x)}La_xTi_4O_{15}$ Ceramics*", International Conference on Physics of Emerging Functional Materials (PEFM-2010), 22nd-24th Sept. 2010, Bhabha Atomic Research Center, Mumbai, India.